Publicly Accessible Penn Dissertations

2017

Singlet Oxygen Dosimetry For Pleural Photodynamic Therapy

Michele Kim
University of Pennsylvania, mickim@sas.upenn.edu

Singlet Oxygen Dosimetry For Pleural Photodynamic Therapy

Abstract

Photodynamic therapy (PDT) is a promising treatment modality that involves visible light and a photosensitizer to form reactive cytotoxic species, such as singlet oxygen in the case of type II PDT. Dosimetry of PDT has shown to be challenging due to the complex interactions between the key components of PDT: light, photosensitizer, and oxygen. Existing methods of quantifying dose involve monitoring one or two of these quantities. In conventional clinical settings, PDT is prescribed by the light fluence rate (mW/cm^2) and total light fluence (J/cm^2). However, many additional factors influence the effective ``dose'' that is being delivered. Variations in photosensitizer uptake in tumors, tissue oxygenation, and light penetration in tissues of varying tissue optical properties affect the photodynamic efficiency. Using explicit dosimetry, reacted singlet oxygen is calculated based on the measured light fluence, photosensitizer concentration, and oxygen concentration. A macroscopic singlet oxygen model is used for explicit dosimetry, which involves various photochemical parameters.

Relevant photochemical parameters for in vivo explicit dosimetry for a type II photosensitizer benzoporphyrin monoacid ring-A (BPD) were determined using a mouse model, and further validated using a study evaluating long term treatment outcome. Phantom studies were also performed to model the generation of singlet oxygen and compare it with direct measurements using singlet oxygen luminescence dosimetry (SOLD). Fluorescence spectroscopy methods were used to measure the drug concentration. Tissue optical properties were determined by measuring the light fluence and using the diffusion approximation for a point source at a fixed distance. Oxygenation was measured by using a phosphorescence-based probe to measure oxygen partial pressure. These in vivo and in-phantom models provide controlled environments where extensive explicit measurements can be performed to validate the model and recognize which aspects of explicit dosimetry are more critical to correctly correlate treatment outcome and the calculated dosimetric quantity.

The light component of PDT dosimetry was investigated further in a clinical setting. Patients undergoing surgery for malignant pleural mesothelioma are treated with intraoperative PDT. The current treatment protocol for a clinical trial at the University of Pennsylvania involves monitoring light fluence at 8 discrete locations within the pleural cavity. Quantifying and planning treatment can be greatly improved by monitoring the light fluence throughout the entire treatment area in real-time.

This work aims to provide details for singlet oxygen explicit dosimetry (SOED) to quantify the reacted singlet oxygen species during PDT in in vivo and in-phantom models. Furthermore, the light fluence modeling and calculation aspect of PDT dosimetry was developed and improved for an ongoing pleural PDT study at the University of Pennsylvania.

Degree Type
Dissertation

Degree Name
Doctor of Philosophy (PhD)

Graduate Group
Physics & Astronomy

First Advisor
Timothy C. Zhu

Keywords
photodynamic therapy

Subject Categories
Biophysics | Physics

SINGLET OXYGEN DOSIMETRY FOR PLEURAL PHOTODYNAMIC

THERAPY

Michele M. Kim

A DISSERTATION

in

Physics and Astronomy

Presented to the Faculties of the University of Pennsylvania

in

Partial Fulfillment of the Requirements for the

Degree of Doctor of Philosophy

2017

Supervisor of Dissertation:

_____

Timothy C. Zhu, Ph.D.
Professor of Radiation Oncology
Adjunct Associate Professor of Physics

Graduate Group Chairperson:

_____

Joshua R. Klein, Ph.D.
Professor of Physics and Astronomy

Dissertation Committee:
    Jarod C. Finlay, Ph.D., Assistant Professor of Radiation Oncology
    Arjun Yodh, Ph.D., James M. Skinner Professor of Science, Department of
        Physics and Astronomy
    A. T. Charlie Johnson, Ph.D., Professor, Department of Physics and Astronomy
    Masao Sako, Ph.D., Associate Professor, Department of Physics and Astronomy

SINGLET OXYGEN DOSIMETRY FOR PLEURAL PHOTODYNAMIC

THERAPY

COPYRIGHT

2017

Michele M. Kim

Acknowledgements

Thank you to the many people who have been there for me as mentors, colleagues, friends, and family throughout my doctoral education. All of your support made the process that much easier and more interesting.

First, I must thank my advisor, Dr. Timothy Zhu, for providing me with the opportunity to explore avenues of research that allow me to expand my skills as a scientist. With his mentorship, I was always pushing myself, and it has positively affected my work ethic as well as my interest in interdisciplinary fields.

I would also like to thank Dr. Jarod Finlay for his continuous advice and helpful discussions throughout the years. His words and actions have always given me perspective on how to approach challenges in both science and life.

I would not be here today without the help of my various colleagues and collaborators at the University of Pennsylvania. Thank you to my committee members for their time and valuable advice. Rozhin Penjweini, Yi Hong Ong, Baochang Liu, Arash Darafsheh, Xing Liang, Haixia Qiu, and Anna Sharikova were post doctoral researchers in our group throughout the years. They lead by example on how to develop as an experimentalist and as a scientific writer. Conversations with them have helped me tremendously day to day. I must also thank my many mentors and colleagues in the department of Radiation Oncology, Dr. Theresa Busch, Dr. Keith Cengel, Dr. Charles Simone, Dr. Andreea Dimofte, Carmen Rodriguez, Dr. Richard Davis,

ABSTRACT

SINGLET OXYGEN DOSIMETRY FOR PLEURAL PHOTODYNAMIC THERAPY

Michele M. Kim

Dr. Timothy C. Zhu

Photodynamic therapy (PDT) is a promising treatment modality that involves visible light and a photosensitizer to form reactive cytotoxic species, such as singlet oxygen in the case of type II PDT. Dosimetry of PDT has shown to be challenging due to the complex interactions between the key components of PDT: light, photosensitizer, and oxygen. Existing methods of quantifying dose involve monitoring one or two of these quantities. In conventional clinical settings, PDT is prescribed by the light fluence rate (mW/cm^2) and total light fluence (J/cm^2). However, many additional factors influence the effective "dose" that is being delivered. Variations in photosensitizer uptake in tumors, tissue oxygenation, and light penetration in tissues of varying tissue optical properties affect the photodynamic efficiency. Using explicit dosimetry, reacted singlet oxygen is calculated based on the measured light fluence, photosensitizer concentration, and oxygen concentration. A macroscopic singlet oxygen model is used for explicit dosimetry, which involves various photochemical parameters.

Relevant photochemical parameters for *in vivo* explicit dosimetry for a type II photosensitizer benzoporphyrin monoacid ring-A (BPD) were determined using a mouse model, and further validated using a study evaluating long term treatment outcome. Phantom studies were also performed to model the generation of singlet oxygen and compare it with direct measurements using singlet oxygen luminescence dosimetry (SOLD). Fluorescence spectroscopy methods were used to measure the drug concentration. Tissue optical properties were determined by measuring the light fluence and

using the diffusion approximation for a point source at a fixed distance. Oxygenation was measured by using a phosphorescence-based probe to measure oxygen partial pressure. These *in vivo* and in-phantom models provide controlled environments where extensive explicit measurements can be performed to validate the model and recognize which aspects of explicit dosimetry are more critical to correctly correlate treatment outcome and the calculated dosimetric quantity.

The light component of PDT dosimetry was investigated further in a clinical setting. Patients undergoing surgery for malignant pleural mesothelioma are treated with intraoperative PDT. The current treatment protocol for a clinical trial at the University of Pennsylvania involves monitoring light fluence at 8 discrete locations within the pleural cavity. Quantifying and planning treatment can be greatly improved by monitoring the light fluence throughout the entire treatment area in real-time.

This work aims to provide details for singlet oxygen explicit dosimetry (SOED) to quantify the reacted singlet oxygen species during PDT in *in vivo* and in-phantom models. Furthermore, the light fluence modeling and calculation aspect of PDT dosimetry was developed and improved for an ongoing pleural PDT study at the University of Pennsylvania.

Table of Contents

List of Tables

List of Figures

Chapter 1

Introduction

Photodynamic therapy (PDT) is a treatment modality that uses a photosensitizing drug, light, and oxygen to cause local cell damage [1]. The FDA has approved PDT for use with esophageal cancers [2], non-small cell lung cancer [3,4], actinic keratosis [5], and age-related macular degeneration [6,7]. There are also numerous off-label uses and pre-clinical, as well as clinical trials using PDT to treat other cancers including skin cancers [8], bladder cancers [9], prostate cancers [10], head and neck cancers [11], and malignant mesothelioma [12,13]. Unlike chemotherapy, PDT is a highly localized treatment method that can spare healthy cells. Furthermore, conventional radiation therapy uses ionizing radiation that causes DNA damage. PDT uses non-ionizing light and since most PDT photosensitizers do not accumulate in cell nuclei, PDT has a low potential of causing DNA damage, mutations, and carcinogenesis [3,14].
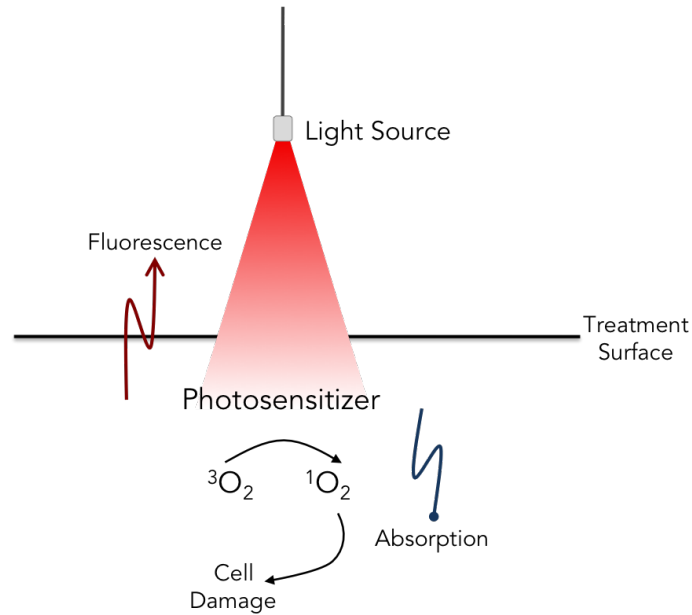
Figure 1.1: Schematic diagram of the light-sensitizer-tissue interactions

Figure 1.1 shows a schematic of the PDT process. The photosensitizer is administered either intravenously, orally, or topically. After the proper drug-light interval (DLI), which depends on the sensitizer, light is delivered to the treatment area. Despite the clear advantages of PDT, much work needs to be done in optimizing treatment doses, PDT delivery methods, and PDT dosimetry. While PDT is the standard care of treatment for certain skin lesions and esophageal cancers in certain areas of the world, improvements in PDT dosimetry are necessary before it is used as a standard in conjunction with existing treatment modalities.

1.1 PDT Dosimetry

Four different dosimetric methodologies can be used for PDT dosimetry: implicit dosimetry, biophysical/biological tissue response monitoring, explicit dosimetry, and direct dosimetry [15]. Two or more of the treatment parameters can be incorpo-

rated into a single metric. Such a metric is PDT dose, the product of light fluence (J/cm^2) and the sensitizer concentration. Other metrics include implicit dosimetry with photosensitizer photobleaching through monitoring the photosensitizer fluorescence. Photobleaching during PDT is the irreversible destruction of ground state sensitizer. This has the advantage of being relatively simple and practical to implement. Fluorescence spectroscopic measurements of photoproducts associated with photobleaching have also been used as a metric; however, this is not applicable to all photosensitizers. Biophysical and biological tissue response monitoring can also be used as a dosimetric method. This includes monitoring vascular shut down, treatment induced necrosis, and blood flow monitoring by laser Doppler or diffuse correlation spectroscopy. It is not yet clear whether any of these specific techniques could be used to predict the biological response and hence, outcome.

In conventional clinical settings, PDT is prescribed by the light fluence (mW/cm^2) rate and total light fluence (or "light dose," J/cm^2). However, there are many additional factors which may influence the effective "dose" actually delivered to any particular lesion [16]. Variation in photosensitizer uptake in tumors is present both in humans and in mice [17]. Different tissues show a large range of wavelength dependent optical absorption and scattering coefficients of different tissues, which will affect the light penetration and distribution of light in the target volume [18, 19]. Variability in tissue oxygenation will affect the photodynamic efficiency [20]. Photosensitizers with higher extinction coefficients can significantly increase the absorption to affect the light penetration and cause "self shielding" [21]. Furthermore, faster tissue oxygen depletion with high fluence rate treatment leads to reduced photodynamic effect [22–25].

Explicit dosimetry involves the measurement of the main components involved in the photodynamic reaction (light, drug, and oxygen) and incorporation of these mea-

surements into a dose model. Sections 3 and 4 will discuss explicit and direct methods (singlet oxygen luminescence dosimetry) in detail, as well as a plan to implement both dosimetry methods concurrently *in vivo*.

Development of photosensitzers that are appropriate for PDT is ongoing, with optical absorption designed to be in the "therapeutic window" (650-850 nm) where the absorption spectrum of hemoglobin permits deeper penetration. Furthermore, treatment light in this region penetrates deeper into the tissue since optical absorption is lower than in other parts of the spectrum [1]. For this work, the photosensitizers considered were benzoporphyrin derivative monoacid ring A (BPD), porfimer sodium (Photofrin), and 2-[1-hexyloxyethyl]-2-devinyl pyropheophorbide-a (HPPH). These have already been used in a clinical setting. Another photosensitizer, Rose Bengal (4,5,6,7-tetrachloro-2',4',5',7'-tetraiodofluorescein) was also investigated in phantoms (liquid solution models to simulate *in vivo* settings) for certain studies.

1.2 Malignant Pleural Mesothelioma (MPM) and PDT

At the University of Pennsylvania, PDT is used as an adjuvant surgically-based treatment modality for patients with malignant pleural mesothelioma. The source of malignant mesothelioma is in the cells lining the pleura and peritoneal cavities, and while naturally occurring mesothelioma is rare, risk is increased with exposure to asbestos [12]. The incidence of mesothelioma in the United States is estimated to be 2500-3000 cases per year, and the most commonly affected patients have a median age of onset of 60 years. Regardless of treatment, median survival is reported to be 6-15 months [12]. Part of the difficulty in treatment of mesothelioma comes from eradicating all of the cancerous cells from the pleural cavity during surgical resec-

tion. In surgical debulking of the cancerous tissue, cells are left behind in the cavity leading to further disease propagation [26]. Several treatment modalities are being investigated that combine surgery with follow-up treatments to kill these remaining cells including chemotherapy, radiation therapy, and PDT [12].

PDT is a promising treatment modality for patients with mesothelioma as it presents only minor toxicities to affect the original treatment course [26]. For this treatment, the patient is administered with the photosensitizer systematically at the appropriate time before surgery and light application. During surgery, the pleural cavity is opened, and light can be delivered using a modified endotracheal (ET) tube that contains the fiber optic light source and is filled with scattering media. Currently at the Hospital of the University of Pennsylvania, the pleural PDT treatment protocol monitors light fluence (measured in J/cm^2) with eight isotropic detectors sutured at different locations in the pleural cavity of a patient, without consideration of the unique qualities of the patient's thoracic cavity. This protocol monitors light at discrete locations, but does not provide information of fluence for the cavity as a whole. It has been shown that the light fluence on the entire pleural surface can be determined for assessing the light fluence uniformity using an infrared (IR) navigation system to track the treatment light [27]. The clinical protocol is approved by the IRB of the University of Pennsylvania.

1.3 Three-dimensional Light Dosimetry

A commercial IR navigation system (Polaris Spectra, NDI, Waterloo, Canada) was introduced to monitor the light source during treatment and to provide real-time treatment guidance. The camera has a pair of stereo cameras that measures the light reflection from a modulated laser source ($\lambda = 850$ nm). This device tracks 9

reflectors that are in a fixed geometry and attached to the light delivery ET tube. The 9 reflectors make up 3 faces with 3 reflectors each and are used to determine the 3D Cartesian coordinates and orientation of the light source with 2 mm accuracy.
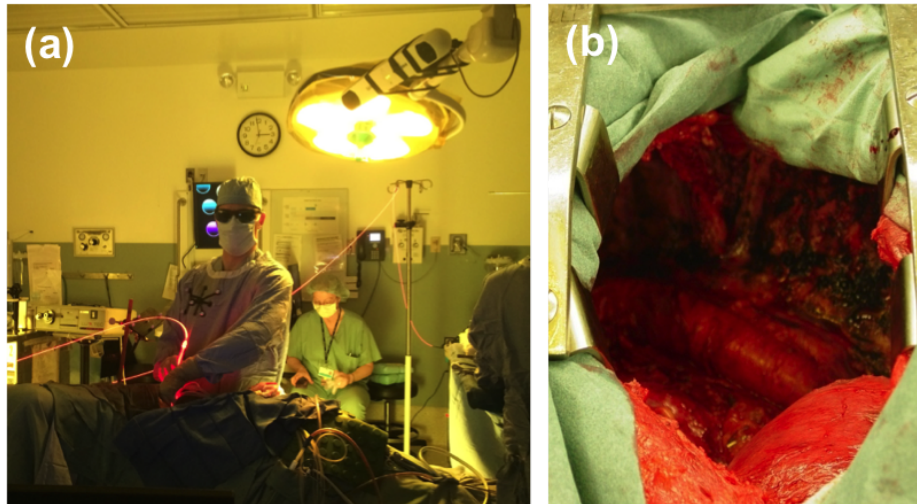
Figure 1.2: PDT of the pleural cavity. (a) The physician delivers the light via a modified endotracheal tube filled with scattering media. The light source is being tracked by an IR camera mounted above the patient (upper right corner). (b) The treatment area is an irregularly-shaped cavity.

1.4 Project Aims and Outline of Thesis

This work aims to provide *in vivo* singlet oxygen-based dosimetry for patients undergoing PDT in the pleural cavity. This involves monitoring the delivered light in real-time during treatment, quantifying the sensitizer concentration throughout the cavity, and determining the reacted singlet oxygen.

Chapter 2 describes the theory behind explicit dosimetry and its requirements. A review of existing photochemical parameters necessary for explicit dosimetry was done to investigate which parameters are already present and studied for in *in vitro* models, such as cell spheroid models, and which need further study. Chapter 3 ad-

dresses the experimental techniques, instrumentation, and algorithms used to perform *in vivo* studies in mouse models and phantom studies. Using these methods, chapter 4 investigates the explicit dosimetry model in liquid phantoms. In addition, explicit dosimetry is compared with singlet oxygen luminescence dosimetry (SOLD) methods. Chapter 5 discusses the parameters determined in *in vivo* environments for the photosensitizer BPD using a mouse model. Chapter 6 expands on verification of the model as well as the parameters by looking at tumor re-growth rates of treated mice. Chapter 7 discusses a translational application, looking deeper into the light dosimetry aspect of clinical PDT dosimetry. Data collected from the Photofrin phase II/III randomized clinical trial is presented in chapter 7. By providing a way to determine the dose being delivered to areas lacking isotropic detectors to directly measure the light fluence, the physician can adjust the treatment to ensure that treatment is uniform. Finally, chapter 8 concludes this work by summarizing the findings and discussing future applications and expansions of the work presented.

Chapter 2

General Theory of Reactive Oxygen Species (ROS) Explicit Dosimetry

Photosensitizer photochemical parameters are crucial data in accurate dosimetry for PDT based on photochemical modeling. Progress has been made in the last few decades in determining the photochemical properties of commonly used photosensitizers, mostly in solution or *in vitro*. Recent developments allow for the estimation of some of these photochemical parameters *in vivo*. Furthermore, photochemical parameters that are independent of environmental factors or are universal for different photosensitizers are examined. Most photosensitizers discussed in this chapter are of the type II (singlet oxygen) photooxidation category, although type I photosensitizers that involve other reactive oxygen species (ROS) will be discussed as well. The compilation of these parameters will be essential for ROS modeling of PDT.

2.1 Type I and II oxidation reactions

2.1.1 Photochemical reactions

The PDT kinetics process was described using rate equations in the literature for microscopic and macroscopic models [22, 28–30]. Figure 2.1 shows the energy diagram for the process. The PDT process is started by the absorption of light by the photosensitizer in the ground state, S_0. It is excited into the singlet state, S_1. The S_1 state can spontaneously decay to the ground state with the emission of a photon or heat [30].
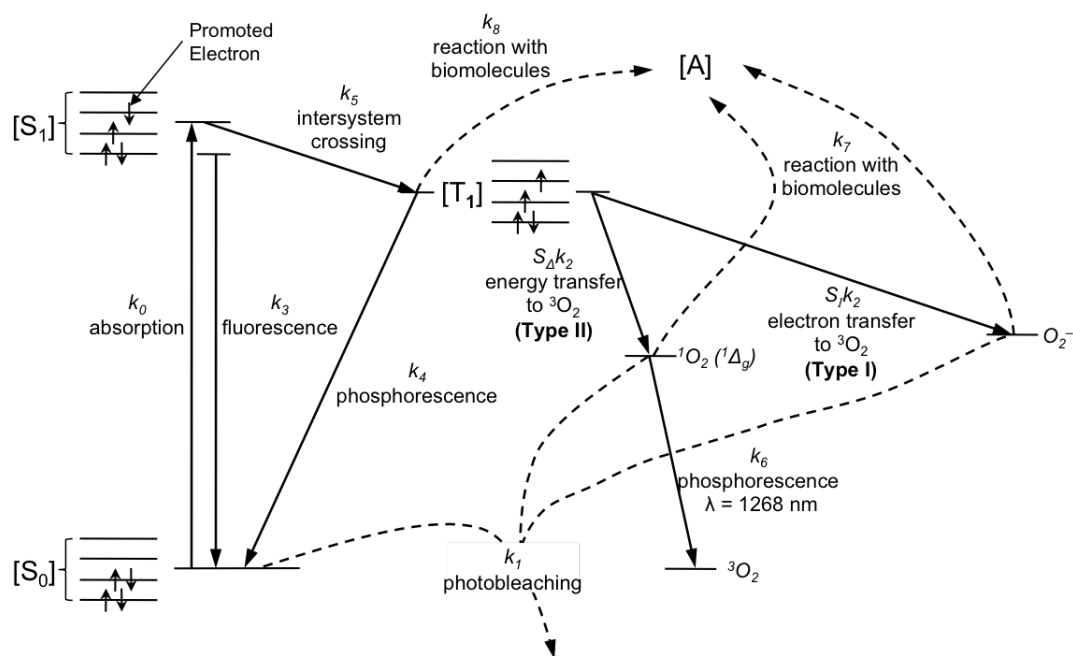
Figure 2.1: Jablonski diagram for the photoactivation of photosensitizer in the presence of oxygen and biomolecules. The photosensitizer in its ground state (S_0) absorps a photon and is excited to its first singlet state (S_1). It converts to its excited triplet state (T_1) via intersystem crossing (ISC). From T_1, energy is transferred to ground state molecular oxygen ($^3O_2$), creating reactive singlet oxygen ($^1O_2$) for a typical type II reaction. In type I reactions, the triplet photosensitizer will transfer an electron to $^3O_2$ which will react with molecular targets to produce radical species, or alternatively, interact directly with the acceptor [A], without oxygen mediation.

$$[S_0] \; \underset{k_3}{\overset{k_0}{\rightleftarrows}} \; [S_1] \tag{2.1}$$

This is a reversible process. The monomolecular absorption rate, k_0 (s^{-1}), is proportional to the light fluence, ϕ, and the extinction coefficient, ε. The monomolecular decay rate, k_3(s^{-1}) is the rate from S_1 to S_0. The decay rate due to fluorescence (radiative) is k_{3R} (s^{-1}) and the internal conversion (non-radiative) decay rate is k_{3NR} (s^{-1}), so that $k_3 = k_{3NR} + k_{3R}$ [31]. The photosensitizer in its ground state can interact with singlet oxygen and ROS to form a photoproduct $[SO_2]$. This can be described by the decay rate constant, $k_1 = k_{11} + k_{12}$ (μM^{-1}s^{-1}).

$$[S_0] + [^1O_2] \; \xrightarrow{k_{12}} \; [SO_2] \text{ (type II)} \tag{2.2a}$$

$$[S_0] + [O_2^-] \; \xrightarrow{k_{11}} \; [SO_2] \text{ (type I)} \tag{2.2b}$$

Similarly, the bimolecular decay rate, k_2 (μM^{-1}s^{-1}), describes the rate of interactions by collisions between the triplet state photosensitizer $[T_1]$ and ground state oxygen $[^3O_2]$. A fraction (S_Δ) of the interactions yields singlet oxygen (2.3), while another fraction (S_I) yields the superoxide anion $(O_2^{-\cdot})$ as in (2.4).

$$[T_1] + [^3O_2] \; \xrightarrow{S_\Delta k_2} \; [S_0] + [^1O_2] \text{ (type II)} \tag{2.3}$$

$$[T_1] + [^3O_2] \; \xrightarrow{S_I k_2} \; [S_0^{+\cdot}] + [O_2^-] \text{ (type I)} \tag{2.4}$$

$$[T_1] + [^3O_2] \; \xrightarrow{S_{NL} k_2} \; [S_0] + [^3O_2] \tag{2.5}$$
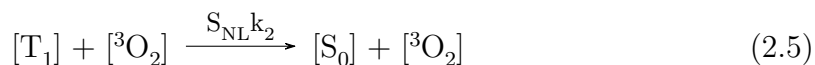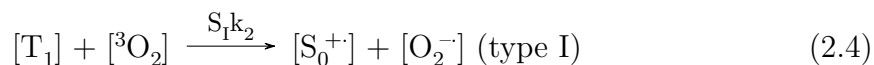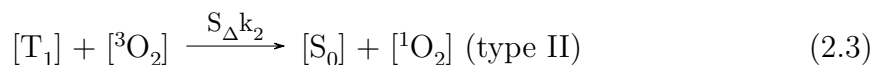
The last equation shows the fraction ($S_{NL} = 1 - S_\Delta S_I$) of the interactions between the triplet state photosensitizer and ground state oxygen to produce non-luminescent decay of $[T_1]$ and do not yield singlet oxygen and/or superoxide anion. Physical quenching can also occur where singlet oxygen is converted back to triplet oxygen ($^1O_2 \longrightarrow {}^3O_2$).

Triplet decay rate and intersystem crossing of the photosensitizer are described by the monomolecular reaction rates k_4 and k_5 (s^{-1}), respectively. The triplet decay rate includes both the radiative (k_{4R}) and non-radiative (k_{4NR}) decay rate constants.

$$[T_1] \xrightarrow{k_4} [S_0] \tag{2.6}$$

$$[S_1] \xrightarrow{k_5} [T_1] \tag{2.7}$$

The phosphorescence (or luminescence) of singlet oxygen is described by the monomolecular decay rate k_6 (s^{-1}).

$$[^1O_2] \xrightarrow{k_6} [^3O_2] \tag{2.8}$$

This reaction produces the signature luminescence at 1270 nm. However, there are also non-luminescent reactions of $^1O_2$, such as solvent quenching or physical quenching of $^1O_2$, mentioned above [32].

The oxidation of biomolecular acceptors, $[A]$, is described by the decay rate $k_7 = k_{71} + k_{72}$ (μM^{-1}s^{-1}).

$$[^1O_2] + [A] \xrightarrow{k_{72}} [AO_2] \text{ (type II)} \tag{2.9a}$$

and

$$[O_2^{-}] + [A] \xrightarrow{k_{71}} [AO_2] \text{ (type I)} \qquad (2.9b)$$

Triplet state photosensitizer can also react with the biological substrate $[A]$ with the bimolecular rate constant, k_8 ($\mu M^{-1}s^{-1}$). For typical type II reactions, however, this term is considered to be small since singlet oxygen is much more reactive than triplet state photosensitizer.

$$[T_1] + [A] \xrightarrow{k_8} [T_1A] \qquad (2.10)$$

In *in vivo* settings, the concentration of biomolecular acceptors is very large, resulting in a dominant $k_7[A]$ term. However, there can be singlet oxygen quenchers ($[Q]$) that convert $^1O_2$ back to ground state $^3O_2$. This can be described by the bimolecular reaction rate constant k_9 ($\mu M^{-1}s^{-1}$).

$$[^1O_2] + [Q] \xrightarrow{k_9} [^3O_2] + [Q] \qquad (2.11)$$
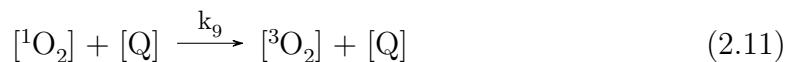
Table 2.1 summarizes the definition of all rate constants used here along with their conventional names.

Table 2.1: Definition of photochemical reaction rate constants

Symbol*	Definition
k_0, k_a (s^{-1})	Photon absorption rate of photosensitizer as a function of photosensitizer concentration (in μM), $k_0 = \varepsilon\phi/h\nu$, for $\phi =$100 mW/cm^2.
k_1, k_{os} (μM^{-1}s^{-1})	Bimolecular decay rate for ^{1}O$_2$ (k_{12}) and ROS (k_{11}) reactions with ground-state photosensitizer
k_2, k_{ot} (μM^{-1}s^{-1})	Bimolecular rate of triplet photosensitizer quenching by ^{3}O$_2$
	$\quad S_I k_2$ Reactions involving triplet state and electron transfer to ^{3}O$_2$ (type I)
	$\quad S_\Delta k_2$ Reactions involving triplet state and energy transfer to ^{3}O$_2$ (type II)
k_3, k_f (s^{-1})	Fluorescence decay rate of first excited singlet state photosensitizer to ground state photosensitizer including internal conversion (non-radiative, k_{3NR}) and fluorescent (radiative, k_{3R}) terms
k_4, k_p (s^{-1})	Phosphorescence decay of the photosensitizer triplet state to ground state photosensitizer, including radiative (k_{4R}) and non-radiative (k_{4NR}) components
k_5, k_{isc} (s^{-1})	Intersystem crossing (ISC) decay rate from first excited photosensitizer to triplet state photosensitizer
k_6, k_d (s^{-1})	Phosphorescence (or luminescence) decay rate of ^{1}O$_2$ to ^{3}O$_2$
k_7, k_{oa} (μM^{-1}s^{-1})	Bimolecular decay rate of reaction of type II ^{1}O$_2$ (k_{72}) and type I ROS (k_{71}) with biological substrate $[A]$
k_8, k_{ta} (μM^{-1}s^{-1})	Bimolecular decay rate constant for reaction of triplet photosensitizer with substrate $[A]$
k_9, k_{oq} (μM^{-1}s^{-1})	Bimolecular decay rate constant for the quenching reaction of ^{1}O$_2$ by a quencher $[Q]$

* The first symbol is used in this thesis. The second symbol is also commonly found in the literature

2.1.2 Kinetics of type I reactions

Type I photooxidation reactions are described by the bimolecular reaction rate $S_I k_2$ ($\mu M^{-1} s^{-1}$) with the fraction of triplet interactions that lead to type I reactions, described in Eq. (2.4). In a type I reaction, the photosensitizer can undergo electron transfer with oxygen to generate a superoxide anion ($O_2^{-\cdot}$). Superoxide anion, its protonated form $HO_2^{\cdot}$, and other radicals such as hydroxyl radicals ($HO^{\cdot}$) cause cell damage to different degrees. Notice that even though all ROSs are generated by the superoxide anion ($O_2^{-\cdot}$) for type I photosensitizer, there are many additional pathways to generate ROS that are not all included in Fig. 2.2, details of which can be found elsewhere [33]. For simplicity, we have combined these interactions as a direct interaction with superoxide anion (2.9b). Other reactions involve the reaction of the triplet state $[T_1]$ with the molecular substrate directly, described by the reaction rate k_8 ($\mu M^{-1} s^{-1}$) and Eq. (2.10).
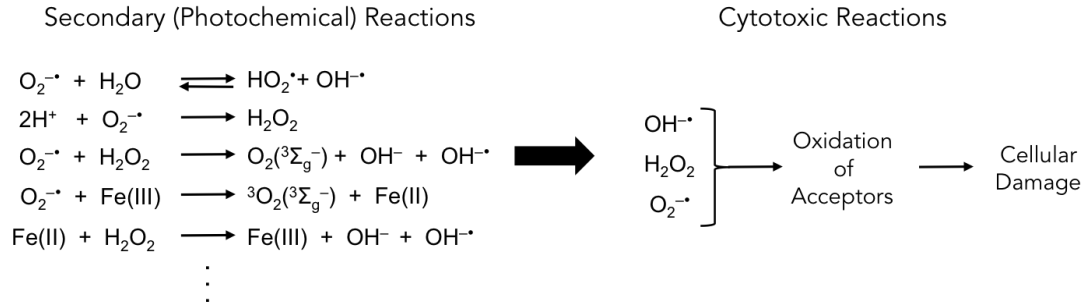
Figure 2.2: Secondary (photochemical) reactions for type I photosensitizers to generate the resulting reactive oxygen species ($HO^{\cdot}$, H_2O_2, $O_2^{-\cdot}$). Other redox active metals are also pertinent for generation of ROS and should be included as part of secondary reactions in "...". ROS will in turn oxidate acceptors in cells to cause cellular damage [33, 34].

2.1.3 Kinetics of type II reactions

Diatomic Oxgen Energy States

The electronic behavior of molecular oxygen results from the arrangement of two electrons in the outer π_g shell (it has a total of 16 electrons since Z $=$ 8 for each O atom) [35, 36]. Molecular oxygen has an electron configuration in which orbitals are designated as even parity (g $=$ gerade) or odd parity (u $=$ ungerade) [34]:

$$(1\sigma_g)^2(2\sigma_u)^2(2\sigma_g)^2(2\sigma_u)^2(3\sigma_g)^2(1\pi_u)^4(1\pi_g)^2$$

where the π_g orbital (formally an open shell) has three possible electron spin arrangements giving rise to three energetically different species: Ground state molecular oxygen ($^3\Sigma_g^-$), and two singlet states($^1\Sigma_g^+$ and $^1\Delta_g$). Because $^1\Delta_g$ oxygen lifetimes are in the microsecond range, they can undergo bimolecular reactions whereas the $^1\Sigma_g^+$ oxygen lifetime is short (due to its fast interconversion to $^1\Delta_g$ oxygen) and is therefore chemically unreactive [37].

Photosensitization routes to $^1\Delta_g$ and $^1\Sigma_g^+$ are of interest; however, the longer lifetime of the former relates to its reactivity. Chemical reactivity has been generated for $^1\Delta_g$ oxygen with biomolecules. Consequently, the bimolecular reaction rates have been investigated for the disappearance of and oxidation by $^1\Delta_g$ oxygen (labeled as $^1O_2$ in this thesis).

The reactions of singlet oxygen with substrates can be defined by the rate constants (k_{72}, k_6). k_{72} (also commonly referred to as k_{oa} in the literature) is the the chemical reaction rate constant of $^1O_2$ which accounts for the rate of formation of oxygenated products and gives the rate of disappearance of $^1O_2$ induced by the substrate, $[A]$. This is related to how readily the product is consumed and can depend on the reaction environment. k_6 (also commonly referred to as k_d in the literature) is the rate constant for the natural decay of $^1O_2$ back to $^3O_2$ (also called solvent quench-

ing). For example, amines efficiently deactivate $^1O_2$ back to $^3O_2$ by charge-transfer quenching, and carotenoids efficiently deactivate $^1O_2$ back to $^3O_2$ by energy-transfer quenching [38–41].

2.1.4 Explicit model of type I and II photodynamic interactions

For both type I and II primary photochemical reactions, a set of coupled differential equations can be used to describe the PDT process [30, 34, 42–46]

$$\frac{d[S_0]}{dt} = -k_0[S_0] - k_{12}[^1O_2]([S_0]+\delta) - k_{11}[O_2^{-\cdot}]([S_0]+\delta) + k_2[T_1][^3O_2] + k_3[S_1] + k_4[T_1]$$

(2.12)

$$\frac{d[S_1]}{dt} = -(k_3+k_5)[S_1] + k_0[S_0]$$

(2.13)

$$\frac{d[T_1]}{dt} = -k_2[T_1][^3O_2] - k_4[T_1] + k_5[S_1] - k_8[T_1][A]$$

(2.14)

$$\frac{d[^3O_2]}{dt} = -S_\Delta k_2[T_1][^3O_2] - S_I k_2[T_1][^3O_2] + k_6[^1O_2] + k_9[Q][^1O_2] + \Gamma$$

(2.15)

$$\frac{d[^1O_2]}{dt} = -k_{12}[^1O_2]([S_0]+\delta) + S_\Delta k_2[T_1][^3O_2] - k_6[^1O_2] - k_{72}[A][^1O_2] - k_9[Q][^1O_2]$$

(2.16)

$$\frac{d[O_2^{-\cdot}]}{dt} = -k_{11}[O_2^{-\cdot}]([S_0]+\delta) + S_I k_2[T_1][^3O_2] - k_{71}[A][O_2^{-\cdot}]$$

(2.17)

$$\frac{d[A]}{dt} = -k_{72}[A][^1O_2] - k_{71}[A][O_2^{-\cdot}] - k_8[T_1][A]$$

(2.18)

These equations are based on the kinetic equations of the photochemical reactions using their rate constants, k_0, ..., k_9 (see their definitions in table 2.1). Here, $[S_0]$, $[S_1]$, and $[T_1]$ are the ground, first excited singlet, and triplet photosensitizer concentrations respectively. $[^3O_2]$ and $[^1O_2]$ are the ground triplet and excited state oxygen concentrations. $[O_2^{-\cdot}]$ is the concentration of superoxide anion and represents

the amounts of ROS in a type I mechanism. Γ and $[A]$ are the oxygen supply rate and the concentration of ($^1O_2$ and ROS) acceptors excluding the photosensitizer molecule. $[Q]$ is the concentration of $^1O_2$ quenchers present that will quench $^1O_2$ and convert it back to $^3O_2$. Depending on the methods used to determine the oxygen supply rate in (2.15), the model is divided into microscopic and macroscopic models. In the microscopic model, oxygen diffusion into capillaries, from capillaries into tissue, and diffusion within tissue are used to calculate the Γ term [43]. More details can be found in Ref. [47]. Based on the kinetic equations of the photochemical reactions, the oxygen supply term in a macroscopic theory can be expressed as [28, 30, 44]:

$$\Gamma = g \left(1 - \frac{[^3O_2]}{[^3O_2]_0} \right),\tag{2.19}$$

where g is the macroscopic maximum oxygen supply rate and $[^3O_2]_0$ is the initial tissue oxygen concentration. This term ensures that the oxygen level does not exceed the initial value. In the macroscopic model, the Γ term is assumed to be uniformly distributed everywhere without consideration of oxygen diffusion through the vasculature. The functional form of Eq. (2.19) was validated using forward calculations with standard vascular parameters [48]. Since the spatial scale of light transport is much larger than the spatial scale of oxygen diffusion ($\sim$1 mm versus $\sim$65 μm), the light fluence rate was also set to be a constant within the vasculature model [48, 49].

Due to the short lifetime and diffusion distance of $^1O_2$ in biological media, the term for photobleaching kinetics for ground state photosensitizer undergoing $^1O_2$-mediated bleaching has the low concentration correction constant, δ [50, 51]. $^1O_2$ is generated at the site of the parent photosensitizer molecule. Due to the short diffusion distance (10-100 nm [51, 52]), it has a higher probability of reacting with the parent photosensitizer molecule than with adjacent photosensitizer molecules.

For low photosensitizer concentrations, the rate of photobleaching depends only on the rate of $^1O_2$ generation because the volume through which each $^1O_2$ can diffuse before reacting will contain exactly one photosensitizer molecule, independent of the total photosensitizer concentration. In other words, δ is the concentration of $[S_0]$ where intermolecular distance is equal to the $^1O_2$ diffusion distance [53]. The value of this critical low photosensitizer concentration is estimated to be between 3 and 3000 μM [54]. δ can be expressed as

$$\delta = \frac{1}{d^3 N_A}.$$ (2.20)

Here, d is the diffusion distance of $^1O_2$ in the environment of interest, which can be related to the singlet oxygen lifetime, τ_Δ, by $d = (6D\tau_\Delta)^{1/2}$, where D is the diffusion coefficient for $^1O_2$ and N_A is Avogadro's number [53].

If one only cares about the dynamic processes of PDT in the time scale of a few seconds to hours, then the time derivative on the right hand sides of equations (2.13), (2.14), (2.16), and (2.17) can be set to zero because these processes are known to be very fast ($\sim \mu$s or less) and converge to equilibrium states. Solving for this equilibrium state, the equations become

$$[S_1] = \frac{1}{k_3 + k_5} \frac{\varepsilon}{h\nu} \phi[S_0],$$ (2.21)

$$[T_1] = \frac{k_5}{k_3 + k_5} \frac{1}{k_2} \frac{1}{[^3O_2] + \beta} \frac{\varepsilon}{h\nu} \phi[S_0],$$ (2.22)

$$[^1O_2] = \frac{1}{k_{12}([S_0] + \delta) + k_6 + k_{72}[A] + k_9[Q]} \xi_{II} \frac{[^3O_2]}{[^3O_2] + \beta} \phi[S_0],$$ (2.23)

$$[O_2^{\cdot-}] = \frac{1}{k_{11}([S_0] + \delta) + k_{71}[A]} \xi_I \frac{[^3O_2]}{[^3O_2] + \beta} \phi[S_0],$$ (2.24)

$$\frac{d[S_0]}{dt} = -\left(\xi_{II}\sigma_{II} + \xi_I\sigma_I\right)\frac{[^3O_2]}{[^3O_2] + \beta}([S_0] + \delta)\phi[S_0] - \eta\frac{1}{[^3O_2] + \beta}\phi[S_0], \qquad (2.25)$$

$$\frac{d[^3O_2]}{dt} = \left[-\left(\xi_{II} + \xi_I\right) + \xi_{II}\tau_\Delta(k_6 + k_9[Q])\right]\frac{[^3O_2]}{[^3O_2] + \beta}\phi[S_0] + \Gamma, \qquad (2.26)$$

$$\frac{d[A]}{dt} = -(k_{72}\xi_{II}\tau_\Delta + k_{71}\xi_I\tau_S)[A]\frac{[^3O_2]}{[^3O_2] + \beta}\phi[S_0] - \eta\frac{1}{[^3O_2] + \beta}\phi[S_0]. \qquad (2.27)$$

All of the parameters (ξ, ξ_I, ξ_{II}, σ, σ_I, σ_{II}, τ_f, τ_Δ, τ_S) have been defined in table 2.2. $\sigma = (\sigma_{II}\xi_{II} + \sigma_I\xi_I)/\xi$ where $\xi = \xi_I + \xi_{II}$. For the *in vivo* scenario, it is assumed that the concentration of biological acceptors is large, so $k_{72}[A]\tau_\Delta \approx 1$ and $k_{71}[A]\tau_S \approx 1$. Furthermore, $\sigma_{II}([S_0] + \delta) \ll 1$, and it is assumed that $k_9[Q] \ll k_7[A]$. The simplified model to describe the *in vivo* environment is described in section 3.5. For the in-phantom scenario, while there are no biomolecular singlet oxygen acceptors, Intralipid that was added can react with singlet oxygen to form oxygenated products, so the $k_7[A]$ term was calculated by using a reduced singlet oxygen lifetime in phantoms. Without the addition of a quencher, the $k_9[Q]$ term can be set to 0. When type II reactions dominate, it can be assumed that $\xi \approx \xi_{II}$.

Utilizing equation (2.27), the amount of biological acceptor that has reacted with a reactive oxygen species ($[ROS]_{rx}$) can be defined by the following

$$\frac{d[ROS]_{rx}}{dt} = -f\xi\frac{[^3O_2]}{[^3O_2] + \beta}\phi[S_0] - \eta\frac{1}{[^3O_2] + \beta}\phi[S_0], \qquad (2.28)$$

where f is the fraction of ROS interacting with $[A]$. Here, the first term relates

to the fraction of acceptors that reacted due to ROS-mediated reactions, and the second term relates to the fraction that reacts under hypoxic conditions or any other non-oxygen-mediated reactions, such as triplet interactions. In cases where type II reactions dominate ($S_\Delta \gg S_I$ and $\eta = 0$), the reacted singlet oxygen ($[^1O_2]_{rx}$) can be described by

$$\frac{d[^1O_2]_{rx}}{dt} = -f\xi \frac{[^3O_2]}{[^3O_2] + \beta}\phi[S_0], \tag{2.29}$$

The required photochemical parameters can be reduced from 12 (δ, g, k_0, ..., k_9) to 6 (δ, β, ξ, σ, η, g), with some of the latter expressed as ratios of the former, if one is not interested in modeling $[S_1]$, $[T_1]$, $[^1O_2]$, and $[O_2^{\cdot-}]$. The definitions for the photochemical parameters, ξ, β, η, δ, σ, and g, are shown in table 2.2, along with their relationships to the reaction rate constants.

The specific oxygen consumption rate, ξ, is the PDT oxygen consumption rate per light fluence rate and photosensitizer concentration under the condition that there is an infinite $^3O_2$ supply. σ, the specific photobleaching ratio, is the probability ratio of a ROS (including $^1O_2$ molecule) to react with ground state photosensitizer compared to the ROS (including $^1O_2$ molecule) reacting with a cellular target, $[A]$. Notice that ξ and σ consider interactions of both type I and type II nature. β represents the ratio of the monomolecular decay rate of the triplet state photosensitizer to the bimolecular rate of the triplet photosensitizer quenching by $^3O_2$ [44] and is called the oxygen quenching threshold concentration, meaning the oxygen concentration where the quantum efficiency of singlet oxygen generation is reduced by half [27]. η is the hypoxic consumption rate that describes interactions between the triplet state photosensitizer and the cellular target. It is considered to be "hypoxic" as there is no oxygen involved in the reaction.

Table 2.2 also provides the definitions of several other important photochemi-

cal parameters for a specific photosensitizer. Fluorescence quantum yield (Φ_f) of a compound is defined as the fraction of molecules that emit a photon after direct excitation [55]. The triplet quantum yield (Φ_t) describes the crossover efficiency for photosensitizer to go from the singlet state to the triplet state via intersystem crossing [56]. Similarly, the singlet oxygen quantum yield (Φ_Δ) is given as the efficiency to produce singlet oxygen from the triplet state of a photosensitizer [32]. We have introduced a quantity of superoxide anion quantum yield (Φ_{ROS}) as the efficiency of producing superoxide anion from the triplet state of a photosensitizer. In addition to the quantum yields, the fluorescence lifetime (τ_f), triplet lifetime (τ_t), and singlet oxygen lifetime (τ_Δ) represent mean lifetime of each state (i.e. of the fluorescence state, the triplet state, and of singlet oxygen) [57]. ε is the extinction coefficient (cm^{-1} μM^{-1}) defined as the absorption coefficient of the photosensitizer per concentration.

Table 2.2: Definition of some key parameters used in PDT modeling [34]

Symbol	Definition
β (μM)	Oxygen quenching threshold concentration $\frac{k_4+k_8[A]}{k_2}$
δ (μM)	Low concentration correction
η (cm^2 mW^{-1} s^{-1} μM)	Hypoxic reaction consumption rate $\Phi_t \frac{\varepsilon}{h\nu} \frac{k_8[A]}{k_2}$
ξ (cm^2 mW^{-1} s^{-1})	Specific oxygen consumption rate $\xi = \xi_{II} + \xi_I = S_\Delta \Phi_t \frac{\varepsilon}{h\nu} + S_I \Phi_t \frac{\varepsilon}{h\nu}$
σ (μM^{-1})	Specific photobleaching ratio $\sigma = (\xi_{II}\sigma_{II}+\xi_I\sigma_I)/\xi$ where $\sigma_{II} = k_{12}\tau_\Delta$ and $\sigma_I = k_{11}\tau_S$
g (μM s^{-1})	Macroscopic maximum oxygen supply rate
ε (cm^{-1} μM^{-1})	Photosensitizer extinction coefficient
τ_f (s)	Fluorescence lifetime $\frac{1}{k_3+k_5}$
τ_Δ (s)	Singlet oxygen lifetime $\frac{1}{k_{12}([S_0]+\delta)+k_6+k_{72}[A]+k_9[Q]}$
τ_S (s)	Superoxide anion lifetime $\frac{1}{k_{11}([S_0]+\delta)+k_{71}[A]}$
τ_t (s)	Triplet state lifetime $\frac{1}{k_4+k_2[^3O_2]+k_8[A]}$
$[A]$ (μM)	Singlet oxygen receptors, considered a constant during PDT because it is too large to be changed during PDT.
S_Δ	Fraction of triplet state photosensitizer-$^3O_2$ reactions to produce $^1O_2$
S_I	Fraction of triplet state photosensitizer reactions involved in type I reactions
S_{NL}	Fraction of triplet state photosensitizer reactions that are non-luminescent $S_\Delta + S_I + S_{NL} = 1$
Φ_Δ	Singlet oxygen quantum yield $S_\Delta \frac{k_5}{k_3+k_5}$
Φ_{ROS}	Reactive oxygen species/superoxide anion quantum yield $S_I \frac{k_5}{k_3+k_5}$
Φ_f	Fluorescence quantum yield $\frac{k_5}{k_3+k_5} \frac{k_{3R}}{k_3}$, where k_{3R} is fluorescence radiative decay rate between S_I and S_0
Φ_t	Triplet quantum yield $\frac{k_5}{k_3+k_5}$

2.1.5 Relationship between rate parameters and the photo-chemical parameters

The rate constants for each of the reactions described previously can be determined by knowing some of the basic photochemical parameters mentioned before including the singlet oxygen lifetime (τ_Δ), the fluorescence lifetime (τ_f), the triplet lifetime (τ_t), and the triplet quantum yield (Φ_t), all of which are measurable quantities with existing technologies.

The photon absorption rate of the photosensitizer is given by knowing the extinction coefficient (ε) of the photosensitizer, the fluence rate ($\phi = 100$ mW cm^{-1}), Plank's constant (h), and the frequency of light used for treatment (ν)

$$k_0 = \frac{\varepsilon}{h\nu} \tag{2.30}$$

The reaction rates involving $^1O_2$ (k_{12}, k_6, k_{72}) can be determined by measuring the singlet oxygen lifetime using SOLD. The relationship between τ_Δ and the rate constants is the following

$$\tau_\Delta^{-1} = k_{12}([S_0] + \delta) + k_6 + k_{72}[A] + k_9[Q] \tag{2.31}$$

By varying the concentration of $[S_0]$ in water in the absence of any singlet oxygen acceptors, ($[A] = 0$), the plot of τ_Δ^{-1} versus $[S_0]$ will yield a slope which will be k_{12} with a low concentration correction (δ) [53, 58]. Furthermore the extrapolation to $[S_0] = 0$ will yield the value of k_6, provided that the values of δ and k_{12} are known. Adding known concentrations of acceptors will allow for extrapolation of the value k_{72}. The value of δ can be found by investigating photobleaching kinetics and the steady-state singlet oxygen concentration approximation [54].

Similarly, the reactive oxygen species lifetime can be written as

$$\tau_S^{-1} = k_{11}([S_0] + \delta) + k_{71}[A] \tag{2.32}$$

Triplet quantum yield (Φ_t) and fluorescence decay time (τ_f) can be used to calculate k_3 and k_5 with the following equations [31]

$$\tau_f = \frac{1}{k_3 + k_5} \tag{2.33}$$

$$k_3 = \frac{1 - \Phi_t}{\tau_f} \tag{2.34}$$

$$k_5 = \frac{\Phi_t}{1 - \Phi_t} k_3 = \frac{\Phi_t}{\tau_f} \tag{2.35}$$

Rate reactions involving the triplet state photosensitizer (k_2, k_4, k_8) are related to the triplet state lifetime by

$$\tau_t^{-1} = k_4 + k_2[^3O_2] + k_8[A] \tag{2.36}$$

Triplet state lifetime can also be measured by SOLD. Measurement of the ground state oxygen in a phantom will enable extrapolation of k_2 and k_4 in a linear fit of τ_t^{-1} versus $[^3O_2]$ with the slope gives k_2 and extrapoliation to $[^3O_2] = 0$ gives $k_4 + k_8[A]$. The oxygen quenching threshold concentration β ($= (k_4 + k_8[A])/k_2$) in the macroscopic model can be calculated with the ratio of the two. k_8 can be determined as the slope between τ_t^{-1} and $[A]$. All other photophysical parameters (ξ, σ, η) can be determined using the rate constants and expressions in table 2.2.

The quantum yield for generation of singlet oxygen (Φ_Δ) and reactive oxygen species or superoxide anion (Φ_{ROS}) are important quantities in determining the concentrations of the cytotoxic oxygen species. Both are related to the photosensitizer

triplet quantum yield by

$$\Phi_\Delta = S_\Delta \Phi_t \tag{2.37}$$

$$\Phi_{ROS} = S_I \Phi_t \tag{2.38}$$

Using SOLD techniques, values of Φ_Δ, Φ_t, and Φ_{ROS} can be measured so that S_Δ and S_I can be calculated.

2.2 Experimental methods to determine the rate parameters

The advent of spectroscopic techniques to measure rate constants of photosensitization and oxygenation has opened the way to the determination of their photochemical and photophysical parameters. This section describes a sampling of methods to determine experimental rate parameters and other key photochemical factors. The scope of this review is focused mainly on photochemical parameters *in vivo*. At present, this is only achievable through indirect methods (section 2.2.4) — namely, extrapolation of the parameters in table 2.2 by applying the macroscopic model directly in *in vivo* systems or in phantoms. The potential for direct methods to be applied to *in vivo* systems will be pointed out whenever possible.

2.2.1 Direct methods

Absorption spectroscopy

Absorption spectroscopy refers to a technique that measures the absorption of radiation by a sample. By using a spectrophotometer and a white light source, the extinction coefficient (ε; units cm^{-1} μM^{-1}) of a photosensitizer can be determined by the Beer-Lambert law [59, 60]

$$A = -\ln\frac{I}{I_0} = \varepsilon l c \tag{2.39}$$

where I is the output light intensity, I_0 is the input light intensity, l is the path length of the measured sample, and c is the concentration of the sample (in μM). Typically, absorbance, A, is defined for $l = 1$ cm. Notice the definition of extinction coefficient is $\log_e$ based rather than $\log_{10}$ based. The latter is often the case in chemistry literature and causes ε to be decreased by a factor of 2.30 ($\ln 10$). Figure 2.3 and 2.4 shows an example of the wavelength dependence of ε, also called absorption spectra for photosensitizers BPD and Photofrin from both the literature and experimentally measured methods. Using equation (2.30), the value of k_0 can easily be determined from the measured ε and knowing the measured wavelength, λ, of the light ($h\nu = hc\lambda^{-1}$).

Transient absorption spectroscopy

Transient absorption spectroscopy is an extension of absorption spectroscopy. Also called pump-probe spectroscopy, the absorbance of a sample is measured as a function of time after excitation by a flash of light, usually a pulsed laser, mainly to determine the triplet lifetime of the sensitizer, τ_t [61]. This technique can be used to measure the singlet oxygen quantum yield (Φ_Δ) for a photosensitizer utilizing another chemical

with known singlet oxygen quantum yields [62, 63].

2.2.2 Fluorescence spectroscopy

Photosensitizer fluorescence can be used to determine the concentration ($[S_0]$) of photosensitizer present both *in vivo* and *in vitro* [64, 65]. However, fluorescence signal *in vivo* is affected by the tissue optical properties of scattering and absorption. The reduction of fluorescence signal due to absorption can be accounted for by incorporating an empirical correction factor based on tissue optical properties [10]. Many commonly used photosensitizers produce unique fluorescence spectra when excited at a certain wavelength. Figure 2.3 and 2.4 shows an example of two photosensitizers (BPD and Photofrin) and their fluorescence spectra from both the literature and the basis spectra used for *in vitro* measurements. Fluorescence basis spectra were obtained by excitation of samples with photosensitizer in water by 405 nm laser light. Such emission spectra, corrected for instrument response and tissue optical properties, can be analyzed as a linear combination of fluorescence basis spectra using a singular value decomposition (SVD) fitting algorithm [42]. Fluorescence spectra from phantoms with known photosensitizer concentrations can be used to determine the correction factor for fluorescence due to tissue optical properties as well as the absolute value of $[S_0]$ in an *in vivo* environment [10].
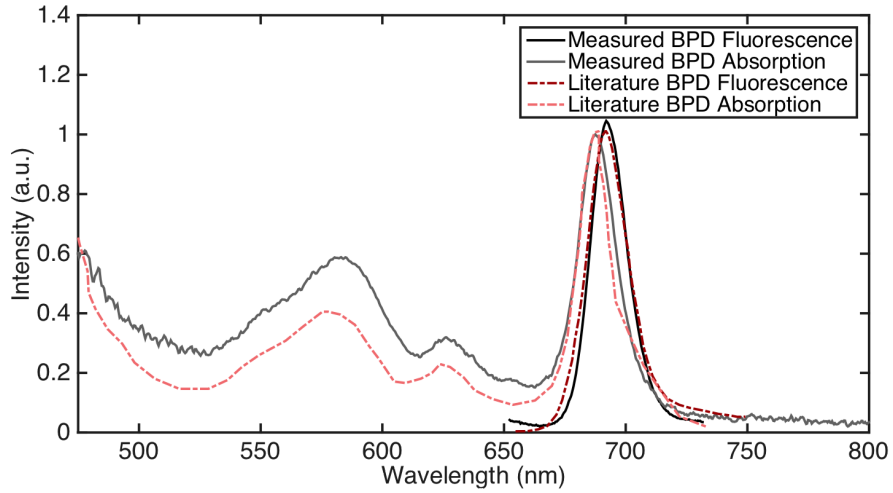
Figure 2.3: Our own experimentally measured fluorescence and absorption spectra (solid black and grey lines) of BPD in water, and fluorescence and absorption spectra (dashed red and light red lines) of BPD in PBS solution from [66–68]. Measured fluorescence was of BPD in water excited by 405 nm laser light, and measured absorption was of BPD in water excited by a white light source.
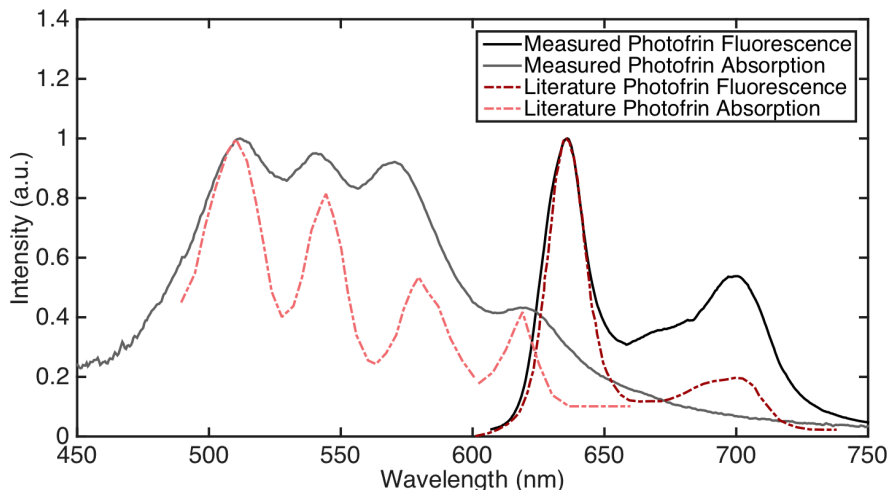
Figure 2.4: Our own experimentally measured fluorescence and absorption spectra (solid black and grey lines) of Photofrin in Intralipid solution, and fluorescence and absorption spectra (dashed red and light red lines) of Photofrin in PBS solution from [68]. The literature absorption curve for Photofrin above 480 nm has been multiplied by 10× for clarity. Measured fluorescence was of Photofrin in water excited by 405 nm laser light, and measured absorption was of Photofrin in water excited by a white light source. Solvent differences account for variations in fluorescence and absorption intensity between measured and literature spectra.

Fluorescence lifetime spectroscopy and imaging (FLI)

Time-resolved fluorescence decay measurements can be used to study details about the structure and dynamics of macromolecules. These measurements are commonly performed with microsecond to picosecond laser sources with high-speed photodetectors [69].

The fluorescence lifetime, τ_f, of photosensitizer can be determined from time-gated spectra along with single photon counting, using a picosecond to microsecond pulsed diode laser for fluorescence excitation. Specific wavelength ranges can be selected to plot the fluorescence exponential decay curve ($e^{-(k_3+k_5)t}$) to yield the decay constant ($k_3 + k_5$), which can be used to calculate $\tau_t = 1/(k_3 + k_5)$ [70].

2.2.3 Phosphorescence spectroscopy

Phosphorescence is similar to fluorescence in that absorbed energy by a substance is released in the form of light. However, phosphorescence occurs on a longer time scale than fluorescence. Besides the decays from monomol $^1O_2$ to $^3O_2 + h\nu$ at 1270 nm (22 kcal mol^{-1}), dimol singlet oxygen molecules ($2\ ^1O_2$) can also decay to 2 moles $^1O_2$ to $^3O_2 + h\nu$ at 634 nm (44 kcal mol^{-1}) and 701 nm [71–75]. The latter (634 nm and/or 701 nm) is readily observed in the gas phase but is often not detected in solution due to other optical signals at these wavelengths. The detection of $^1O_2$ luminescence at 1270 nm is potentially difficult *in vivo* because of the short lifetime of $^1O_2$.

Singlet oxygen luminescence (SOL) detection (or laser flash photolysis)

SOLD (or laser flash photolysis) is a standard technique for identification of short-lived, excited states of photosensitizers and characterization of their reactions [76–78]. It is a popular and precise technique used to directly measure k_6 and k_{72}, where the photosensitizer solution of the substrate is saturated with O_2 and irradiated with a laser at a specific absorption wavelength. The resulting phosphorescence of $^1O_2$ at 1270 nm as a function of time is measured with a time-correlated detector [79]. With the time-correlated singlet photon counting (TCSPC) module, phosphorescence decay characteristics can be measured with a time resolution of $\leq$ 100 ps and a spatial resolution in the subcellular region. With a high pulse repetition rate (40 MHz), the total acquisition time is short (less than 1 s) for each fluorescence decay curve [70]. Production of $^1O_2$ by laser excitation occurs in less than 2 μs, its decay is approximated by a first order exponential decay model (derived from Eq. (2.31)). A Stern-Volmer plot of concentration of substrate $[A]$ versus $1/\tau_\Delta$ (where τ_Δ is the experimentally measured singlet oxygen lifetime), gives a straight line with the slope equal to k_{72} and the y-intercept is equal to k_6

The rate constants for oxidized product formation, k_7, are obtained by competition technique reported by Higgins et al. [80] where the substrate solution containing photosensitizer and an alkene for comparative trapping to deduce the contribution from physical quenching, k_9, can be obtained by difference using equation (2.31), which can also be written as $k_6 + k_7[A] + k_9[Q]$ [81,82]. Unlike unsaturated compounds such as alkenes, amines and polyenes are effective singlet oxygen physical quenchers and protect against photooxygenation [83].

Singlet oxygen quantum yields (Φ_Δ) can be determined from the phosphorescence intensity at 1270 nm from singlet oxygen. Intensity can be recorded as a function of excitation laser energy and of the concentration of the photosensitizer. The slope of this linear plot is proportional to Φ_Δ and is compared to the slope of the same plot for a reference photosensitizer with a known value of Φ_Δ [84].

Measurements of this near-infrared (NIR) luminescence of singlet oxygen in biological environments is difficult due to the short $^1O_2$ lifetime (which can be less than the triplet state photosensitizer lifetime) and its low quantum yield for phosphorescence. However, this can be achieved using a NIR-sensitive photomultiplier tube. Time-resolved analysis shows that $^1O_2$ lifetime is reduced *in vivo* ($\tau_\Delta = 0.03 - 0.18$ μs) compared to lifetime *in vitro* ($\tau_\Delta = 3.0 \pm 0.3$ μs). This may be due to the protein binding to $^1O_2$ in cellular environments [52]. The detector must be sufficiently fast (with a rise time of $\sim$3 ns) for phosphorescence single-photon counting, and it must have a broad, flat spectral response that enables spectral resolution of the $^1O_2$ signal [15]. Examples of detectors used for this purpose include photomultiplier tubes, superconducting nanowire single-photon detectors (SNSPDs) and semiconductor-based single-photon avalanche diodes (SPADs) [85].

The shorter lifetime has been attributed to the rapid quenching of $^1O_2$ by biomolecules combined with a lack of adequately sensitive detectors at NIR wavelengths, since the

luminescence emission is proportional to the lifetime. When exchanging the H_2O solvent for D_2O, the lifetime of singlet oxygen increases by 20-fold. The τ_Δ in D_2O is 69 μs at 20°C and in H_2O 3.5 μs at 20°C [32, 86, 87].

The triplet state lifetime is highly dependent on the molecular oxygen concentration according to a Stern-Volmer relationship described by Eq. (2.36). k_4 can be written as the sum of k_{4R} and k_{4NR}, which are the radiative and non-radiative photosensitizer triplet state decay rate constants. The changes in triplet state lifetime (τ_t) can be used to determine changes in $[^3O_2]$, given k_2 and k_4 are known. In biological systems, $\tau_t \gg \tau_\Delta$ so that the exponential decay of the singlet oxygen luminescence curves are govered by τ_t [15, 88, 89].

Most singlet oxygen luminescence dosimetry (SOLD) studies have been done on microspheres of cells. Detection of SOL from a murine tumor using Photofrin and ATX-S10NAa(II) has been reported [90]. The full luminescence spectrum can be measured by placing a monochromator in front of the detector.

The great impact of SOLD techniques comes with reports that show detection of $^1O_2$ in complex biological systems directly. The integrated detected $^1O_2$ luminescence counts is proportional to the total amount of $^1O_2$ created in the target during PDT and thus is predictive of PDT response [15]. Ultimately it is the cumulative $^1O_2$ dose that determines the biological effect. Furthermore, changes in the effective PDT dose due to oxygen depletion or due to photosensitizer photobleaching can be evaluated with time-resolved SOLD measurements.

2.2.4   Indirect methods

Singlet oxygen explicit dosimetry (SOED) methods have been developed to calculate the reacted singlet oxygen, $[^1O_2]_{rx}$, *in vivo* and *in vitro* for type II photosensitizers. The main cytotoxic agent in type II PDT has been attributed to $^1O_2$ [91]. PDT

efficacy can be correlated to the calculated $[^1O_2]_{rx}$, thus making SOED an effective method of dosimetry for *in vivo* studies as well as in clinical settings. The methodology for SOED for type II photosensitizer can be expanded for reactive oxygen species involving type I photosensitizers, even though it has not been used in existing studies. However, the parameters obtained should include photodynamic action from both type I and type II even though singlet oxygen is predominant for the type II photosensitizers studied. These methods are discussed in more detail in following chapters.

2.2.5 Other methods

In addition to the experimental methods mentioned in this section, there are other techniques that can be used to investigate the presence of the reactive oxygen species. These methods have been mostly used *in vitro*; however, some may be applicable in *in vivo* systems as well. These methods involve fluorescent markers and analytical methods.

Several methods are developed to detect the presence of singlet oxygen and/or HO·. Singlet oxygen can be detected from dioxetanes from [2 + 2] cycloadditions, endoperoxides from [2 + 4] cycloadditions, and allylic hydroperoxides from 'ene' reactions [92, 93]. Simple alkenes often take up 1 equivalent of $^1O_2$. Tandem $^1O_2$ reactions can take place in polyunsaturated compounds, and there are also instances where bisperoxides rearrange to spiro compounds. Peroxides can also be generated through type I reactions that do not involve singlet oxygen. For example, there are electron transfer photooxidation reactions with 9-mesityl-10-methylacridinium ion [94, 95]. It may be noted that ene-derived hydroperoxides and cycloaddition-derived endoperoxides have a toxicity of their own that is separate of singlet oxygen's toxicity [96, 97].

Aromatic compounds such as 9,10-disubstituted anthracenes can trap $^1O_2$ and

be detected by UV-vis spectroscopy [98–100]. Another trapping reaction is 9,10-anthracene-9,10-endoperoxide dipropionate dianion that arises from a [2 + 4] cycloaddition of $^1O_2$ with 9,10-anthracene dipropionate dianion at pH = 10 in water dtected by UV-vis spectroscopy.

Analytical methods such as low-temperature NMR spectroscopy can be used to detect unstable peroxide compounds in reaction mixtures. For example, dioxetane ^{13}C NMR signals are fairly characteristic [101]. Electron-rich olefins such as alkoxy-substituted alkenes react with singlet oxygen and form dioxetanes. Decomposition of dioxetanes is often accompanied by chemiluminescence due to a fragmented excited carbonyl compound [102,103].

Singlet oxygen sensor green (SOSG) is a $^1O_2$-specific fluorescent probe reagent that has been used to quantitatively measure $^1O_2$ that has been produced by determining the reaction rate of SOSG with $^1O_2$. SOSG is a fluorescein-anthracene dye that fluoresces after its initial reaction with $^1O_2$. The endoperoxide product from a [2 + 4] cycloaddition of $^1O_2$ closes off the FRET quenching channel of precursor SOSG [98, 104]. SOSG reacts with $^1O_2$ to produce SOSG endoperosides, which emits a strong fluorescence signal at 531 nm. Φ_Δ has also been determined using SOSG for a porphyrin-based photosensitizer, hematoporphyrin monomethyl ether [105].

Fluorescence probes can also be used to detect highly reactive singlet oxygen species such as hydroxyl radical (HO$^\cdot$) and reactive intermediates of peroxidase. 2-[6-(4?-hydroxy)phenoxy-3H-xanthen-3-on-9-yl] benzoic acid (HPF) and 2-[6-(4?-amino)phenoxy-3H-xanthen-3-on-9-yl] benzoic acid (APF) are two examples of such fluorescent probes [106]. Both probes are reported to be cell-permeable, relatively insensitive to superoxide anion, nitric oxide, $^1O_2$, and alkyl peroxides [107, 108]. APF is ∼5 times more fluorescent during HO$^\cdot$ than HPF [107]. Other fluorescent probes of hydroxyl radical include coumarin- and rhodamine nitroxide-based com-

pounds [109–111].

The methods mentioned in this section can be useful tools to determine *in vivo* and *in vitro* photochemical parameters as well as characteristics of reactive species relevant for a specific photosensitizer.

2.3   A review of existing values of photochemical parameters

Photosensitizers are typically delivered systemically or topically for PDT. The systemic administration involves either oral administration or intravenous injection so that the drug will circulate through the whole body system, and preferentially there will be more drug localized in the target site than in others. An ideal photosensitizer should have low or no toxicities and a fast clearance process. Some systemically delivered photosensitizer are benzoporphyrin derivative (BPD), Photofrin, and 2-[1-hexyloxyethyl]-2-devinyl pyropheophorbide-a (HPPH), which were also used for pre-clinical studies in this work. In contrast with the systemic administration, ALA a pro-drug that reacts with heme to generate the photosensitizer protoporphyrin IX (PpIX), can also be applied topically to perform more localized delivery, which is commonly used for skin treatment.

There are several photosensitizers that have been approved for standard clinical use by the US Food and Drug Administration (FDA) or the European Medicines Agency (EMA) [112, 113]. ALA (a pro-drug that produces PpIX) was approved for the treatment of actinic keratoses in 1999 by the FDA under the trade name Levulan [114] and in 2009 and 2011 by the EMA under the trade name Alacare and Ameluz, respectively. Similar photosensitizer derivatives were developed to also produce PpIX: methyl-ALA was approved by the FDA in 2004 for the treatment of

non-hyperkeratotic actinic keratoses, and hexyl-ALA was approved in Europe in 2006 for the diagnosis of bladder cancer under the trade name Hexvix [115]. In 2000 the FDA approved use of BPD in the treatment of age-related macular degeneration [116]. mTHPC was approved by the EMA for the treatment of head and neck squamous cell carcinomas. Photofrin was approved by the FDA for multiple treatment sites. It was approved for treatment of microinvasive endobronchial non-small cell lung cancer in 1998 and high-grade dysplasia in Barrett's esophagus in 2003.

The photochemical parameters, β, δ, ξ, σ, and g, can be determined using indirect methods that will be described in detail for BPD in chapter 5. Other studies for HPPH and Photofrin have been performed as well [44, 117]. The fundamental photophysical parameters are fairly well-established for most photosensitizers (e.g. ε, τ_f, τ_t) and they can be used to determine some parameters, such as ξ. However, indirect methods *in vivo* can only be used to determine the ratios of rate constants (k_i's, where $i = 1 - 8$), thus additional measurements are necessary to determine individual reaction rate constants.

The photochemical parameters were determined mostly for *in vitro* systems; however, it is reasonable to expect that they will largely remain the same in *in vitro* systems (such as ε, k_0 k_3, and k_5). Some parameters (k_6, and k_{72}) are photosensitizer independent since they are properties of either $^1O_2$ or other reactive oxygen species and they should behave the same. Assumptions can be made that they are the same for all type II photosensitizers.

For BPD, the extinction coefficient (ε) was found to be 0.0783 cm^{-1} μM^{-1} using absorption spectroscopy [66, 118]. The value of k_0 was found at a fluence rate of 100 mW cm^{-2} using equation (2.30) and ε. k_{21} was found by using the approximation $k_{12} \approx \sigma_{II} \cdot k_{71}[A]$, where σ_{II} is the specific photobleaching ratio determined *in vivo* using SOED described in section 5. k_2 was found to be 3×10^3 μM^{-1} s^{-1} using the

observed triplet lifetime (τ_t) in the presence and abscence of $^3O_2$ (equation (2.36)) [66]. Using this value and the measured value for β *in vivo*, k_4 can be found to be $k_4 = \beta \times k_2 = (11.9\mu M) \times (3 \times 10^3 \mu M^{-1} s^{-1}) = 3.6 \times 10^4 s^{-1}$. The values for k_3 and k_5 were found by using the fluorescence lifetime (ε_f) and the triplet quantum yield (Φ_t) and equations (2.33)-(2.35). The value of τ_f was taken from literature using a time-correlated single photon counting method [66]. The value of Φ_t was obtained from literature using laser-induced opto-acustic calorimetry (LIOAC) [66]. The resulting values were $k_3 = (1 - \Phi_t)/\tau_f = (1 - 0.79)/(5.2 \times 10^{-9} s) = 4.04 \times 10^7 s^{-1}$ and $k_5 = \Phi_t/\tau_f = 0.79/(5.2 \times 10^{-9} s) = 1.52 \times 10^7 s^{-1}$. The singlet oxygen lifetime (τ_Δ) in water with no acceptors to react with $^1O_2$ can be used with equation (2.31) to obtain the value of k_6, which is only a property of singlet oxygen and should be photosensitizer independent. Therefore, for all type II photosensitizers, $k_6 = \tau_\Delta^{-1} = (3\mu s)^{-1} = 3.3 \times 10^5 s^{-1}$ [27]. The value of $k_{72}[A]$ *in vivo* is only a property of singlet oxygen and is thus assumed to be the same for all type II photosensitizers. By using the value of τ_Δ in tissue (0.1 μs) and the known value for k_6, $k_{72} = \tau_\Delta^{-1} - k_6 = (0.1\mu s)^{-1} = (3.3 \times 10^5 s^{-1}) = 1 \times 10^7 s^{-1}$ [53]. Since BPD is a type II photosensitizer, there is no significant contribution of type I reactions between $[T_1]$ and $[A]$ so $k_8[A]$ and η were assumed to be 0. The values of ξ, σ, and g were found *in vivo* using the SOED method described in more detail in chapter 5 [119–121]. The low concentration correction, δ, was assumed to be the same for BPD as that of Photofrin. Further experiments are needed to confirm this value for BPD. The fraction of $^1O_2$ producing reactions between $[T_1]$ and $^3O_2$ was determined using the definition of ξ: $S_\Delta = \xi/\Phi_t/\varepsilon \times (h\nu) = (51 \times 10^{-3}$ cm^{2}mW^{-1}s^{-1})/(0.79)/(0.0312μM^{-1}cm^{-1}) $\times$ (6.022 $\times 10^{14}$ cm$^3\mu M^{-1}$) $\times$ (2.72 $\times 10^{-16}$ mW s) = 0.144.

For Photofrin, the extinction coefficient (ε) was found to be 0.0035 cm^{-1} μM^{-1} using absorption spectroscopy [118, 122]. The value of k_0 was found at a fluence

rate of 100 mW cm^{-2} using equation (2.30) and ε. k_{21} was found by using the approximation $k_{12} \approx \sigma_{II} \cdot k_{71}[A]$, where σ_{II} is the specific photobleaching ratio determined *in vivo* using SOED [44]. k_2 was found to be 1.4×10^3 μM^{-1} s^{-1} using the observed triplet lifetime (τ_t) in the presence and abscence of ^{3}O$_2$ (equation (2.36)) [31]. Using this value and the measured value for β *in vivo*, k_4 can be found to be $k_4 = \beta \times k_2 = (11.9\mu\text{M}) \times (1.4 \times 10^3 \mu\text{M}^{-1}$ s$^{-1}) = 1.67 \times 10^4$ s^{-1}. The values for k_3 and k_5 were found by using the fluorescence lifetime (ε_f) and the triplet quantum yield (Φ_t) and equations (2.33)-(2.35). The value of τ_f was taken from literature using a time-correlated single photon counting method [123]. The value of Φ_t was obtained from literature [22, 124]. The resulting values were $k_3 = 2.9 \times 10^7$ s^{-1} [31] and $k_5 = \Phi_t k_3/(1 - \Phi_t) = (0.63) \times (2.9 \times 10^7$ s$^{-1})/(1 - 0.63) = 4.94 \times 10^7$ s^{-1}. Values of k_6 and k_7 were found for Photofrin in the same method described above for BPD. Since Photofrin is a type II photosensitizer, there is no significant contribution of type I reactions between $[T_1]$ and $[A]$ so $k_8[A]$ and η were assumed to be 0. The values of ξ, σ, and g were found *in vivo* using the SOED methods described in more detail in chapter 5 [34, 44]. The low concentration correction, δ, was found from the literature to be 33 μM [53]. The fraction of ^{1}O$_2$ producing reactions between $[T_1]$ and ^{3}O$_2$ was determined using the definition of ξ: $S_\Delta = (3.7 \times 10^{-3}$ cm^{2}mW^{-1}s$^{-1})/(0.63)/(0.0035$ μM^{-1}cm$^{-1}) \times (6.022 \times 10^{14}$ cm$^3\mu$M$^{-1}) \times (3.16 \times 10^{-16}$ mW s$) = 0.319$.

Table 2.3: Selected photosensitizers and their *in vivo* photophysical parameters

Parameter	Photofrin	BPD
ε (cm$^{-1}\mu$M^{-1})	0.0035 @630 nm [122]	0.0783 @690 nm [27, 66]
k_0 (s^{-1}) @100 mWcm^{-2}	1.84[a]	45.13[a]
k_1 (μM^{-1}s^{-1})	7.6×10^2[b][125]	1.7×10^2 [b] (150-550) [119, 121]
k_2 (μM^{-1}s^{-1})	1.4×10^3 [31]	3×10^3 [66]
k_3 (s^{-1})	2.9×10^7 [31]	4.04×10^7[c][66]
k_4 (s^{-1})	1.67×10^4[d]	3.6×10^4[d]
k_5 (s^{-1})	4.94×10^7[e]	1.52×10^7[e]
k_6 (s^{-1})	3.3×10^5[f]	3.3×10^5[f]
$k_7[A]$ (s^{-1})	1×10^7[h] (3×10^6 -3×10^7)	1×10^7[h] (3×10^6 -3×10^7)
$k_8[A]$ (s^{-1})	(0)[h]	(0)[h]
β (μM)	11.9 [125]	(11.9)[i]
δ (μM)	33 [53] (33-150)	33[i] (33-260) [45]
ξ (cm^{2}mW^{-1}s^{-1})	3.7×10^{-3} [27, 124, 125] $(2.9 - 3.7) \times 10^{-3}$	$(55 \pm 15) \times 10^{-3}$ [119, 120, 126]
σ (μM^{-1})	7.6×10^{-5} [125]	$(1.8 \pm 0.3) \times 10^{-5}$ $((1 - 5) \times 10^{-5})$ [119, 120, 126]
η (cm^{2}mW^{-1} s$^{-1}\mu$M)	(0)[h]	(0)[h]
g (μM^{-1} s^{-1})	0.76 [44]	1.7 ± 0.4 [119, 120, 126]
S_Δ	0.319[j]	0.144[j]
Φ_t	0.63 (0.63-0.80) [22, 27, 124]	0.79 [66]
Φ_Δ	0.20[k] (0.12-0.56) [124, 127]	0.11[k] (0.11-0.84) [128, 129]
Φ_f	0.16 [129]	0.05 [66]
τ_f (s)	$(5.5 \pm 1.2) \times 10^{-9}$ [123]	5.2×10^{-9} [66]

[a] Calculated based on the value of ε and $\phi = 100$ mW cm^{-2}: $k_0 = \varepsilon\phi/(h\nu)$. Photofrin: $k_0 = (0.0035\ \mu$M^{-1}cm$^{-1})/(6.022 \times 10^{14}$ cm$^2\mu$M$^{-1}) \times (100$ mW cm$^{-2})/(3.16 \times 10^{-16}$ mW s$) = 1.84$ s^{-1}. BPD: $k_0 = (0.0783\ \mu$M^{-1}cm$^{-1})/(6.022 \times 10^{14}$ cm$^2\mu$M$^{-1}) \times (100$ mW cm$^{-2})/(2.88 \times 10^{-16}$ mW s$) = 45.13$ s^{-1}.

[b] Calculated based on the value of σ and k_7: $k_1 = \sigma \times k_7[A]$. Photofrin: $k_1 = (7.6 \times 10^{-5}\ \mu$M$^{-1}) \times (1 \times 10^7$ s$^{-1}) = 7.6 \times 10^2\ \mu$M^{-1}s^{-1}.

[c] Calculated based on the value of Φ_t and τ_f: $k_3 = (1 - \Phi_t)/\tau_f$. BPD: $k_3 = (1 - 0.79)/(5.2 \times 10^{-9}) = 4.04 \times 10^7$ s^{-1}

[d] Calculated based on the value of β and k_2: $k_4 = \beta \times k_2$. Photofrin: $k_4 = (11.9\ \mu$M$) \times (1.4 \times 10^3\ \mu$M^{-1}s$^{-1}) = 1.67 \times 10^4$ s^{-1}. BPD: $k_4 = (11.9\ \mu$M$) \times (3 \times 10^3\ \mu$M^{-1}s$^{-1}) = 3.6 \times 10^4$ s^{-1}.

^{e} Calculated based on the value of k_3 and Φ_t: $k_5 = \Phi_t k_3/(1-\Phi_t)$.
Photofrin: $k_5 = (0.63) \times (2.9 \times 10^7 \text{ s}^{-1})/(1-0.63) = 4.94 \times 10^7 \text{ s}^{-1}$.
BPD: $k_5 = (0.79) \times (4.04 \times 10^7 \text{ s}^{-1})/(1-0.79) = 1.52 \times 10^7 \text{ s}^{-1}$.

^{f} $\tau_\Delta = 3$ μs in water and 0.16 μs in tissue [53]. $k_6 = \tau_\Delta^{-1} - k_7[A] = (3 \text{ }\mu s)^{-1} = 3.3 \times 10^5 \text{ s}^{-1}$.

^{g} $k_7[A] = \tau_\Delta^{-1} - k_6 = (0.1\mu s)^{-1} - (3.3 \times 10^5 \text{ s}^{-1}) = 1 \times 10^7 \text{ s}^{-1}$, taken from Zhu et al. [47]. The value of $[A]$ is unknown but can be estimated from the value of $k_7 = 235$ μM^{-1}s^{-1} for a well-known singlet oxygen quencher, NaN$_3$ [130]: $[A] = 10^7 \text{ s}^{-1}/235$ μM^{-1}s$^{-1} = 42$ mM. The magnitude of $[A]$ is reasonable considering the singlet oxygen threshold dose can be up to 12 mM [27], without causing any effect on singlet oxygen lifetime. $k_7 = k_{71} + k_{72}$. k_7 is assumed to be $k_7 = k_{72}$ for type II photosensitizers and $k_7 = k_{71}$ for type I photosensitizers.

^{h} Assuming no hypoxic interactions.

^{i} Assumed to be similar to the values for Photofrin.

^{j} *In vivo* values calculated based on the values of ξ, Φ_t, and ε: $S_\Delta = \xi/\Phi_t \varepsilon \times (h\nu)$. Photofrin: $S_\Delta = (3.7 \times 10^{-3} \text{ cm}^2\text{mW}^{-1}\text{s}^{-1})/(0.63)/(0.0035 \text{ }\mu\text{M}^{-1}\text{cm}^{-1}) \times (6.022 \times 10^{14} \text{ cm}^3\mu\text{M}^{-1}) \times (3.16 \times 10^{-16} \text{ mW s}) = 0.319$. BPD: $S_\Delta = (51 \times 10^{-3} \text{ cm}^2\text{mW}^{-1}\text{s}^{-1})/(0.79)/(0.0312 \text{ }\mu\text{M}^{-1}\text{cm}^{-1}) \times (6.022 \times 10^{14} \text{ cm}^3\mu\text{M}^{-1}) \times (2.72 \times 10^{-16} \text{ mW s}) = 0.144$.

^{k} *In vivo* values calculated based on the values of S_Δ and Φ_t: $\Phi_\Delta = S_\Delta \times \Phi_t$. Photofrin: $\Phi_\Delta = (0.319) \times (0.63) = 0.20$. BPD: $\Phi_\Delta = (0.144) \times (0.79) = 0.11$.

Photochemical parameters in phantoms were also investigated using in phantom experiments (described further in chapter 4). The two photosensitizers utilized for these studies were Photofrin (for its clinical relevance) and Rose Bengal (for its availability and higher quantum yield to produce singlet oxygen). The parameters used for calculations in phantom studies are summarized in table 2.4.

Table 2.4: Selected photosensitizers and their in-phantom photophysical parameters

Parameter	Photofrin	Rose Bengal
ε (cm$^{-1}\mu$M^{-1})	0.0035 @ 632 nm[a] 0.0089 @ 523 nm[a]	0.095 @ 549 nm[a] 0.059 @ 523 nm[a]
k_0 (s^{-1}) @100 mWcm^{-2}	1.84[b]	25.69[b]
k_1 (μM^{-1}s^{-1})	6.6×10^{2}[c]	50 [131]
k_2 (μM^{-1}s^{-1})	1.4×10^3 [31]	1.6×10^3 [132]
k_3 (s^{-1})	2.9×10^7 [31]	1.89×10^7 [133]
k_4 (s^{-1})	1.67×10^{4}[d]	1.90×10^{4}[d]
k_5 (s^{-1})	4.9×10^{7}[e]	5.7×10^{8}[e]
k_6 (s^{-1})	2.2×10^{5}[f]	2.7×10^{5}[f]
$k_7[A]$ (s^{-1})	1.9×10^{6}[g]	1.7×10^{6}[g]
$k_8[A]$ (s^{-1})	(0)[h]	(0)[h]
$k_9[Q]$ (s^{-1})	1.17×10^{6}[f]	1.15×10^{5}[f]
β (μM)	11.9 [125]	11.9 [124][i]
δ (μM)	26 ± 5[j]	25 ± 9[j]
ξ (cm^{2}mW^{-1}s^{-1})	$(10.0 \pm 2.6) \times 10^{-3}$ @ 632 nm[k]	$(169 \pm 38) \times 10^{-3}$ @ 523 nm[k]
σ (μM^{-1})	$(6.8 \pm 5) \times 10^{-5}$[l]	$(9.4 \pm 1.2) \times 10^{-6}$[l]
η (cm^{2}mW^{-1})	(0)[h]	(0)[h]
τ_Δ (s)	0.5×10^{-6}[m]	0.5×10^{-6}[m]
τ_f (s)	$(5.5 \pm 1.2) \times 10^{-9}$ [123]	1.18×10^{-10} [134]
τ_t (s)	$(0.43 \pm 0.03) \times 10^{-6}$[m]	$(2.1 \pm 0.2) \times 10^{-6}$[m]
Φ_Δ	0.56 [124, 127]	0.76 [135]
Φ_t	0.63 [22, 27]	0.75 [129, 136]

[a] Measured from absorption spectroscopy

[b] Calculated based on the value of ε and $\phi = 100$ mW cm^{-2}: $k_0 = \varepsilon\phi/(h\nu)$. Photofrin: $k_0 = (0.0035\ \mu$M^{-1}cm$^{-1})/(6.022 \times 10^{14}$ cm$^2\mu$M$^{-1}) \times (100$ mW cm$^{-2})/(3.16 \times 10^{-16}$ mW s$) = 1.84$ s^{-1}. Rose Bengal: $k_0 = (0.059\ \mu$M^{-1}cm$^{-1})/(6.022 \times 10^{14}$ cm$^2\mu$M$^{-1}) \times (100$ mW cm$^{-2})/(3.8 \times 10^{-16}$ mW s$) = 25.69$ s^{-1}.

[c] Calculated based on the value of σ and k_7: $k_1 = \sigma \times k_7[A]$. Photofrin: $k_1 = (6.6 \times 10^{-5}\ \mu$M$^{-1}) \times (1 \times 10^7$ s$^{-1}) = 6.6 \times 10^2\ \mu$M^{-1}s^{-1}.

[d] Calculated based on the value of β and k_2: $k_4 = \beta \times k_2$. Photofrin: $k_4 = (11.9\ \mu$M$) \times (1.4 \times 10^3\ \mu$M^{-1}s$^{-1}) = 1.67 \times 10^4$ s^{-1}. Rose Bengal: $k_4 = (11.9\ \mu$M$) \times (1.6 \times 10^3\ \mu$M^{-1}s$^{-1}) = 1.90 \times 10^4$ s^{-1}.

[e] Calculated based on the value of k_3 and Φ_t: $k_5 = {}^{\Phi_t}/_{(1-\Phi_t)} \cdot k_3$. Photofrin: $k_5 = (0.63)/(1-0.63) \times (2.9 \times 10^7$ s$^{-1}) = 4.94 \times 10^7$ s^{-1}. Rose Bengal: $k_5 = (0.75)/(1-0.75) \times (1.89 \times 10^8$ s$^{-1}) = 5.67 \times 10^8$ s^{-1}.

[f] Determined from measurements described in chapter 4 and figure 4.5, for Photofrin phantoms with Intralipid and Rose Bengal in water. For $k_9[Q]$, $[Q]$ assumed to be 5 mM of NaN$_3$ as per the experiment settings, resulting in $k_9 = 234\ \mu$M^{-1}s^{-1} for Photofrin and 23 μM^{-1}s^{-1} for Rose Bengal.

[g] Calculated for phantom studies with Intralipid using $\tau_\Delta^{-1} = k_1([S_0] + \delta) + k_6 + k_7[A]$ for $[S_0] = 50\ \mu$M and the values of k_1, k_6, and δ provided in the table.

^{h} Assuming no hypoxic or type I interactions. Fig. 4.2 and 4.3 show contributions from η do not model the measured data and require ξ to be larger than possible.

^{i} Assumed to be similar to the value for Photofrin and mTHPC [124].

^{j} Obtained from fitting shown in figure 4.6c (for Photofrin) and 4.7c (for Rose Bengal) using equation (4.3). $\delta = b/m$ where b is the intercept and m is the slope of the linear fit .

^{k} Values were determined from fit to in-phantom experiments described in section 4.1.1 and shown in figure 4.6 and 4.7. Initial guesses were calculated from $\xi = \Phi_{\Delta}\varepsilon/h\nu$. Photofrin: $\xi = (0.56)(0.0035 \text{ cm}^{-1}\mu\text{M}^{-1})/(3.2\times10^{-16} \text{ mWs})/(6.022\times10^{14} \text{ cm}^{-3}\mu\text{M}^{-1} = 10.3\times10^{-3} \text{ cm}^2 \text{ mW}^{-1}\text{s}^{-1}$ @ 632 nm. Rose Bengal: $\xi = (0.76)(0.059 \text{ cm}^{-1}\mu\text{M}^{-1})/(3.8\times10^{-16} \text{ mWs})/(6.022\times10^{14} \text{ cm}^{-3}\mu\text{M}^{-1} = 195\times10^{-3} \text{ cm}^2 \text{ mW}^{-1}\text{s}^{-1}$ @ 523 nm.

^{l} Obtained from fitting shown in figure 4.6c (for Photofrin) and 4.7c (for Rose Bengal) using equation (4.3). $\sigma = m/\xi$ where m is the slope of the linear fit.

^{m} Assumed values to simulate short singlet oxygen lifetime with Intralipid (at 0.2%) acting as a singlet oxygen acceptor (see Fig. 4.1). Measured values from SOLD experiment when $[A] = 0$ and $[Q] = 0$ (i.e. without Intralipid or NaN$_3$) were found to be 9.4±0.2 μs for Photofrin and 3.8±0.3 μs for Rose Bengal (see Fig. 4.5).

2.4 Conclusions

This chapter reviews the photochemical parameters for the photosensitizers BPD, Photofrin, and Rose Bengal. These parameters are needed for explicit dosimetry and modeling the kinetic processes during PDT. Parameters for several other commonly used photosensitizers are summarized in a review elsewhere [34]. Many fundamental rate constant values are unavailable for many photosensitizers, and experimental efforts to determine these parameters are required in order to perform explicit dosimetry of reactive oxygen species.

Chapter 3

Explicit Dosimetry Techniques

Much of the pre-clinical studies to investigate singlet oxygen explicit dosimetry were performed using methods summarized in this chapter. The key components of explicit dosimetry involved measurement of the light fluence, photosensitizer concentration, and oxygen concentration.

3.1 Light Transport and Optical Properties

The amount of light that reaches the targeted tissue accounts for the treatment efficacy in PDT. Light transport in biological matter is characterized by the absorption and scattering of photons. These qualities are characterized by the optical properties of that tissue, namely, the absorption coefficient (μ_a) and the reduced scattering coefficient (μ_s').

3.1.1 Measurement of light fluence

Light fluence was measured in various geometries depending on the treatment geometry not only to determine the fluence delivered, but also for measurement of optical

properties using a point source placed interstitially. Isotropic detectors (IP85 probe, Medlight SA, Ecublens, Switzerland) were used to monitor fluence measured by an in-house made dosimetry system, shown in Fig. 3.1.
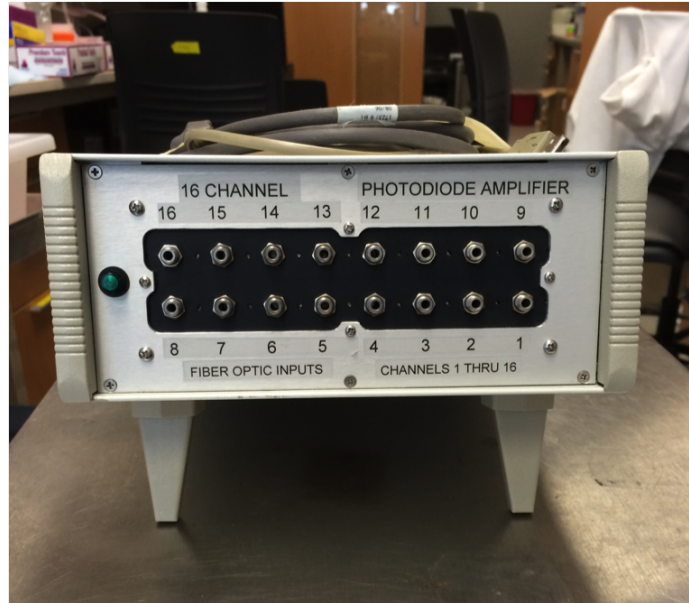
Figure 3.1: In-house made dosimetry system. Fiber optic probes are connected via SMA connector to channels on the dosimetry system to measure light fluence rate and cumulative fluence.

3.1.2 Diffusion theory for spherical geometry

For accurate dosimetry during pleural PDT, it is important to understand the effects of light scattering in a cavity surrounded by tissue. The total fluence at the boundary is larger than the non-scattered irradiance from a point source due to multiple light scattering [9]. The diffusion theory can be used to derive an equation to calculate the photon flux for tissue with a spherical cavity and an isotropic point source in the center [137]. In an integrating sphere, the light does not penetrate deeply into the wall and is back scattered close to the point where the light initially hit the wall, which leads to the condition that the effective optical penetration depth is small compared

to the dimension of the model. So $1/\mu_{eff} \gg r$, where r is the radius of the cavity, and at the boundary, the total fluence can be written as [137]

$$\frac{\phi_t(r)}{S} \approx \frac{1}{4\pi r^2} \left[\frac{\mu_{eff}}{\mu_a} - 2 \right]. \tag{3.1}$$

where S is the source power. The primary component of the light fluence (or the non-scattered component) is calculated by $\frac{\phi_p(r)}{S} = \frac{1}{4\pi r^2}$. When the refractive indices of the tissue and non-scattering and non-absorbing material in the cavity do not match, the fluence rate in the tissue is the same as with matched indices. The fluence rate in the cavity does, however, depend on the difference in refractive index. On the boundary, the total fluence can be calculated using Eq. (3.1). The scattered component of fluence in the tissue is then written as

$$\frac{\phi_s(r)}{S} \approx \frac{1}{4\pi r^2} \left[\frac{\mu_{eff}}{\mu_a} - 3 \right]. \tag{3.2}$$

The scattered fluence rate in the cavity is the same in the inward and outward directions. The scattered fluence rate in the cavity is [137]

$$\frac{\phi_s(r)}{S} \approx \frac{1}{4\pi r^2} (1 - r_{21}) \left(\frac{\mu_{eff}}{\mu_a} - 3 \right) \tag{3.3}$$

where the reflection factor, r_{21} is calculated from

$$r_{21} = 2 \int_{\theta_2=0}^{\theta_2=\theta_c} \left[1 + A_2 \left(\exp(b_2 \sqrt{\cos\theta_2 - \cos\theta_c}) - 1 \right) \right] \cos\theta_2$$
$$\times \sin\theta_2 d\theta_2 + \int_{\theta_2=\theta_c}^{\theta_2=\pi/2} \cos\theta_2 \sin\theta_2 d\theta_2. \tag{3.4}$$

Here, θ_c is the critical angle, and θ_2 is the angle between the incident ray in the medium (tissue) with the normal to the surface. Using an air-water interface with $n_{air} = 1$

and $n_{water} = 1.33$, $r_{21} = 0.4476$. The term $1 + A_2 \left(\exp(b_2\sqrt{\cos\theta_2 - \cos\theta_c}) - 1\right)$ is equal to $R_{fresnel}$.

Using the diffusion theory, the scattered light fluence per power can be calculated in two ways for arbitrary geometries. In particular, experiments were conducted in ellipsoid shapes

$$\frac{\phi_s}{S} = \frac{4}{SA}\frac{R_d}{1 - R_d} \tag{3.5}$$

$$\frac{\phi_s}{S} = \frac{\left(\mu_{eff}/\mu_a - 3\right)\left(1 - r_{21}\right)}{SA} \tag{3.6}$$

Here, SA is the surface area of the cavity volume. R_d is the diffuse reflectance and is calculated using the following formula [138, 139]:

$$R_d = \frac{a'}{2}\left(1 + e^{-4/3A\sqrt{3(1-a')}}\right)e^{-\sqrt{3(1-a')}} \tag{3.7}$$

where the transport albedo is given by $a' = \mu'_s/(\mu_a + \mu'_s)$ and A is the internal reflection parameter. This is a function of the ratio of the index of refraction of the two media: $n_{rel} = n_{tissue}/n_{non-scattering}$ and $A = (1 + r_d)/(1 - r_d)$, where $r_d = -1.44n_{rel}^{-2} + 0.710n_{rel}^{-1} + 0.668 + 0.0636n_{rel}$ [140]. For an air-tissue interface, a good approximation is $A = 3.25$ [139]. Experiments were conducted in phantoms to validate the scattered light components, and results are shown in chapter 7.

3.1.3 Measurement of tissue optical properties

Optical properties of the tumor tissue was measured by using a two-catheter method (shown in figure 3.2) described in detail elsewhere [141, 142]. Treatment wavelength light was delivered through an isotropic 2 mm point source. The point source was inserted into one of two parallel cathethers with a 3 mm separation. An isotropic

detector was placed in the other catheter. This detector was connected to a light dosimetry system and the position of the detector was controlled by a computer-controlled step motor system to obtain a scanned profile of the light fluence from the point source along the catheter. Using the diffusion approximation, the light fluence rate per source power at a distance r from a point source can be expressed as

$$\frac{\phi}{S} = \frac{\mu_{eff}^2}{4\pi r \mu_a} e^{-\mu_{eff} r} = \frac{3\mu_s'}{4\pi r} e^{-\mu_{eff} r} \tag{3.8}$$

where S is the source power of the point source in mW, $\phi(r)$ is the fluence rate in mW/cm^2 at a distance r, and $\mu_{eff} = \sqrt{3\mu_a \mu_s'}$. The point source was moved along the catheter inside the tumor at 1 mm steps to obtain multiple fluence profiles inside the tumor. The optical properties were determined by fitting the measured data to the equation using a Matlab-based program.
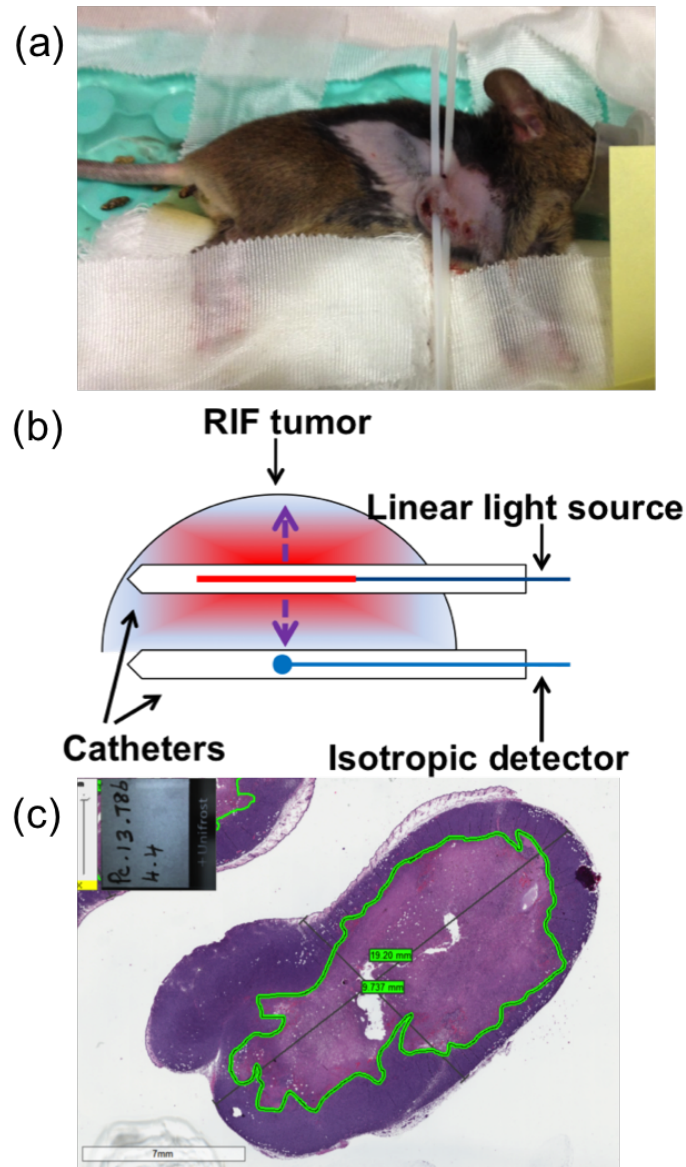
Figure 3.2: (a) Treatment set-up of interstitial PDT in a mouse RIF tumor. (b) Schematic of parallel catheters in a tumor. One catheter is inserted in the center of the tumor to contain the cylindrically diffusing fiber to deliver the treatment light or the point source to measure the optical properties, and a second catheter is inserted 3 mm away to contain the isotropic detector for light fluence profile measurements for the optical properties or the side-firing fiber to obtain fluorescence spectra. (c) Sample tumor section stained with H & E to determine necrosis radius.

3.2 Tumor Model

Radioactively induced fibrosarcoma (RIF) cells were cultured and 30 μl were injected at 1×10^7 cells/ml in the right shoulders of 6-8 week old female C3H mice (NCI - Frederick, Frederick, MD, USA). All animals were under the care of the University of Pennsylvania Laboratory Animal Resources. All studies were approved by the University of Pennsylvania Institutional Animal Care and Use committee. Tumors were treated when they were ~8-10 mm in diameter. The fur of the tumor region was clipped prior to cell inoculation. After the appearance of a visible tumor (~3 mm in diameter), the treatment area was depilated with a topical hair remover, Nair (Church & Dwight Co., Inc., Ewing, NJ, USA). Mice were provided with a chlorophyll-free (alfalfa-free) rodent diet (Harlan Laboratories Inc., Indianapolis, IN, USA) starting at least 10 days prior to treatment to eliminate the fluorescence signal from chlorophyll breakdown products, which have a similar emission range to the BPD fluorescence spectra (details are described in Appendix A).

3.3 Measurement of Photosensitizer Concentration

Photosensitizer concentration was determined using the characteristic fluorescence spectra for each photosensitizer. Changes in photosensitizer concentration can be observed by measuring the fluorescence spectra before, after, and during PDT. For different studies, different techniques were used to obtain the fluorescence spectra. Methods included interstitial fluorescence excited by 405 nm, surface fluorescence obtained via a contact probe excited by 405 nm, and surface fluorescence obtained with excitation by the treatment light. Obtained spectra were then analyzed by a fitting algorithm described by Finlay et al. [42]. The spectra were fit as a linear combination of fluorescence basis spectra using a single value decomposition (SVD) algorithm in

Matlab. The components for a representative spectra with BPD is shown in figure 3.3. Basis spectra included those for the photosensitizer and the autofluorescence (background) of the mouse. The algorithm employed also includes a 61-term Fourier series to account for fluorescence of unknown origin. Spectra were corrected for CCD integration time and background was also subtracted before analysis. SVD analysis reduces the measured spectrum to a set of amplitudes of the components. To account for variations in lamp intensity, the photosensitizer amplitude was divided by the background amplitude from the same spectrum, to result in a normalized BPD amplitude. Due differences in solvent between in-phantom and *in vivo* cases as well as differences in absorption and scattering at both the excitation and emission wavelengths of BPD, the measured BPD amplitude was multiplied by an empirically determined correction factor described in the following sections.
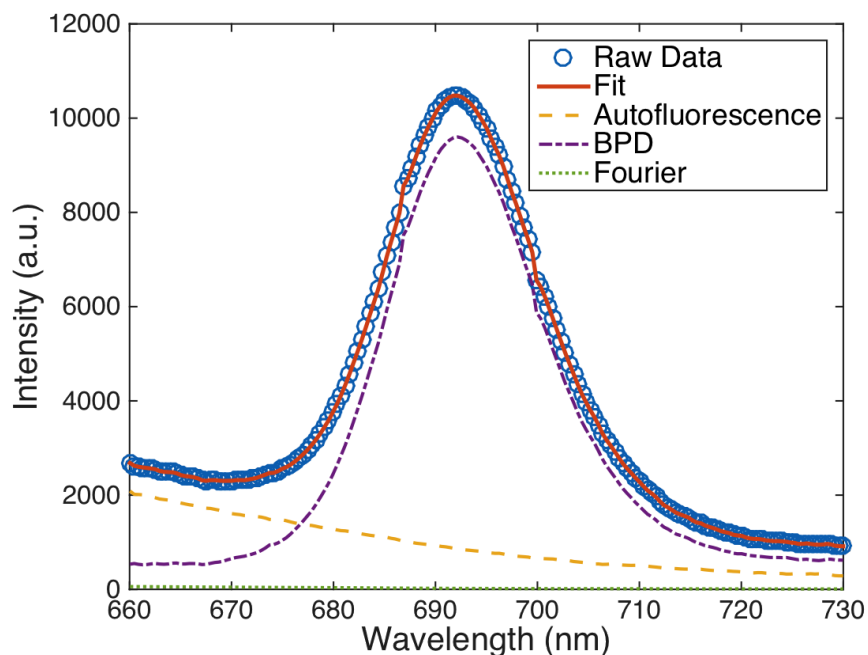
Figure 3.3: BPD fluorescence spectra analyzed using SVD. The raw data (circles) are fit (solid line) using a linear combination of basis spectra of BPD (dot-dashed line) and autofluorescence (dashed line) components. Spectra was obtained from interstitial fluorescence excited by 405 nm light.

3.3.1 Interstitial photosensitizer measurements

Interstitial fluorescence measurements were made by inserting a side-cut fiber into one of the two catheters that were inserted into the tumor. The side-cut fiberwas connected to a 405 nm laser (Power Technology Inc., Little Rock, AR, USA), a dichroic beam splitter, and a multichannel CCD spectrograph (InSpectrum, Princeton Instruments, Trenton, NJ, USA). Collected spectra were analyzed using single value decomposition (SVD) fitting [42]. Spectra were measured both before and after treatment to investigate the effects of and relationship between photobleaching and outcome. The *in vivo* photosensitizer concentration was obtained by comparing the *in vivo* BPD fluorescence with that of phantoms with known BPD concentrations.

An empirical correction factor was obtained from phantom experiments with known constant BPD concentrations and varying absorption and scattering coefficients (μ_a and μ'_s). A set of experiments in tissue-simulating phantoms containing Intralipid (Fresenius Kabi, Uppsala, Sweden) as a scatterer and Parker Quink (Parker Pen Company, New Haven, East Sussex, England) as an absorber were designed. μ_a and μ'_s were varied for a fixed BPD concentration (0.25 mg/kg), and fluorescence spectra were analyzed with SVD [42] to determine the spectral component magnitudes for BPD and the autofluorescence from the 690 nm excitation laser light. The data was then used to determine the empirical optical property correction factor for the fluorescence method used to determine the PS concentration (Fig. 2 (a)). A more accurate method would involve knowledge of the optical properties at the excitation wavelength (405 nm) as well as the emission wavelength (690 nm) [10], the former is beyond the current fluorescence spectroscopy range. The effects of absorption and scattering on measured fluorescence in semi-infinite media can be modeled using a forward-adjoint fluorescence scheme proposed by Crilly *et al..* [143]. This models the forward propagation of excitation light from the source and the time reversed propagation of positional importance from the detector. The positional importance is defined as the probability that a photon emitted at a point is eventually caught by a detector. The measured signal is proportional to the volume integral of the product of the excitation fluence rate and the positional importance. An analytical solution to this model has been derived by Finlay and Foster for the case of an isotropic point source and an isotropic detector in an infinite homogeneous medium for the diffusion approximation [10, 144]. To account for the actual measurement situation, it is assumed that the light beam exiting or entering the probe is a pencil beam.

An empirical correction factor was introduced to account for differences in optical properties between the phantom studies and *in vivo* measurements that depends on

measured optical properties at 690 nm. Ideally, the measured optical properties could be used as inputs for the full theoretical expression, however, the calculation would require accurate knowledge of the optical properties at the excitation wavelength as well as te emission wavelength, which is beyond the measurement system capabilities. A multiplicative empirical correction factor of the following form can be determined, which is an approximate inverse of the solution to the analytical solution described by Finlay and Foster [144]. This is for the case of high albedo and unchanging optical properties at the excitation wavelength.

$$CF = a\frac{e^{b \cdot \mu_{eff}}}{\mu'_s} \qquad (3.9)$$

The raw SVD amplitude obtained from the *in vivo* fluorescence spectra was corrected by multiplying it with CF to get corrected SVD (SVD_{corr}). The values of a and b were optimized so that SVD_{corr} for phantoms with the same concentration of BPD were matched (Fig. 3.4 (a)). Upon optimization using *fminsearch* in Matlab, it was found that $a = 1.2$ cm^{-1} and $b = 0.5016$ cm. A separate tissue-simulating phantom with fixed optical properties ($\mu_a = 0.7$ cm^{-1} and $\mu'_s = 10.1$ cm^{-1}) and varying concentrations of BPD (μM) were used to determine a calibration curve for SVD_{corr} (Fig. 5.2 (b)). The correction factor for motexafin lutetium fluorescence emission with optical properties measured using 732 nm from Finlay et al. had values of $a = 3.1$ cm^{-1} and $b = 0.97$ cm [10]. The value of a is dependent on the measurement set-up and the intensity of the incident excitation light. For the same geometry, the value of b should not vary greatly depending on the photosensitizer and wavelength used for optical property measurements. From these measurements, the range of values of b is from 0.50 to 0.97 cm.
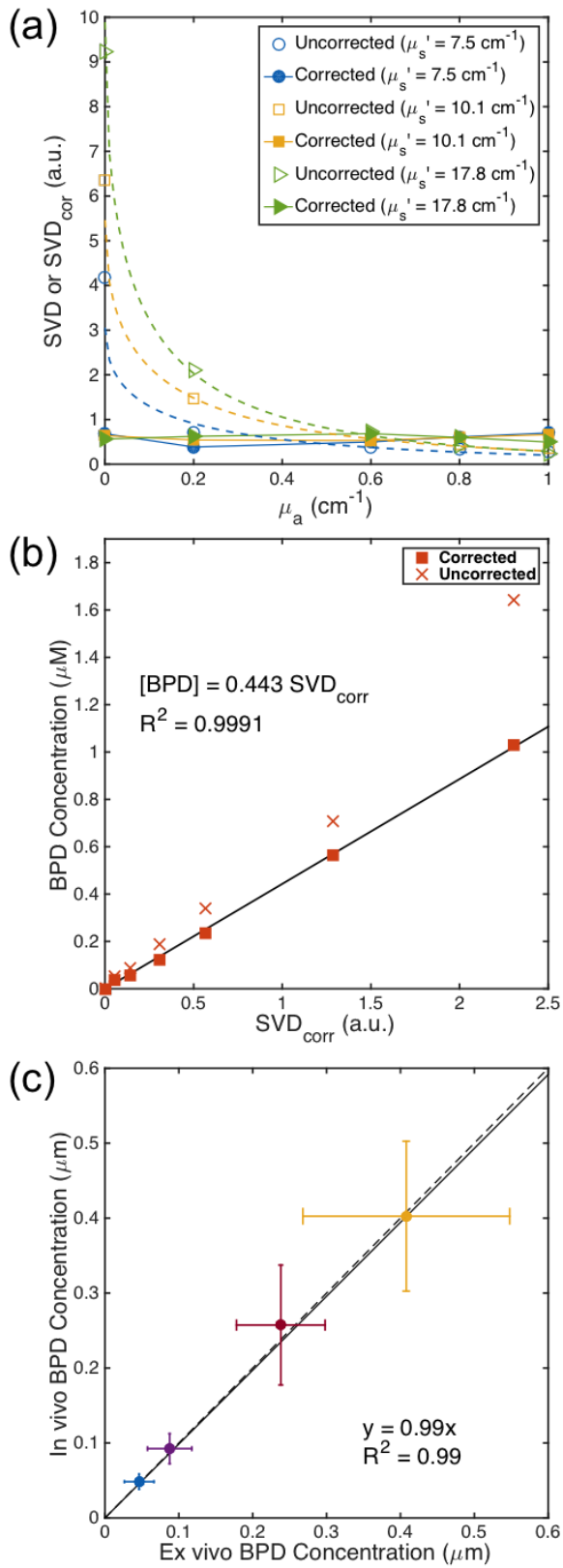
Figure 3.4: Optical property correction of fluorescence signal for interstitial measurements. (a) Fluorescence single value decomposition (SVD) amplitude for BPD in tissue-simulating phantom experiments with different optical properties but constant BPD concentration. An empirical correction factor (CF) of the form described in Eq. (3.9) was obtained so that the corrected SVD_{corr} amplitudes were the same. (b) A calibration curve of BPD concentration (in μM) versus SVD_{corr}. (c) Interstitially measured *in vivo* BPD concentration versus *ex vivo* measured BPD concentration. Each data point represents the average of three *in vivo* and *ex vivo* measurements performed in the same RIF tumor. The solid line represents the best linear fit ($y = 0.99x$) to the data with $R^2 = 0.99$. The dashed line represents $y = x$.

3.3.2 Surface photosensitizer measurements

Fluorescence measurements were made by a custom-made multi-fiber spectroscopic contact probe (Fig. 6.1 (b)) described elsewhere [145]. The probe is placed in physical contact with the tumor tissue both pre- and post-PDT to obtain fluorescence spectra of BPD. The probe is comprised of two source optical fibers and a series of detection fibers spaced between 0,14 and 0.88 cm away from the first source fiber. The source fibers are connected to (i) a white light source to collect diffuse reflectance (Avalight; Avantes, Broomfield, CO, USA) and (ii) a 405 nm laser source (Power Technologies, Inc., Little Rock, AK, USA) for fluorescence excitation. The detection fibers were connected to a multi-channel CCD spectroscopy system (InSpectrum; Roper Scientific, Trenton, NJ). Fluorescence spectra were collected both before and after treatment and analyzed using single value decomposition (SVD) fitting to obtain fluorescence intensity due to BPD. An empirical optical property correction factor (CF) that is different than that of the interstitial geometry used in section 3.3.1 was determined. CF was defined as the ratio of SVD between fluorescence with tissue optical properties of interest (μ_a, μ'_s) and the corresponding fluorescence SVD for a reference system with optical properties of $\mu_a = 0.69$ cm^{-1} and $\mu'_s = 11$ cm^{-1}, with BPD as the photosensitizer and optical properties measured at 690 nm. A multiplicative CF of the following form was used to multiply raw SVD to obtain corrected SVD (SVD_{corr}):

$$CF = \frac{C_1(1 + C_2\mu'_s)}{\mu'_s} \cdot \exp\left[(b_1 + b_2\mu'_s)\mu_{eff}\right] \tag{3.10}$$

The input optical properties are those measured at 690 nm. This formulation for the correction factor is an expansion of the expression in equation (3.9). Raw SVD was multiplied by CF to get SVD_{corr}. The values were optimized so that SVD_{corr} for phantoms with the same concentration of BPD were matched (Fig. 3.5 (a)). Upon

optimization, it was found that $C_1 = 0.41 \pm 0.16$ cm^{-1}, $C_2 = 0.142 \pm 0.013$ cm, $b_1 = 0.85 \pm 0.16$ cm, and $b_2 = -0.032 \pm 0.014$ cm^2. A separate tissue-simulating phantom with constant scattering and absorption and varying amounts of BPD were used as a calibration curve to correlate SVD_{corr} to actual concentration in μM (Fig. 3.5 (b)). The line of best fit (shown as a solid line in Fig. 3.5 (b)) is $[BPD] = (0.0301 \pm 0.0009) \times SVD_{corr}$ is used to convert SVD_{corr} to $[BPD]$ in units of μM. The values for CF for Photofrin studies were found to be $C_1 = 3.881$ cm^{-1}, $C_2 = 0.00265$ cm, $b_1 = 0.5043$ cm, and $b_2 = -0.01622$ cm^2 [146]. Using a Monte Carlo simulation for a tissue-air interface, the resulting values were $C_1 = 2.4258$ cm^{-1}, $C_2 = -0.0033$ cm, $b_1 = 0.4879$ cm, and $b_2 = -0.01559$ cm^2. The values of C_1 and C_2 are dependent on the measurement set-up and the intensity of the excitation light. The values for b_1 and b_2 provide the range for the fit parameters for CF.

Fluorescence spectra were also obtained via surface illumination of tumors with the treatment light at 690 nm. A bare fiber was placed next to the collimated beam source facing the tumor. Between the fiber and the spectrometer, a long-pass filter (FF01-715/LP-25, Semrock Inc., Rochester, NY, USA) was used eliminate the treatment light. An example of spectra obtained using this method is shown in Fig. 3.6. Intensity from the fluorescence signal obtained using this method was used to do continuous monitoring of photosensitizer concentration during treatment for a set of mice described in chapter 6. Initial photosensitizer concentration was measured using contact probe methods described earlier.
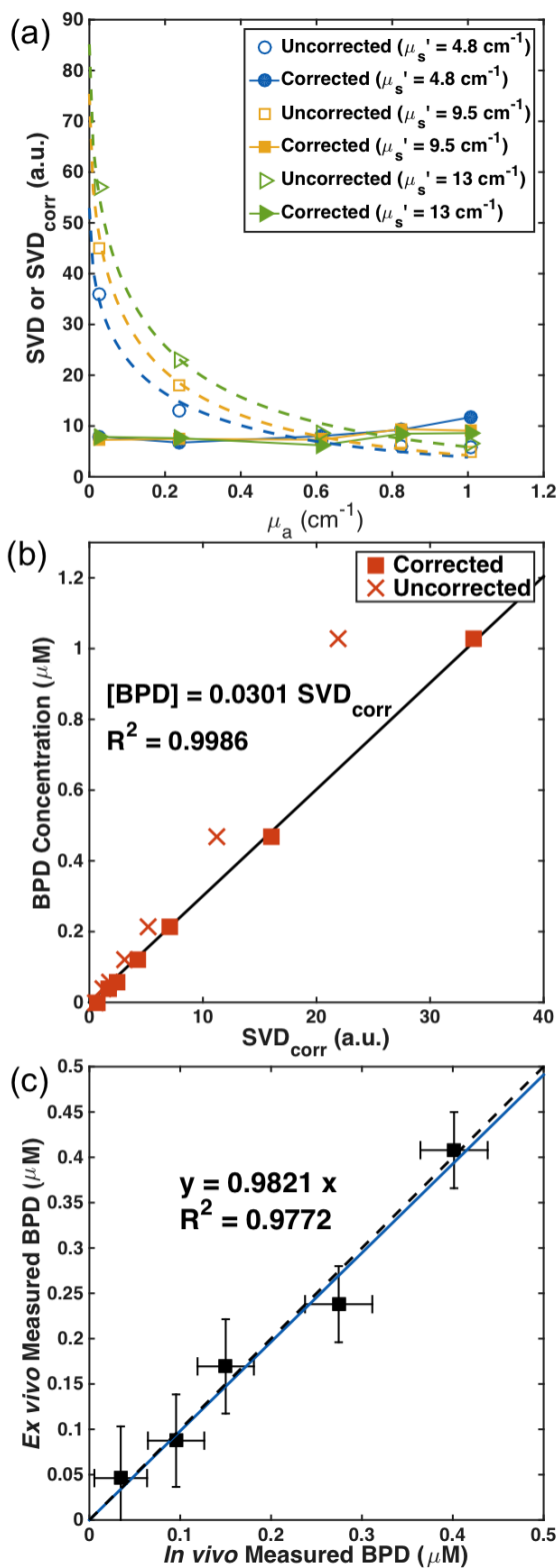
Figure 3.5: Optical property correction of fluorescence signal for surface fluorescence measurements. Fluorescence optical property correction phantoms and verification with *in vivo* and *ex vivo* comparison. (a) Fluorescence SVD amplitude for phantom experiments with varying optical properties and the same BPD concentration (0.25 mg/kg). The best-fit (shown as dashed lines) is of the form a/CF, where CF is given by Eq. (3.10) and $a = 7.645$. (Note, $CF = 1$ is normalized for mean optical properties of $\mu_a = 0.69$ cm^{-1}, $\mu_s' = 11$ cm^{-1}) (b) BPD concentration (in μM) versus the corrected SVD (SVD_{corr}). The line of best fit $[BPD] = (0.0301\pm0.0009)\times SVD_{corr}$ with $R^2 = 0.9986$ is used to convert SVD_{corr} to $[BPD]$. (c) The measured *in vivo* photosensitizer concentration using the multi-fiber contact probe obtained fluorescence spectra versus *ex vivo* measured BPD concentration. The line of best fit is of the form $y = 0.9821x$ with $R^2 = 0.9772$. The dashed line represents the line for $y = x$.
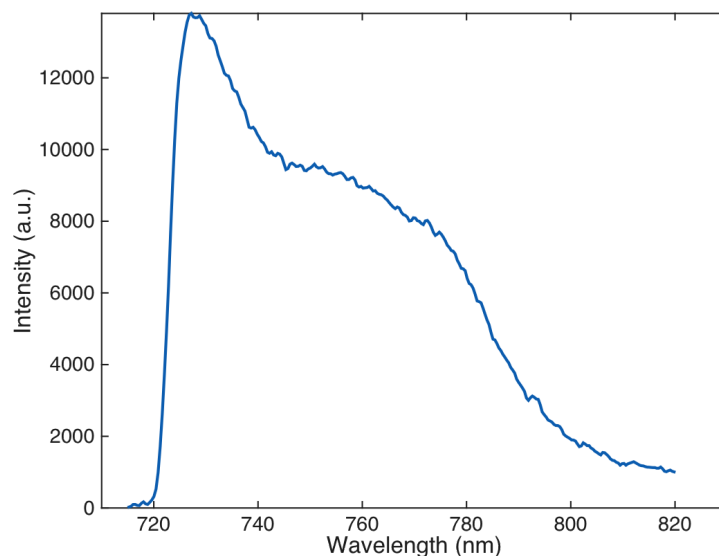
Figure 3.6: BPD fluorescence spectra collected with excitation by the treatment light (690 nm). A long-pass filter (cutoff at 715 nm) was used to eliminate the treatment light signal.

3.3.3   Verification of *in vivo* BPD concentration

In order to verify the *in vivo* photosensitizer concentration measured using fluorescence spectroscopy, *ex vivo* experiments were performed on another set of tumors on mice injected with BPD. Measurements of BPD levels in tissue were done based on published *ex vivo* procedures [147–149]. After the correct incubation time (3 hours for BPD), tumor tissue samples were excised and immediately frozen for later use. At the time of measurement, samples were thawed to room temperature, weighed, minced, and placed in a vial with the appropriate amount of tissue solubilizer, Solvable (Packard, Meriden, CT, USA). The samples were then heated at 50 °C in the dark for 4 hours. After the solution was cooled, an equal volume of water was added, and with thorough mixing, the solution was transferred to a cuvette to be measured. The fluorescence of the solubilized samples was measured using a spectrofluorometer

(FluoroMax-3, Jobin Yvon, Inc., Edison, NJ, USA) with an excitation wavelength of 435 nm. The concentration of BPD was calculated based on the increase in fluorescence signal resulting from the addition of a known amount of BPD to each sample after its initial reading. The *ex vivo* measurements were compared to *in vivo* measurements using the method described in section 3.3.1 and 3.3.2 for the same tumors (Fig. 3.2 (c) and 3.4 (c)). The good agreement between the two confirmed the accuracy of the interstitial method used *in vivo* both pre- and post-PDT.

3.4   Treatment Delivery

Mice were administered with photosensitizer via the tail vein prior to treatment with the appropriate drug-light interval (DLI) for the photosensitizer being used. For the treatment, mice were anesthetized by inhalation of isoflurane in medical air (VetEquip anesthesia machine, VetEquip, Livermore, CA, USA). For some studies, treatment light was delivered interstitially with a fiber optic through a catheter inserted into the tumor (see Fig. 3.2). Mice treated with this method of light delivery were sacrificed one day following treatment, and the tumors were resected for pathology and sectioning, as described in chapter 5. For those mice whose tumors needed to be monitored over time (chapter 6), the catheters were not a viable option to deliver light, as they would create damage to the surface of the skin, leaving the mouse prone to infections and other tumor injury. These mice were treated with a broad beam of light on the surface of the tumor to minimize non-PDT-related damage.

3.5 Macroscopic Singlet Oxygen Model *in vivo*

The typical type II PDT process can be described by a set of kinetic equations, described in detail in chapter 2. For the *in vivo* modeling scenario, an assumption is made that the number of singlet oxygen acceptors present in the tissue is very large, resulting in a large $k_{72}[A]$ term ($k_{72}[A] \gg k_6 + k_{12}([S_0] + \delta) + k_9[Q]$) and assuming $\eta = 0$. Then, the relevant equations are simplified as the following:

$$\frac{d[S_0]}{dt} = -\frac{[^3O_2]}{[^3O_2] + \beta} \xi\sigma([S_0] + \delta)\phi[S_0], \tag{3.11}$$

$$\frac{d[^3O_2]}{dt} = -\frac{[^3O_2]}{[^3O_2] + \beta} \xi\phi[S_0]([S_0] + \delta) + g\left(1 - \frac{[^3O_2]}{[^3O_2](t = 0)}\right), \tag{3.12}$$

$$\frac{d[^1O_2]_{rx}}{dt} = \frac{[^3O_2]}{[^3O_2] + \beta} \xi\phi[S_0], \tag{3.13}$$

where the photosensitizer-specific parameters were determined for BPD in chapter 5 and validated in chapter 6. If the parameters are 10% over- or underestimated, calculated $[^1O_2]_{rx}$ will deviate up to 12%. An increased σ estimates a smaller $[^1O_2]_{rx}$, while an increased g or ξ estimates larger $[^1O_2]_{rx}$.

The accumulated $[^1O_2]_{rx}$ that is used to kill cellular targets can be expressed as

$$[^1O_2]_{rx} = -f\int_0^t \frac{d[A]}{dt}dt = fk_7\int_0^t [A][^1O_2]dt = f\xi\int_0^t \frac{[^3O_2]}{[^3O_2] + \beta}\phi[S_0]dt \tag{3.14}$$

where f is the fraction of $^1O_2$ interacting with $[A]$ that effectively leads to tumor cell death. For the pre-clinical studies done in this work, f has been set as 1.

For *in vivo* modeling, calculations were performed in Matlab with input values of treatment conditions (fluence and fluence rate), the measured initial photosensitizer

concentration, and depending on the study, the initial ground state oxygen concentration. Results of these calculations are shown in detail in chapters 5 and 6 using a mouse model.

Chapter 4

Determination of In-Phantom Photochemical Parameters

Most clinically relevant photosensitizers undergo type II processes in which the triplet state transfers energy to ground-state oxygen to produce singlet oxygen [150], which is the main photocytotoxic agent leading to cell death and therapeutic response [91,151]. Use of singlet oxygen concentration was investigated in this study. Direct measurement of $^1O_2$ by its near-infrared luminescence emission is technically challenging *in vivo* due to the weakness of the signal and the short lifetime ($\sim$30-180 ns) of $^1O_2$ [50,51]. Hence, a macroscopic singlet oxygen explicit dosimetry model has been developed and studied *in vivo* and described in sections 3, 5, and 6. SOED was compared in solutions to direct singlet oxygen luminescence dosimetry (SOLD). The relevant photophysical parameters for the macroscopic model were verified by performing explicit dosimetry of oxygen concentration and photosensitizer concentration in phantoms. In performing a direct comparison between SOED- and SOLD-measured $^1O_2$, the use of SOED in scenarios where direct luminescence detection is difficult is validated. Furthermore, an analysis was performed to show that SOLD measured

using a 523 nm pulsed laser (currently required by the availability of lasers with suitable pulse length, repetition frequency, and energy) is well-correlated to singlet oxygen generated by Photofrin by a CW 630 nm laser during PDT, by correcting for the tissue optical properties at the two wavelengths.

4.1 Materials and Methods

4.1.1 SOED model in phantoms

From the kinetic equations summarized in section 2.1.4, the interactions of $[^3O_2]$ and $[S_0]$ in the phantom scenario where there is no added singlet oxygen quencher can be described by the following equations

$$\frac{d[S_0]}{dt} = -\left(\xi\sigma\right)\frac{[^3O_2]}{[^3O_2]+\beta}([S_0]+\delta)\phi[S_0] - \eta\frac{1}{[^3O_2]+\beta}\phi[S_0], \tag{4.1}$$

$$\frac{d[^3O_2]}{dt} = [-\xi + \xi_{II}\tau_\Delta k_6]\frac{[^3O_2]}{[^3O_2]+\beta}\phi[S_0] \tag{4.2}$$

The definitions of the parameters are listed in table 2.2. ξ, σ, and δ were varied to fit the measured ground state oxygen data. From the equation set and the measured data, it is difficult to distinguish between type I and type II interactions, so only values of ξ and σ were considered. The values of the parameters used for the calculation are summarized in table 2.4 and described in section 4.2.2. For the in-phantom scenario using Intralipid, the $k_{72}[A]$ term was calculated based on an assumed value of τ_Δ using $\tau_\Delta^{-1} = k_1([S_0]+\delta)+k_6+k_{72}[A]$. Without the addition of a quencher, the $k_9[Q]$ term is set to 0. Here, the definition of σ is $(\sigma_I\xi_I + \sigma_{II}\xi_{II})/\xi$. Measured ground state oxygen concentration and photosensitizer concentration were fit assuming no contributions

from hypoxic interactions between the triplet state photosensitizer and the reactive species acceptor, $[A]$ in the solid lines in Fig. 4.2 and 4.3, for Photofrin and Rose Bengal. The results show good agreement between measured data and calculated values. The dashed line shows the best fit to the photosensitizer data including the η term in Eq. (4.1). A dominant η term was used to fit the data, and then values of σ and ξ were fit accordingly. Resulting values of ξ exceeded the acceptable calculated range using the equation $\xi = \Phi_\Delta{}^\varepsilon/h\nu$ (where $\Phi_\Delta \leq 1$). Furthermore, in phantoms, $\tau_\Delta k_6 \ll 1$, so it is difficult to differentiate between type I and type II reactions. Thus, for the photosensitizers investigated in-phantoms, hypoxic interactions should be considered negligible since it cannot be made to fit the measured data.

τ_Δ was taken to be 0.5 μs in studies with Intralipid, as the lipid emulsion acts as an acceptor for reactions with singlet oxygen [152]. It is seen that the singlet oxygen lifetime is reduced from the typical in-phantom value (3 μs) with the addition of Intralipid, as seen in Fig. 4.1 [85]. Singlet oxygen luminescence counts were not seen for phantoms with Intralipid concentrations of 0.2% in that study. For modeling of the in-phantom studies presented in section 4.2.2, this reduction of τ_Δ was considered with a lifetime value that was undetectable from previous studies.
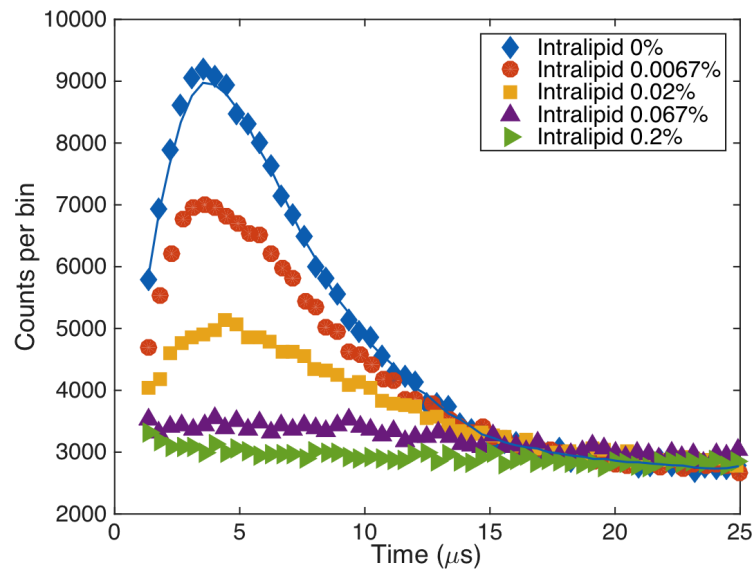
Figure 4.1: Singlet oxygen luminescence photon counts for Rose Bengal (51 μM) phantoms with various amounts of Intralipid. With increasing amounts of Intralipid, the photon counts obtained decreases, indicating a shorter singlet oxygen lifetime (τ_Δ). Data with Intralipid 0% is fit with Eq. (4.10).
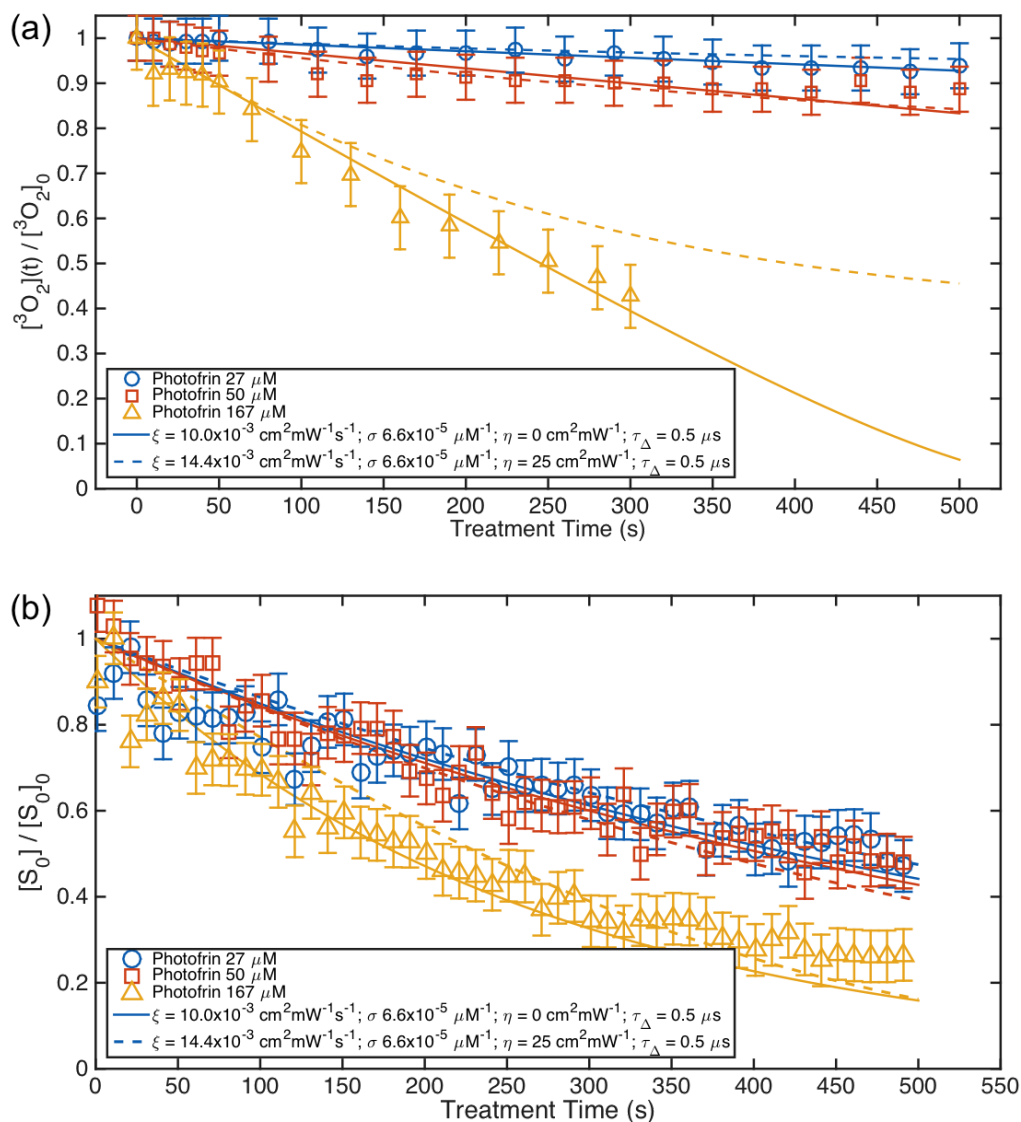
Figure 4.2: Measured (a) oxygen and (b) photosensitizer concentration data is plotted with model calculations that include hypoxic interactions (η term in Eq. 4.1). The symbols represent measured data at various concentrations of Photofrin, and the lines show the calculated oxygen and photosensitizer concentrations over a time of illumination. The solid lines shows the best fit, and the dashed line shows the best fit for photosensitizer that includes hypoxic interactions.
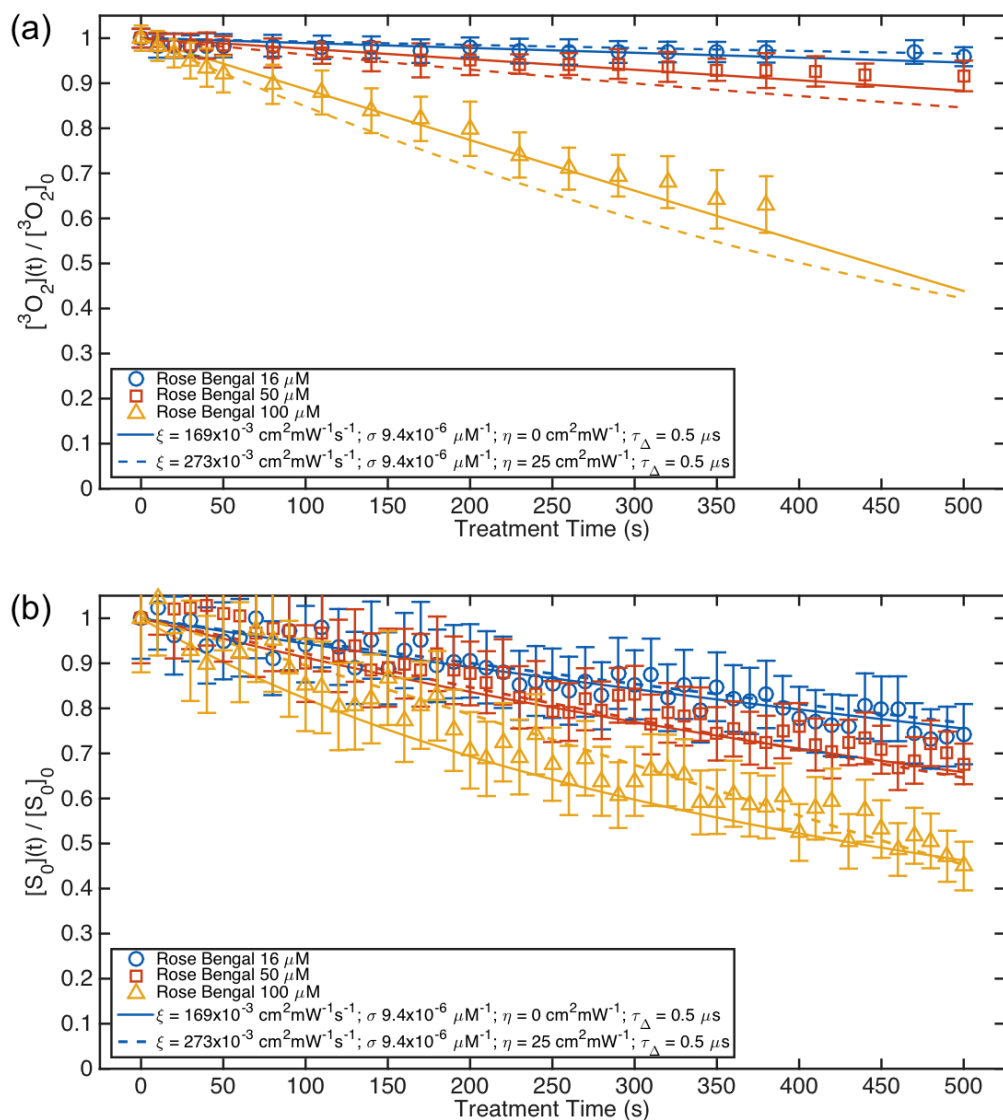
Figure 4.3: Measured (a) oxygen and (b) photosensitizer concentration data is plotted with model calculations that include hypoxic interactions (η term in Eq. 4.1). The symbols represent measured data at various concentrations of Rose Bengal, and the lines show the calculated oxygen and photosensitizer concentrations over a time of illumination. The solid lines shows the best fit, and the dashed line shows the best fit for photosensitizer that includes hypoxic interactions.

Assuming type II interactions, equation (4.1) can be rewritten as the following:

$$-\frac{d[S_0]}{dt} \bigg/ \left(\phi[S_0] \frac{[^3O_2]}{[^3O_2] + \beta} \right) = \xi\sigma([S_0] + \delta) \tag{4.3}$$

The left-hand side of equation (4.3) versus $[S_0](t)$ gives the values of δ and σ. The photobleaching rate $(-d[S_0]/dt)$ was determined at each time point with values of ϕ, $[^3O_2]$, $[S_0]$, and β for the calculation of the left-hand side of equation (4.3). A linear fit to the data yields a value for the intercept and slope, and the intercept divided by the slope gives the value of δ and the slope divided by ξ gives the value of σ. Calculations were performed using Matlab 2014b (MathWorks, Natick, MA, USA).

Oxygen and photosensitizer measurements were performed and compared (Figs. 4.6 and 4.7) with model calculated values using the coupled differential equations above in phantoms with a small amount of Intralipid (0.02% concentration).

To compare explicit dosimetry with direct dosimetry, instantaneous and cumulative singlet oxygen concentration was calculated. Equation (2.23) can be written as

$$[^1O_2] = \xi\tau_\Delta \frac{[^3O_2]}{[^3O_2] + \beta} \phi[S_0]. \tag{4.4}$$

The cumulative reacted singlet oxygen counts can be calculated from the integral of Eq. (2.29)

$$[^1O_2]_{rx} = \int \xi \frac{[^3O_2]}{[^3O_2] + \beta} \phi[S_0] dt. \tag{4.5}$$

Comparisons where performed in phantom solutions with only the photosensitizer and a solvent (MeOH or H_2O), and the relevant parameters are summarized in table 2.4.

Macroscopic model with oxygen quenching

In the biological scenario, $^3O_2$ that is used to produce $^2O_2$ is consumed and replenished by blood flow (described by the g term). In experiments with a singlet oxygen quencher, such as sodium azide (NaN_3), singlet oxygen is not consumed rapidly and returns to the lower energy state of ground state oxygen. Equation (2.12) and (2.16) can be modified as follows:

$$\frac{d[S_0]}{dt} = -k_0[S_0] - k_{12}[^1O_2]([S_0] + \delta) - k_{11}[O_2^-]([S_0] + \delta) + k_2[T_1][^3O_2] + k_3[S_1] + k_4[T_1]$$

(4.6)

$$\frac{d[^3O_2]}{dt} = -S_\Delta k_2[T_1][^3O_2] - S_I k_2[T_1][^3O_2] + k_6[^1O_2] + k_9[Q][^1O_2] + \Gamma$$

(4.7)

where k_9 is the bimolecular rate of reaction of $^1O_2$ with a quencher, $[Q]$, and Γ is the oxygen supply rate which describes diffusion of oxygen *in vivo*. In the phantom scenario, $[A] = 0$ and $\Gamma = 0$. These can be simplified as before, solving for the equilibrium state, to become

$$\frac{d[S_0]}{dt} = -\left(\xi_{II}\sigma_{II} + \xi_I\sigma_I\right)\frac{[^3O_2]}{[^3O_2] + \beta}([S_0] + \delta)\phi[S_0] - \eta\frac{1}{[^3O_2] + \beta}\phi[S_0],$$

(4.8)

$$\frac{d[^3O_2]}{dt} = \left[-\left(\xi_{II} + \xi_I\right) + \xi_{II}\tau_\Delta(k_6 + k_9[Q])\right]\frac{[^3O_2]}{[^3O_2] + \beta}\phi[S_0]$$

(4.9)

Values of each photochemical parameter used is summarized in table 2.4. Some parameters were taken as the reported literature value, such as k_1. The value for ξ was calculated for the in-phantom scenario and is described in table 2.4. Using methods described later in section 4.2.1 and Fig. 4.5, the values for k_6 and $k_9[Q]$ were determined using singlet oxygen luminescence and lifetime measurements. Phantoms with various concentrations of Photofrin and Rose Bengal with added amounts of

NaN$_3$ were made and illuminated with a broad beam. Oxygen changes were monitored over time, and the measured values were compared (Fig. 4.5) to the modeled values using eqs. (4.8) and (4.9) for both Photofrin and Rose Bengal.

4.1.2 SOLD instrumentation

Singlet oxygen luminescence dosimetry (SOLD) was performed using a compact, fiber optic near-infrared probe-based system [85,153]. The probe was coupled to a compact InCaAs/InP single photon avalanche diode (SPAD) detector (Micro Photon Devices, Bolzano, Italy). Samples were illuminated with a 523 nm wavelength pulsed laser (QL-523-200-S, CrystaLaser, Reno, NV, USA) coupled into the delivery fiber via a collimation package. The laser emits 10 ns duration pulses at a repetition rate of 18.2 kHz with an average power of 200 mW. Patterned time gating was used to limit the unwanted dark counts and eliminate the strong photosensitizer luminescence background. The luminescence signal from singlet oxygen at 1270 nm was confirmed through spectral filtering and lifetime fitting for Photofrin.

Figure 4.4 shows a photograph and schematic of the experimental setup. The pulsed laser was coupled into the delivery fiber. The laser also outputs an electrical signal that is sent to a programmable pulse pattern generator (PPG) (Agilent 81110A, Keysight Technologies, Inc., Santa Rosa, CA, USA). Each pulse generates outputs on two separate channels, each with pulse shape designed to match the intended input. The first output is a single pulse sent to the start channel of the time-correlated single-photon counting (TCSPC) module (HydraHarp, PicoQuant GmbH, Berlin, Germany), while the second is a pattern of pulses sent to the SPAD control module. The SPAD is turned on for a preassigned time, only when the control module receives a pulse from the PPG. The electrical signal from the laser to the PPG triggers the release of two signals: one acts as the start signal for the photon counting

module and the other triggers the SPAD gating.
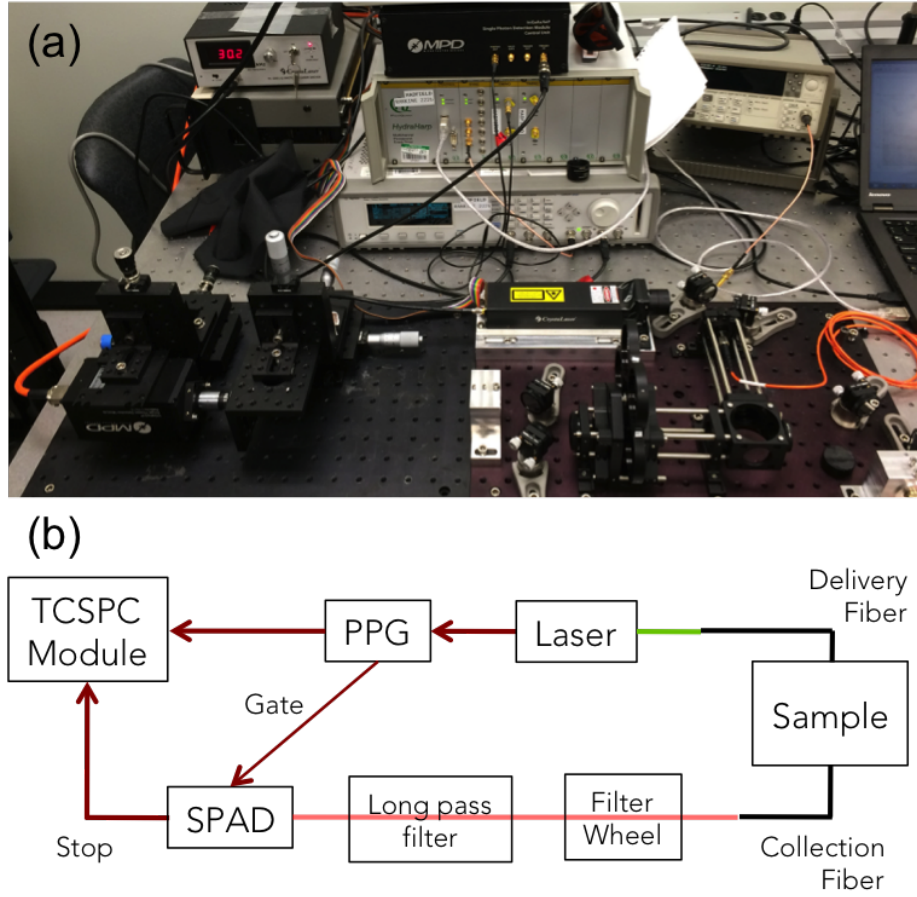
Figure 4.4: Singlet oxygen luminescence dosimetry (SOLD) instrumentation set-up (a) on an optical bench; and (b) schematic diagram of the experimental arrangement. PPG - pulse pattern generator; SPAD - single photon avalanche diode; TCSPC - time-correlated single-photon counting

The TCSPC module generates a timing histogram of photon counts versus time. The background was removed by subtracting the histogram taken through a 1210 nm filter from that through the 1270 nm filter. Equation (4.10) describes the $[^1O_2]$ signal as a function of time following a short illumination pulse.

$$[^1O_2](t) = N\sigma_A[S_0]\Phi_\Delta \frac{\tau_\Delta}{\tau_t - \tau_\Delta} \left(e^{-t/\tau_t} - e^{-t/\tau_\Delta} \right) \tag{4.10}$$

The cumulative SOLD singlet oxygen count can be calculated as the integral of equation (4.10) per τ_R [154].

$$\int_0^\infty \frac{1}{\tau_R}[^1O_2](t)dt = \frac{N\sigma_A[S_0]\Phi_\Delta\tau_\Delta}{\tau_R} \tag{4.11}$$

where N is the number of photons in the illumination pulse, σ_A is the photosensitizer absorption cross-section ($\sigma_A = (\varepsilon/N_A) \times 10^9$), N_A is Avogadro's constant (6.022×10^{23}), ε is the extinction coefficient, and τ_R is the $^1O_2$ phosphorescence lifetime (k_6^{-1}). A fit of the background-subtracted histograms was performed to equation (4.10) (with a y-axis offset as a free parameter to account for any change in the background level) using Origin software with a Levenberg-Marquardt algorithm to iterate the parameter values (see Fig. 4.1) [130].

4.1.3   Measurements in tissue-simulating phantoms

Explicit dosimetry of phantom studies was performed using tissue-simulating liquid phantoms. Intralipid (Fresenius Kabi, Uppsala, Sweden) was added to solutions as a scatterer. A broad beam was produced by a fiber with a microlens attachment (Pioneer Optics Company, Bloomfield, CT, USA) onto cuvette phantoms. Oxygen measurements were made with a bare-fiber OxyLite probe (Oxford Optronix, Oxford, United Kingdom) on the side closest to beam entry in the middle of the beam field. In the in vitro set-up, there is very little oxygen diffusion to the point of measurement. Therefore, oxygen measurements were performed with interruption of the excitation laser at 1-30 second intervals. Illumination light was briefly turned off during these measurements, and multiple values were recorded for a single phantom. Oxygen partial pressure was measured in mmHg and converted to μM by using a factor of α = 1.3 [48, 117].

4.2 Results

4.2.1 SOED photophysical parameters

Photophysical parameter values for Photofrin were determined for *in vitro* macroscopic modeling from the literature as well as measurements to be used in the calculation of $[^1O_2]_{rx}$. The values of the parameters are summarized in table 2.4.

Singlet oxygen lifetime was determined using the SOLD instrumentation for the Photofrin and Rose Bengal phantoms and summarized in table 4.1. Lifetimes were also determined for phantoms with varying concentrations of NaN$_3$. Figure 4.5 shows the plot of τ_Δ^{-1} versus concentration of NaN$_3$ with their best linear fits for (a) Photofrin (83 μM) and (b) Rose Bengal (50 μM). As NaN$_3$ is a singlet oxygen quencher, the line of best fit describes $k_9[Q] + k_6$ rather than $k_7[A]$.

Table 4.1: Measured singlet oxygen and photosensitizer triplet state lifetimes (in μs) from fits to Eq. (4.10) for Photofrin in methanol and Rose Bengal in water [85]

	Photofrin in methanol	Rose Bengal in water
Triplet state lifetime, τ_t (μs)	0.43±0.03	2.1±0.2
Singlet oxygen lifetime, τ_Δ (μs)	9.4±0.2	3.8±0.3
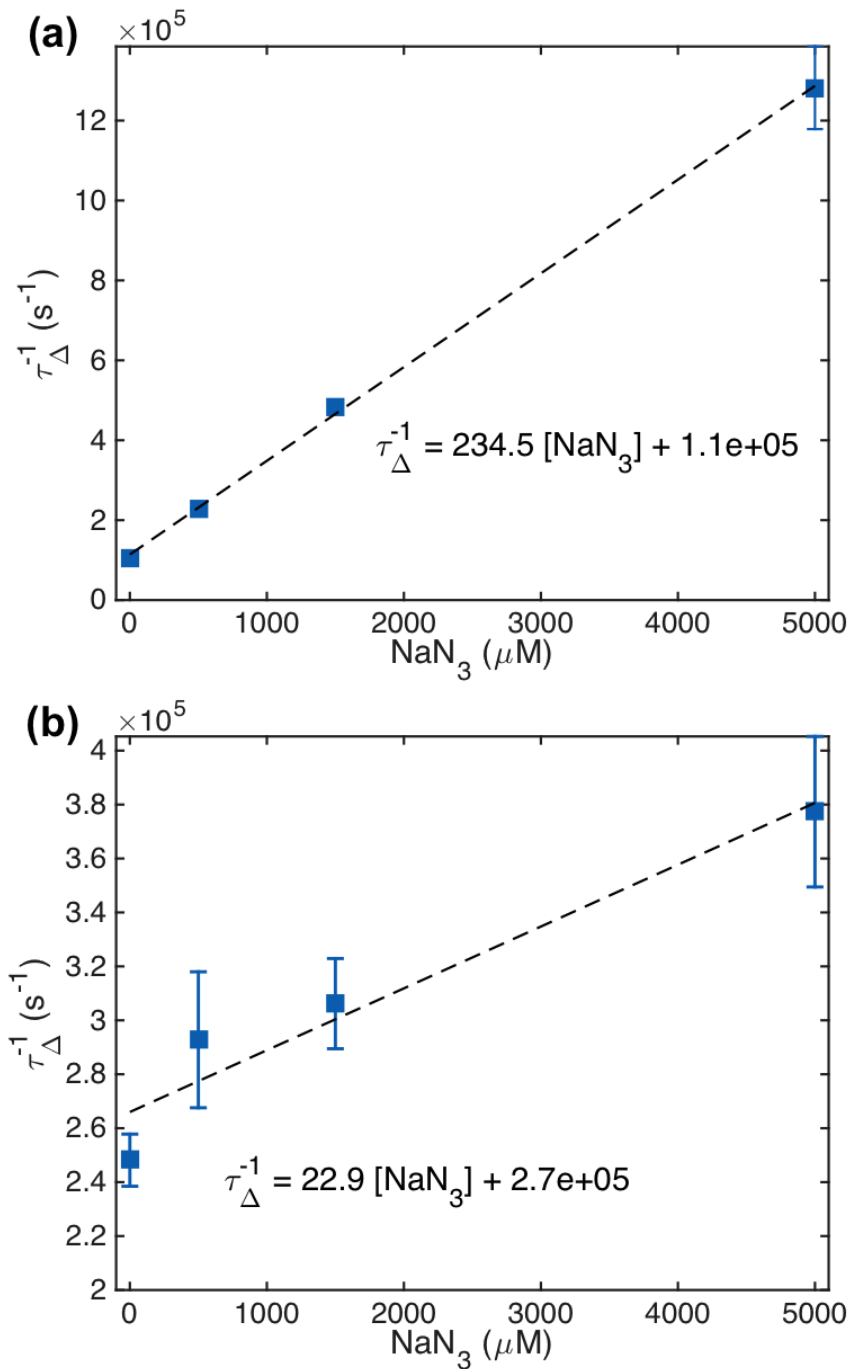
Figure 4.5: Singlet oxygen lifetime (τ_Δ) changes due to quenching with various concentration of sodium azide (NaN_3) for (a) Photofrin (83 μM) in MeOH and (b) Rose Bengal (50 μM) in water. $\tau_\Delta^{-1} = k_{12}([S_0] + \delta) + k_6 + k_9[Q]$. Symbols represent measured data and the solid line is the best linear fit

From this study, it was found that the value of $k_9[Q]$ for a NaN_3 concentration of 5 mM is 1.17×10^6 s^{-1} for Photofrin and 1.15×10^5 s^{-1} for Rose Bengal. This value is dependent on the concentration and efficiency of the singlet oxygen quencher that is being investigated. For the purposes of *in vivo* modeling, it is assumed that any singlet oxygen produced is biologically consumed in the process of cell destruction, so there is no quenching effect. The value of $k_{12}([S_0] + \delta) + k_6$ was found to be 1.1×10^5 s^{-1} for Photofrin and 2.7×10^5 s^{-1} for Rose Bengal. Using the values of k_{12} and δ provided in table 2.4 along with the concentration of photosensitizer used (83 μM and 50 μM for Photofrin and Rose Bengal, respectively), the value of k_6 can be calculated by using $k_6 = \text{intercept} - k_{12}([S_0] + \delta)$. For Photofrin, $k_6 = 3.8 \times 10^4$ s^{-1} in methanol and for Rose Bengal, $k_6 = 2.7 \times 10^5$ s^{-1} in water. Using Photofrin in Intralipid phantoms (see Fig. 4.1), the value of τ_Δ was found to be 3.4 μs, resulting in a calculated value of $k_6 = 2.2 \times 10^5$ s^{-1}.

4.2.2   SOED in phantom

Photofrin phantoms with Intralipid as optical scatterer and absorption due to both the photosensitizer and water (or Intralipid) were used to measure the time dependence of $[^3O_2]$ and photosensitizer concentration, $[S_0]$, under CW 630 nm laser excitation. $[^3O_2](t)$ was measured using an oxygen phosphorescence probe and the photophysical parameters summarized in table 2.4.

Figure 4.6a and b show the measured $[^3O_2]$ and $[S_0]$ at just below the surface ($d = 0$) versus time in an Intralipid phantom (with $\mu'_s = 0.2$ cm^{-1}) for three different initial Photofrin concentrations (27, 50, 167 mM). The symbols are measured values and the lines are SOED-calculated results. Figure 4.6c shows the photosensitizer photobleaching rate per PDT dose, $-\frac{d[S_0]}{dt} \frac{1}{[S_0]\phi[^3O_2]/([^3O_2]+\beta)}$ versus $[S_0]$. The symbols are calculated values using equation (4.3), and the line is the best linear fit. Figure 4.6d

shows the expected SOED-calculated cumulative reacted singlet oxygen concentration, $[^1O_2]_{rx}$, during illumination. The same is shown for Rose Bengal concentrations of 16, 50, and 100 μM in Fig. 4.7.

In Fig. 4.6c and 4.7c, the linear fit to the data plotting $-\frac{d[S_0]}{dt}\frac{1}{[S_0]\phi[^3O_2]/([^3O_2]+\beta)}$ versus $[S_0]$ is shown as a red dashed line. The values found for the slope (m) and intercept (b) can be used to calculate values of δ and σ. If the linear fit is given as $y = mx + b$, then $\delta = b/m$ and $\sigma = m/\xi$. The value of ξ used for these phantom studies is calculated using known values of extinction coefficient, Planck's constant, wavelength of interest, and the singlet oxygen quantum yield from literature. This is described further in chapter 3 and, in particular, table 2.4. For Photofrin, the linear fit shown in Fig. 4.6c has a slope of $(6.9\pm0.5)\times10^{-6}$ and an intercept of $(1.8\pm0.3)\times10^{-5}$, resulting in calculated values of $\delta = 26\pm5$ μM and $\sigma = (6.6\pm5)\times10^{-5}$ μM^{-1}. For the case of Rose Bengal, the linear fit shown in Fig. 4.7c has a slope of $(1.6\pm0.2)\times10^{-6}$ and an intercept of $(3.9\pm1.4)\times10^{-5}$, resulting in calculated values of $\delta = 25\pm9$ μM and $\sigma = (8.1\pm1.2)\times10^{-6}$ μM^{-1}.
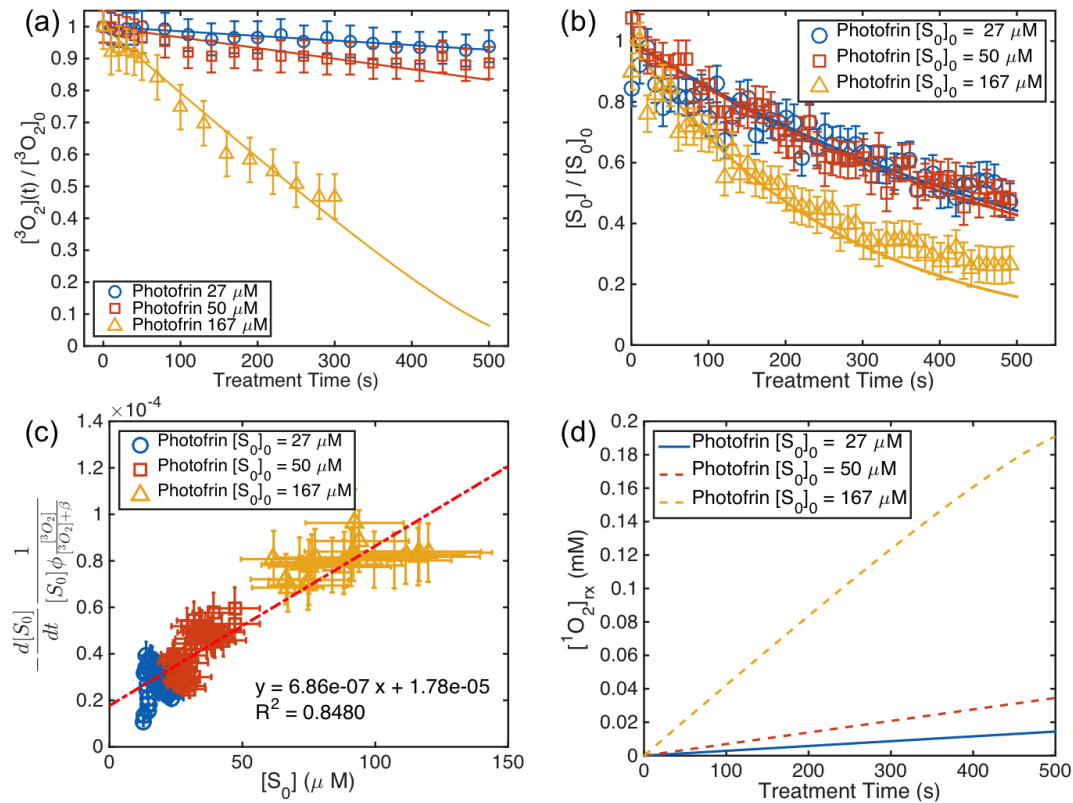
Figure 4.6: Comparison of measured and singlet oxygen explicit dosimetry (SOED)-calculated values of (a) $[^3O_2](t)$ and (b) $[S_0](t)$ at $d = 0$ for three initial photosensitizer concentrations, $[S_0]_0 = 27, 50, 167$ μM. Measurements of ground-state oxygen were made at 5-30 s intervals while photosensitizer spectra were obtained every 10 s. The average initial $[^3O_2]_0$ value was 160.4 μM. (c) The left-hand side of equation (4.3) versus the Photofrin concentration, with the line of best fit. (d) Calculated volume-averaged $[^1O_2]_{rx}$ over time. Eqs. (4.1) and (4.2) were used for this set of data.
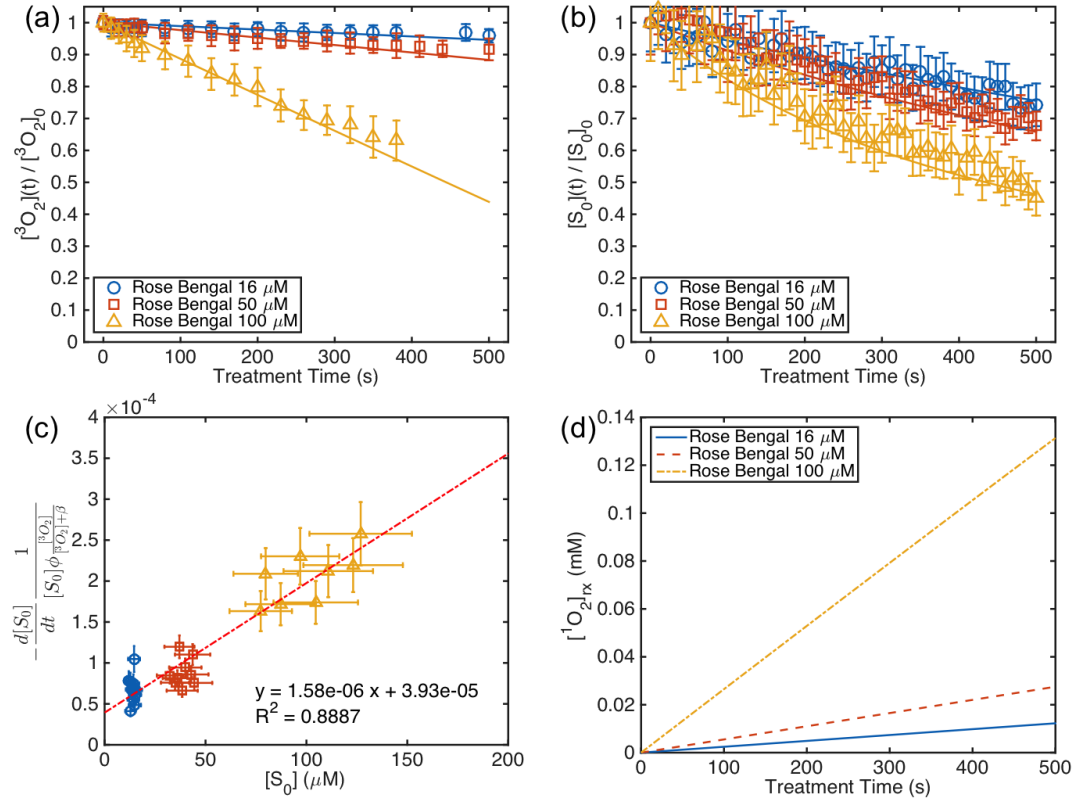
Figure 4.7: Comparison of measured and singlet oxygen explicit dosimetry (SOED)-calculated values of (a) $[^3O_2](t)$ and (b) $[S_0](t)$ at $d = 0$ for three initial photosensitizer concentrations, $[S_0]_0 = 16, 50, 100$ μM. Measurements of ground-state oxygen were made at 5-30 s intervals while photosensitizer spectra were obtained every 10 s. The average initial $[^3O_2]_0$ value was 164.2 μM. (c) The left-hand side of equation (4.3) versus the Rose Bengal concentration, with the line of best fit. (d) Calculated volume-averaged $[^1O_2]_{rx}$ over time. Eqs. (4.1) and (4.2) were used for this set of data.

In phantoms with NaN_3, changes in $[^3O_2]$ were measured using the Oxylite phosphorescence based oxygen probe. Figure 4.8 shows a plot of measured $[^3O_2]/[^3O_2]_0$ in symbols for different concentrations of Photofrin and Rose Bengal. Solid lines show the calculated changes in ground state oxygen using the modified equations to account for singlet oxygen quenching (eqs. (4.8) and (4.9)). A broad beam was used to illuminate a cuvette with a fluence rate of 820 mW/cm^2 at the surface. It is seen that changes in oxygen are not as dramatic as those shown in Fig. 4.6 and 4.7 since

the NaN₃ quenching of singlet oxygen produced ground state oxygen.
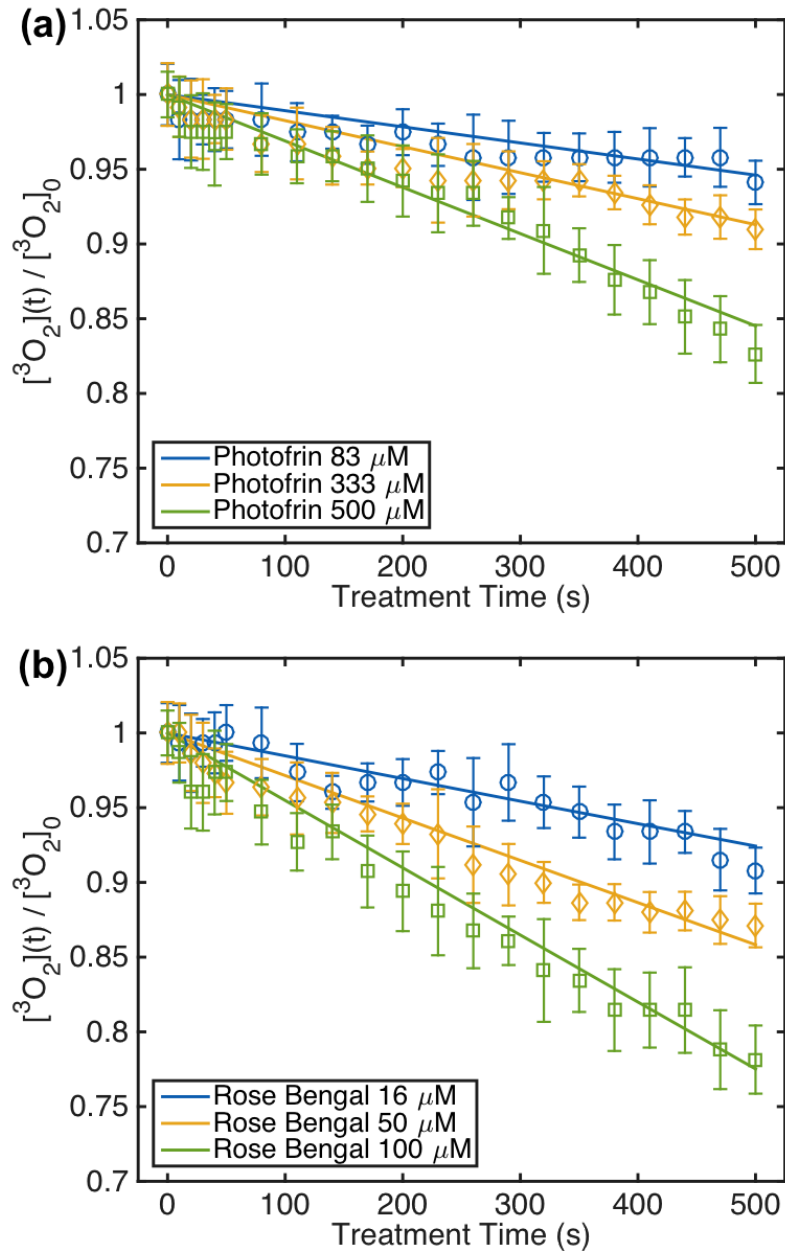
Figure 4.8: Ground state oxygen relative to the initial oxygen ($[^3O_2]_0$) was measured (symbols)for phantoms with NaN₃ and photosensitizers (a) Photofrin (83, 333, and 500 μM) and (b) Rose Bengal (16, 50, and 100 μM). Calculations are shown in solid lines. Eqs. (4.6) and (4.7) were used for this set of data.

4.2.3 SOED/SOLD comparison in solution

The singlet oxygen generated in Photofrin-containing solutions and Rose Bengal-containing solutions was calculated using SOED and the results were compared to SOLD-determined luminescence counts of $^1O_2$. The latter was correlated with the amount of $^1O_2$ produced instantaneously and cumulatively. Instantaneous $[^1O_2]$ accounts for the singlet oxygen generated for each pulse of laser excitation, while cumulative $[^1O_2]_{rx}$ is the integral of all singlet oxygen produced during the entire illumination time over the entire illumination volume. The agreement between the two methods (SOED and SOLD) is shown in figure 4.9: (a) shows SOLD counts per accumulation time (in seconds, $t = 300$ s before and after PDT) and (b) shows cumulative SOLD counts over the entire treatment time of 900 s. Photofrin was dissolved in MeOH solution and Rose Bengal was dissolved in water [130].
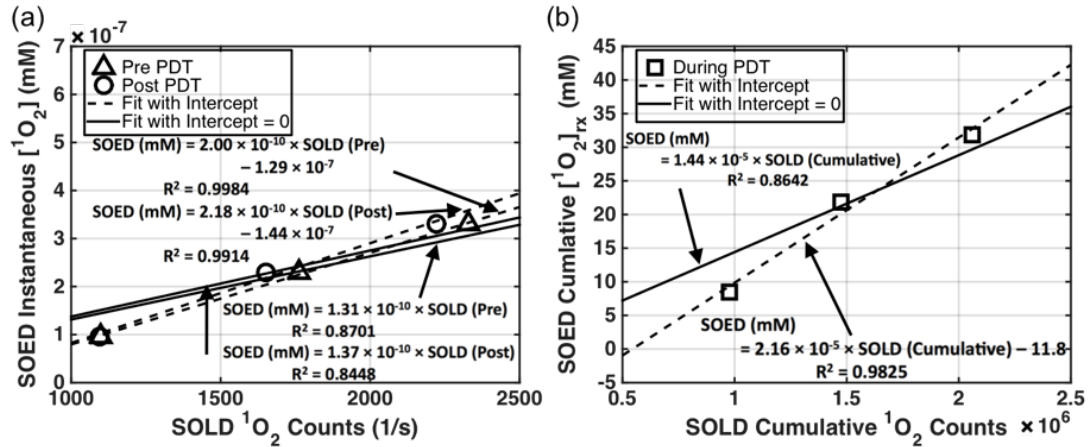
Figure 4.9: (a) Comparison of SOLD-obtained $^1O_2$ counts (equation (4.10)) per accumulation time (in seconds) at 523 nm and SOED-calculated instantaneous $[^1O_2]$ (equation (4.4)) for Photofrin concentrations in MeOH of 17, 50, and 83 μM, and light fluence $\phi_0 = 30$ mW/cm^2. The initial oxygen concentration was measured as 175 ± 6 μM. (b) Comparison of SOLD cumulative $^1O_2$ counts (equation (4.11)) and reacted singlet oxygen concentration ($[^1O_2]_{rx}$) calculated with SOED (equation (4.5)) for Photofrin concentration of 17, 50, and 83 μM. PDT was performed with 523 nm light at $\phi_0 = 30$ mW/cm^2 for 900 s.
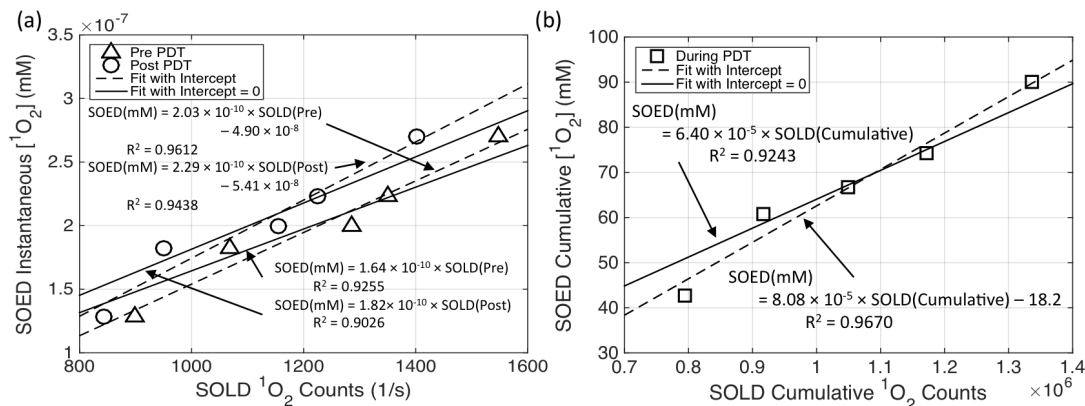
Figure 4.10: (a) Comparison of SOLD-obtained $^1O_2$ counts (equation (4.10)) per accumulation time (in seconds) at 523 nm and SOED-calculated instantaneous $[^1O_2]$ (equation (4.4)) for Rose Bengal concentrations in water of 9.8, 19.7, 29.5, 39.3, and 49.1 μM, and light fluence $\phi_0 = 30$ mW/cm^2. The initial oxygen concentration was measured as 178 ± 3 μM. (b) Comparison of SOLD cumulative $^1O_2$ counts (equation (4.11)) and reacted singlet oxygen concentration ($[^1O_2]_{rx}$) calculated with SOED (equation (4.5)) for Rose Bengal concentrations of 9.8, 19.7, 29.5, 39.3, and 49.1 μM. PDT was performed with 523 nm light at $\phi_0 = 30$ mW/cm^2 for 900 s.

4.3   Discussion

4.3.1   SOED and SOLD intercomparison

The SOED calculated $[^1O_2]$ value in solution in Figure 4.8a corresponds to the volumetric averaged instantaneous singlet oxygen concentration over a volume of 1 cm depth and 1 cm^2 area. SOED-calculated $[^1O_2]_{rx}$ in Figure 4.9b corresponded to the volumetric average reacted singlet oxygen concentration of the same 1 cm^3 volume. In these solutions, the light fluence was calculated by introducing only the attenuation that is due to the photosensitizer absorption, since no scatterer was added and solutions were of pure Photofrin: $\phi = \phi_0 \cdot e^{-\mu_a \times d}$, where ϕ_0 is the light fluence rate (mW/cm^2) measured directly on the back of the front wall of the solution facing the laser. Absorption coefficients (μ_a) were 0.15, 0.45, and 0.74 cm^{-1} for Photofrin

concentrations of 17, 50, and 83 μM, respectively, at 523 nm.

In order to experimentally determine the photophysical parameters of the spontaneous phosphorescence rate of $^1O_2$ to $^3O_2$ (k_6) and the bimolecular reaction rate of $^1O_2$ with the substrate (k_7) in Photofrin phantoms, photosensitizer triplet-state and singlet oxygen lifetime measurements were obtained using the SOLD system. Varying amounts of the singlet oxygen quencher, sodium azide (NaN$_3$), were added to the PhotofrinMeOH solutions. The resulting fits to obtain k_6 and k_7 are shown in Figure 4.5. For Photofrin with NaN$_3$, k_6 was found to be $1.14 \times 10^5 s^{-1}$ (the intercept of the line of best fit in Figure 4.5) and k_7 was found to be 235 μM^{-1}s^{-1} (the slope of the line of best fit in Figure 4.5). k_7 is pH-dependent, but is in the range of the reported value of 300400 μM^{-1}s^{-1} for the quenching rate constant in water [155]. These values were used to calculate τ_Δ for the *in vitro* condition (without NaN$_3$) and the *in vivo* condition (taken from the literature for biological tissue [125]). Assuming that k_7 for NaN$_3$ is greater than or equal to that of *in vivo* conditions (assuming biological tissue is less efficient than NaN$_3$ in quenching $^1O_2$), it can be estimated that *in vivo* acceptor concentration $[A] \geq 10^7$ (s^{-1})/235 mM^{-1}s^{-1} = 42 mM. This value is much higher than $[A] = 0.83$ mM in the literature [28], but we feel that it is more reasonable since the singlet oxygen lifetime *in vivo*, τ_Δ, does not change for reacted singlet oxygen concentrations $[^1O_2]_{rx}$ as high as 12 mM [27], indicating there are still plenty of acceptors *in vivo* at this level.

The light fluence rate distribution in a semi-infinite medium as a function of distance (d) was calculated by a Monte Carlo (MC) simulation [156] of a circular parallel beam (diameter 0.8 cm, Figure 4.9a) and broad beam (diameter 16 cm, Figure 4.11b) for absorption coefficient (μ_a) of 0.09, 0.18, and 0.58 cm^{-1}, and reduced scattering coefficient (μ_s') of 0.2 cm^{-1}. The resulting ϕ/ϕ_0 is shown in Figure 4.11 along with an exponential fit based on μ_a. For the tissue-simulating phantoms with

Photofrin shown in Figure 4.6, ϕ_0 is the measured local fluence rate at the front inner surface of the phantom facing the laser and d is the depth from surface. At 630 nm, $\mu_a = 0.09$, 0.18, and 0.58 cm^{-1} for Photofrin concentrations of 27, 50, and 167 mM, respectively. It is clear that the function $e^{-\mu_a \cdot d}$, while working well for the broad beam, does not work very well for the 0.8 cm diameter beam at the deepest depths investigated. As a result, MC-generated light fluence rate ϕ/ϕ_0 was used directly for the SOED calculations in phantom.
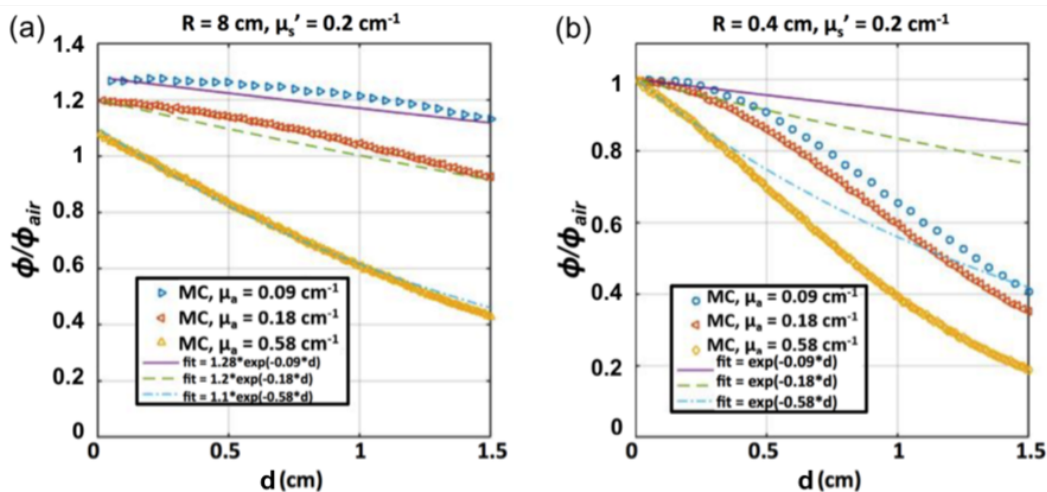
Figure 4.11: Monte Carlo (MC) simulation of fluence rate distribution by a circular beam of radius (a) 0.4 cm and (b) 8 cm incident on a semi-infinite liquid surface as a function of depth (d) for $\mu_a = 0.09$, 0.18, and 0.58 cm^{-1} and $\mu'_s = 0.2$ cm^{-1}. Fits of exponential forms are shown along with the MC data. The exponential form of $e^{-\mu_a \cdot d}$ fits the simulation well up to a depth of 0.4 cm, while overestimating ϕ/ϕ_0 at larger depths. Broad-beam simulations agree with the simple exponential form up to a depth of 1.3 cm.

SOED calculations of singlet oxygen concentration are highly dependent on the photophysical parameters used as input (table 2.4). In turn, these parameters depend on the photosensitizer used, as well as the treatment environment. The necessary parameters for Photofrin-mediated PDT for *in vitro* studies were validated with explicit measurements of the $[^3O_2]$ and $[S_0]$. In particular, the consumption rate of $[S_0]$ per

PDT dose was used to determine a more accurate value of σ (slope/ξ) and δ (intercept/slope) for the experimental setup used (Fig. 4.6 and 4.7 and Eq. (4.3)). This was used to determine δ and σ using a method from reference [45] that is also described in section 4.1.1. Photosensitizer concentration was measured over time to determine the photobleaching rate $(-d[S_0]/dt)$ and $[S_0]$. Along with the measured $[^3O_2]$, the photosensitizer photobleaching rate per PDT dose can be calculated and plotted as in Fig. 4.6c. The slope and intercept were used to determine the values $\delta = 26 \pm 5\mu M$ and $\sigma = (6.8 \pm 5) \times 10^{-5}\mu M^{-1}$. The value of β was set to be 11.9 μM for this set of experiments [125]. Figure 4.6a and b show the SOED calculations using equations (4.1) and (4.2), which agree with $[S_0](t)$ and $[^3O_2](t)$ measurements at the surface $(d = 0$ cm$)$ of the Intralipid phantom. Figures 4.6d and 4.7d show the magnitude of SOED-calculated $[^1O_2]_{rx}$ for Photofrin and Rose Bengal to be in the sub mM range.

It can be concluded from the intercomparison of SOED and SOLD in Photofrin solutions (figure 4.9b) that the cumulative SOLD $[^1O_2]$ counts, $[SOLD]$, and SOED-calculated $[^1O_2]_{rx}$ values track each other very well $(R^2 = 0.98)$ for Photofrin, with a conversion factor of the following form:

$$[^1O_2]_{rx}(mM) = \left(2.16 \times 10^{-5}\right) \times [SOLD] - 11.8 \qquad (4.12)$$

The ratio of slopes between the two panels ((a) and (b)) in Fig. 4.9 is 9.6×10^{-6} s, which is consistent with the value of τ_Δ obtained $(9.4 \times 10^{-6}$ s$)$. The reason for the intercept is not known, and a linear fit without the intercept reduces the correlation $(R^2 = 0.86)$. The good correlation of SOED-calculated $[^1O_2]$ and $[SOLD]$ demonstrates that SOED can be utilized in scenarios where direct phosphorescence measurement of $^1O_2$ is difficult.

4.3.2 Feasibility of using SOLD at 523 nm for predicting $[^1O_2]_{rx}$ at 630 nm

Currently, the only available pulsed laser suitable for the SOLD application is at 523 nm (CrystaLaser, QL-523-200-S, CrystaLaser, Reno, NV, USA). As a result, the effective tissue-sampling depth for $[^1O_2]$ is not the same as that of the 630 nm treatment light used clinically with Photofrin. Figure 4.12 shows the measured values of μ_a and μ'_s at various sites measured *in vivo* in patients, including the anterior chest wall, apex of the heart (apex), posterior chest wall, diaphragm (diaph), serratus (ser), anterior sulcus, posterior sulcus, pericardium (peri), and normal tissue (norm). This data is from patients undergoing an institutional review board (IRB)-approved clinical trial at the University of Pennsylvania. Details of which are included in chapter 7
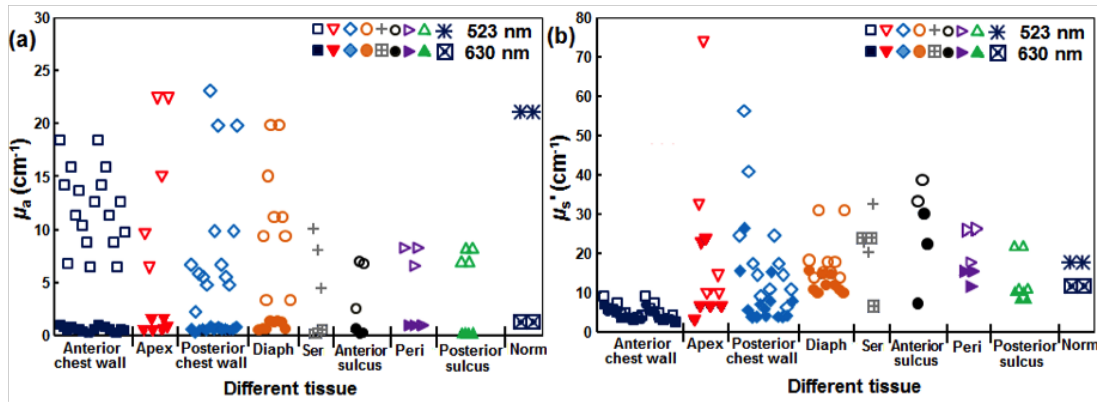
Figure 4.12: Tissue (a) μ_a and (b) μ'_s at 523 nm (hollow symbols) and 630 nm (filled symbols) measured *in vivo* in patients pleural cavities undergoing radical pleurectomy and PDT for the treatment of malignant pleural mesothelioma

Using an analytical fit [157] to MC simulations [158–161], the longitudinal distribution of ϕ in tissue with different optical properties was calculated. Figure 4.13 shows the ratio of ϕ and in-air fluence rate (ϕ_{air}) versus tumor depth for (a) 523 nm and (b) 630 nm. The grey area shows the region of ϕ/ϕ_{air} with the upper and lower

bounds of the tissue optical properties obtained *in vivo* as dark blue and light blue, respectively. The dashed black lines show the calculated light fluence distribution using the mean optical properties of $\mu_a = 5.52$ cm^{-1} and $\mu'_s = 17.61$ cm^{-1} for 523 nm and $\mu_a = 0.58$ cm^{-1} and $\mu'_s = 15.61$ cm^{-1} for 630 nm. As expected, the optical penetration is much deeper with 630 nm than with 523 nm *in vivo*.
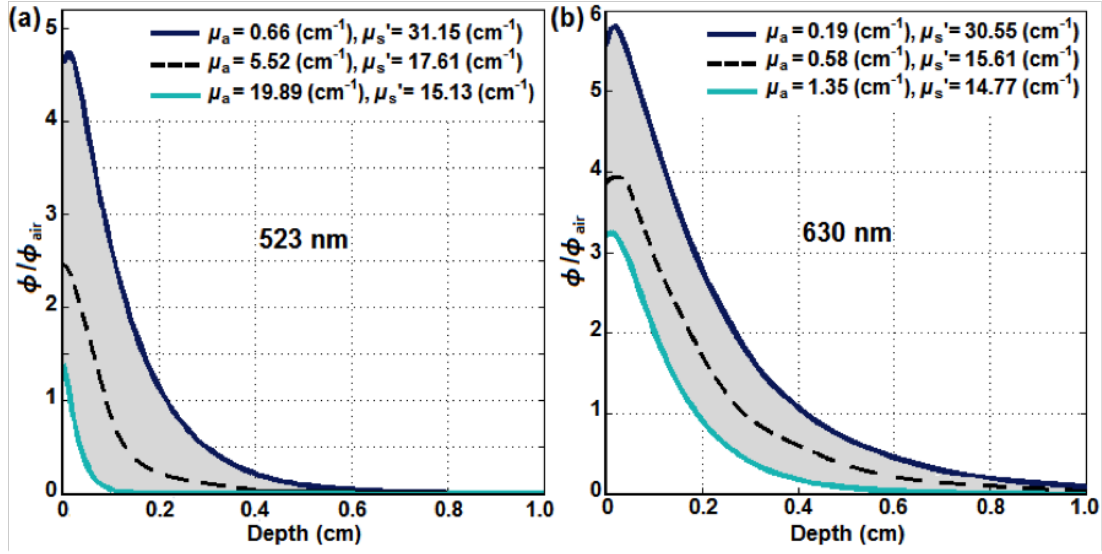
Figure 4.13: The ratio of ϕ and in-air fluence (ϕ_{air}) versus tumor depth for (a) 523 nm and (b) 630 nm optically broad laser beams on an air-tissue interface using an analytical formula that fits MC simulations using optical properties obtained *in vivo* from patients undergoing treatment for MPM

The ϕ distributions were then used to calculate the reacted singlet oxygen concentration for the two wavelengths to study whether SOLD signals measured at 523 nm can be used to monitor $[^1O_2]_{rx}$ at 630 nm. PDT is currently performed at 630 nm for patients undergoing Photofrin-mediated PDT in conjunction with radical pleurectomy. Correlation between the calculated $[^1O_2]_{rx}$ for 630 nm and 523 nm is shown in figure 4.14. μ_a ranges from 0.66 to 23.1 cm^{-1} at 523 nm and 0.17 to 1.35 cm^{-1} at 630 nm, while μ'_s ranges from 2.80 to 73.7 cm^{-1} at 523 nm and 2.55 to 30.5 cm^{-1} at 630 nm (figure 4.12). To investigate the effects of different ϕ on the resulting

calculated $[^1O_2]_{rx}$, the SOED calculations were repeated for $\phi = 5, 25, 50, 75,$ and 150 mW/cm^2. Different colors of the symbols represent different ϕ. The black solid lines are the lines of best fits in figure 4.14. At 523 nm, the range of $[^1O_2]_{rx}$ changed from 0-0.1, 0-0.63, and 0-5.6 mM for photosensitizer concentrations of 0.21, 2.1, and 21 μM, respectively, while the range of $[^1O_2]_{rx}$ at 630 nm changed from 0-0.24, 0-2.5, and 0-20 mM, respectively, for the same photosensitizer concentrations.

The resulting correspondence for a range of photosensitizer concentrations (c) of 0.21, 2.1, and 21 μM (based on the average Photofin concentration obtained from patient data) and light fluences of 10-120 J/cm^2 [162] can be expressed as

$$[^1O_2]_{rx}(630 \text{ nm}) = a(c)[^1O_2]_{rx}(523 \text{ nm}) + b(c, \phi) \tag{4.13}$$

where

$$a(c) = 0.05814c + 1.922 \tag{4.14}$$

and

$$b(c, \phi) = (0.000618c - 0.000033)\phi \tag{4.15}$$

where c is the photosensitizer concentration (in μM) and ϕ is the light fluence (in J/cm^2). We thus conclude that the SOLD measurements performed at 523 nm can be used to monitor the $[^1O_2]_{rx}$ at 630 nm if a conversion formula (such as that of Eq. (4.13) - (4.15)) is used to convert the measured SOLD signal.

When SOLD signal from patients are used to determine the generation of singlet oxygen, it is important to develop a tissue optical properties correction factor to account for the absorption and scattering of luminescence by tissue, similar to the optical properties correction factor needed for using fluorescence to determine the photosensitizer concentration (described in section 3). This is beyond the scope of

this study.
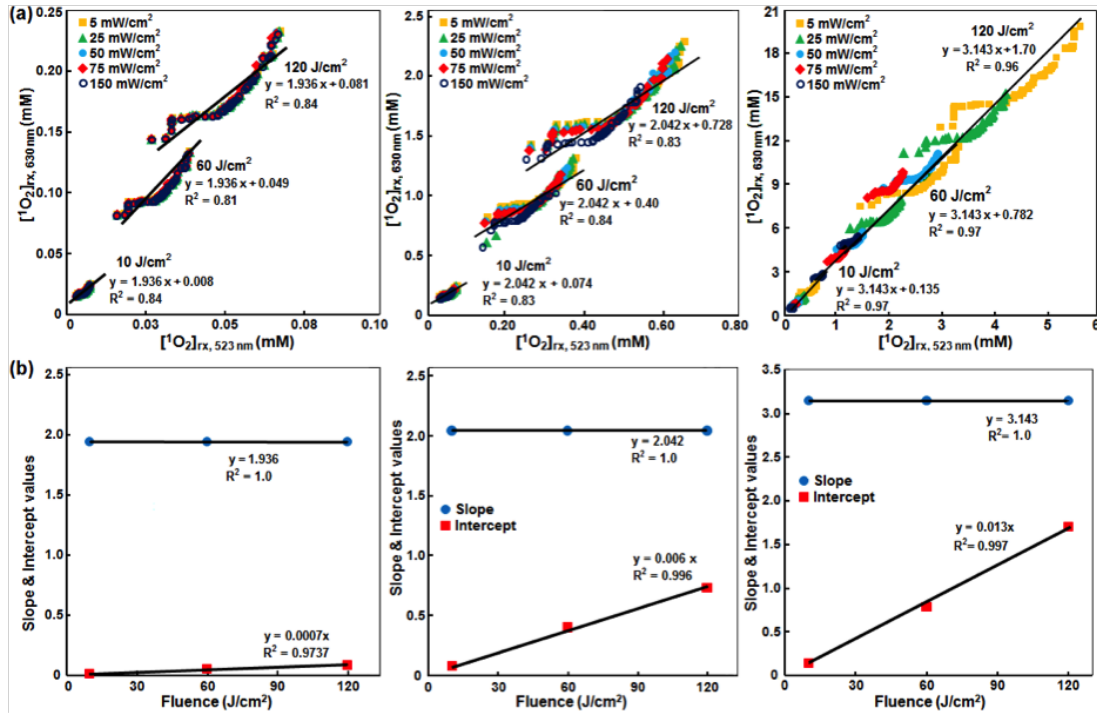
Figure 4.14: (a) $[^1O_2]_{rx}$ calculated at 630 nm and 523 nm for different total fluences ($\phi = 10$, 60, 120 J/cm^2 for mean Photofrin concentrations (c) of (from left to right) 0.21, 2.1, and 21 μM. Absorption and scattering coefficients were obtained at the two wavelengths from figure 4.11. SOED calculations of $[^1O_2]_{rx}$ were averaged over a 1 cm depth and 1 cm^3 volume using the photophysical parameters for the *in vivo* conditions (listed in table **??**); (b) Slope and intercept of the correlation of $[^1O_2]_{rx}$ at 630 nm and 523 nm as a function of fluence and photosensitizer concentration

4.4 Conclusions

Studies using Photofrin and Rose Bengal were performed to investigate explicit singlet oxygen modeling in phantoms as well as the required in-phantom parameters. Use of singlet oxygen luminescence detection enabled measurements changes in τ_Δ with the addition of NaN$_3$. These results were able to be used to determine k_6 and $k_9[Q]$. Literature values were used for k_1 and Φ_Δ in the calculation of ξ. Absorption studies

were used to determine the value of ε. Photosensitizer fluorescence was used to measure relative changes in $[S_0]$ after the addition of a known amount to a phantom. Light fluence was modeled as a broad beam with known fluence rate at the surface.

Direct singlet oxygen luminescence dosimetry (SOLD) measurements were compared with singlet oxygen explicit dosimetry (SOED) calculations for phantoms using Photofrin. Oxygen and photosensitizer concentration measurements were compared with SOED predictions to validate the SOED model and to obtain the needed photophysical parameters (table 2.4, $\delta = 26 \pm 5\mu M$ and $\sigma = (6.8 \pm 5) \times 10^{-5}\mu M^{-1}$). Using lifetime measurements obtained with the SOLD system, photophysical parameters of k_6 $(2.2 \times 10^4 \text{ s}^{-1})$ and k_9 $(235\mu M^{-1}s^{-1})$ were found for *in vitro* solutions with NaN$_3$. A linear relationship between SOLD singlet oxygen photon counts at 1270 nm and SOED-calculated reacted singlet oxygen (equation (4.12)) was established for Photofrin for 523 nm light excitation. Based on our SOED calculations, a formula (equations (4.13)-(4.15)) for converting cumulative SOLD signal measured at 523 nm to the corresponding $[^1O_2]_{rx}$ at 630 nm was established using optical properties measured at the two wavelengths as a part of an ongoing clinical protocol.

These results indicate that, with suitable correction for the tissue optical properties at the two wavelengths, there is excellent correlation between the direct (SOLD) and indirect (SOED) estimates of singlet oxygen generated during PDT. Since, at the present time, the SOED approach is technically simpler and the instrumentation is significantly less expensive, this validation supports the use of SOED in clinical dosimetry. It should be noted, however, that the SOLD technique is intrinsically more robust in that no simplifying assumptions are made as in SOED. Hence, care must be taken in applying SOED to ensure that the treatment parameters lie within the range of validity of these assumptions. Furthermore, the validation of SOED must be carried out for each photosensitizer and set of clinical conditions. In the

future, developments such as a recent report of fiber optic-coupled SOLD techniques based on novel superconducting nanowire single-photon detector technologies of direct SOLD [153], may accelerate movement towards clinical utilization of SOLD alongside SOED. For type I PDT where a reactive oxygen species (e.g. oxygen radicals) other than singlet oxygen is the main cytotoxic agent, it is still possible to model the photophysical process using SOED, as described in section 2 and a recent review [34]. However, it still remains a challenge to find the value of the photophysical parameters needed to describe the type I interactions for those photosensitizers.

Chapter 5

Determination of *in vivo* Photochemical Parameters

The macroscopic singlet oxygen model can be used for singlet oxygen explicit dosimetry (SOED) as long as the relevant photochemical parameters are known. Determination of the *in vivo* photochemical parameters is critical for the use of SOED for the photosensitizer of interest. A study was performed to optimize the values of the photochemical parameters (ξ, σ, δ, β, and g) for *in vivo* benzoporphyrin monoacid ring A (BPD)-mediated PDT with a 3 hour drug-light interval (DLI). Furthermore, the singlet oxygen threshold dose ($[^1O_2]_{rx,th}$) was determined to induce necrosis in a radioactively induced fibroscarcoma (RIF) tumor in a murine model.

5.1 Theory and Methods

5.1.1 Macroscopic model for *in vivo* studies

The macroscopic singlet oxygen model was described previously in chapter 2 and in section 3.5. To summarize, the photochemical reactions to describe the production

and consumption of photosensitizer, oxygen, and singlet oxygen can be described by the following equations:

$$\frac{d[S_0]}{dt} = -\frac{[^3O_2]}{[^3O_2] + \beta}\xi\sigma([S_0] + \delta)\phi[S_0],$$ (5.1)

$$\frac{d[^3O_2]}{dt} = -\frac{[^3O_2]}{[^3O_2] + \beta}\xi\phi[S_0]([S_0] + \delta) + g\left(1 - \frac{[^3O_2]}{[^3O_2](t=0)}\right),$$ (5.2)

$$\frac{d[^1O_2]_{rx}}{dt} = \frac{[^3O_2]}{[^3O_2] + \beta}\xi\phi[S_0],$$ (5.3)

The parameters of ξ, σ, g, and threshold concentration of reacted singlet oxygen to induce necrosis were determined in this study. The parameters β and δ were taken from the literature that involved *in vitro* cell studies [53, 125].

5.1.2 Treatment delivery

Mice were treated with linear source strength (LS), power released per length, of 12-150 mW/cm and total energy released per length of 24-135 J/cm. A 1 cm long cylindrical diffusing fiber (CDF) light source was connected to an 8W, 690 nm diode laser (B & W Tek Inc., Newark, DE, USA) via a SMA connector. Two catheters were inserted parallel with a 3 mm separation into the mouse tumor (Fig. 3.2 (a)). One catheter included the treatment light and was central to the tumor, and the second catheter held the isotropic detector or a side-cut fiber for optical properties or fluorescence measurements. Treatment conditions are summarized with the measured data in table 5.1.

5.1.3 RIF tumor necrosis measurement and analysis

The tumors were excised 24 hours after PDT and stored in formalin until time for embedding and sectioning. Tumors were sectioned at 200 μm slices perpendicular to the treatment linear source orientation and placed onto slides to be stained with hematoxylin and eosin (H & E) to see the necrotic area. Slides were then scanned digitally with a ScanScope microscope (Leica Microsystems Inc., Buffalo Grove, IL, USA), and necrotic radii were obtained. Controls were included for each group of animals studied, with the average necrotic radius among these controls (r_0) being 1.6 mm. This was calculated by determining the necrotic area (A_c) on the digitally scanned slide and using the formula $A_c = \pi r^2$. The PDT-induced necrosis for each treated mouse was determined by $r_n = r_t - r_0$, where r_t is the measured raw necrosis for treated mice. For all necrosis radii, a shrinkage factor (SF) was included due to the tumor shrinkage induced by preservation in formalin. This was determined by measuring the tumor dimensions prior to formalin fixation and after at least 24 hours of fixation time. The standard error for each necrosis radius was determined by propagating the uncertainty from each source of error. The standard deviation of each individual mouse tumor necrosis radius as well as the uncertainty in radius measurement due to the ellipsoidal shape of certain tumor sections was included in this calculation. For ellipsoidal tumors, the radius was measured from the light delivery source (central catheter) insertion point to the edge of the necrotic area at various angles to determine the uncertainty due to this shape [120].

Table 5.1: BPD-mediated Necrosis Study Treatment Conditions, Optical Properties, Necrosis Radii

Group	LS [a] (mW/cm)	Time (s)	Energy [b] (J/cm)	BPD Conc. (μM)	μ_a (cm^{-1})	μ'_s (cm^{-1})	Necrosis Radius, r_t (mm)	Control Radius, r_0 (mm)	PDT-Induced Necrosis (mm)
(a)	Experiment Group 1; each treatment group contains 3 mice								
1	12	2000	24	0.90±0.14	0.8±0.1	8.0±0.5	2.8±0.7	1.6	1.2±0.7
2	12	3000	36	0.71±0.03	0.7±0.1	9.4±1.1	3.0±0.7	1.3	1.7±0.7
3	20	1600	32	0.49±0.07	0.7±0.1	8.0±0.5	1.9±0.7	1	0.9±0.7
4	30	1020	30.6	0.98±0.02	0.9±0.1	7.9±1	3.4±0.7	1.3	2.1±0.7
5	75	660	49.5	0.59±0.13	0.8±0.1	10.3±0.7	2.6±0.4	1.7	0.9±0.4
6	75	1800	135	0.47±0.10	0.6±0.1	12.5±1	3.2±0.2	1	2.2±0.2
7	150	420	63	0.99±0.03	0.8±0.1	9.9±0.6	2.9±0.6	1.3	1.6±0.6
(b)	Experiment Group 2 from 2013 [119]; individual ungrouped mice were used								
8	12	4000	48	0.43	0.7	6.5	2.5	1.3	1.2
9	12	6000	72	0.17	0.7	11.2	3.1	2.3	0.8
10	20	3000	60	0.17	0.7	13.5	2.4	2.3	0.1
11	20	4000	80	0.32	0.7	15.2	3	1.3	1.7
12	30	1980	59.4	0.42	0.6	10.8	2	0.8	1.2
13	30	4500	135	0.35	0.5	14.3	1.4	0.8	0.6
14	75	300	22.5	0.25	0.7	12.2	2.6	2.3	0.4
15	150	180	27	0.17	0.5	9.8	2.8	2.3	0.5
16	150	660	99	0.17	0.8	9.4	2	2.3	0

[a] Linear source strength
[b] Total energy delivered per unit length

5.1.4 Macroscopic singlet oxygen model to fit necrosis

The equations for the macroscopic singlet oxygen model first described in chapter 2 and specified for *in vivo* environments in Eq. (5.1)-(5.3) were used in the calculation of reacted singlet oxygen to fit the necrotic radius and to determine the *in vivo* photochemical parameters. For a given value of ϕ, spatially resolved light fluence rate profiles can be constructed using the diffusion equation

$$\mu_a \phi \nabla \cdot \left(\frac{1}{3\mu'_s} \nabla \phi \right) = S \tag{5.4}$$

where ϕ is the light fluence rate, S is the source term, and μ_a and μ'_s are the absorption and scattering coefficients, respectively. For a given value of ϕ, spatially resolved light fluence rate profiles can be constructed using equation (5.4), which were then

used in the calculation of the PDT kinetic equations. For this study, a 1 cm CDF was used as the treatment source. From the simulation results, it can be seen in Fig. 5.3 that the light fluence rate distribution within a 5 mm radial distance with respect to the center of the linear source does not show significant differences for the case of experimentally varying optical properties.

In order to fit the necrotic radius, a fitting quantity called "apparent singlet oxygen threshold concentration" ($[^1O_2]_{rx,sd}$) was introduced. An initial estimate for each photochemical parameter (g, ξ, and σ) as well as the singlet oxygen threshold dose ($[^1O_2]_{rx,sh}$) is used to calculate $[^1O_2]_{rx}$ for each treatment group described in table 5.1. The differential evolution algorithm adjusts the photochemical parameters of g, ξ, and σ to match the calculated $[^1O_2]_{rx}$ at the necrosis radius to match the assigned $[^1O_2]_{rx,sd}$. Values of σ and β were kept constant according to values obtained from the literature throughout the fitting process to avoid convergence issues from having too many free-floating parameters [44, 54, 125]. Furthermore, the calculated $[^1O_2]_{rx}$ is less sensitive to these quantities than other model parameters [44]. The initial tissue oxygen concentration was set as 40 μM [48]. After calculating the time series solution for $[^1O_2]_{rx}$, the value at the radius of necrosis was determined and compared to the $[^1O_2]_{rx,sd}$ by minimizing the standard deviation according to the following objective function:

$$f = \sqrt{\frac{\sum_i^N \left|1 - \frac{[^1O_2]_{rx}(r_i)}{[^1O_2]_{rx,sd}}\right|^2}{(N(N-1)}}$$

(5.5)

Here, N is the total number of groups or individual mice, and r_i is the measured radius of necrosis for group/mouse number i. Multi-variable optimization using the functional minimization function *fminsearch.m* from Matlab (Mathworks, Natick, MA) was implemented.

Error margins for the fitted parameters were determined by propagating the sys-
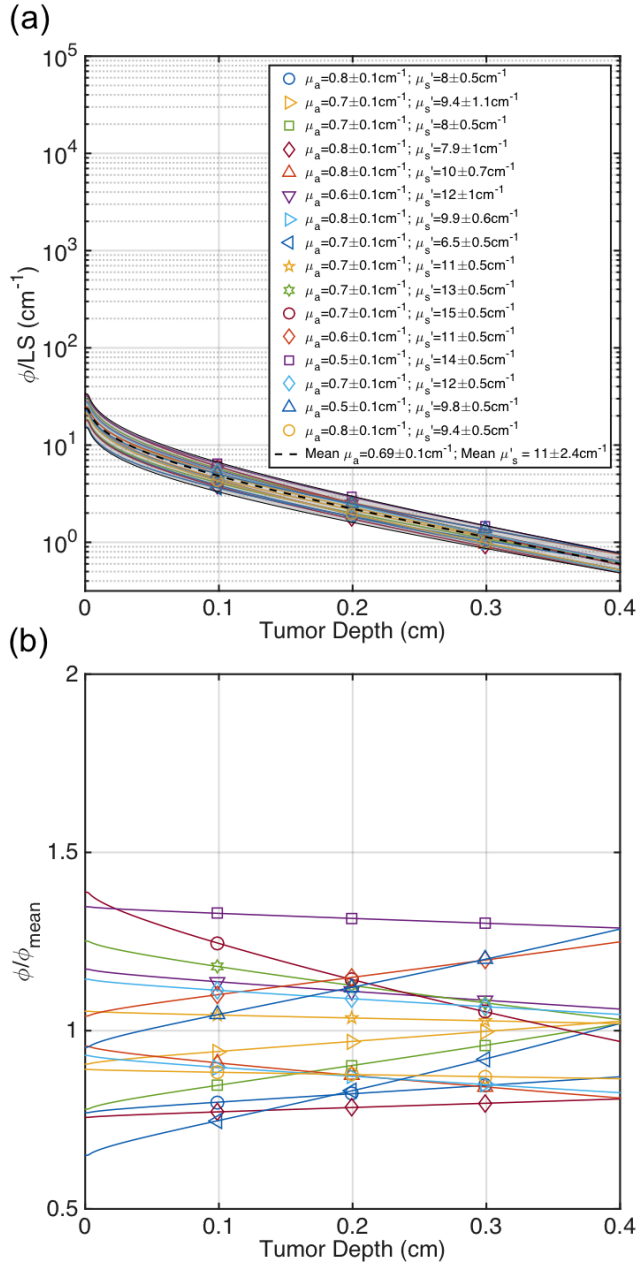
Figure 5.1: (a) Fluence rate (in mW/cm²) per linear source strength (LS, in mW/cm) in RIF tumors tissue for various optical properties measured in mice. Calculations were made with a linear source model. (b) The fluence rate relative to the mean fluence rate for all measured optical properties. The maximum deviation at 3 mm away from the light source is around 20% for the first 7 treatment groups with 3 mice each, indicating that variations in optical properties account for less than 20% of the experimental error with consistent measurements.

tematic and random error from the experiment through the fitting process. To determine the variation in the resulting parameters that were fit, over 500 combinations of initial input parameters were chosen to start the fitting. The initial estimated parameters ranged from $\sigma = (0.5 - 10) \times 10^{-5} \mu M^{-1}$, $\xi = (10 - 100) \times 10^{-3}$ cm^{2}mW^{-1}s^{-1}, $g = 0.5 - 2.0 \mu M$s^{-1}, and $[^1O_2]_{rx,sd} = 0.5 - 2.0 mM$. In each iteration, only one parameter was changed within the range presented while the others were set to standard initial estimates ($\sigma = 5 \times 10^{-5} \mu M^{-1}$, $\xi = 85 \times 10^{-3}$ cm^{2}mW^{-1}s^{-1}, $g = 0.7 \mu M$s^{-1}, and $[^1O_2]_{rx,sd} = 0.7 mM$). Each round of optimization minimized the objective function equation (5.5) and output parameters were collected and analyzed for their maximum deviations. Final values determined from the best optimization of the objective function are presented along with their minimum and maximum ranges in table 5.2.

Using the macroscopic model, $[^1O_2]_{rx}$ and PDT dose were calculated and compared to PDT-induced necrosis. $[^1O_2]_{rx}$ and PDT dose at 3 mm from the CDF was used as a dose metric, where 3 mm was chosen since it happened to be the distance used in the measurements between the two catheters. $[^1O_2]_{rx}$ and PDT dose at the necrosis radius were also calculated as second dose metrics. These values are summarized in table 5.3.

Necrosis radii, along with their standard uncertainties are presented in table 5.1. The error includes the sum of squares of variations in radius measured between mice treated with the same condition as well as the systematic error of necrosis. Some of the tumor sections obtained exhibited an ellipsoidal shape due to the treatment and sectioning. The variation in necrosis due to the ellipsoidal shape was taken into account as systematic error. Standard deviation of each calculated value of fluence, PDT dose, and $[^1O_2]_{rx}$ are also presented in table 5.3. For the most part, 3 mice were used in each treatment group.

All fitting and simulation were performed using Matlab R2014b on an iMac OSX

version 10.10.5 (processor 2.9 GHz Intel Core i5, 16 GB memory). The calculation times were in seconds for the rate equations and in minutes for the spatially coupled differential equations.

5.2 Results

The photochemical parameters found for explicit dosimetry modeling *in vivo* for BPD-mediated PDT are summarized in table 5.2. Initial fitting was performed with the estimate for these parameters in ranges found for other *in vitro* and *in vivo* studies of other photosensitizers. These parameters were further validated using an outcome modeling study described in chapter 6.

The concentration of BPD in tumors was acquired interstitially. The method was verified with an *ex vivo* method described in section 3.3.3. The results of the comparison are shown in figure 3.4. Each data point represents the average value of three separate measurements made in the same tumor using both interstitial and *ex vivo* methods. The best linear fit obtained when comparing the two was $y = 0.98x$ with $R^2 = 0.98$ (black solid line). The dashed line represents a line with a slope of 1, which would be the case if both measurements were in perfect agreement. However, the results from the comparison show that the fluorescence correction for interstitial measurements is fairly accurate.

Table 5.2: *In vivo* photochemical parameters obtained for BPD [120]

Photochemical Parameter	Initial Value [a]	Fit Value [b]
ε (cm^{-1} μM^{-1})	0.0783	
δ (μM)	33 [53]	
β (μM)	11.9 [125]	
σ (μM^{-1})	$(0.5-10) \times 10^{-5}$	$(1.8 \pm 3) \times 10^{-5}$
ξ (cm^{2}mW^{-1}s^{-1})	$(10-100) \times 10^{-3}$	$(55 \pm 40) \times 10^{-3}$
g (μM s^{-1})	0.5-2.0	1.7 ± 0.7
$[^1O_2]_{rx,sh}$ (mM)	0.5-2.0	0.67 ± 0.13
$[^3O_2]_0$ (μM)	40 [c][48]	

[a] The initial guess of parameters were assigned randomly within the presented ranges

[b] The obtained values by the macroscopic model with their overall error. Each value is presented as the mean $\pm$ standard deviation

[c] The initial ground state oxygen concentration was kept constant for all mice using a value from Ref. [48]

The distribution of ϕ in tumor tissue was calculated using the diffusion equation and the linear light source characteristics. Measured optical properties in tumors were used as input parameters to see the effect of varying μ_a and μ'_s on the light fluence distribution. Figure 5.1 shows the drop of ϕ/LS along the tumor depth. With varying measured μ_a and μ'_s, the deviation of ϕ/LS inside tumors at depths up to 3 mm was within the deviation of the measured μ_a and μ'_s (indicated by the grey region). The mean measured optical properties were $\mu_a = 0.7 \pm 0.1$ cm^{-1} and $\mu'_s = 11 \pm 2.4$ cm^{-1}.
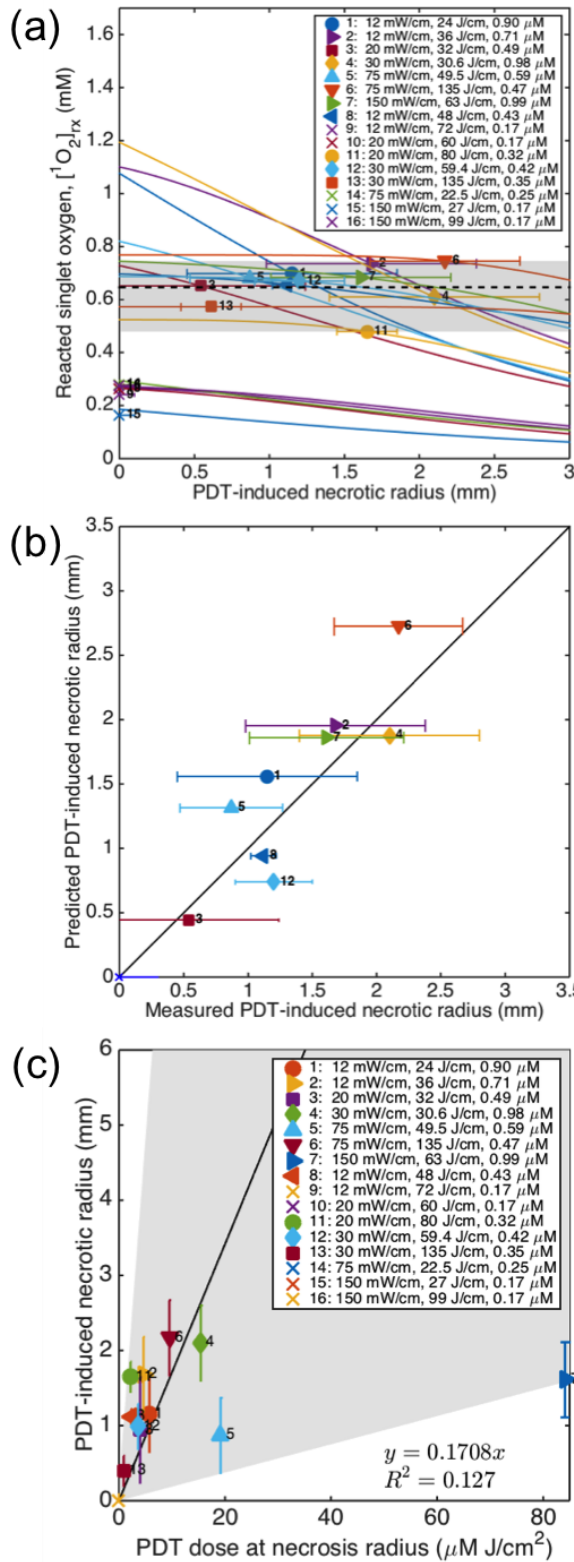
Figure 5.2: (a) $[^1O_2]_{rx}$ profile versus radius for mice calculated using the singlet oxygen explicit dosimetry model and the photochemical parameters in table 5.2. Data points 1-7 were obtained by averaging a group of 3 mice with the same treatment conditions while data points 8-16 were individual mice. The bold dashed black line indicates $[^1O_2]_{rx,sh}$ determined by this study (0.67 mM), and the grey region indicates the range. (b) The PDT-induced necrosis radius that is calculated by the model versus the measured PDT-induced necrosis radius. The dashed line indicates a perfect correspondence between calculated and measured data ($y = x$). The solid line is a linear fit to the data, $y = 1.085x$ with $R^2 = 0.8384$. (c) PDT-induced necrosis radius versus PDT dose calculated at the necrosis radius. The solid line shows a linear fit to the data using functional form $y = 0.1708x$ with $R^2 = 0.127$. The grey area shows the upper ad lower bounds of the fit with a 95% confidence interval
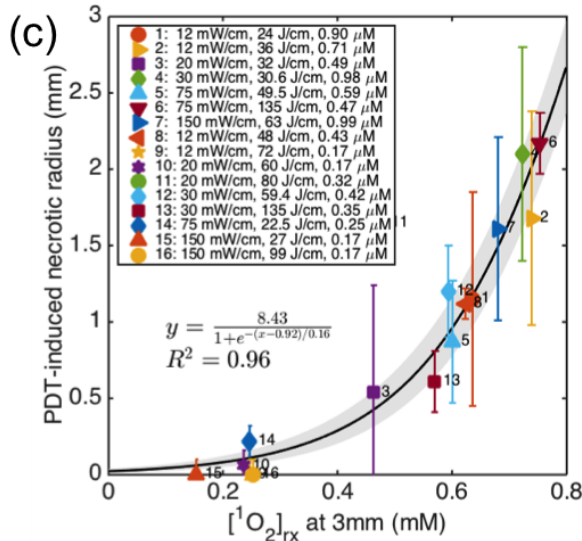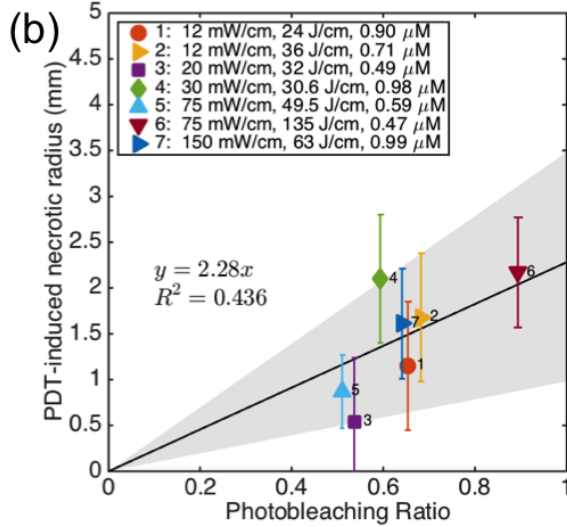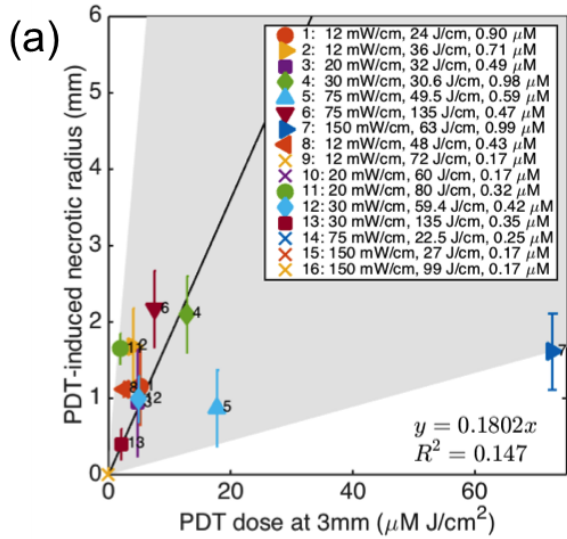
Figure 5.3: PDT-induced necrosis versus (a) PDT dose at 3 mm, (b) photobleaching ratio, and (c) $[^1O_2]_{rx}$ at 3 mm. PDT dose was calculated for those groups of mice where there was a PDT-effect due to treatment. Photobleaching ratio was calculated by $1 - [SVD]_{post}/[SVD]_{pre}$ for those groups of mice where pre- and post-PDT BPD fluorescence components were measured. $[^1O_2]_{rx}$ was calculated for all treated groups of mice. The solid lines show the best fits to the data using functional forms (a) $y = 0.1802x$ with $R^2 = 0.147$, (b) $y = 2.28x$ with $R^2 = 0.436$, and (c) $y = 8.43/(1 + \exp(-(x-0.92)/0.16))$ with $R^2 = 0.96$. The grey area shows the upper and lower bounds of the fits with a 95% confidence interval.

Table 5.3: BPD-mediated Necrosis Study Calculated Dosimetric Metrics

	Calculated Dosimetric Metrics					
Group	Fluence rate at 3 mm (mW/cm²)	Fluence rate at r_t (mW/cm²)	PDT dose at 3mm (µM J/cm²)	PDT dose at r_t (µM J/cm²)	$[O_2]_{rx}$ at 3mm (mM)	$[^1O_2]_{rx}$ at r_t (mM)
(a)	Experiment Group 1; each treatment group contains 3 mice					
1	11.5 ± 1.7	13.2 ± 1.4	5.2 ± 1.7	5.8 ± 0.9	0.6 ± 0.3	0.7 ± 0.3
2	13.5 ± 2.1	15.5 ± 1.7	4.0 ± 1.1	4.6 ± 1.1	0.7 ± 0.3	0.7 ± 0.2
3	21.7 ± 2.9	24.7 ± 2.5	4.8 ± 0.6	4.0 ± 0.1	0.5 ± 0.1	0.7 ± 0.2
4	26.2 ± 2.6	30.0 ± 1.9	12.9 ± 3.8	15.5 ± 3.5	0.7 ± 0.3	0.6 ± 0.2
5	71.3 ± 9.8	83.0 ± 9.4	17.8 ± 3.1	19.2 ± 3.6	0.6 ± 0.3	0.7 ± 0.3
6	91.9 ± 16.8	106.6 ± 13.4	7.5 ± 1.5	9.5 ± 1.9	0.8 ± 0.4	0.8 ± 0.4
7	143.7 ± 24.2	166.9 ± 15.9	72.7 ± 9.0	84.1 ± 7.8	0.7 ± 0.1	0.7 ± 0.1
(b)	Experiment Group 2 from 2013 [119]; individual ungrouped mice were used					
8	21.4	23.4	2.5	2.3	0.62	0.66
9	13.9	16.1	0.6	0.8	0.25	0.24
10	24.3	28.4	1.2	1.1	0.24	0.26
11	23.8	27.9	1.9	2.2	0.48	0.48
12	40.6	46.4	4.9	3.6	0.59	0.67
13	44.1	51.0	2.1	0.9	0.57	0.57
14	137.3	155.4	15.3	16.1	0.25	0.28
15	203.4	231.3	15.7	17.3	0.15	0.16
16	147.5	170.5	6.5	4.6	0.25	0.28

Figure 5.2 shows PDT-induced necrosis radius versus the $[^1O_2]_{rx}$ at the necrosis radius. The legend indicates each treatment condition. Figure 5.2 (b) shows the model predicted PDT-induced necrosis versus the measured PDT-induced necrosis. The good correlation is an indicator of the accuracy of the optimization fit. Table 5.2 summarizes the photochemical parameters obtained from the fitting routine as well as their initial values for the model. The best fit estimated values (along with their standard deviation) of $\sigma = (1.8 \pm 3) \times 10^{-5} \mu M^{-1}$, $\xi = (55 \pm 40) \times 10^{-3} cm^2 mW^{-1} s^{-1}$, $g = 1.7 \pm 0.7 \mu M s^{-1}$, and $[^1O_2]_{rx,sh} = 0.67 \pm 0.13 mM$. The values for β and δ were held constant at 33 μM and 11.9 μM, respectively. The grey region in Fig. 5.2 (a) shows the range for the singlet oxygen threshold concentration, $[^1O_2]_{rx,sh}$. The PDT dose was calculated at the necrosis radius and compared with the PDT-induced necrosis radius in Fig. 5.2 (c). The grey region indicates the upper and lower bounds of the fit with a 95% confidence interval. The best fit to the data was $y = 0.1708x$ with $R^2 = 0.127$, indicating that PDT dose at the necrosis radius is not well-correlated with the necrotic outcome.

Figure 5.3 (a) shows the PDT dose at 2 mm versus PDT-induced necrosis radius. The solid line represents the best fit to the data using a functional form of $y = 1802x$ with a goodness of fit of $R^2 = 0.147$. Figure 5.3 (b) shows the photobleaching ratio versus PDT-induced necrosis radius. Photobleaching ratio was calculated as $1 - ([SVD]_{post}/[SVD]_{pre})$, where $[SVD]_{pre}$ and $[SVD]_{post}$ are the measured BPD fluorescence components pre- and post-PDT. While there is a positive correlation with PDT-induced necrosis as indicated by the linear fit of $y = 2.28x$, it is not a good fit of the data since the goodness of fit $R^2 = 0.436$. Fig. 5.3 (c) shows the $[^1O_2]_{rx}$ at a depth of 3 mm versus PDT-induced necrosis. The solid line is the best fit to the data $y = 8.43/(1 + \exp(-(x - 0.92)/0.16))$ with a goodness of fit of $R^2 = 0.96$. The grey regions indicate the upper and lower bounds of the fit with a 95% confidence

interval.

5.3 Discussion

PDT promises to be an effective treatment modality for diseases. However, clinical application of PDT has been hindered due to the complicated dosimetry [44, 163]. BPD-mediated PDT has been shown to correlate well with calculated $^1O_2$ as shown in this study. A DLI of 3 hours was used for this study. By this time, the drug has systemically extravasated into the tumor interstitial and cellular components [164]. With a shorter DLI, vascular-targeted PDT can be achieved [121, 164].

Currently, the common approach in clinical PDT dosimetry is based on the photosensitizer concentration that is administered to the patient and the amount of light delivered to the treatment site. This method does not account for many of the complexities that arise with PDT. If the treatment site is hypoxic, or becomes hypoxic through the course of the treatment, the expected $^1O_2$ produced will be higher than what is produced and treatment will be less effective [163, 165]. As seen in the data from table 5.3, the photosensitizer uptake is very heterogeneous even though the administered dose is the same. The variation in photosensitizer concentration in the treatment tissue from site to site within the same individual (intra-tumor variation) and from individual to individual (inter-tumor variation) results in varied PDT treatment response [44, 163, 166]. Optical properties of the treatment tissue affect the penetration of light into the target area and are tissue-type dependent [18]. Furthermore, optical properties can be affected by the tissue and blood oxygenation, which is a key component in PDT [18, 22, 28]. All of these factors are dynamically changing during PDT, making accurate clinical dosimetry a challenge.

Singlet oxygen explicit dosimetry is of particular interest as it involves measure-

ment of the key components involved in PDT and modeling $^1O_2$, the major cytotoxic agent in type II PDT. Pre-clinical studies were performed using a murine model to determine the range of relevant photochemical parameters needed for BPD-mediated PDT explicit dosimetry. A range of source strengths and exposure times were performed on mice with RIF tumors to generate varying amounts of $^1O_2$ and induce necrosis. $[^1O_2]_{rx}$ were calculated using the macroscopic model using the information obtained from pre-PDT measurements regarding the tumor tissue optical properties (μ_a and μ'_s) and the photosensitizer concentration. The distribution of ϕ was also calculated using the diffusion approximation for a linear source. Photosensitizer concentration was measured with interstitial fluorescence spectra, and the method was validated by comparing the *in vivo* and *ex vivo* measurements on separate mice.

Measured optical properties were used to calculate ϕ distribution in the tumor tissue using the light source characteristics and the diffusion equation. The first 7 treatment groups included 3 mice per treatment condition. The deviation in ϕ at depths up to 3 mm varied 20% indicating that variations in optical properties account for less than 20% of the experimental error with consistent, long-term measurements with the same experimental set-up (Fig. 5.1 (b)). Some of the measurements in individual mice made in an earlier experiment with a different batch of mice (experiment group 2 in table 5.1 and 5.3 (b)) shows larger deviations of ϕ (up to 40%), which contain additional measurement uncertainties.

Figure 5.2 shows the most important results of this study. The threshold dose model only works to an extent if the threshold concentration for $[^1O_2]_{rx}$ is allowed a range as shown by the grey shaded area in Fig. 5.2 (a). Those that do not achieve the threshold singlet oxygen dose (indicated by the dashed black line and its uncertainty as indicated by the grey area) do not exhibit any PDT-induced necrosis (data points 9, 10, 14, 15, and 16). The other points that achieve the threshold dose delineate

the upper and lower bounds of uncertainty for $[^1O_2]_{rx,sh}$. By plotting the measured PDT-induced necrosis radius against the model-predicted values (the values from each $[^1O_2]_{rx}$ profile curve that intersect the $[^1O_2]_{rx,sh}$ dashed line) in Fig. 5.2 (b), the goodness of the macroscopic model in predicting the necrosis radius can be evaluated. A good correlation indicates a good fit. The dashed line indicates a perfect correlation and the fit to the data yields $y = 1.085x$ with $R^2 = 0.838$. The grey region indicates the 95% confidence interval of the fit. Figure 5.2 (d) shows that unlike $[^1O_2]_{rx}$, PDT dose at the necrosis depth is a very poor predictor for the necrosis radius, with $R^2 = 0.127$.

The calculated $[^1O_2]_{rx}$ was fit to the *in vivo* BPD-mediated necrosis radius so that the photochemical parameters g, ξ, and σ could be determined along with the $[^1O_2]_{rx,sh}$. The uncertainty for the resulting photochemical parameters (g, ξ, σ) was quite large based on the fitting algorithm and incorporating experimental uncertainties.

The parameters obtained for BPD ($\xi = 55 \times 10^{-3}$ cm^{2}mW^{-1}s^{-1}, $\sigma = 1.8 \times 10^{-5}\mu M^{-1}$, and $g = 1.7\mu M$ s^{-1}) were compared to those obtained for HPPH ($\xi = 70 \times 10^{-3}$ cm^{2}mW^{-1}s^{-1}, $\sigma = 1 \times 10^{-5}\mu M^{-1}$ [117], and $g = 1.5\mu M$ s^{-1}), Photofrin ($\xi = (2.1 - 3.7) \times 10^{-3}$ cm^{2}mW^{-1}s^{-1} and $\sigma = 7.6 \times 10^{-5}\mu M^{-1}$) [44], mTHPC ($\xi = 30 \times 10^{-3}$ cm^{2}mW^{-1}s^{-1} and $\sigma = 3.0 \times 10^{-5}\mu M^{-1}$) [124], and ALA-PpIX ($\xi = 3.7 \times 10^{-3}$ cm^{2}mW^{-1}s^{-1} and $\sigma = 9.0 \times 10^{-5}\mu M^{-1}$) [167]. The value of ξ for BPD was found to be larger than that of other photosensitizers except HPPH, which corresponds to the proportionality of ξ with the absorption coefficient and the larger absorption coefficient of BPD. The fit value of σ was found to be smaller than those of other photosensitizers, but in the same range as that of HPPH. The $[^1O_2]_{rx,sh}$ was found to be 0.67 ± 0.13 mM, which is similar to the reported value for that of Photofrin ($[^1O_2]_{rx,sh} = 0.7 \pm 0.3$ mM) [44]. The values are presented with

their standard deviations.

Figure 5.3 compares three dosimetric quantities PDT dose, photobleaching ratio, and $[^1O_2]_{rx}$ versus PDT-induced necrosis. The grey area shows the upper and lower bounds of the fits with the 95% confidence level. It is clear that $[^1O_2]$ is the best dosimetric indicator compared to PDT dose and photobleaching ratio, as defined by $1 - [SVD]_{post}/[SVD]_{pre}$, the $[SVD]_{pre}$ and $[SVD]_{post}$ were determined from the BPD fluorescence components before and after PDT. THe solid lines in the figure represent the best fit to the data. Their goodness of fit $R^2 = 0.96$, 0.436, and 0.147 for $[^1O_2]_{rx}$, photobleaching ratio, and PDT dose, respectively. The reason PDT dose is not a good indicator may be due to ignoring the oxygen consumption during PDT. The reason that photobleaching ratio is not a very good indicator may be associated to the fact that $[S_0]$ concentration *in vivo* (0.2 - 1 μM) is much lower than the value of $\delta = 33\mu M$ used for BPD. $[^1O_2]_{rx}$ was calculated using the macroscopic model and incorporating information regarding the spatial distribution of ϕ based on measured tissue optical properties and the photosensitizer concentration in tissue. For this study, the initial ground state oxygen concentration ($[^3O_2]_0$) was fixed to 40 μM. However, this could be further improved by performing direct $[^3O_2]$ measurements directly for each mouse.

For the practical application of SOED in clinical PDT, it is not generally necessary to determine the tissue optical properties in order to calculate $[^1O_2]_{rx}$. $[^1O_2]_{rx}$ can be calculated directly using the measured ϕ and photosensitizer concentration. The other unknowns for a specific photosensitizer are the photochemical parameters, which can be found in the literature for most commonly used photosensitizers [34].

5.4   Conclusion

An explicit dosimetry model for BPD-mediated PDT was investigated on mice bearing RIF tumors. Since direct measurement of $^1O_2$ concentration is difficult *in vivo*, SOED can be useful as a measure of PDT dosimetry The photochemical parameters needed for the macroscopic modeling of $^1O_2$ were found. The threshold dose of singlet oxygen to induce necrosis in the tumor was determined by correlating the calculated $[^1O_2]_{rx}$ and the tumor necrosis induced by PDT. Correlation of PDT-induced necrosis with photobleaching ratio, PDT dose, and $[^1O_2]_{rx}$ was compared. It showed that $[^1O_2]_{rx}$ serves as a better dosimetric quantity than photobleaching ratio or PDT dose in predicting the treatment outcome. This study is important in understanding the effect of $^1O_2$-based dosimetry for BPD-mediated PDT as well as determining the range of photochemical parameters required for SOED. A further study was necessary to investigate the correlation between SOED calculated $[^1O_2]_{rx}$ to a more meaningful PDT treatment efficacy, such as local tumor control rather than necrosis. This is described in the following chapter 6. However, this was the first study of its kind to find relevant *in vivo* photochemical parameters for BPD-mediated PDT.

Chapter 6

In vivo Outcome Study

Utilizing the macroscopic model, the effectiveness of reacted singlet oxygen concentration ($[^1O_2]_{rx}$) as a dosimetric quantity to predict outcome for BPD-mediated PDT. In addition, a few other dose metrics were evaluated in this study, including total light fluence, photobleaching ratio, and PDT dose, in their ability to predict PDT outcome. For each PDT treatment group, explicit measurements of BPD concentration in tumor and tissue optical properties were performed pre- and post-treatment. Mice bearing radiation-induced fibrosarcoma (RIF) tumors were treated with BPD-PDT and a range of in-air fluences (30 to 350 J/cm^2) and in-air fluence rates (50 to 150 mW/cm^2). For a subset of mice, real-time *in vivo* measurements of BPD concentration and tissue oxygenation level ($[^3O_2]$) throughout PDT were taken to optimize the photosensitizer-specific PDT photochemical parameters (ξ, σ, and g), reduce their uncertainty from the necrosis study described in chapter 5, and calculate $[^1O_2]_{rx}$. These photochemical parameters were used to calculate $[^1O_2]_{rx}$ for each PDT treatment group. Other dose metrics, such as photobleaching ratio and PDT dose, were determined either directly using explicit measurements pre- and post-PDT or calculated using the time dependence of BPD concentration based on the macroscopic model and

the definition of PDT dose. This study is the first, to our knowledge, to investigate the threshold value of $[^1O_2]_{rx}$ and the relationship between various dose metrics and cure index (CI) at 14 days in an *in vivo* mouse model for BPD-mediated PDT. The results of this study with additional real-time measurements of BPD concentration and $[^3O_2]$ provide reduced uncertainties for the photochemical parameters determined for BPD-mediated PDT, as well as a validation that our macroscopic model can accurately predict the oxygen consumption for BPD-mediated PDT, making it feasible to determine $[^1O_2]_{rx}$ without oxygen measurements.

6.1 Materials and Methods

6.1.1 Photodynamic therapy treatment

An optical fiber with a microlens attachment was coupled with a 690 nm diode laser with a maximum output power of 8 W (B&WTek Inc., Newark, Delaware, USA) to produce a collimated beam with a diameter of 1 cm on the surface of the tumor, as shown in Fig. 6.1 (a). The surface illumination of the tumor is non-invasive, compared to the interstitial treatment of chapter 5, which is necessary to monitor the tumor volume after treatment for 2 weeks. Mice were treated with in-air fluence rates (ϕ_{air}) of 50 to 150 mW/cm^2 and total in-air fluences from 30 to 350 J/cm^2 at 690 nm to induce different PDT outcomes and assess the reciprocity between BPD concentration and light fluence. The "in-air fluence rate" is defined as the calculated irradiance determined by laser power divided by the treatment area. The "in-air fluence" was calculated by multiplying the "in-air fluence rate" by the treatment time. All mice were injected with 1 mg/kg BPD via tail vein injection at 3 hours prior to light illumination. RIF tumor-bearing mice with (i) no BPD and no light excitation and mice with (ii) no BPD but the highest light fluence ($\phi_{air} = 150$ mW/cm^2 and

2333 second exposure) were used as controls ($n = 5$).
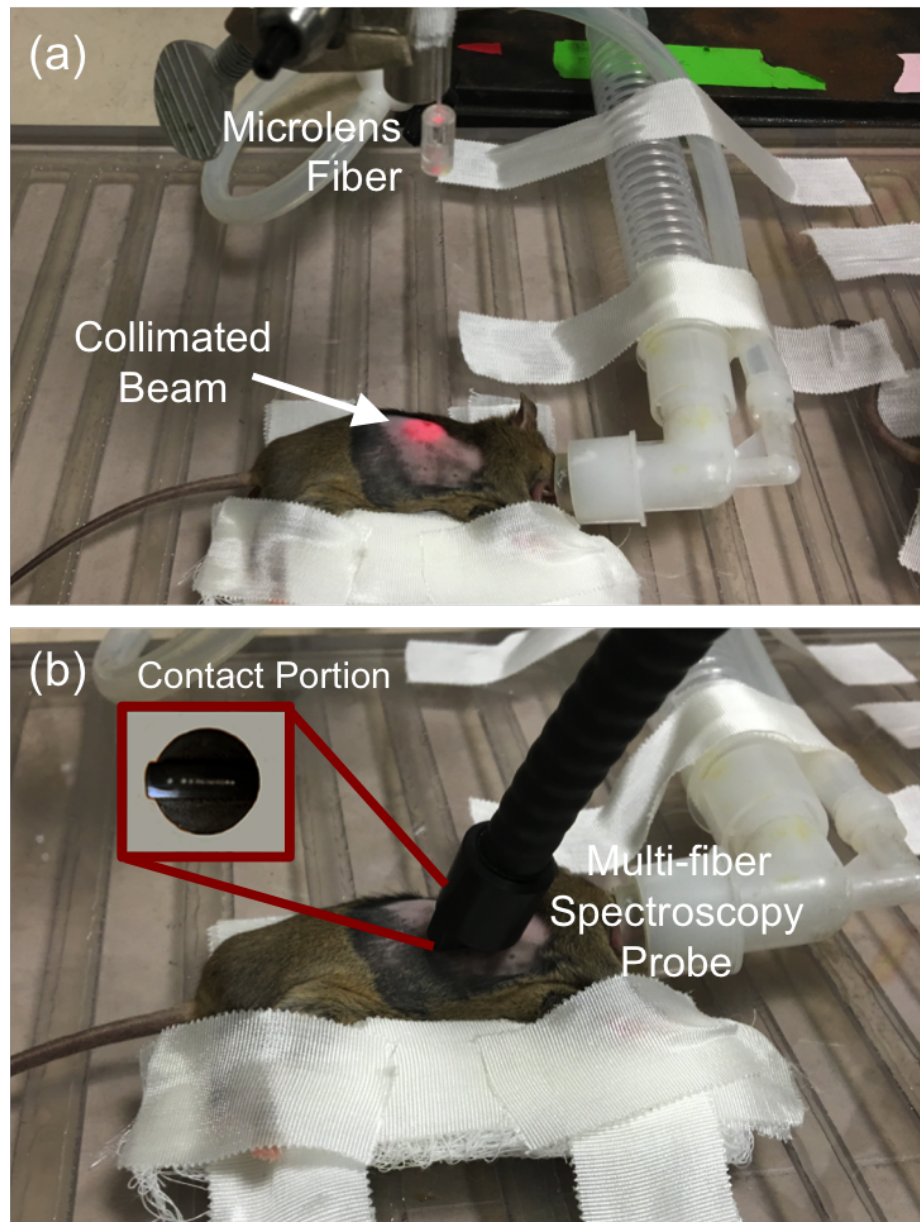
Figure 6.1: Experimental set-up with the (a) collimate beam treatment of RIF tumors on mouse shoulder and (b) the multi-fiber contact spectroscopy probe

6.1.2 Tissue oxygen concentration and photosensitizer concentration measurements

Real-time in vivo BPD concentration and tissue oxygen concentration over the course of treatment (80 mW/cm^2, 2000 s exposure time) was also determined for a subset of four mice using characteristic fluorescence spectra obtain at 30 to 300 s time intervals with excitation by the treatment light. SVD fitting was used to determine the BPD concentration. Measured data are shown in Fig. 6.2 (a) with symbols. The *in vivo* tissue oxygen partial pressure, pO_2 was measured during PDT treatment using a phosphorescence-based bare fiber-type $^3O_2$ probe (OxyLite Pro with NX-BF/O/E, Oxford Optronix, Oxford, United Kingdom). Measurements are presented for each 30 s interval during treatment. $^3O_2$ concentration ($[^3O_2]$) was calculated by multiplying the measured pO_2 with $^3O_2$ solubility in tissue, which is 1.295 μM/mmHg [48]. Measured $[^3O_2]$ was used to refine the photochemical parameters determined in chapter 5. for the singlet oxygen explicit dosimetry model used to calculate $[^1O_2]_{rx}$, and obtained values are summarized in table 7.1. Individually measured $[^3O_2](t)$ for each mouse were fit with the model-calculated values. Measured data are shown as symbols and calculated fits are shown with lines in Fig. 6.2 (b).
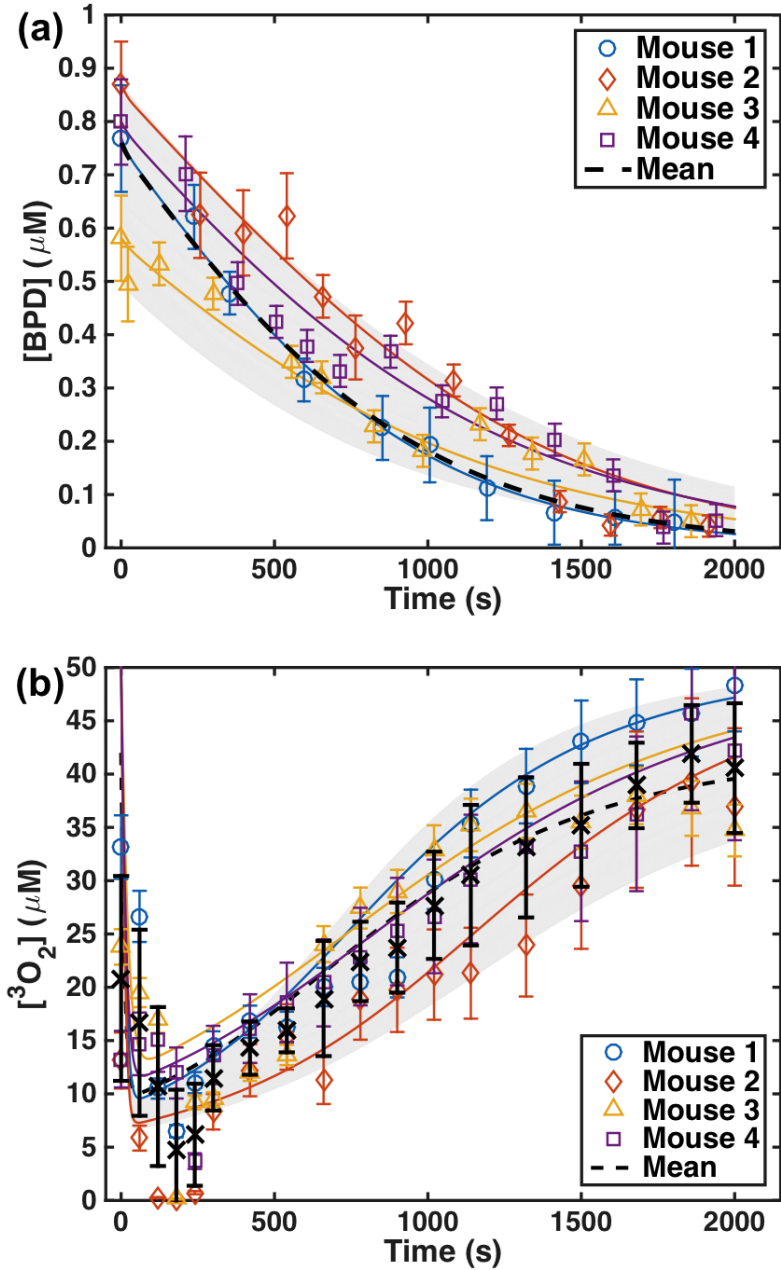
Figure 6.2: Real-time *in vivo* measurements of (a) BPD concentration ($[BPD]$) at the tumor surface and (b) $[^3O_2]$ concentration at a 3 mm depth measured for four mice over the course of PDT light delivery (80 mW/cm^2, 160 J/cm^2). The open symbols represent measured data and the solid curves represent the model-calculated $[BPD]$ and $[^3O_2]$ using eqs. (3.11) and (3.12) and the photochemical parameters listed in table 6.2. The black 'x' symbols and dashed black line represents the mean data and fit to data, respectively. The PDT parameters used to model the mean data are summarized in table 7.1

6.1.3 Tumor regrowth rate analysis

Tumor volumes were tracked daily after PDT. Width (a) and length (b) were measured with slide calipers, and tumor volumes (V) were calculated using $V = \pi \times a^2 \times b/6$ [168]. Tumor volumes were tracked for 15 days and the tumor regrowth factor (k) was calculated by an exponential fit to the data with the form $f(d) = e^{kd}$ to the measured volume over days (d). CI was calculated for each treatment group by

$$CI = 1 - \frac{k}{k_{ctr}} \tag{6.1}$$

where k is the tumor regrowth factor for each group and k_{ctr} is the regrowth factor for the control group, which has no injection of BPD or illumination of light.
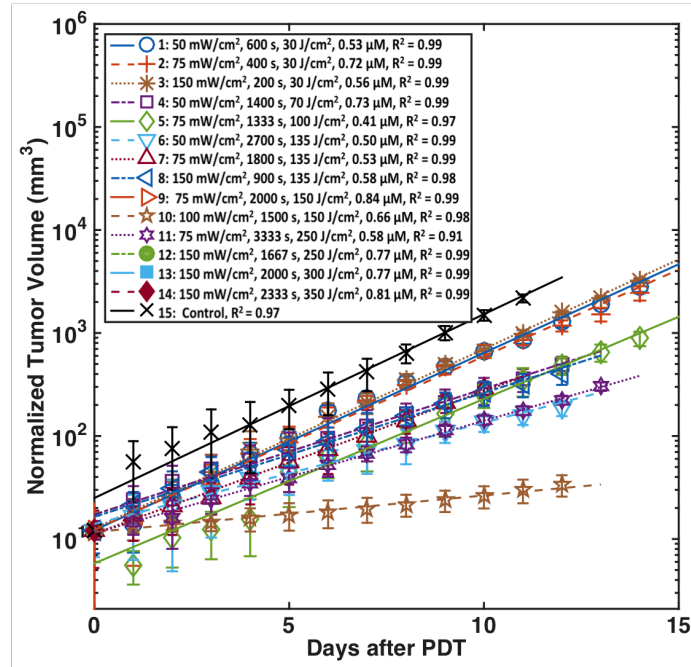
Figure 6.3: Tumor volumes over days after PDT treatment. Solid lines are the exponential fit to the data with a functional form of e^{kd}, where d is days after PDT treatment. The resulting tumor regrowth rates, k, and uncertainty, δk, are listed in table 6.3

6.1.4 Monte Carlo simulation of ϕ distribution in tumors

The diffusion theory is not valid for the simulation of ϕ in tissue when the lateral dimension of the beam geometry becomes comparable to the mean-free-path of the photons or when the region of interest is near the air-tissue interface [157,169]. Based on a previous study by Ong et al. [157], an empirical six-parameter fitting equation was used to fit the Monte Carlo (MC) calculated light fluence rate data for a 1 cm diameter field with $\mu_a = 0.52$ to 0.80 cm^{-1} and $\mu'_s = 7.9$ to 14.1 cm^{-1}. The equation is of the following form:

$$\phi/\phi_{air} = INV \times \left(1 - b \times e^{-\lambda_1 d}\right)\left(C_2 e^{-\lambda_2 d} + C_3 e^{-\lambda_3 d}\right), \qquad (6.2)$$

where the parameters λ_1, λ_2, λ_3, b, C_2, and C_3 are functions of μ_a and μ'_s and described elsewhere [157]. For $\mu_a = 0.5$ cm^{-1} and $\mu'_s = 10$ cm^{-1}, $\lambda_1 = 17.1$, $\lambda_2 = 4.88$, $\lambda_3 = 0$, $b = 0.3579$, $C_2 = 5.207$, and $C_3 = 0$. $INV = [SSD/(SSD + d)]^2$, where the source-to-surface distance SSD $= 9.34$ cm based on the measurement of light fluence rate in water for the same collimated beam as a function of depth and fit to the inverse-square law formula. The inverse-square law factor was added to the MC simulation results, which is suitable for parallel beams to account for the divergence of the collimated beam from the microlens. The mean tissue optical properties were found to be $\bar{\mu}_a = 0.69 \pm 0.12$ cm^{-1} and $\bar{\mu}'_s = 11 \pm 3$ cm^{-1} for RIF tumors at 690 nm, and the maximum error for using the mean optical properties is $\pm 15\%$, as seen in chapter 5.

6.2 Results

6.2.1 Parameter verification

BPD-mediated PDT with different in-air fluences, different ϕ_{air}, and different exposure times was performed in mouse models bearing RIF tumors. Tissue optical properties, photosensitizer concentration, and tissue oxygenation were measured to calculate photobleaching percentage, PDT dose, and $[^1O_2]_{rx}$. Table 6.3 summarizes all of the treatment conditions, as well as the measured and calculated quantities using the photochemical parameters summarized in table 7.1.

Table 6.1: Photochemical parameters for BPD based on those determined in chapter 5. The standard deviation for each parameter is reduced [126]

Photochemical Parameter	Definition	Value
ε (cm^{-1} μM^{-1})	Photosensitizer extinction coefficient	0.0783
δ (μM)	Low-concentration correction	33
β (μM)	Oxygen quenching threshold concentration	11.9
σ (μM^{-1})	Specific photobleaching ratio	$(1.8 \pm 0.3) \times 10^{-5}$
ξ (cm^{2}mW^{-1}s^{-1})	Specific oxygen consumption rate	$(55 \pm 15) \times 10^{-3}$
g (μM s^{-1})	Macroscopic maximum oxygen supply rate	1.7 ± 0.4
$[^1O_2]_{rx,sh}$ (mM)	Singlet oxygen threshold dose for tumor regrowth	0.99 ± 0.12
$[^3O_2]_0$ (μM)	Initial oxygen concentration	40

Four mice, summarized in table 6.2, were used to monitor the photosensitizer concentration and $[^3O_2]$ throughout the treatment using $\phi_{air} = 80$ mW/cm^2 and total fluence of 160 J/cm^2. The measured results (open symbols) were compared to calculated values (solid lines) in Fig. 6.2 to validate the photochemical parameters used in the calculation of $[^1O_2]_{rx}$. R^2 values are provided to evaluate their fits. The photochemical parameters found from individual fits of $[^3O_2](t)$ are summarized in

table 6.2. The mean data was fit using the photochemical parameters summarized in table 7.1.

Table 6.2: PDT parameters obtain for four mice treated with an in-air fluence of 160 J/cm^2 and in-air fluence rate of $\phi_{air} = 80$ mW/cm^2 using individual fitting to $[^3O_2](t)$ and $[S_0](t)$ simultaneously (Fig. 6.2). The other photochemical parameters ($\delta = 33\mu M$ and $\beta 11.9\mu M$)are kept the same as in table 7.1

Mouse	$[BPD]_0$ (μM)	ξ (cm^2 mW^{-1} s^{-1})	σ (μM^{-1})	g (μM s^{-1})	$[^1O_2]_{rx}$^a(mM)	$[^1O_2]_{rx}$^b(mM)
1	0.76 ± 0.10	$(60 \pm 8) \times 10^{-3}$	$(1.8 \pm 0.3) \times 10^{-3}$	1.6 ± 0.4	1.23 ± 0.24	1.21 ± 0.40
2	0.87 ± 0.19	$(60 \pm 10) \times 10^{-3}$	$(1.5 \pm 0.4) \times 10^{-3}$	1.5 ± 0.4	1.64 ± 0.31	1.37 ± 0.17
3	0.58 ± 0.16	$(50 \pm 10) \times 10^{-3}$	$(1.5 \pm 0.4) \times 10^{-3}$	1.3 ± 0.3	1.05 ± 0.33	0.93 ± 0.13
4	0.80 ± 0.19	$(50 \pm 7) \times 10^{-3}$	$(1.5 \pm 0.3) \times 10^{-3}$	1.7 ± 0.4	1.44 ± 0.28	1.26 ± 0.21

^a Calculated $[^1O_2]_{rx}$ using individually fit PDT photochemical parameters and $[^3O_2]_0 = 50\mu M$
^b Calculated $[^1O_2]_{rx}$ using the mean PDT photochemical parameters from table 7.1

6.2.2 Explicit dosimetry and treatment outcome evaluation

Measured tumor volume over 14 days after treatment for each treatment group is shown in Fig. 6.3. Compared to control mice, all treatment conditions had significant control of the tumor regrowth after PDT. CI was calculated for each treatment group using Eq. (6.1). PDT using 150 J/cm^2 with 75 mW/cm^2 was a more effective treatment than with 100 mW/cm^2. Each tumor volume was normalized to the mean initial volume, so that they are equal on day 0 (treatment date) before fitting for the tumor regrowth rate.

BPD concentration was measured both before and after PDT treatment. Measured $[BPD]$ was compared to model-calculated values for all the treatment conditions and is shown in Fig. 6.4 (a). The symbols represent the measured values, and the solid lines are model-calculated photosensitizer concentration during treatment. Figure 6.4 (b) shows the spatial distribution of reacted singlet oxygen in the RIF tumor model. The symbols indicate $[^1O_2]_{rx}$ at a 3 mm tumor depth for each treatment condition. The depth of 3 mm was chosen as it encompasses the initial tumor size of all treatment tumors. Previous publications also calculated $[^1O_2]_{rx}$ at 3 mm, and

results of this study can be compared to those directly.

Several dose metrics were evaluated for predicting the treatment outcome. Figure 6.5 shows the correlation of CI (tumor control) versus in-air fluence, photobleaching ratio (%), PDT dose at 3 mm depth, and $[^1O_2]_{rx}$ at 3 mm depth. The mean of k and k_{ctr} for all mice in each treatment group (number of mice per group is shown in table 6.3) was used to determine CI using Eq. (6.1). Photobleaching was determined by the ratio of BPD SVD_{corr} measured immediately following treatment ($[SVD_{corr}]_{post}$) to the BPD concentration measured prior to treatment ($[SVD_{corr}]_{pre}$) and calculating $1 - ([SVD_{corr}]_{post}/[SVD_{corr}]_{pre})$. PDT dose is defined by the time integral of the product of the ϕ at a 3 mm tumor depth and the local BPD concentration. Figures 6.5 (a)-(d) show the correlation of CI to fluence, photobleaching percentage, PDT dose, and mean $[^1O_2]_{rx}$ along with their line of best-fit. The lines of best-fit (shown with solid lines) are $CI = (3.309 \times 10^{-3})x$, $CI = (1.118 \times 10^{-3}e^{0.06731x}$, $CI = 1.052/(1 + 1014.4e^{-0.08172x})$, and $CI = 1.08/(1 + 3490e^{-8.301x})$ with $R^2 = 0.6260, 0.6274, 0.9360$, and 0.9850 for fluence, photobleaching percentage, PDT dose, and $[^1O_2]_{rx}$ at 3 mm, respectively [126].
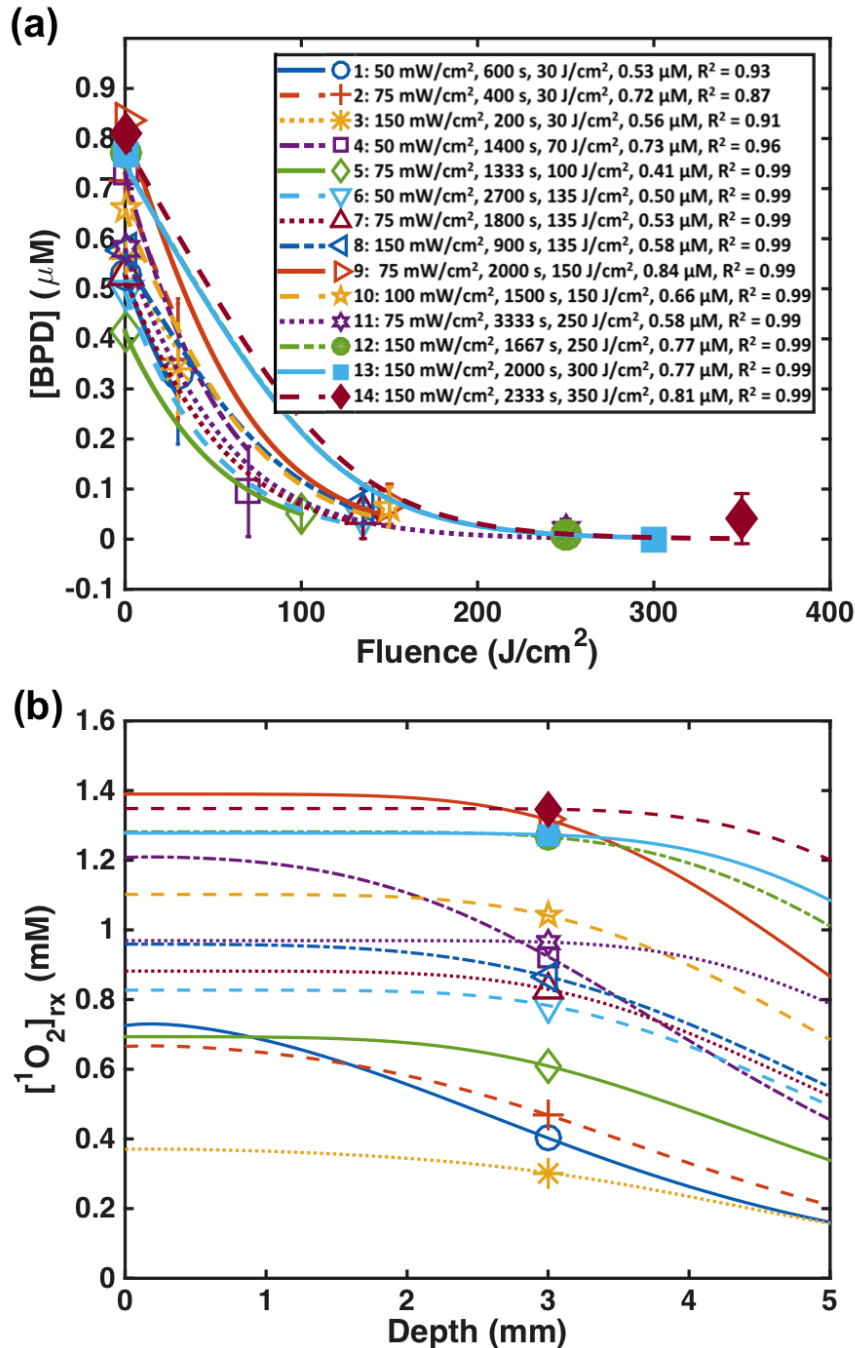
Figure 6.4: (a) The temporal changes of BPD concentration versus fluence at 3 mm depth for the treatment conditions. The lines represent the calculated changes of photosensitizer concentration during treatment. The symbols show the measured BPD concentration pre- and post-PDT. Initial drug concentrations for the calculation were matched to measured values. (b) The spatial distribution of reacted singlet oxygen ($[^1O_2]_{rx}$) in the RIF tumors calculated for different treatment conditions. $[^1O_2]_{rx}$ at 3 mm tumor depth is shown by the symbols. R^2 values for each calculation are shown in the legend.

Table 6.3: In-air light fluence, in-air light fluence rate, ϕ_{air}, photosensitizer concentrations pre- and post-PDT, $[BPD]_{pre}$ and $[BPD]_{post}$, PDT dose at 3 mm depth, reacted singlet oxygen concentration $[^1O_2]_{rx}$, at 3 mm depth, tumor regrowth rate, k, and CI for each PDT treatment group. Number of mice per group is shown in the second column. The same index for each PDT treatment group is used for figs. 6.3 and 6.5

Index	Number of mice	In-air fluence (J/cm²)	ϕ_{air} (mW/cm²)	Time (s)[a]	$[BPD]_{pre}$ (μM)	$[BPD]_{post}$ (μM)	PDT dose[b] (μM J/cm²)	$[^1O_2]_{rx}$[c] (μM)	k (1/days)	Cure index, $CI = 1 - k/k_{ctr}$
1	5	30	50	600	0.53 ± 0.24	0.33 ± 0.14	14.1 ± 6.0	0.39 ± 0.15	0.40 ± 0.03	0.0337 ± 0.02
2	5		75	400	0.72 ± 0.22	0.32 ± 0.12	19.2 ± 6.0	0.45 ± 0.05	0.38 ± 0.03	0.0556 ± 0.03
3	5		150	200	0.56 ± 0.29	0.27 ± 0.09	15.2 ± 7.9	0.29 ± 0.05	0.40 ± 0.03	0.0237 ± 0.02
4	3	70[d]	50	1400	0.73 ± 0.21	0.07 ± 0.09	39.6 ± 8.1	0.90 ± 0.21	0.28 ± 0.02	0.3151 ± 0.08
5	3	100[d]	75	1333	0.41 ± 0.09	0.05 ± 0.03	28.7 ± 5.9	0.60 ± 0.20	0.37 ± 0.05	0.1037 ± 0.05
6	3	135[d]	50	2700	0.50 ± 0.18	0.04 ± 0.02	41.0 ± 8.4	0.78 ± 0.18	0.34 ± 0.08	0.1646 ± 0.04
7	5		75	1800	0.53 ± 0.21	0.05 ± 0.02	44.2 ± 10.9	0.82 ± 0.28	0.32 ± 0.02	0.2139 ± 0.07
8	5		150	900	0.58 ± 0.12	0.07 ± 0.02	50.2 ± 18.8	0.85 ± 0.31	0.28 ± 0.08	0.0340 ± 0.10
9	2	150[d]	75	2000	0.84 ± 0.27	0.10 ± 0.02	75.4 ± 17.9	1.30 ± 0.42	0	1 ± 0.08
10	5		100	1500	0.66 ± 0.24	0.07 ± 0.72	59.9 ± 12.2	1.03 ± 0.37	0.11 ± 0.02	0.7432 ± 0.08
11	3	250[d]	75	3333	0.58 ± 0.19	0.02 ± 0.02	64.0 ± 14.7	0.96 ± 0.26	0.25 ± 0.01	0.3878 ± 0.07
12	5		150	1667	0.77 ± 0.20	0.01 ± 0.02	93.0 ± 17.8	1.26 ± 0.29	0	1
13	5	300	150	2000	0.77 ± 0.26	0	97.9 ± 28.2	1.27 ± 0.24	0	1
14	5	350	150	2333	0.81 ± 0.34	0.04 ± 0.05	108.3 ± 20.8	1.35 ± 0.30	0	1
15	5	Control	0	0	0	0	0	0	0.41 ± 0.05	1

[a] Total treatment time.
[b] PDT dose is defined as the time integral of the product of the photosensitizer concentration and the light fluence rate listed in table 7.1 calculated using the parameters listed in table 7.1
[c] $[^1O_2]_{rx}$ is calculated using the parameters listed in table 7.1
[d] Optical properties were measured for one mouse per group
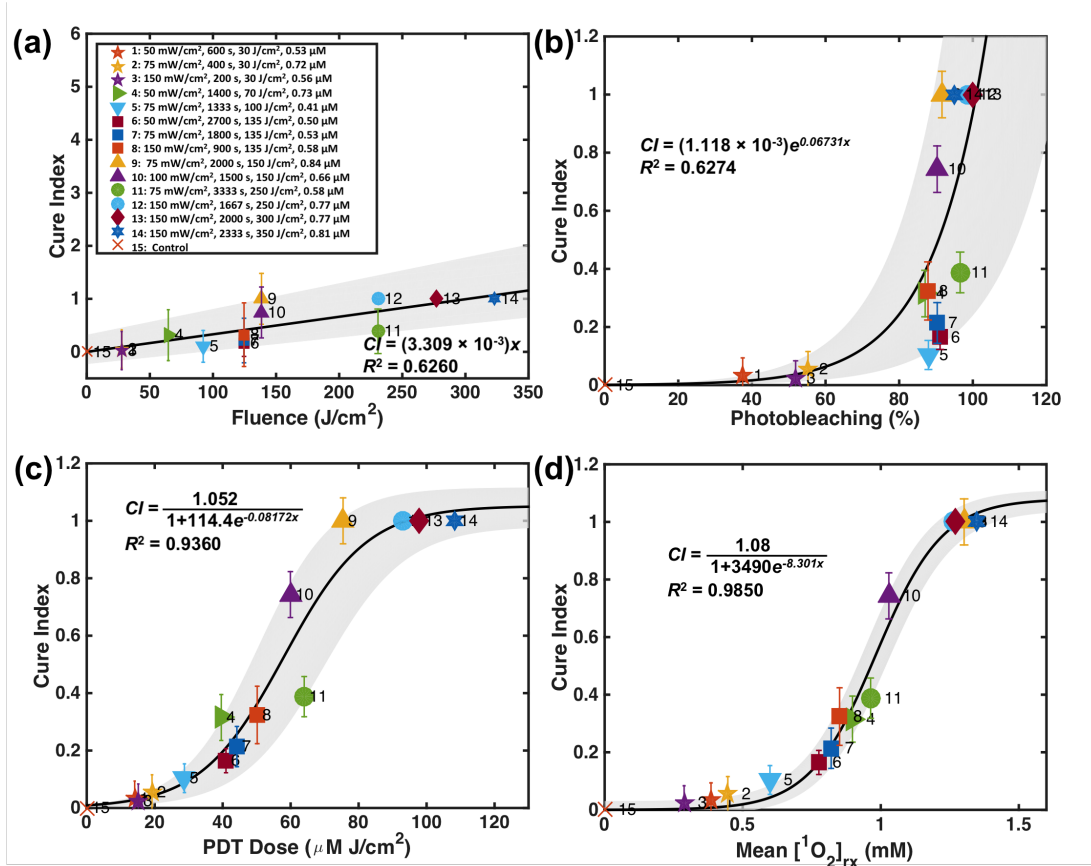
Figure 6.5: CI plotted against (a) fluence at a 3 mm tumor depth, (b) measured photosensitizer photobleaching (%), (c) calculated PDT dose at 3 mm depth, and (d) mean reacted singlet oxygen at 3 mm depth ($[^1O_2]_{rx}$) calculated using the parameters summarized in table 7.1. The solid lines show the best-fit to the data with functional forms $CI = (3.309 \times 10^{-3})x$, $CI = (1.118 \times 10^{-3}e^{0.06731x}$, $CI = 1.052/(1 + 1014.4e^{-0.08172x})$, and $CI = 1.08/(1 + 3490e^{-8.301x})$ with $R^2 = 0.6260$, 0.6274, 0.9360, and 0.9850 for (a), (b), (c), and (d), respectively. The grey region indicates the upper and lower bounds of the fit with 95% confidence level.

6.2.3 Long term local tumor control

Local tumor control for a more long-term treatment endpoint was investigated for a group of mice. Treatment was delivered with the same collimated beam and administration of BPD as before. Explicit dosimetry was used to calculate reacted singlet

oxygen ($[^1O_2]_{rx}$). The dose metrics of light fluence, photobleaching ratio, and PDT dose were compared to reacted singlet oxygen to evaluate their effectiveness in correlating with long term tumor control. Kaplan-Meier survival analyses were done for long-term local tumor control rate (LCR) for an endpoint of tumor volume ≤ 100 mm^3. Tumors were monitored for up to 90 days. The treated mice are summarized in table 6.4.

Table 6.4: Summary of treated mice for long term tumor control. Delivered fluence rate (ϕ_{air}), treatment time, initial BPD concentration ($[BPD]_0$), photobleaching ratio (Pb.), PDT dose, and calculated reacted singlet oxygen ($[^1O_2]_{rx}$) are summarized with the tumor response to the treatment at the end of the 90 day monitoring period.

Mouse No.	ϕ_{air} (mW/cm^2)	Time (s)	$[BPD]_0$ (μM)	Pb. (%)	PDT Dose (μM J/cm^2)	$[^1O_2]_{rx}$ (mM)	Survival (90 Days)
1	75	4000	0.43	65.7	54.8	0.72	Regrowth
2	75	4000	0.57	89.7	73.4	0.95	Regrowth
3	75	4000	0.64	82.5	80.4	1.07	Regrowth
4	75	4000	0.58	92.0	75.2	0.97	Regrowth
5	75	4000	0.54	89.9	69.8	0.91	Regrowth
6	75	4000	0.52	90.9	66.4	0.86	Regrowth
7	75	4000	0.42	60.3	53.7	0.70	Regrowth
8	75	4000	0.30	84.9	37.6	0.50	Regrowth
9	75	4000	0.47	88.1	59.8	0.78	Regrowth
10	75	4000	0.60	91.3	77.4	1.00	Regrowth
11	75	4000	0.49	88.4	62.6	0.82	Regrowth
12	75	4000	0.38	83.3	48.4	0.64	Regrowth
13	75	4000	0.31	93.4	39.7	0.52	Regrowth
14	75	4000	0.48	93.1	61.5	0.80	Regrowth
15	75	4000	0.56	89.8	72.2	0.94	Regrowth
16	75	4000	0.25	46.1	32.2	0.43	Regrowth
17	75	4000	0.25	78.3	31.0	0.41	Regrowth
18	75	4000	0.34	56.9	43.3	0.57	Regrowth
19	75	4000	0.31	78.4	39.0	0.51	Regrowth
20	75	4000	0.76	92.7	98.8	1.26	No Tumor
21	75	3600	0.73	92.6	89.0	1.21	No Tumor
22	75	5400	0.69	91.9	93.5	1.15	No Tumor
23	75	3600	0.75	91.8	92.1	1.24	No Tumor
24	75	3600	0.46	84.5	54.9	0.76	Regrowth
25	75	3600	0.44	82.6	52.6	0.73	Regrowth
26	75	3600	0.30	56.9	36.2	0.48	Regrowth
27	75	3600	0.69	91.7	84.5	1.15	No Tumor
28	75	3600	0.67	90.4	81.1	1.10	No Tumor
29	75	3600	0.72	90.8	87.9	1.19	No Tumor

| 30 | 75 | 3600 | 0.64 | 89.0 | 78.5 | 1.10 | No Tumor |

Comparing dose metrics, it is seen that singlet oxygen does the best of predicting
LCR. Furthermore, the $[^1O_2]_{rx}$ dose required to have LCR for 90 days with BPD-
mediated PDT is 1.1 mM [170]. Figure 6.6 shows the survival curves that compares
the dose metrics. A correlation of the delivered light fluence, BPD photobleaching
ratio, and PDT dose with LCR showed that less than 25% of the tumors exhibit a
complete response at 90 days to the treatment with a light fluence greater than 270
J/cm^2. Photobleaching ratio and PDT dose were also not sufficient in correlating
with tumors that responded with a complete response. However calculated $[^1O_2]_{rx} >$
1.1 mM was able to predict long term complete tumor control.
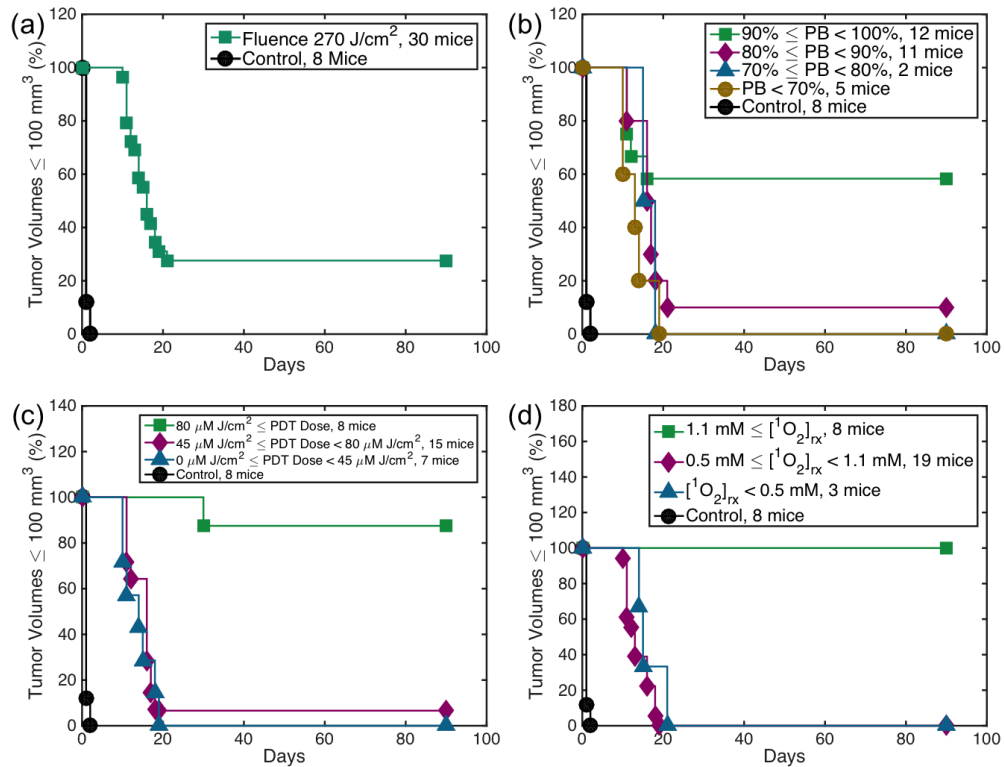
Figure 6.6: Survival curves based on (a) in-air delivered light fluence, (b)
BPD photobleaching ratio, (c) PDT dose, and (d) calculated $[^1O_2]_{rx}$. Tu-
mor volumes less than 100 mm^3 and control at 90 days were considered as
treatment end points.

6.3 Discussion

As shown in Fig. 6.2, the photochemical parameters σ, ξ, and g were validated by measuring $[BPD]$ changes and $[^3O_2]$ during the PDT treatment for individual mice and applying the parameters to the explicit dosimetry model. Based on a previous study, the parameters of σ, ξ, and g werefound to be $(1.8 \pm 0.3) \times 10^{-5}$ μM^{-1}, $(55 \pm 15) \times 10^{-3}$ cm^{2}mW^{-1}s^{-1}, and 1.7 ± 0.4 μM^{-1}, respectively. The standard deviation of each parameters is reduced based on the fitting of $[S_0]$ and $[^3O_2]$ as shown in Fig. 6.2, which is a more robust data set for deriving the photochemical parameters. Each individually measured $[^3O_2]$ in Fig. 6.2 was fitted to validate the photochemical parameters as shown in table 6.2. RMSE between measured and calculated values of $[^3O_2]$ was used as a measure of good fit.

To asses the effect of photochemical parameters, the values of calculated reacted singlet oxygen concentration using the individually obtained photochemical parameters for each mouse (from table 6.2) were compared to $[^1O_2]_{rx}$ calculated using the phtochemical parameters from the necrosis-based study in chapter 5 and table 7.1. For the same mouse, $[^1O_2]_{rx}$ calculated using the two sets of photochemical parameters agree with each other within a maximum uncertainty of 20% and a standard deviation of 8%. The good agreement between measurement and caluclation of photosensitizer concentration and oxygen concentration provided a validation of the photochemical parameters determined previously and allowed for reduction in the uncertainty of each parameter. For BPD, the comparisons between the measured and calculated $[^3O_2]$ for a subset of four mice show that the macroscopic model can accurately predict $[^3O_2]$ for the mice studied with R^2 values ranging from 0.70 to 0.90. The agreement between measured and calculated $[^3O_2]$ makes it unnecessary to measure the oxygen concentration directly during PDT. One complication of the comparison between

measurement and calculation for *in vivo* oxygen concentration is the uncertainty of the depth at which oxygen concentration was measured, which lies at around 3 mm. To illustrate this effect, spatial and temporal variations of $[^3O_2]$ are shown for various ϕ_{air} (20, 50, 75, and 150 mW/cm^2) in Fig. 6.7. The temporal changes of $[^3O_2]$ at 1, 3, and 5 mm with $[BPD] = 0.57$ μM (the mean value of BPD concentration for all mice studied) are shown in Fig. 6.7 (a)-(c). Figure 6.7 (d)-(f) show the temporal changed of $[^3O_2]$ at 1, 3, and 5 mm with $[BPD] = 0.87$ μM. Initial $[^3O_2]$ of 40 μM and the photochemical parameters in table 7.1 were used for the calculations. As the depth increases from 1 to 5 mm, the minimum value of $[^3O_2]$ increases, while the rate of $[^3O_2]$ recovery due to photobleaching (for 50 to 2000 s) deceases. Higher initial $[BPD]$ will cause a larger drop of $[^3O_2]$, depending on the light fluence rate. Lower light fluence rates will have less $[^3O_2]$ consumption during PDT. The optimized depth for the best agreement between model and measurement is found to be 3 mm, corresponding to the placement of the oxygen probe during PDT.
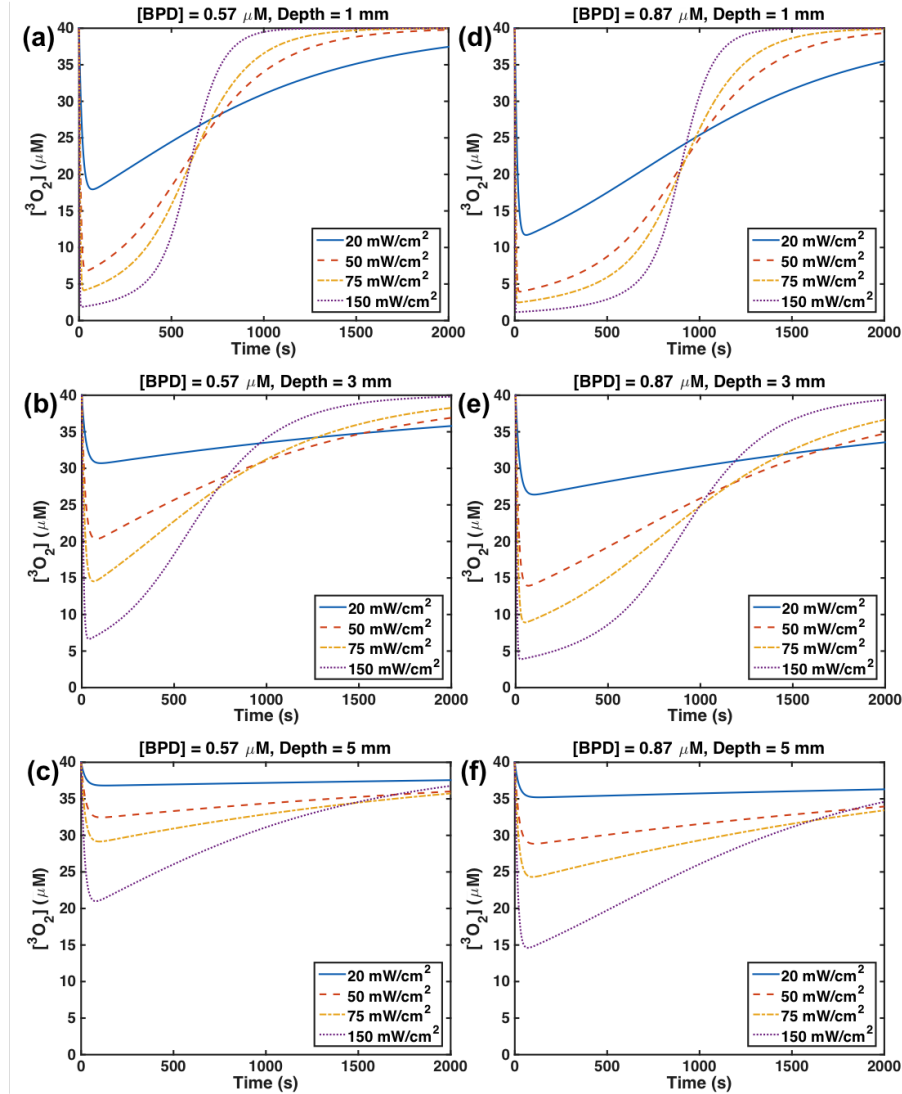
Figure 6.7: Temporal dependence of $[^3O_2](t)$ calculated for various ϕ_{air} (20, 50, 75, and 150 mW/cm^2) at depths of 1, 3, and 5 mm in the tumor for two initial BPD concentrations, (a)-(c) $[BPD] = 0.57$ μM and (d)-(f) $[BPD] = 0.87$ μM. Photochemical parameters in table 7.1 are used for $[^3O_2]$ are used for the calculations.

Compared to control mice, all treated mice with total fluence larger than 30 J/cm^2 had significant control of the tumor regrowth after PDT (see Fig. 6.3). However, mice with tumors of about the same size, administered with the same BPD dose, and treated with identical fluence exhibited different survival and tumor control as ϕ_{air} was changed. In the group of mice treated to 150 J/cm^2, CI increased as the

source strength was lowered from 100 to 75 mW/cm^2. This is in agreement with prior reports of increased therapeutic response with a reduced ϕ_{air} by expanding the radius of $^1O_2$ formation around a tumor capillary in a multicell tumor spheroid model [23].

Figure 6.4 (a) compares the measured pre- and post-PDT BPD concentration versus calculated $[BPD]$ during treatment for each treatment condition using the photochemical parameters summarized in table 7.1. The good agreement (for mean $[S_0]$, $R^2 = 0.88$) between measured $[BPD]$ pre- and post-PDT further validates the photochemical parameters used for the modeling. Figure 6.4 (b) shows the spatial distribution of $[^1O_2]_{rx}$ for each treatment condition. The value of $[^1O_2]_{rx}$ at 3 mm is shown with symbols. While the comparison of CI versus $[^1O_2]_{rx}$ was done using these values at 3 mm, the value of $[^1O_2]_{rx}$ is almost a constant for depths between 1 and 4 mm for most of the PDT treatment groups, indicating that the correlation between $[^1O_2]_{rx}$ and CI in Fig. 6.5 (d) should be equally valid for any depth between 1 and 4 mm.

Fluence, photosensitizer photobleaching ratio, PDT dose, and $[^1O_2]_{rx}$ at 3 mm were compared as dosimetric quantities to estimate the outcome of BPD-mediated PDT for RIF tumors on a mouse model. The outcome was evaluated by the calculation of CI. No tumor regrowth up to 15 days after the treatment resulted in a CI of 1. The goodness of fit and the corresponding upper and lower bounds of the fits (grey area) to each of the dosimetric quantities are shown in Fig. 6.5. As seen in Fig. 6.5 (a), while fluence correlates linearly with the PDT outcome, it exhibits large uncertainties as defined by the large bounds of the grey area, as well as by the low value of $R^2 = 0.67$. As evident by the lower value of $R^2 = 0.63$ and a relatively large bound of grey area in Fig. 6.5 (b), the BPD photobleaching ratio is not a better dosimetric quantity for predicting the PDT outcome as compared to fluence. The BPD concentration ($\sim$0.2 to 0.8 μM) as used clinically is much lower than the value of δ

(=33 μM), and this may be a reason for the poor correlation of the photobleaching ratio and CI. In photobleaching-based implicit dosimetry, a much more sophisticated model than simple bleaching fraction is used, and the result of this study does not mean that other methodologies of photobleaching-based implicit dosimetry will not be applicable for PDT dosimetry. As shown in Fig. 6.5 (c), PDT dose allows for reduced subject variation and improved predictive efficacy as compared to fluence and photobleaching. PDT dose showed a better correlation with CI with a higher value of $R^2 = 0.97$ and a narrower band of grey area as it accounts for both light fluence and tissue $[BPD]$ levels. However, PDT dose over-estimates $[^1O_2]_{rx}$ in the presence of hypoxia as it does not account for the oxygen dependence of $^1O_2$ quantum yield. The goodness of fit $R^2 = 0.99$ and the narrowest grey area in Fig. 6.5 (d) shows that the mean $[^1O_2]_{rx}$ correlates best with CI. $[^1O_2]_{rx}$ accounts for the key quantities of light fluence, photosensitizer concentration, and tissue oxygen level.

Based on the findings of this study, PDT dose and $[^1O_2]_{rx}$ exhibit threshold dose behavior as they can be fit by a sigmoid function of the form $S(x) = 1/[1+e^{-(x-x_0)/w_0}]$, where $x_0 = 58$ μM J/cm^2 with uncertainty $w_0 = 12$ μM J/cm^2 and $x_0 = 0.98$ mM with uncertainty $w_0 = 0.12$ mM for PDT dose and $[^1O_2]_{rx}$, respectively. For PDT dose, x_0 can be converted to the absorbed dose by BPD by multiplying by the extinction coefficient ($\varepsilon = 0.0783 \mu$M^{-1}cm^{-1}), resulting in 4.5 J/cm^3, which corresponds to $(16 \pm 4) \times 10^{18}$ photons/cm^3 (by dividing by the energy per photon $hc/\lambda = 2.88 \times 10^{-19}$ J for $\lambda = 690$ nm). The PDT dose threshold for BPD is in agreement with those reported for 2-(1-hexyloxyethyl)-2-devinyl pyropheophorbide-a (HPPH) (19×10^{18} photons/cm^3) [171]. The mean $[^1O_2]_{rx}$ threshold concentration of $x_0 = 0.98 \pm 0.12$ mM is similar to that which is published for HPPH (1.00 mM) [171]. The definition of the threshold dose for both PDT dose and $[^1O_2]_{rx}$ is the value for when $CI = 0.5$ [126].

6.4 Conclusion

The response of mouse RIF tumors to PDT depends on the tissue oxygenation, photosensitizer uptake, total energy delivered, and the ϕ at which the treatment is delivered. An accurate dosimetry quantity for the evaluation of the treatment outcome should account for all of these parameters. This study evaluated the efficacy and outcomes of different PDT treatments and how fluence, BPD photobleaching, PDT dose, and $[^1O_2]_{rx}$ compare as dosimetric quantities. The correlation between CI and $[^1O_2]_{rx}$ suggests that $[^1O_2]_{rx}$ at 3 mm is the best quantity to redict the treatment outcome for a clinically relevant tumor regrowth endpoint. PDT dose is the second most effective dosimetry quantity when compared to fluence or photosensitizer photobleaching, but is worse than $[^1O_2]_{rx}$ as it does not account for the consumption of $[^3O_2]$ for different ϕ. For BPD in RIF tumors, the measurements show consistent temoral dependence of *in vivo* oxygen concentration during PDT that can be well modeled by the macroscopic model, implying that it is not necessary to make $[^3O_2]$ measurements during PDT to obtain $[^1O_2]_{rx}$ as well as by using model-calculated values. This study validated the model and photochemical parameters for BPD-mediated PDT for an endpoint that is clinically relevant.

Chapter 7

IR Navigation System

Pleural photodynamic therapy (PDT) is performed intraoperatively for the treatment of microscopic disease in patients with malignant pleural mesothelioma. Accurate delivery of light fluence is critical to PDT efficiency. As a standard of care, light fluence is delivered to the prescribed fluence using 8 isotropic detectors in pre-determined discrete locations inside the pleural cavity that is filled with a dilute Intralipid solution. An optical infrared (IR) navigation system was used during light delivery to monitor the position of the light source within the treatment cavity. The light source is tracked using a modified and improved treatment delivery wand with reflective passive markers that are seen by the infrared camera-based navigation system. This information was used to calculate the light fluence, incorporating a constant scattered light fluence and using a dual correction method. Calculation methods were extensively compared for 8 detector locations and 6 patient case studies. The light fluence uniformity was also quantified by representing the unraveled three-dimensional geometry on a two-dimensional plane. Calculated light fluence at the end of treatment delivery was compared to measured values from isotropic detectors. Using a constant scattered dose for all detector locations along with a dual correction method, the

agreement between calculated and measured values for each detector was less than 15%. Primary light fluence alone does not fully account for the light delivered inside the cavity. This is useful in determining the light fluence delivered to areas of the pleural cavity between detector locations, and can prove to improve treatment delivery with implementation in real-time in the surgical setting.

7.1 Pleural Photodynamic Therapy

PDT typically uses light in the near infrared region, which will penetrate only several millimeters into tissue. For that reason, PDT is utilized for the treatment of regions that are easily accessible, such as the skin or oral cavities. In the treatment of pleural malignant mesothelioma, treatment involves radical pleurectomy. This surgical opening of the pleural cavity allows for intraoperative delivery of the treatment light. Radical pleurectomy and surgical debulking of the macroscopic tumor leaves behind microscopic tumor cells that can develop into larger tumors. PDT is used to treat the microscopic disease after the debulking. It has been seen that with the addition of PDT, patients see prolonged survival despite recurrence [13].

As a part of a Phase II/III clinical trial at the Hospital of the University of Pennsylvania, patients were enrolled in a randomized trial to under surgical resection or surgical resection with interoperative PDT. Photofrin was used as the photosensitizing agent and was intravenously administered to the patient 24 hours prior to surgery at a concentration of 2 mg per kg of body weight. 630 nm wavelength laser light was delivered by a Laser Scope dye and KTP-YAG laser system (630 XP, Laserscope, Inc., San Jose, CA, USA). PDT was delivered to a prescribed 60 J/cm2, which was measured by 8 isotropic detectors (Medlight SA, Ecublens, Switzerland) placed in pre-determined locations within the pleural cavity: apex, posterior chest wall (PCW),

anterior chest wall (ACW), posterior sulcus (PS), anterior sulcus (AS), posterior mediastinum (PM), pericardium (Peri), diaphragm (Diaph). The current standard of treatment involves treatment to the prescribed light fluence at each of the isotropic detectors.

7.2   Optical Infrared (IR) Navigation System

A commercial IR navigation system (Polaris, NDI, Waterloo, Canada) was used for tracking the light delivery during pleural PDT [172–175]. The camera consists of a pair of cameras that measure the light reflection from a modulated laser source (with a wavelength of 850 nm). The stero-cameras typically track 3-4 passive reflective markers with known geometry in real-time at a rate of 20-60 Hz). The reflective markers track the position of a point at the end of a rigid wand. The wand used to track treatment, however, was modified to have 3 faces with 3 passive markers so that position data could be collected at more angles around the wand. The position of the point is given by the 3D Cartesian coordinates (x, y, and z) and the orientation (Q0, Q1, Q2, Q3). With the IR navigation system, position of the light source being used to deliver laser light inside the pleural cavity is continuously tracked, and raw position data is used to determine the cavity contour. The accuracy of the system is ∼0.5 mm in 3D, and the maximum detection volume for the extended system ∼205 × 186 × 147 cm^3, which is optical for use during treatment of the pleural cavity for the patient population studied. The IR camera is positioned above the patient from the ceiling prior to treatment.

7.2.1 Modified treatment delivery wand

During pleural PDT, light is delivered through a bare fiber connected to the laser source that is enclosed in a modified endotracheal (ET) tube (Fig. 7.1). Previous versions of the treatment light delivery system included a rigid metal rod that clipped onto the ET tube. The passive reflective markers were calibrated so that the position information obtained by the camera was that of the tip of the metal rod. There would be a shift between the location that the camera tracks and the location of the fiber tip inside the balloon. The shift would have to be determined and applied throughout the set of data obtained. An updated treatment delivery wand was created so that the passive reflective spheres would track the location of the fiber tip directly with an expected shift in x, y, and z of 0 mm each. Prior to sterilization, the wand was calibrated so that the markers tracked the position of the fiber tip. The calibrated wand was equipped with an ET tube to be filled with Intralipid to facilitate light scattering. The calibration consistency was evaluated by determining the shift between the calibrated point to the fiber point after treatment and is summarized in table 7.1.
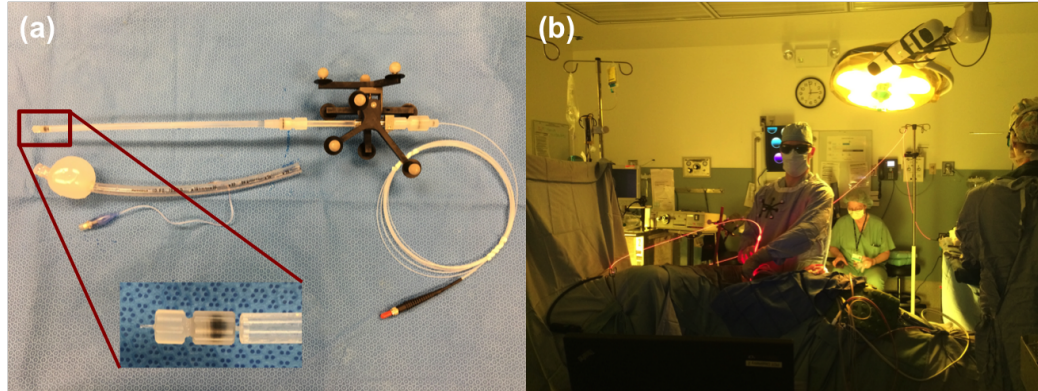
Figure 7.1: (a) Modified treatment delivery wand. Magnification shows the tip of the treatment wand, which is the tip of the bare fiber used to deliver laser light. The wand is calibrated so that the passive markers (9) are tracking the tip of the light source, eliminating the need for a separate calibration calculation to determine the light source position. (b) Image of the IR camera in use during pleural PDT. The camera is positioned above the patient body.

Table 7.1: Light source point shift from calibration point

Case No.	Shift x (mm)	Shift y (mm)	Shift z (mm)	Average
008	0.88±0.72	0.98±0.12	-0.52±0.42	0.45±0.84
012	1.27±0.11	-0.17±0.04	-0.46±0.26	0.21±0.93
014	0.70±0.42	0.80±0.78	-0.62±0.45	0.29±0.79
016	-0.28±0.13	-0.92±0.19	-0.53±0.35	-0.58±0.32
017	1.20±0.43	0.51±0.24	-0.75±0.23	0.32±0.99
018	1.64±0.17	0.46±0.27	-0.48±0.35	0.54±1.06
020	-0.68±0.19	0.44±0.20	-0.89±0.24	-0.37±0.72
Average	0.68±0.85	0.30±0.65	-0.61±0.16	

Prior to the development of the modified treatment delivery wand, there was a fixed shift between the calibrated tip of the metal rod that was attached to the reflective spheres and the tip of the fiber optic laser source inside the inflated balloon of the ET tube. The shift in x, y, and z needed to be determined for each assembly of the wand. The unassembled wand required sterilization prior to use in the operating room. The shift was determined by using a device that held one isotropic detector.

The location of that isotropic detector was determined using a different tracking wand. The treatment delivery wand was then used to determine the fluence at 8 different positions. Using the information of light fluence, distance, and calculated values of fluence (using Eq. (7.1)), the shift between the actual light source position and the treatment wand tip was determined. In the surgical setting, this would be time consuming and occasionally, the ET tube would have to be replaced mid-surgery. In this instance, the shift may not be determined, or would have to be determined in the laboratory setting after surgery is complete.

An updated light source positioning tool was developed, which used 8 detectors in fixed locations inside an acrylic ring device (Fig. 7.2). Detectors were placed both near and far from the central opening on two layers. The location of the ring was determined with a separate wand, and the treatment wand would be placed inside the ring for one measurement (compared to 8). While this was an improvement to the first generation light source locator, the new modified treatment wand with calibration directly to the light source fiber eliminates the need for an extra measurement prior to surgery and reduces uncertainty in shift determination.
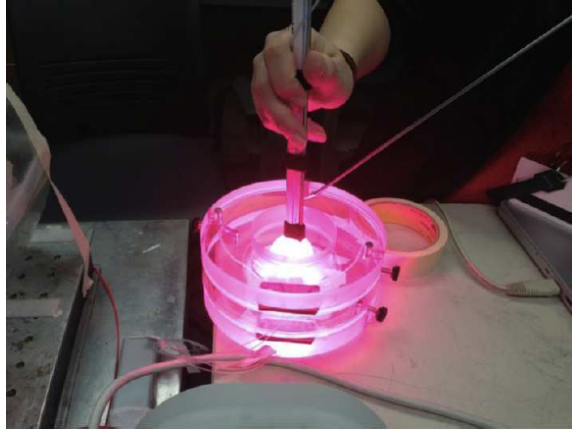
Figure 7.2: Light source position relative to the calibrated metal tracking wand tip was determined using a tool with 8 isotropic detectors. Light fluence at 8 known positions was optimized to find the shift in x, y, and z.

With the acrylic ring device, it was critical to determine the location of the 8 isotropic detectors inside the ring relative to the reference to the ring body. Each isotropic detector needed to be calibrated prior to use and connected to the dosimetry system in the operating room setting. The modified wand saved much-valuable time in the operating room and requires less pre-surgery set-up. Furthermore, the wand was lighter and less cumbersome without the metal rod, creating a better treatment delivery experience for the physician delivering the light while maintaining the rigid geometry required for accurate positioning.

7.2.2 Pleural cavity geometry reconstruction

The pleural geometry was determined using position data obtained inside the pleural cavity. A more detained description of the algorithm to reconstruct the cavity contour can be found elsewhere [172]. Briefly, the Cartesian coordinates of the contour were converted to spherical coordinates. For each defined grid, the boundary was found by

selecting data points from the largest radial distance. These points were interpolated to find surface information. At the time of surgery, a standard coordinate was determined by recording a position with a wand parallel to the patient and the reflective sphere end of the wand towards the head of the patient. The obtained pleural cavity contour was oriented to have the apex location at the top aligned with the z-axis. Figure 7.3 shows the geometry reconstructed from treatment data with the locations of the 8 isotropic detectors. Using the standard coordinate, all treated geometries can be oriented the same way for intercomparison.
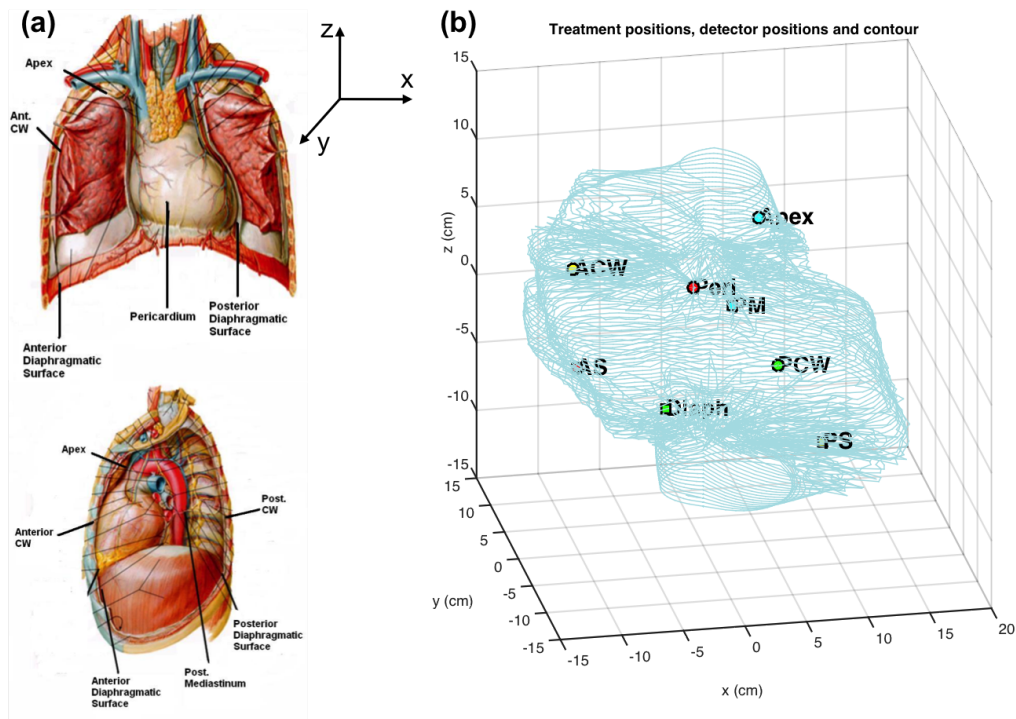
Figure 7.3: (a) Schematic of detector locations (8) used for each pleural PDT patient. (b) Detector positions inside a patient cavity contour determined from raw data.

7.2.3 Light fluence calculations

Using the position data obtained throughout the treatment using the optical IR navigation tracking system, the position of the light source is known as well as the surface of the pleural cavity geometry that is being treated. The light fluence to each point on the cavity is a sum of the primary (direct) component and the scattered component of the light [172]. The primary component of the light fluence rate ($\phi_{primary}$) can be calculated by

$$\phi_{primary} = \frac{S}{4\pi r^2} \tag{7.1}$$

where S is the source power and r is the distance from the point light source to the point of interest on the pleural cavity surface. To improve agreement between the measured light fluence from the isotropic detectors and the calculated values, a constant scattered light contribution was considered in the calculation. During treatment, the pleural cavity is filled with a dilute solution of Intralipid (0.1% lipid content) to facilitate scattering. To account for the general scattering in the pleural cavity, the light fluence rate ($\phi_{scatter}$) can be calculated by

$$\phi_{scatter} = \frac{S}{4\pi r^2} + b \tag{7.2}$$

where b is the constant scattered light fluence rate that is added for every calculation point. Total light fluence is calculated as the time integral of the light fluence rate (ϕ), which is a function of r and time, t. The agreement between measured and calculated light fluence, a dual correction method was applied to the light fluence rate. The method involves a time-dependent multiplication correction factor ($CF(t)$) that is applied to the entire calculated light fluence rate. A value of CF is applied to match the measured light fluence rate every 30 seconds, and another CF is applied

every 150 seconds to match the total cumulative light fluence at the detector location with the largest sum fluence over the past 30 seconds. A correction is applied only if the difference is more than 5%. This second correction ensures that the total fluence is in agreement. The time intervals for the correction factor was chosen from trial and error. With the addition of the scattered light fluence, the light fluence rate can be calculated by

$$\phi(r,t) = \left(\frac{S}{4\pi r(t)^2} + b \right) \cdot CF(t) \tag{7.3}$$

The value of CF is determined for one of the eight detectors that has the largest sum fluence at the time interval of interest and is applied to the entire volume, as well as the locations of the other detectors.

For an integrating-sphere-like cavity, such as the pleural cavity, the scattered light fluence rate inside the sphere can be calculated according to [138]

$$b = \frac{4S}{A_s} \cdot \frac{R_d}{1 - R_d} \tag{7.4}$$

where A_s is the surface area of the cavity, and R_d is the diffuse reflectance of the scattering wall surface. This is assuming that the area is a sphere and the infinite number of reflections is uniform. Setting equations (7.2) and (7.4) equal to each other, $R_d/(1 - R_d)$ was calculated for each patient case and summarized in table 7.9 The relationship between R_d and tissue optical properties can be found in Ong et al. [157].

7.2.4   Anisotropy modeling

The treatment light is delivered through a polished bare-tip optical fiber that is inside of a modified endotracheal (ET) tube filled with Intralipid. The ET tube balloon is filled with scattering fluid but still exhibits anisotropy around the perimeter. This anisotropy was measured, modeled, and applied in the calculation for light fluence at

detector locations.
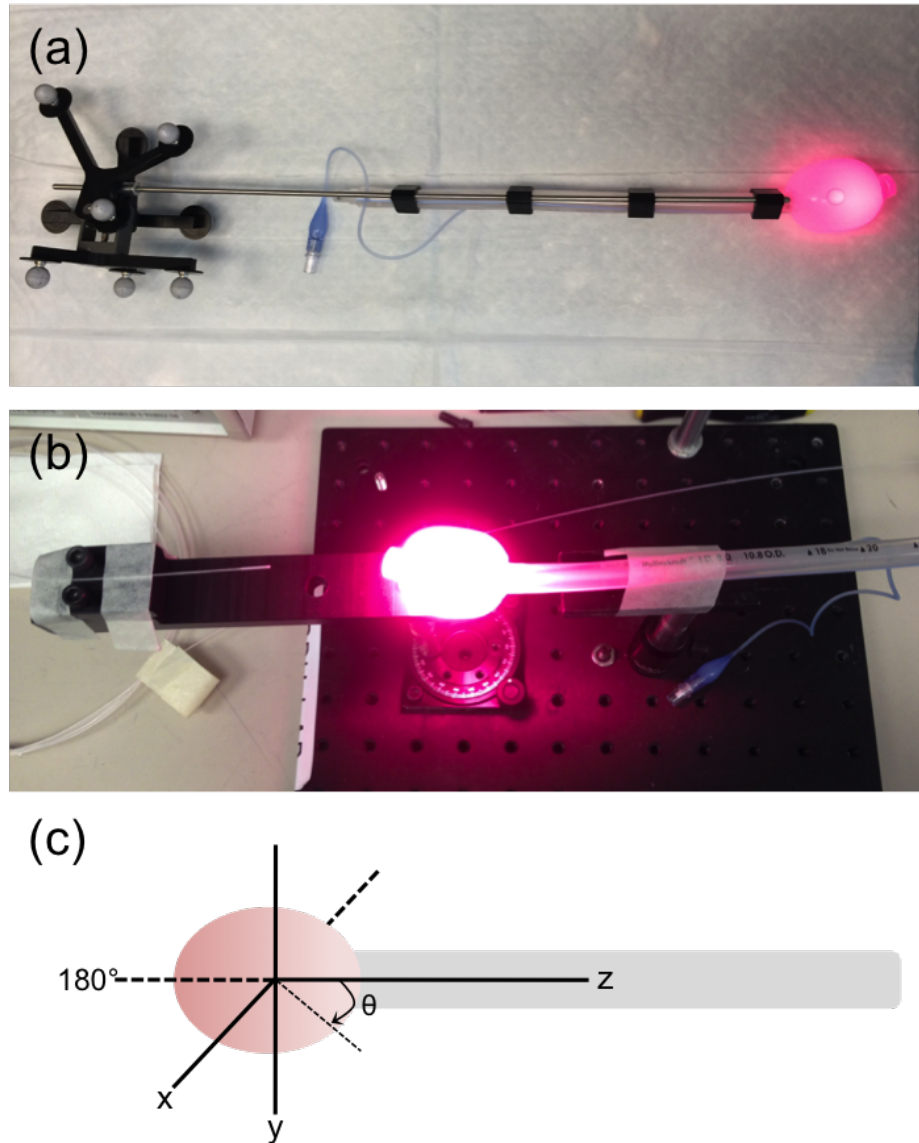
Figure 7.4: (a) Balloon illuminated with low light to illustrate the anisotropy (b) Set-up to measure angular anisotropy with an isotropic detector (c) Angle definition for the anisotropy function

Using an isotropic detector, the anisotropy of the light being emitted from the balloon was measured on an angular platform (shown in Fig. 7.4b). Assuming azimuthal symmetry about the wand, the measurements taken at 5° intervals were fit to a polynomial of order 2 (Eq. (7.5)). As seen in Fig. 7.4a, the least attenuated light

results from the capped end of the balloon (defined as $\theta = 180°$), which is oriented closest to the polished face of the bare fiber. The anisotropy function was fit to the following form

$$A(\theta) = p_1\theta^2 + p_2\theta + p_3 \tag{7.5}$$

where θ is described as the angle from the axis of the wand, as shown in figure 7.4c. The fit model is shown in figure 7.5 with two sets of measured data. The parameters for the model were found to be $p_1 = 2.764 \times 10^{-5}$, $p_2 = 0.01027$, and $p_3 = 0.03685$.
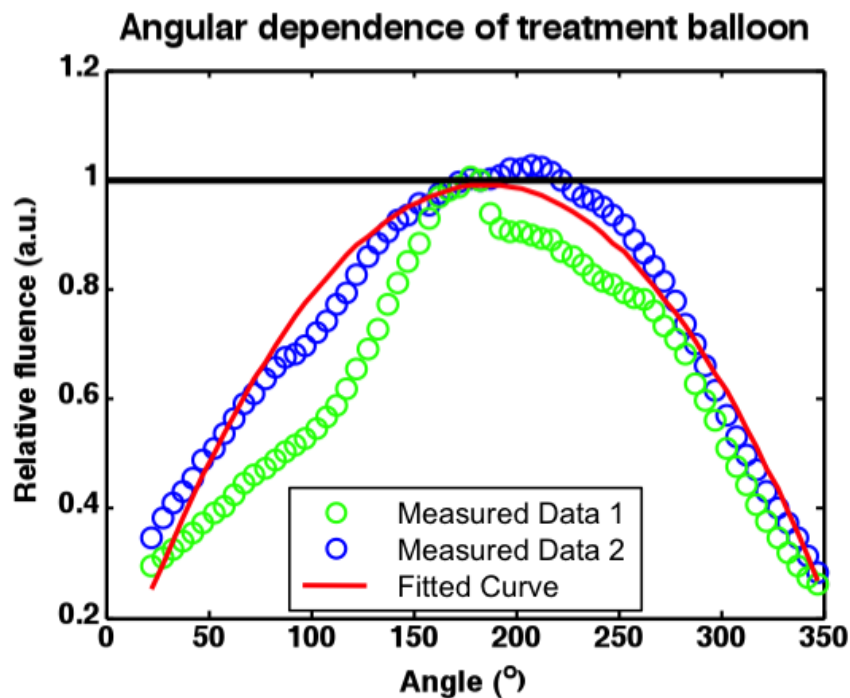
Figure 7.5: Treatment wand balloon anisotropy. Relative light fluence measurements (circles) were obtained every 5°. Assuming azimuthal symmetry, an anisotropy function (solid red line) was fitted according to equation (7.5). The solid black line represents the function $A(\theta)$ without the anisotropic model (constant)

To verify the model, a treatment was done on a chest phantom of known geometry. Four isotropic detectors were placed in the chest cavity and treated to 10 J/cm^2. The measured fluence values were compared with the calculations using the position

from the navigation tracking system. Since there was no scattering media inside the treatment cavity, only the primary component of light was considered for calculations (Eq. (7.1)). The anisotropy function was applied by multiplying it with the calculated primary light component.

The navigation system provides the treatment delivery point source location in Cartesian coordinates along with rotation quaternions (Q_1, Q_2, Q_3, Q_4) [172]. The raw coordinates $(R = (x, y, z))$ obtained are relative to the camera (camera coordinates) and can be converted to the wand coordinate system, described in Fig. 7.4c $(R' = (x', y', z'))$. The coordinate transformation is performed by

$$R' = M^{-1}R \tag{7.6}$$

where the rotation matrix, M, is given by

$$M = \begin{bmatrix} \begin{aligned} Q_1Q_1 + Q_2Q_2 \\ -Q_3Q_3 - Q_4Q_4 \end{aligned} & 2(Q_2Q_3 - Q_1Q_4) & 2(Q_2Q_4 + Q_1Q_3) \\ 2(Q_2Q_3 + Q_1Q_4) & \begin{aligned} Q_1Q_1 - Q_2Q_2 \\ +Q_3Q_3 - Q_4Q_4 \end{aligned} & 2(Q_3Q_4 - Q_1Q_2) \\ 2(Q_2Q_4 - Q_1Q_3) & 2(Q_3Q_4 + Q_1Q_1) & \begin{aligned} Q_1Q_1 - Q_2Q_2 \\ -Q_3Q_3 + Q_4Q_4 \end{aligned} \end{bmatrix} \tag{7.7}$$

From the wand coordinates, the angle of the balloon that is closest to the treatment surface can be found by the following

$$\theta = \arctan\left(\frac{\sqrt{x'^2 + y'^2}}{z'}\right) \tag{7.8}$$

The angle is then used in the anisotropy function $A(\theta)$, and applied to the light fluence calculations.

In a phantom with no scatterer, only primary light component was calculated and compared with and without application of $A(\theta)$. Four detectors in a chest phantom

compared and the results are shown in Fig. 7.6. With the balloon anisotropy function, the fluence data is better matched; however, the larger variation after a long treatment time is not taken into account. Any attenuation of the light from the wand itself was not considered for this study.
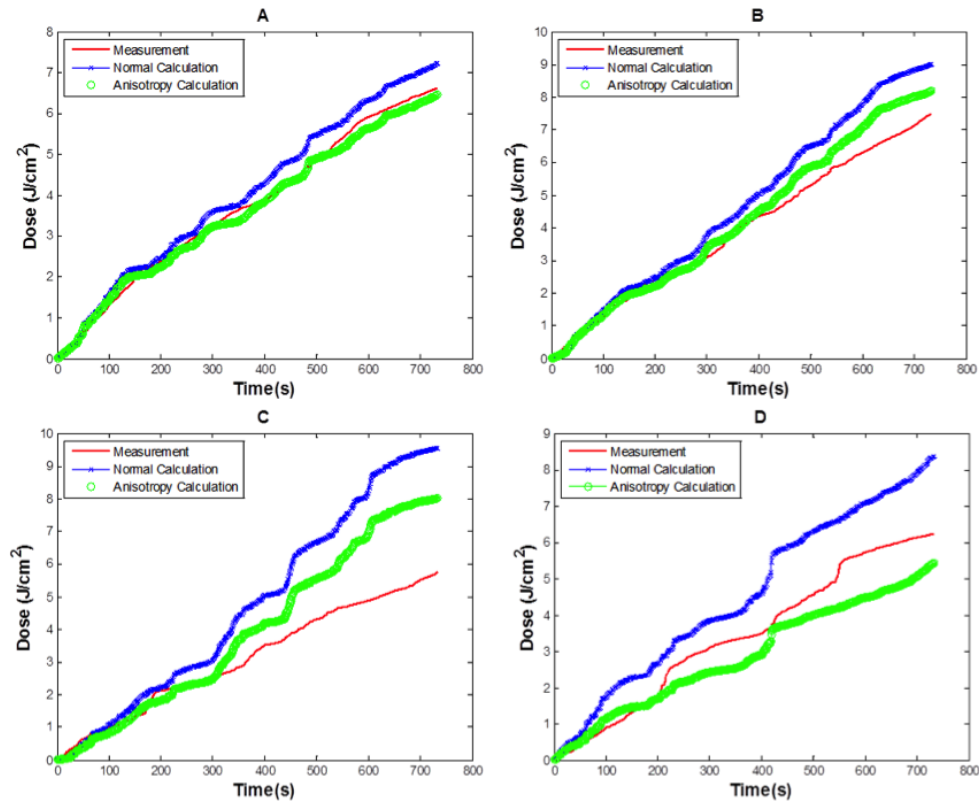
Figure 7.6: Measured fluence (red lines) compared to calculated fluence using primary light calculations only (blue lines) versus those incorporating balloon anisotropy (green lines). Four detectors were placed inside a open chest phantom and treated.

A large factor affecting the modeling of the balloon anisotropy is variations in the ET tube balloons. Each balloon has its own unique shape and anisotropy. Further studies would have to be done with numerous different treatment wands and better angular resolution as well as measurements from various distances from the balloon center. However, this initial study shows one improvement in light fluence calculations

using the IR navigation system.

7.2.5 Light fluence dosimetry in lung shaped cavities

Scattered fluence dosimetry was investigated in phantoms to simulate the clinical treatment environment. Lung shaped cavities with different dimensions surrounded by turbid media with varying optical properties were used to simulate the intracavity lung geometry. Equations (3.5) and (3.6) were used to calculate scattered light. Distances from the point source to each detector position were measured and verified from a CT scan of the phantom. In-air fluence measurements with the same geometry were used to determine the primary component ($\phi_{primary}$) of the light and subtracted from the total measurement (ϕ_{total}). The measured scattered light component ($\phi_{scattered}$) is determined by subtracting the primary from the total light fluence: $\phi_{scattered} = \phi_{total} - \phi_{primary}$. This was then compared to the calculated values. The surface area (SA) was determined using (i) the volumetric average of the phantom and the (ii) the CT-determined surface area. Optical phantoms were prepared by using Intralipid and ink as scattered and absorbing media, respectively. The optical properties of the surrounding media were measured using a two-catheter method described in section 3.1.3. Measurements were made with two point source locations – centered in the phantom and 1.5 cm lowered.
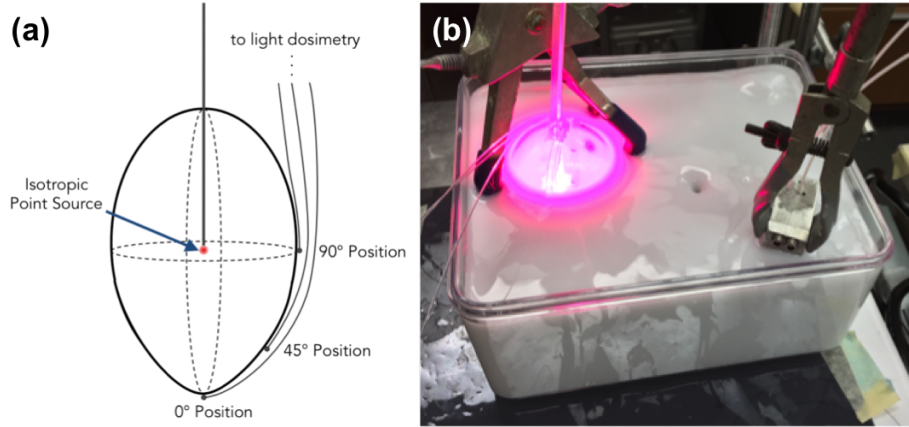
Figure 7.7: (a) Schematic of pleural cavity simulating phantom. Isotropic detectors were placed around the phantom at different positions relative to the isotropic point source. (b) Photograph of the experimental set up. The phantom was submerged in a tissue-simulating optical phantom. The optical properties of the surrounding phantom were measured using the two-cathether system, shown on the right.

The measured and calculated scattered dose in the pleural cavity simulating phantom agreed best using the CT surface area (ii) and equation (3.5). The measured values are summarized for the centered and off-center point source positions in table 7.2 as $\phi_{scattered}/s$, where s is the source power. Data is shown with a fixed $\mu'_s = 6.7$ cm^{-1} in the surrounding media and varying μ_a for each of the 3 detector locations. Calculated values are shown in table 7.3. The percent error between mean measured scattered dose and each calculated value is summarized in parenthesis.

Table 7.2: $\phi_{scattered}/s$ in phantoms with $\mu'_s = 6.7$ cm^{-1}

Detector μ_a (cm^{-1})	0.088 ($R_d = 0.567$)	0.34 ($R_d = 0.355$)	0.83 ($R_d = 0.220$)
Centered Point Source			
0° Location	0.0465	0.0177	0.0090
45° Location	0.0420	0.0190	0.0085
90° Location	0.0456	0.0218	0.0104
Off-Center Point Source (1.5 cm down)			

0° Location	0.0416	0.0176	0.0094
45° Location	0.0428	0.0164	0.0110
90° Location	0.0410	0.0244	0.0088
Mean ± Std.	0.0433 ± 0.0023	0.0195 ± 0.0030	0.0095 ± 0.0010

Table 7.3: Calculated $\phi_{scattered}/s$ with $\mu'_s = 6.7$ cm^{-1} (% error between calculated and measured mean)

μ_a (cm^{-1}) \ Calculation Method	0.088 ($R_d = 0.567$)	0.34 ($R_d = 0.355$)	0.83 ($R_d = 0.220$)
Eq. (3.5) with $SA(i)$	0.0414 (-4.37%)	0.0174 (-10.79%)	0.0089 (-6.27%)
Eq. (3.5) with $SA(ii)$	0.0465 (7.45%)	0.0195 (0.24%)	0.0100 (5.32%)
Eq. (3.6) with $SA(i)$	0.0533 (23.15%)	0.0213 (9.40%)	0.0097 (1.88%)
Eq. (3.6) with $SA(ii)$	0.0599 (38.37%)	0.0240 (22.92%)	0.0109 (14.47%)
MC Simulation	0.0366 (-15.50%)	0.0206 (5.81%)	0.0117 (23.16%)

The measurements in an ellipsoid phantom agreed best to the calculated values of $\phi_{scattered}/s$ using Eq. (3.5) and the actual surface area obtained from the CT scan of the phantom (ii) with percent errors less than 10%. MC simulated results are comparable to Eq. (3.6) using the CT-based surface area. Equation (3.5) is derived from diffuse reflectance in an integrating sphere.

7.3 Extrapolation of Detector Locations

For each pleural PDT treatment, the physician must provide the location of the 8 isotropic detectors that are sutured into the pleural cavity by pointing a separate

calibrated wand tip to each detector and recording the position coordinates. While this is an accurate method of determining the detector locations instantly in the clinical setting, sometimes it is not possible to obtain them due to time constraints in the operating room or missed field of view from the camera to the wand. In some scenarios, the detector locations were given, but the coordinate system for the treatment data was changed due to removal or blockage of the global reference to the patient bed. A post-processing procedure was developed and applied to extrapolate the locations of the detectors to compare with the measured detector positions. With the development of this method, the data acquisition process in the operating room can be streamlined.

During the course of treatment, it is rare that multiple detectors are being illuminated by the treatment light since the cavity is fairly large (average volume of $\sim$6.5L). For each of the measured cumulative fluence data for each detector, time points where there are "features" were determined. These are described as areas where the treatment wand is close to a detector and is illuminating that area specifically. Those regions are characterized by their fast increase in cumulative fluence or high fluence rates and are illustrated for patient case 020 at the apex detector in Fig. 7.8.
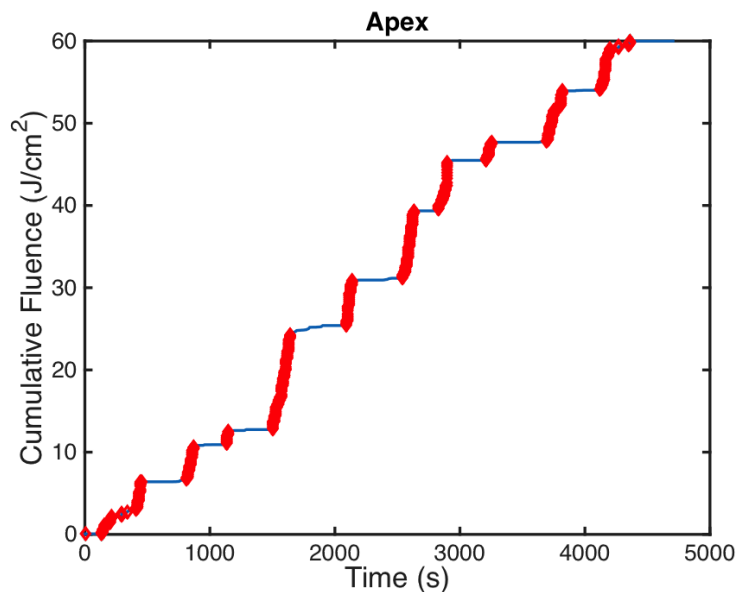
Figure 7.8: Measured cumulative fluence is shown for patient case 020 at the apex detector with regions highlighted in red that display "features." These features were used to determine the time stamps that are indicative of the treatment wand location being near that particular detector.

Using the features for each detector, the times at which the treatment wand was near the detector were found. Times when the treatment light was illuminating the detector were times that show increases in fluence. The locations of the treatment wand for those times were plotted, and the center of mass was used as the extrapolated detector location. These are shown as an '×' symbol next to the measured detector locations in solid circles in Fig. 7.9. A summary of the shifts between the extrapolated and measured detector locations for each patient case is in table 7.4. For case number 016, there is no reported shift between the extrapolated detector location and the measured detector location because there is no data for the measured detector location. In the operating room, if it is proving to be difficult to locate a detector using the IR navigation system, it is possible that the physician will skip that step to minimize the patient's time on the operating table. However, using these

methods, it is possible to extrapolate the location of the detector and calculate the fluence to be compared to the detector-measured fluence.
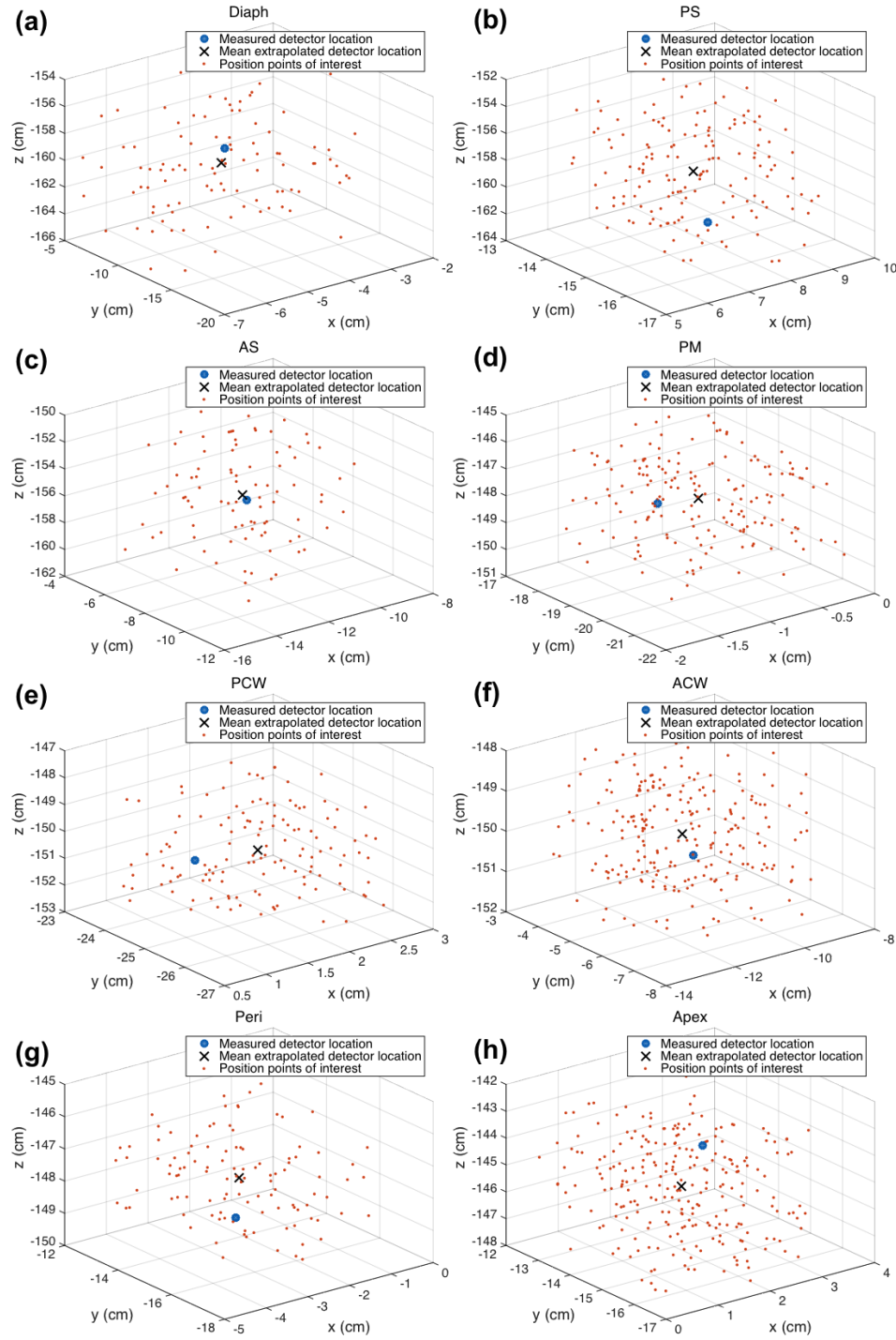
Figure 7.9: Treatment wand locations for times when the detectors were being illuminated are plotted in 3D for each detector for patient case 020. The center of mass was used as the extrapolated detector location, shown as an 'x,' and the measured detector location is shown as a solid circle.

Table 7.4: Shifts between measured and extrapolated detector locations summarized for each patient. Shifts are described in units of cm.

Detector	Δx (cm)	Δy (cm)	Δz (cm)	d (cm)
Case 012				
Diaph	-2.87	2.20	-2.77	4.56
PS	-0.91	1.98	-2.11	3.03
AS	2.10	1.90	-3.19	4.26
PM	0.92	1.12	-1.84	2.34
PCW	1.98	2.09	-1.40	3.20
ACW	2.17	-1.93	-0.98	3.07
Peri	-2.86	-2.47	2.18	4.36
Apex	0.97	0.06	3.69	3.82
Average	0.19±2.13	0.62±1.88	-0.80±2.44	3.58±0.79
Case 014				
Diaph	1.97	-1.28	-4.62	5.18
PS	1.54	2.11	-3.19	4.12
AS	1.77	1.65	3.21	4.02
PM	1.10	0.99	1.28	1.95
PCW	-1.07	2.89	-2.32	3.86
ACW	-0.98	-0.67	-1.97	2.30
Peri	-2.50	-2.01	-1.69	3.62
Apex	-1.11	-1.48	3.88	4.30
Average	0.090±1.70	0.28±1.86	-0.68±3.09	3.67±1.06
Case 016				
Diaph	3.86	-1.18	-4.17	5.81
PS	1.39	2.11	3.27	4.13
AS	1.86	2.11	-3.19	4.26
PM	-1.58	1.09	-4.10	4.53
PCW	-1.57	2.17	-1.01	2.87
ACW	0.98	-0.99	3.86	4.10
Peri	–	–	–	–
Apex	–	–	–	–
Average	0.82±2.11	0.89±1.58	-0.89±3.64	4.28±0.94
Case 017				
Diaph	1.39	-4.20	-1.87	4.80
PS	1.29	1.40	-3.20	3.72
AS	1.13	1.18	-1.78	2.42
PM	2.11	-1.73	-1.98	3.37

PCW	1.09	-0.98	2.09	2.56
ACW	1.33	2.32	-1.20	2.93
Peri	1.72	1.38	-1.78	2.84
Apex	0.91	1.11	2.43	2.83
Average	1.37±0.38	0.06±2.19	-0.91±2.04	3.18±0.78
Case 018				
Diaph	0.99	-1.19	-2.11	2.61
PS	1.19	-0.92	-1.30	1.98
AS	-1.11	4.18	-4.76	6.43
PM	0.91	1.18	-1.41	2.06
PCW	-1.88	1.30	-0.92	2.46
ACW	2.76	-3.20	1.92	4.64
Peri	-2.40	1.20	-1.29	2.97
Apex	1.08	-4.53	2.42	5.24
Average	0.19±1.78	-0.24±2.79	-0.40±2.44	3.55±1.67
Case 020				
Diaph	0.01	-0.27	-1.17	1.20
PS	0.37	0.07	-2.21	2.20
AS	0.90	-0.93	-1.52	1.99
PM	0.01	1.28	-0.92	1.57
PCW	-0.32	0.90	-0.74	1.20
ACW	0.05	-0.28	-0.43	0.52
Peri	-1.02	-1.50	-0.29	1.84
Apex	0.09	-0.52	1.75	1.82
Average	0.010±0.55	-0.16±0.91	-0.40±1.31	1.54±0.55

For patient case 020, the detector locations were able to be determined to an accuracy of under 2 cm, however, this is not always possible for each case. Depending on the geometry of the pleural cavity of the patient and the location of the infrared camera on the day of surgery, some of the detectors may be illuminated without providing any information of the treatment wand location. For those cases, the position data of the wand cannot be used to determine the wand location. The accuracy of this method can be greatly increased with more efficient data collection of the treatment wand location.

For earlier cases (case numbers 012-017), the data obtained from extrapolated

isotropic detector locations is not as accurate as those of later cases (case numbers 018-020). Camera placement is critical prior to surgery and a well-placed camera will be able to collect more treatment light position information during treatment. This process was improved over time with experience and knowledge about patient placement.

The cumulative fluence at the end of treatment was calculated using the extrapolated detector positions compared to the measured fluence from the isotropic detectors. Table 7.5 shows that by using the primary component in addition to the scattering component of light (Eq. (7.2)), the measured and calculated fluence agree to within 21%. With the addition of the dual correction factor (Eq. (7.3)), the agreement is improved to be within 15%.

Table 7.5: Percent error from measured light fluence at the end of treatment with calculated light fluence using the (a) primary and scattering component (Eq. (7.2)) and (b) primary and scattering component with CF (Eq. (7.3)) using extrapolated detector positions

| (a) Primary and Scattering Component | | | | | | | | |
Case No.	Diaph	PS	AS	PM	PCW	ACW	Peri	Apex	Avg.
012	21.0%	12.7%	11.7%	9.6%	9.7%	9.1%	16.7%	16.3%	13.3% ± 4.3%
014	17.0%	10.0%	8.3%	6.7%	11.4%	7.1%	8.2%	13.0%	10.2% ± 3.5%
016	16.6%	7.7%	8.1%	8.2%	6.3%	10.2%	18.6	16.9	11.6% ± 4.9%
017	15.1%	8.1%	8.9%	12.9%	7.8%	10.6%	12.9%	14.5%	11.4% ± 2.9%
018	10.7%	8.8%	15.6%	6.9%	9.8%	9.5%	8.7%	10.6%	10.1% ± 2.5%
020	8.6%	6.5%	6.4%	7.2%	9.0%	1.7%	6.6%	9.6%	7.0% ± 2.4%
Avg.	14.8% ±4.5%	9.0% ±2.2%	9.8% ±3.3%	8.6% ±2.4%	9.0% ±1.8%	8.0% ±3.3%	12.0% ±4.9%	13.5% ±3.0%	

| (b) Primary and Scattering Component with Dual Correction (CF) | | | | | | | | |
Case No.	Diaph	PS	AS	PM	PCW	ACW	Peri	Apex	Avg.
012	13.8%	9.1%	8.2%	7.3%	7.3%	8.6%	13.7%	12.9%	10.5% ± 3.5%

014	10.4%	9.7%	8.3%	6.6%	10.5%	8.2%	7.4%	11.6%	9.1% ± 1.7%
016	13.0%	4.7%	5.4%	6.1%	6.3%	9.9%	12.9	14.0	9.0% ± 3.8%
017	10.6%	5.7%	2.7%	11.0%	6.4%	9.6%	10.0%	13.4%	8.7% ± 3.5%
018	6.1%	8.2%	7.8%	3.8%	4.3%	10.9%	10.6%	7.3%	7.4% ± 2.6%
020	6.0%	3.3%	3.3%	0.7%	6.2%	3.0%	0.1%	3.0%	4.5% ± 5.0%
Avg.	10.5% ±4.1%	6.8% ±2.6%	6.0% ±2.5%	5.9% ±3.5%	6.7% ±2.1%	8.4% ±2.8%	9.1% ±4.9%	10.4% ±4.3%	

It can be seen from both table 7.4 and 7.5 that certain detector locations are more accurately extrapolated than others. The general trend is that detectors in the extremities of the pleural cavity including the diaphragm, anterior sulcus, and apex, show larger errors between measured and extrapolated locations. More specifically, the detector located at the diaphragm shows a larger negative shift in the z direction, indicating that the extrapolated detector location is above the measured detector location. During treatment, it is more likely that the treatment balloon does not fully reach the detector area while it is being illuminated, resulting in a collection of position points above the actual detector and an extrapolated position with a large z shift. Similarly, the apex detector located at the top of the pleural cavity has a larger positive shift in the z direction, consistent with the treatment wand being below the actual detector location during light delivery.

Table 7.6: Shifts between measured and extrapolated detector locations averaged across patient cases for each site. Shifts are described in units of cm.

Detector	$\Delta\bar{x}$ (cm)	$\Delta\bar{y}$ (cm)	$\Delta\bar{z}$ (cm)	$\bar{d}$ (cm)
Diaph	0.89±2.24	-0.99±2.06	-2.79±1.36	4.03±1.75
PS	0.81±0.94	1.13±1.27	-1.46±2.42	3.20±0.95
AS	1.11±1.18	1.68±1.65	-1.87±2.75	3.90±1.58
PM	0.58±1.25	0.65±1.17	-1.49±1.74	2.64±1.11

PCW	-0.30±1.54	1.39±1.36	-0.71±1.49	2.69±0.89
ACW	1.05±1.37	-0.79±1.85	0.20±2.23	2.93±1.45
Peri	-1.41±1.89	-0.68±1.83	-0.57±1.65	3.13±0.94
Apex	0.39±0.93	-1.07±2.14	2.83±0.91	3.60±1.32

Shifts in x, y, and z directions for each extrapolated detector location compared to the measured detector location were averaged across the patient cases studied and summarized in table 7.6. The shift in the extrapolated detector locations for the diaphragm and apex positions show a systematic shift with standard deviations that are smaller. These average shifts were applied to the extrapolated positions and light fluence was calculated and compared in table 7.7. The extrapolated position for the diaphragm detector was shifted in the z direction by -2.79 cm, and the extrapolated position for the apex detector was shifted in the z direction by 2.83 cm. With these new extrapolated positions, the calculated fluence at the end of treatment better matched the measured fluence, as seen in table 7.7. With the adjusted extrapolated diaphragm and apex detector locations, both calculation methods have improved agreement with measured fluence. Using the primary and scattered components of light, the fluence agrees to within 15% for both diaphragm and apex detectors. The addition of the dual correction factor improves the agreement to within 13%. For cases where there is no measured detector location, this method of extrapolating the detector location from the treatment data can be used.

Table 7.7: Percent error from measured light fluence at the end of treatment with calculated light fluence using the (a) primary and scattering component (Eq. (7.2)) and (b) primary and scattering component with CF (Eq. (7.3)) using extrapolated detector positions with average shift for detectors

Case No.	(a) Primary and Scattering Component		(b) Primary and Scattering with Dual Correction	
	Diaph	Apex	Diaph	Apex

012	10.6%	9.3%	4.1%	7.7%
014	14.8%	10.1%	8.1%	9.5%
016	13.9%	12.9%	11.7%	12.4%
017	7.6%	10.9%	7.1%	7.3%
018	8.9%	9.7%	5.9%	6.2%
020	3.7%	6.0%	4.7%	1.3%
Average	9.9%±4.1%	9.8%±2.3%	6.9%±2.8%	7.4%±3.7%

7.4 Clinical Photofrin Pleural PDT Results

The position of the light source being used to deliver light during pleural PDT was tracked throughout the treatment and used to acquire the pleural cavity geometry and calculate the light fluence distribution. Calculation methods were improved from using just the primary (direct) light component to adding a constant scattered light component. The calculation method was further improved by implementing a time-dependent dual correction factor (CF). Evaluation of the light fluence calculation was done by comparing the calculated light fluence at the locations of the 8 isotropic detectors with the measured light dose.

The improved light delivery wand was evaluated for consistency before and after treatment. Calibration of the wand tip location is done prior to sterilization. The design of the wand involves assembly of the reflective spheres immediately before treatment. To ensure that the optical IR tracking system is tracking the fiber tip after assembly, the shift between the calibrated point and the light source fiber tip point was determined after treatment. The results are summarized in table **??**. The maximum shift was 1.64 ± 0.17 mm, which is less than the 2 mm measurement uncertainty from the device. This ensures that the modified treatment delivery wand is an improvement from having to determine and apply a 3 mm shift from the laser source position to the tracking device point position. This eliminates a potential uncertainty

from implementation in the clinical setting, where the shift may not be able to be determined at every case.

Using only the primary light component, the calculated light fluence is consistently lower than the measured dose for all 8 detector locations, as seen in figure 7.10. For the case shown in Fig. 7.10 (case 020), the maximum percent error from the measured light dose at the end of treatment using Eq. (7.1) at each detector location is 67.5% at the Apex location. For 6 patient case studies, the average deviation for all detectors was 51.6% ± 5.6%. From the data, it is clear that $\phi_{primary}$ is not fully accounting for the light fluence that is delivered. The percent error from measurements using $\phi_{primary}$ is summarized for each detector location and each patient case in table 2 (a). The mean values for each detector across all patient cases as well as the mean values for each patient case across all detectors are shown with their standard deviations.
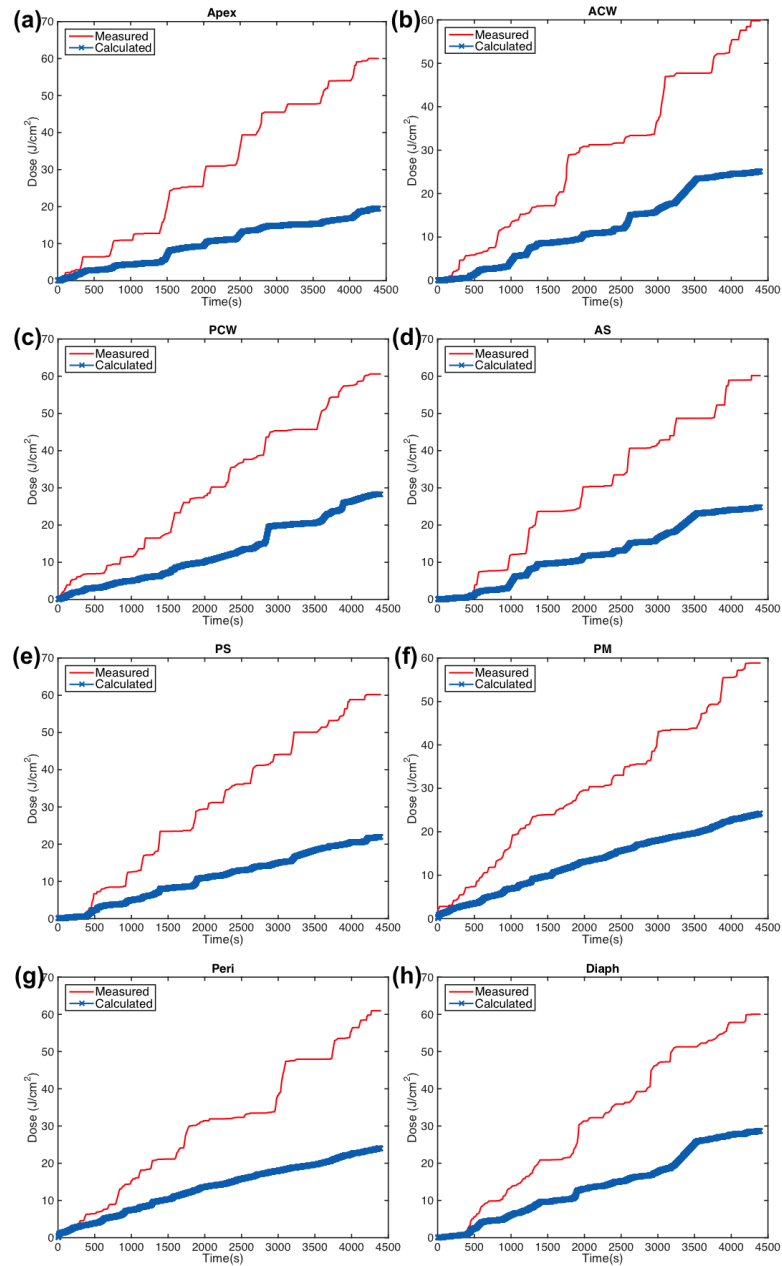
Figure 7.10: Measured (red solid line) light fluence data over the course of treatment along with calculated (blue 'x') light fluence using the primary component (Eq. (7.1)) plotted for 8 detector locations: (a) apex (b) anterior chest wall (ACW) (c) posterior chest wall (PCW) (d) anterior sulcus (AS) (e) posterior sulcus (PS) (f) posterior mediastinum (PM) (g) pericardium (Peri) (h) diaphragm (diaph)

Table 7.8: Percent error from measured light fluence at the end of treatment with calculated light fluence using the (a) primary component (Eq. (7.1)), only the (b) primary component with CF, the (c) primary and scattering component (Eq. (7.2)), and the (d) primary and scattering component with CF (Eq. (7.3))

(a) Primary Component Only

Case No.	Diaph	PS	AS	PM	PCW	ACW	Peri	Apex	Avg.
012	39.8%	56.4%	57.2%	58.5%	51.0%	56.6%	29.2%	45.8%	49.3% ± 10.4%
014	52.9%	46.9%	63.9%	42.4%	46.5%	67.6%	51.8%	50.0%	52.7% ± 8.7%
016	50.0%	47.4%	52.4%	58.3%	41.2%	56.5%	–	–	51.0% ± 6.3%
017	39.4%	49.3%	63.4%	44.5%	28.2%	39.6%	29.2%	45.7%	42.4% ± 11.3%
018	43.2%	52.8%	62.1%	52.1%	45.4%	63.0%	58.9%	61.4%	54.9% ± 7.7%
020	52.2%	63.6%	58.7%	59.0%	53.2%	58.0%	60.6%	67.5%	59.1% ± 5.0%
Avg.	46.2% ±6.2%	52.7% ±6.4%	59.6% ±4.4%	52.5% ±7.5%	44.2% ±9.0%	56.9% ±9.5%	45.9% ±15.7%	54.1% ±9.9%	

(b) Primary and Scattering Component

Case No.	Diaph	PS	AS	PM	PCW	ACW	Peri	Apex	Avg.
012	13.8%	7.4%	10.1%	10.2%	5.4%	8.3%	15.8%	1.3%	9.1% ± 4.6%
014	1.0%	6.3%	3.0%	3.7%	9.0%	3.2%	1.2%	15.1%	5.3% ± 4.8%
016	2.5%	1.7%	5.9%	4.2%	15.4%	13.9%	–	–	7.3% ± 5.9%
017	12.9%	8.7%	6.7%	14.9%	6.6%	14.7%	13.7%	13.1%	11.4% ± 3.5%
018	13.6%	5.7%	9.0%	4.2%	9.2%	9.4%	6.5%	8.9%	8.3% ± 2.9%
020	3.1%	8.3%	3.5%	2.5%	1.6%	2.4%	6.1%	13.1%	5.0% ± 3.7%
Avg.	7.8% ±6.2%	6.4% ±2.6%	6.4% ±2.9%	6.6% ±4.9%	7.9% ±4.6%	8.7% ±5.2%	8.7% ±6.0%	10.1% ±95.4%	

(c) Primary Component with Dual Correction (CF)

Case No.	Diaph	PS	AS	PM	PCW	ACW	Peri	Apex	Avg.
012	20.5%	21.6%	10.1%	26.3%	16.7%	13.3%	0.8%	1.3%	13.8% ± 9.3%
014	1.0%	6.3%	35.0%	3.7%	9.0%	32.1%	1.2%	15.1%	12.9% ± 13.5%
016	2.5%	18.1%	22.5%	4.2%	15.4%	19.3%	–	–	13.7% ± 8.3%
017	15.2%	8.3%	23.5%	17.6%	6.6%	13.5%	19.7%	15.0%	14.9%

Case No.	Diaph	PS	AS	PM	PCW	ACW	Peri	Apex	Avg.
									± 5.6%
018	13.6%	3.8%	9.0%	18.6%	7.2%	18.6%	5.6%	0.4%	9.6% ± 6.7%
020	24.3%	8.9%	6.4%	24.3%	47.1%	6.9%	17.3%	4.4%	17.5% ± 14.4%
Avg.	12.9% ±9.4%	11.2% ±7.1%	17.8% ±11.1%	15.8% ±9.7%	17.0% ±15.3%	17.3% ±8.5%	8.9% ±9.0%	7.2% ±7.3%	

(d) Primary and Scattering Component with Dual Correction (CF)

Case No.	Diaph	PS	AS	PM	PCW	ACW	Peri	Apex	Avg.
012	8.6%	1.2%	4.3%	5.4%	5.1%	5.4%	10.2%	2.9%	5.4% ± 2.9%
014	4.5%	9.0%	7.5%	7.9%	3.5%	4.3%	5.5%	9.0%	6.4% ± 2.2%
016	1.9%	2.8%	5.3%	3.1%	9.8%	8.2%	–	–	5.2% ± 3.2%
017	8.9%	3.8%	1.7%	8.3%	4.3%	11.2%	9.8%	3.5%	6.5% ± 3.5%
018	4.0%	2.3%	8.1%	0.8%	3.4%	7.1%	11.2%	6.6%	5.4% ± 3.4%
020	6.2%	4.7%	1.0%	6.4%	12.4%	2.3%	1.6%	0.4%	4.7% ± 4.9%
Avg.	5.7% ±2.8%	4.0% ±2.8%	4.6% ±2.9%	5.3% ±2.9%	6.9% ±4.8%	6.4% ±3.1%	7.7% ±4.0%	4.5% ±3.4%	

Agreement between the calculated light fluence and measured values are further improved with the addition of a constant scattered light dose. Figure 7.11 shows the data for case 020 with calculations using Eq. (7.2). It is seen that for all of the detectors, a constant value for b (in this case, $b = 7$ mW/cm^2) improved the percent deviation. The maximum deviation for case 020 was seen at the Apex location at 13.1%. The average deviation for all detectors and case studies is 7.7% ± 2.4%, and the data is summarized in table 7.8 (b).

With the use of the dual correction factor to the calculation with $\phi_{primary}$, the agreement is improved slightly and summarized in table 7.8 (c). For case 020, the maximum deviation is 47.1% from the PCS detector location. The average deviation for all detectors and case studies for this calculation method is 13.7% ± 2.6%. While this method of calculation improves the agreement, the CF is large.

Implementation of the dual correction method to the calculation with both primary and scattered light components improved the agreement between measured and calculated final light fluence the most. The comparison is shown in Fig. 7.12. The maximum percent error for case 020 was reduced to 12.4% at the PCW location. The average across all detectors and patient cases was 5.6% ± 0.7%. The deviations are summarized in table 7.8 (d).
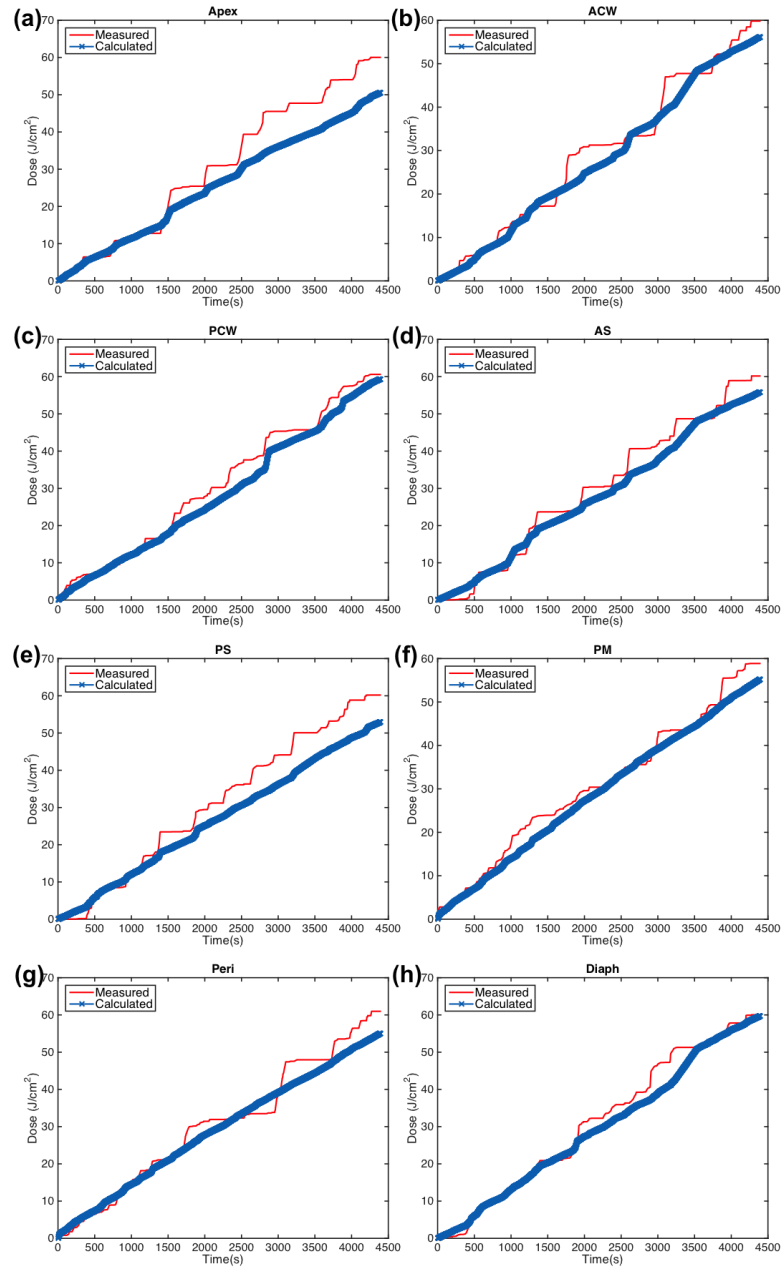
Figure 7.11: Measured (red solid line) light fluence data over the course of treatment along with calculated (blue 'x') light fluence using the primary component with a fixed constant scattering component (Eq. (7.2)) plotted for 8 detector locations: (a) apex (b) anterior chest wall (ACW) (c) posterior chest wall (PCW) (d) anterior sulcus (AS) (e) posterior sulcus (PS) (f) posterior mediastinum (PM) (g) pericardium (Peri) (h) diaphragm (diaph)
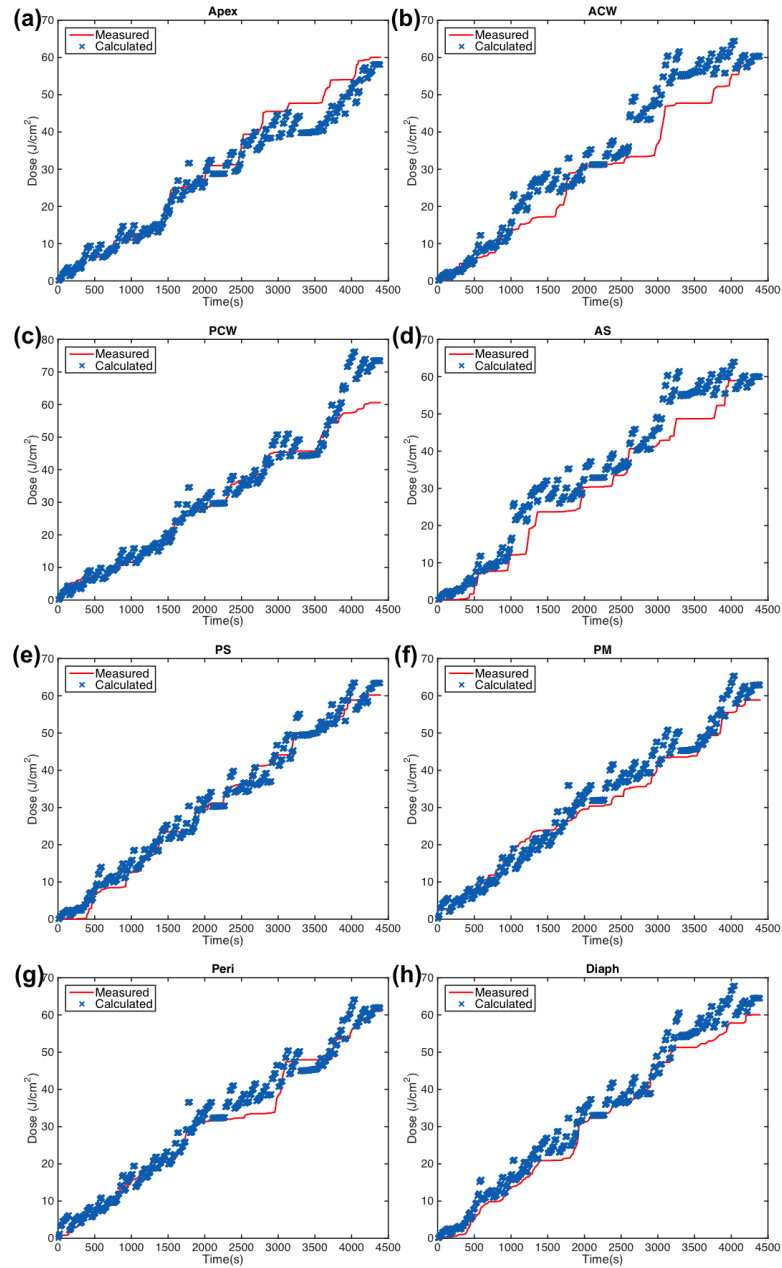
Figure 7.12: Measured (red solid line) light fluence data over the course of treatment along with calculated (blue 'x') light fluence using the primary component with a fixed constant scattering component and dual correction factor (Eq. (7.3)) plotted for 8 detector locations: (a) apex (b) anterior chest wall (ACW) (c) posterior chest wall (PCW) (d) anterior sulcus (AS) (e) posterior sulcus (PS) (f) posterior mediastinum (PM) (g) pericardium (Peri) (h) diaphragm (diaph)

For most cases, larger deviations were seen in the diaphragm, posterior/anterior sulcus, or the apex locations detectors. This may be improved with greater data acquisition at those locations. Due to the cavity geometry and the IR camera location, certain extreme angles or far locations from the center may have less efficient data collection rates. Furthermore, any blockage of the optical path from the reflective spheres to the IR camera will result in loss of position data, which will affect the calculations as well.

Table 7.9: Summary of the pleural cavity surface area, volume, diffuse reflectance (R_d), and scattering component (b) for each study. R_d was calculated using Eq. (7.4)

Case No.	Area (cm^2)	Volume (cm^3)	b (mW/cm^2)	S (mW)	$\frac{R_d}{1-R_d}$	R_d
012	886	2742	7.5	6300	0.264	0.209
014	1710	8192	7.5	6500	0.493	0.330
016	1158	6095	7.5	6500	0.334	0.250
017	1447	7618	6.5	6500	0.362	0.266
018	1766	8103	7.5	6890	0.481	0.325
020	1262	6308	7.0	6500	0.340	0.254
Average	1372 ±337	6510 ±2050	7.3 ±0.4	6531 ±193	0.379 ±0.090	0.272 ±0.047
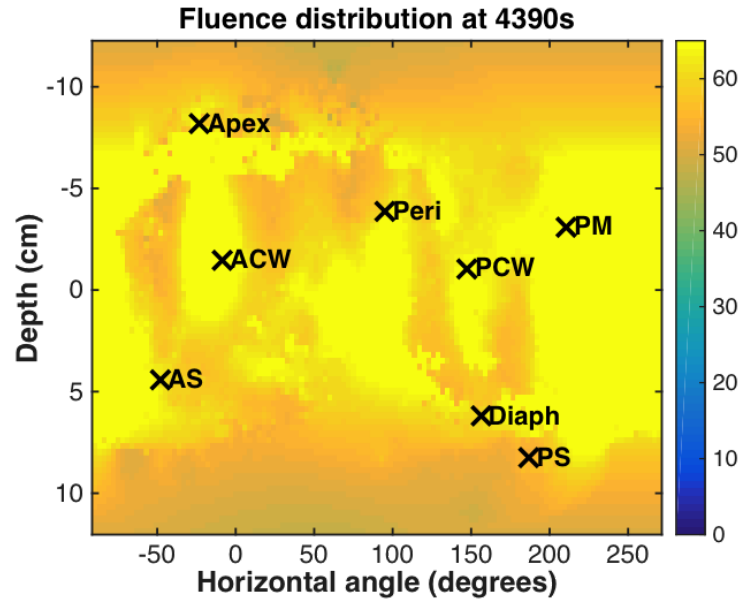
Figure 7.13: Fluence distribution map for a representative patient (Case No. 020). The 3D geometry is unwrapped and displayed on a 2D surface plot with the locations of the isotropic detector locations indicated by × symbols

The uniformity of the treatment delivery was evaluated for all patients. The 3D pleural cavity geometry was unwrapped along the x- and y-axes so that the apex detector location was located at the top of the 2D representation. Figure 7.13 shows the fluence distribution at the end of treatment for case 020 along with labeled detector locations. The profile of light fluence along the z-axis for each horizontal angle is plotted in Fig. 7.14. The mean is shown as a black solid line, the standard deviation is indicated by the grey shaded area, and the dashed line represents the prescribed light fluence of 60 J/cm^2. Most of the cavity excluding the extremities reached the prescribed dose. Large peaks are seen for certain horizontal angles. This is due to the surgical opening and position data that is obtained for movement in and out of the surgical cavity. This region is extrapolated from the data and indicated by the dashed vertical lines in Fig. 7.14. In future studies, the surgical opening will be delineated by the physician so that any position data outside of the treatment cavity

can be properly eliminated.
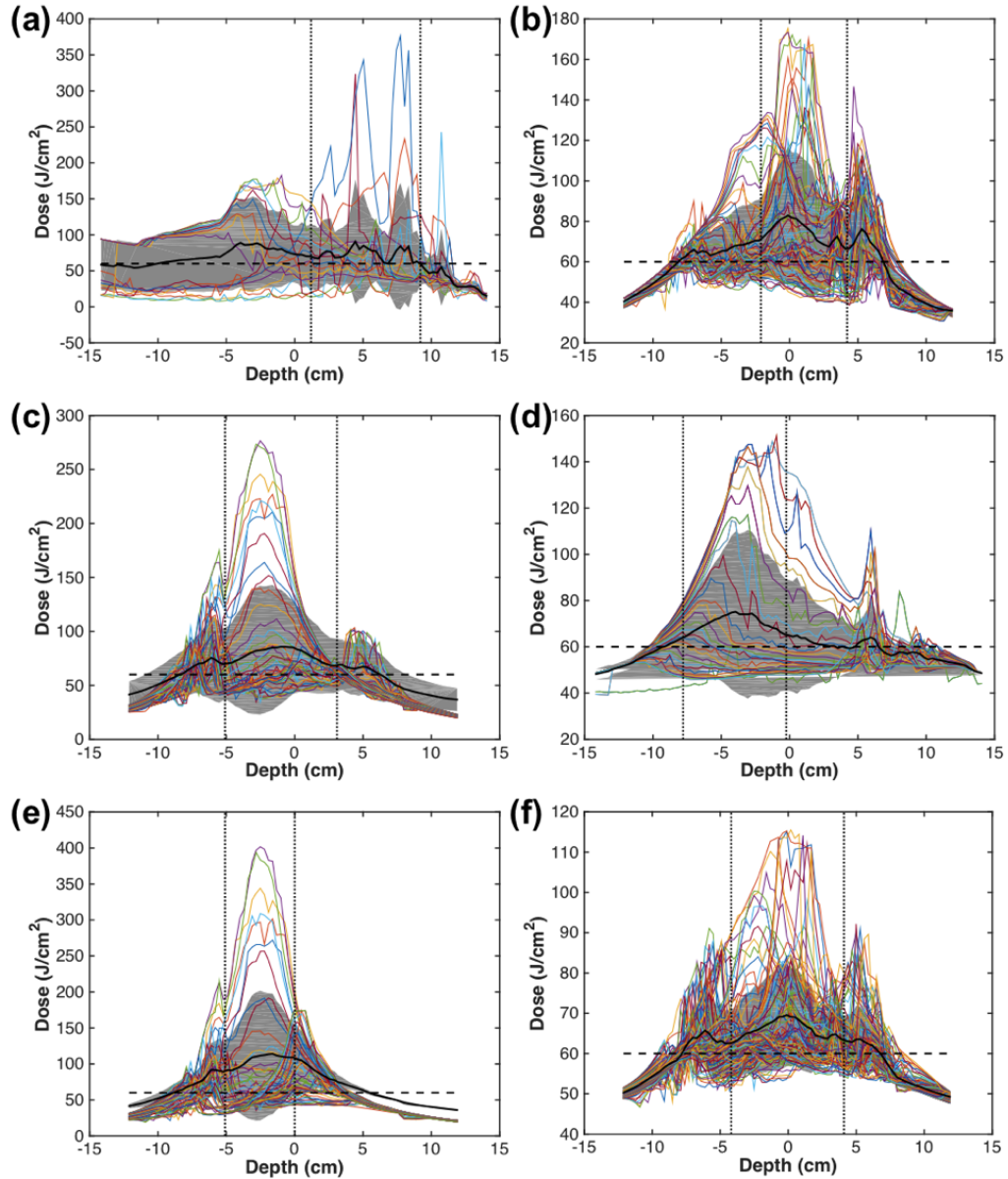
Figure 7.14: Fluence distribution along the z-axis (depth) for each angular location. The mean is shown in a solid black line, and the grey area indicates the standard deviation. Uniformity is calculated as percent variation and summarized for each patient in table 2, excluding the region corresponding to the surgical opening, outlined by the dotted lines. (a)-(f) indicate case numbers 012, 014, 016, 017, 018, and 020, respectively.

The uniformity is quantified as standard deviation from the mean in table 3 for

each case. The standard deviation was calculated as the standard deviation of the mean profile (black line) from the prescribed light fluence (60 J/cm^2). The variation of standard deviation is the standard deviation of the grey region. Across all patients, the uniformity was on average 9.5% with a variation of the standard deviation 17.7%.

Table 7.10: Summary of uniformity across all horizontal angles for profiles shown in Fig. 7.14

Case No.	Standard Deviation (% Difference)	Variation of Std. Deviation (% Difference)
012	3.6%	10.5%
014	6.3%	9.7%
016	14.3%	29.1%
017	9.2%	20.6%
018	13.5%	22.9%
020	9.8%	13.3%
Average	9.5% ± 4.1%	17.7% ± 7.8%

7.5 Conclusions

In this chapter, the light modeling aspect of explicit dosimetry was investigated in depth for a clinical treatment setting. Initial measurements of scattering was performed in ellipsoid shaped phantoms to model scattering in the pleural cavity, which is an improvement from scattering measurements in spherical cavities.

As a standard of care for pleural PDT at the University of Pennsylvania, the light fluence is monitored using 8 isotropic detectors at pre-determined discrete locations. This method does not account for light dose delivered at locations between the detectors and can result in "hot spots" of light fluence when treatment is delivered to the detectors, rather than the entire cavity. A previously developed optical IR navigation system to monitor the light source position during the treatment is im-

proved in this study. Use of the treatment wand position data in conjunction with measured dosimetry data was investigated to consider the possibility of not having to have the physician point to each isotropic detector inside the pleural cavity. For cases with effective position data collection, the detector location could be extrapolated to within 2 cm of the measured location. While this is promising initial data, further improvements will need to be made to increase the data collection efficiency during treatment in the operating room.

The position of the 8 isotropic detectors may not always be measured in the operating room setting. Therefore, a method to extract detector locations from the treatment light wand position data during light illumination was developed and investigated for 6 patient cases. Comparison was done between measured and extracted detector locations, as well as between calculated fluence at the extrapolated detector location and the measured fluence. Fluence was found to be in agreement to within 15% using the extrapolated detector locations, showing promise for use in cases where no detector locations were measured.

Calculation of the light fluence and comparison to measured values is analyzed in depth for each detector for 6 patient cases. Light fluence calculated both the primary component and scattered component of light agrees to within 15% of the measured values. The uniformity of the treatment delivered is also quantified. Using this technology and calculation method, uniform light dose delivery can be aided visually with the fluence distribution map to avoid under-treatment of areas between isotropic detectors.

Chapter 8

Conclusions and Future Work

The project aims of this work was to fully investigate explicit dosimetry modeling *in vivo* and in phantoms for photodynamic therapy. Prior to this work, explicit dosimetry was developed only for *in vivo* in a limited model. This work incorporated measurements of light fluence, photosensitizer concentration, and ground state oxygen concentration to determine reacted singlet oxygen concentration with various treatment scenarios.

The required photochemical parameters for macroscopic singlet oxygen modeling *in vivo* for BPD-mediated PDT was determined with this study and validated with an outcome-evaluation mouse model, which was the first study of its kind. Measured BPD concentration using fluorescence spectra both interstitially and on the surface of the tumor were validated with an *ex vivo* method. The optical property-based correction of the fluorescence signal was also investigated for the two measurement geometries.

Explicit dosimetry of phantom studies was also investigated in detail, with modifications to the prior *in vivo* model to account for singlet oxygen quenching. These studies further validate the use of explicit modeling and can provide insight into pre-

viously unknown photochemical parameters, such as with the photosensitizer Rose Bengal. Future work with new photosensitizers can be performed in phantoms to estimate the photochemical parameters before moving on to the more resource-intensive *in vivo* studies.

The explicit singlet oxygen dosimetry model was compared to the gold-standard method of direct singlet oxygen measurements using singlet oxygen luminescence. This further validated the model by showing that calculated values and measured values in a phantom tracked each other. Further work will be needed to validate the model and direct measurements *in vivo* and to accurately determine the absolute concentration of total reacted singlet oxygen produced while measuring the luminescence counts. This validates the use of explicit dosimetry for the many scenarios where direct measurements are not feasible.

Another important aspect of this work involved improvements to the navigation-based light dosimetry used in the treatment of the pleural cavity in patients with mesothelioma. Scattered light fluence for ellipsoid cavities for various optical properties were measured and compared to a new model. Improvements were made to the light delivery wand as well as the calculation methods. Treatment wand location data was also investigated to extrapolate the isotropic detector locations. With efficient data collection, the extrapolated isotropic detector locations can be found within 2 cm of the measured locations. These isotropic detector locations are important in comparing the calculated light fluence dose on the surface of the cavity with those that are measured continuously in the pre-determined discrete locations. Future work can improve the method to extrapolate the detector locations as well as improve the efficiency of treatment wand position data collection. Currently, the infrared camera placement is dependent on the user and can vary case to case.

Further developments for a fast, real-time light fluence dosimetry model for the

patient treatment scenario remains to be completed. Once this is accomplished, real-time singlet oxygen calculations can be performed in combination with real-time spectroscopy. This knowledge can be used to implement a patient-specific PDT light fluence that is focused on production of the reactive oxygen species to improve overall PDT efficacy.

Appendix A

Chlorophyll Products

The typical mouse diet in the laboratory setting has chlorophyll. It was found that the emission peak for chlorophyll is in the same range as the emission peaks for common photosensitizers, such as BPD and HPPH. A study was performed to determine the decay of this signal after a mouse is put on an alfalfa-free (chlorophyll-free) diet (Harlan Laboratories Inc., Indianapolis, Indiana, USA), so that photosensitizer fluorescence spectra can be collected accurately.

Fluorescence spectra are collected during treatment and used to measure the photosensitizer concentration for use in PDT explicit dosimetry. The characteristic emission peaks of the photosensitizer are fit using known basis spectra. These spectra can be complicated by the presence of chlorophyll and its digestion products. The emission peak for chlorophyll is in the same range as the emission peaks for common photosensitizers, such as BPD and HPPH. Chlorophyll is present in most common laboratory mouse diets [176]. By switching mice to an alfalfa-free diet (thus eliminating chlorophyll), the undesired peak can be eliminated, and characteristic peaks in fluorescence can be attributed to the photosensitizer of interest. In this study, mice were observed for 9 days following a dietary change to see the decay of the chlorophyll

fluorescence over time. No photosensitizer was administered to these mice while being monitored. Figure A.1 shows representative fluorescence spectra for a mouse on a standard diet analyzed with an HPPH basis. While there is no HPPH present in this mouse, it is seen that the emission peak of chlorophyll is very similar to that of HPPH. Using this method of fitting data, mice without any photosensitizer could mistakenly be fit with the photosensitizer basis and found to have a large concentration of photosensitizer.
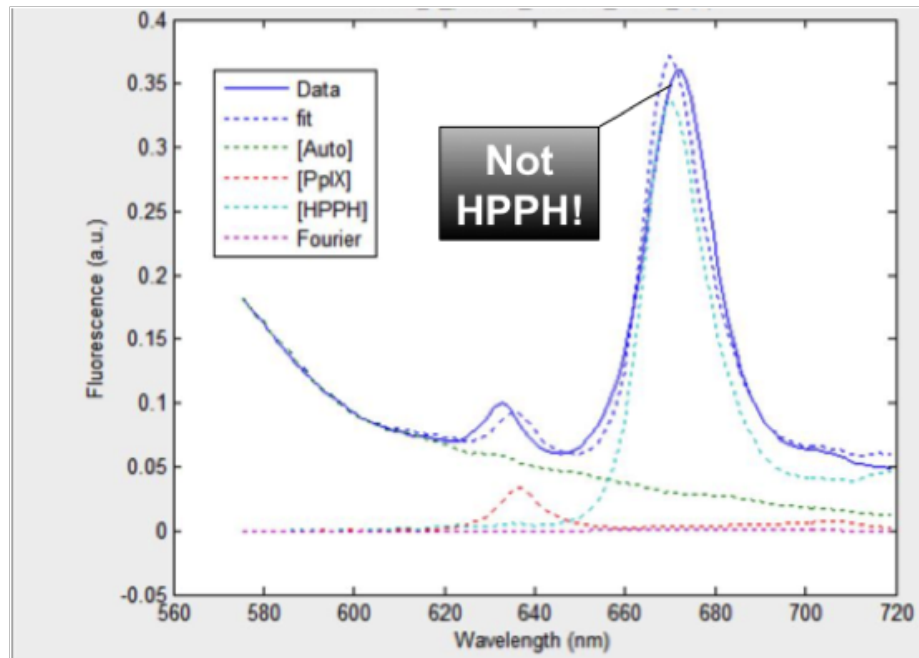
Figure A.1: Fluorescence spectra of a mouse on a standard diet analyzed with an HPPH basis. The emission peak of chlorophyll is very similar to the emission peak of HPPH and is fit as such, which is incorrect.

A small, custom-made multi-fiber contact probe (Fig. A.2) similar to that discussed in chapter 2 was used to measure the fluorescence spectra on mouse tumors as well as the footpad. This probe has smaller source-detector separations, making it possible to detect fluorescence signal from both the shoulder region and the footpad.
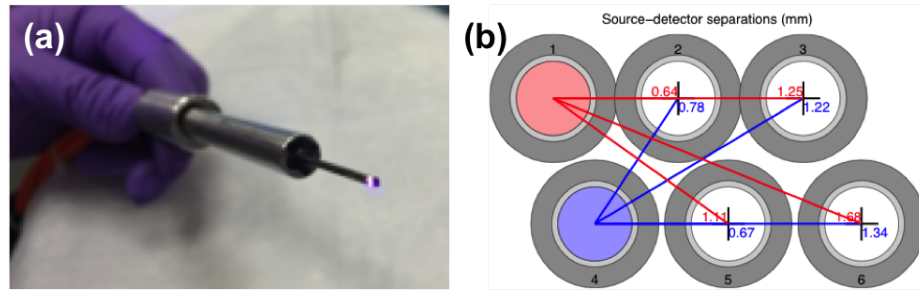
Figure A.2: (a) Multi-fiber contact probe. 6 fibers are collected at one end with two source fibers (white light and 405 nm light) and 4 detector fibers are at different source-detector separations. (b) Schematic diagram of the fiber arrangement on the probe face.

The chlorophyll product signal observed on the first day varied among mice by as much as a factor of 5. This is consistent with previous observations that this emission is variable among animals and over time. In all mice observed in this study, the chlorophyll product component was reduced to less than 3% of the autofluorescence by the 4th day. The time course of the reduction in chlorophyll product emission is shown in figure A.3. These results indicate that fluorescence spectroscopy measurements will be free of chlorophyll product contamination after 4 days on a chlorophyll-free diet. It is noted that this is on the short end of the time scale previously reported [177].
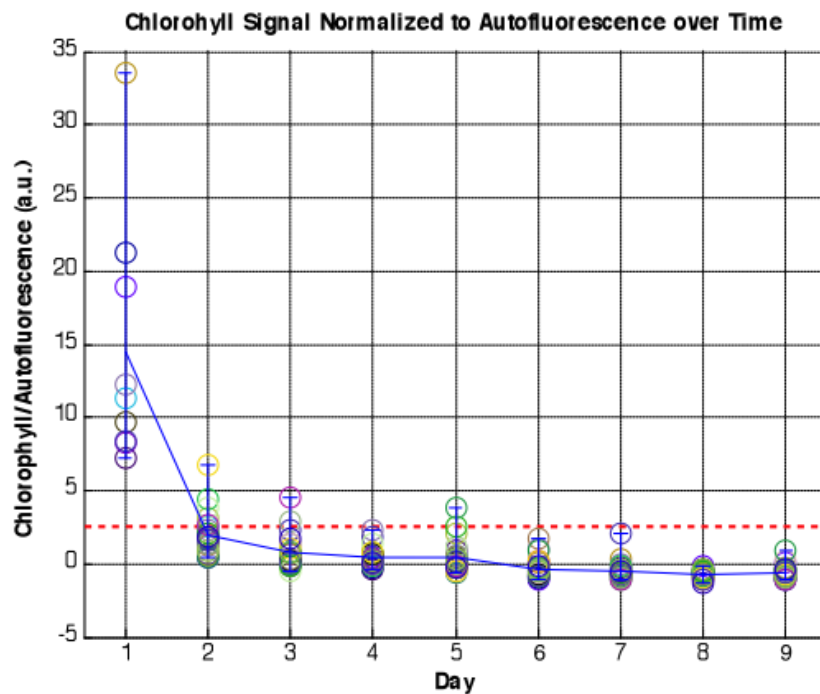
Figure A.3: Chlorophyll signal normalized by autofluorescence observed over 9 days for 25 different mice. The red line indicates 5% of a typical HPPH signal.

The chlorophyll component of the fluorescence spectra had a peak ∼675 nm, which has significant overlap with the spectra of commonly used photosensitizers. This chlorophyll signal could be mistaken for photosensitizer, thus affecting the dose calculations. The red line in Fig. A.3 indicates the point where typical HPPH signal is 5% of the maximum value. This indicates that chlorophyll signal may decay quickly with the modified diet; however, the desired measurements (such as HPPH) could still be affected by the presence of chlorophyll. To evaluate the effect of chlorophyll photoproduct contamination on a typical HPPH measurement, we looked at the spectra of chlorophyll (mice without any other injected photosensitizer) and analyzed them with the basis spectra of HPPH (a commonly used photosensitizer for PDT). Since the emission peaks are very close to each other, chlorophyll spectra could be

mistakenly analyzed as HPPH spectra, indicating a false presence of sensitizer in the tumor.

For all of the *in vivo* studies performed in this work, mice were provided with the alternative, chlorophyll-free diet for at least 5 days prior to photosensitizer administration and fluorescence measurement. Standard laboratory diets were provided upon the completion of PDT treatment if mice were being monitored over time.

Appendix B

P_3 Approximation in an Infinite Medium

B.1 Light Transport and Optical Properties

The amount of light that reaches the targeted tissue accounts for the treatment efficacy in PDT. Light transport in biological matter is characterized by the absorption and scattering of photons. These qualities are characterized by the optical properties of that tissue, namely, the absorption coefficient (μ_a) and the reduced scattering coefficient (μ_s').

B.1.1 Diffusion Approximation for Light Transport

Light propagation can be described by a series of equations and boundary conditions called the diffusion theory of light transport. The radiative transport equation can be solved using several different approximation. The diffusion approximation was used as a solution to the radiative transport equation. The radiance, $L(\vec{r}, \hat{s})$, is defined as the power per unit area per unit solid angle in direction $\hat{s}$ at position $\vec{r}$ and can be

described by the time-independent Boltzmann equation [178, 179].

$$\frac{1}{c}\frac{\partial L\left(r, \hat{s}, t\right)}{\partial t} = -\nabla \cdot L\left(r, \hat{s}, t\right)\hat{s} - \mu_t L\left(r, \hat{s}, t\right) + \mu_s \int_{4\pi} L\left(r, \hat{s}, t\right) f\left(\hat{s}, \hat{s}'\right) d\Omega' + S\left(r, \hat{s}, t\right)$$
(B.1)

$S(\vec{r}, \hat{s})$ represents the source term, and the $f(\hat{s}, \hat{s}')$ is the scattering phase function which describes the probability that a photon incident in direction $\hat{s}'$ will be scattered into direction $\hat{s}$. The right side of equation (B.1) describes the gradient in radiance distribution (first term), the decrease of $L(\vec{r}, \hat{s})$ by absorption and photons that are scattered away from direction $\hat{s}$ (second term), and the increase of radiance by photons scattered into $\hat{s}$ (third term) and by the light source $S(\vec{r}, \hat{s})$ (the remaining terms). The source term $S(\vec{r}, \hat{s})$ is represented in many ways depending on the light source used. For planar geometries, the light can be a wide beam with collimated incidence (often referred to as a pencil beam or a wide beam with diffuse incidence). If the source is an isotropic point source, it can be described as $S_0\delta(r)$, and the solution to equation (B.1) is a Green's function, and the solution for any other source can be obtained by a convolution of the source and Green's function.

The scattering phase function $f(\hat{s}, \hat{s}')$ is assumed to depend only on the deflection angle, θ, between $\hat{s}$ and $\hat{s}'$. $f(\hat{s}, \hat{s}')$ becomes a complicated function in biological media owing to the high particle density and inhomogeneity of tissue. An accepted approximation for $f(\hat{s}, \hat{s}')$ is the Henyey-Greenstein phase function [180, 181].

$$f_{HG}(\cos\theta) = \left(\frac{1}{4\pi}\right)\frac{1 - g^2}{(1 + g^2 - 2g\cos\theta)^{3/2}}$$
(B.2)

where g is the scattering anisotropy given by

$$g = \int_{4\pi} f(\hat{s}, \hat{s}')d\Omega.$$
(B.3)

This quantity, g, is equal to the average of the scattering $\cos\theta$. The scattering anisotropy ranges from -1 to 1, corresponding to backward and forward scattering, respectively. If $g = 0$, then there is no preference for forward or backward scattering. In tissue, g is estimated to be in the range of 0.7-0.9 but is commonly taken to be equal to 0.9 [181, 182].

At the boundary of two different media (L_1 and L_2) with different indicies of refraction, the boundary condition can be specified by following the reflection and transmission attributed to Fresnel's law [183]:

$$L_1(\hat{s})\hat{s} \cdot \hat{n} = R_{Fresnel}(\hat{s})L_1(\hat{s})\hat{s} \cdot (-\hat{n}) + T_{Fresnel}(\hat{s})L_2(\hat{s})\hat{s} \cdot \hat{n}$$

$$L_2(\hat{s})\hat{s} \cdot \hat{n} = R_{Fresnel}(\hat{s})L_2(\hat{s})\hat{s} \cdot (-\hat{n}) + T_{Fresnel}(\hat{s})L_1(\hat{s})\hat{s} \cdot \hat{n}' \tag{B.4}$$

where $\hat{n}$ is the normal direction of the boundary, $\hat{s}$ is the direction of the irradiance under consideration, and $R_{Fresnel}$ and $T_{Fresnel} = 1 - R_{Fresnel}$ are the reflectance and transmission coefficients according to Fresnel's Law [184].

Equation (B.1) can be solved analytically in idealized one-dimensional geometries, but these are not applicable in calculating the light distribution in relevant experimental situations [178]. The spherical harmonic approximation can be used to simply the solution by expanding the radiance and source terms as a series of spherical harmonics and the scattering phase functions as a series of Legendre polynomials. The most common approximations are the first-order (P_1) and the third-order (P_3) approximations [181, 182, 185]

$$L\left(\vec{r}, \hat{s}\right) = \sum_{l=0}^{N} \sum_{m=-1}^{l} \sqrt{\frac{2l+1}{4\pi}} \phi_{lm} Y_{lm}(\hat{s}) \tag{B.5}$$

$$S\left(\vec{r}, \hat{s}\right) = \sum_{l=0}^{N} \sum_{m=-1}^{l} \sqrt{\frac{2l+1}{4\pi}} \sigma_{lm} Y_{lm}(\hat{s}) \tag{B.6}$$

$$f\left(\hat{s}, \hat{s}'\right) = \sum_{l=0}^{N} \frac{2l+1}{4\pi} g_l P_l\left(\hat{s} \cdot \hat{s}'\right) \tag{B.7}$$

In general, $Y_{lm}(\theta, \phi)$ can be written as

$$Y_{lm}(\theta, \phi) = \sqrt{\frac{2l+1}{4\pi} \frac{(l-m)!}{(l+m)!}} P_{lm}(\cos\theta) e^{im\phi} \tag{B.8}$$

where the associated Legendre function, $P_{lm}(x)$, with positive or negative values of $m = -l, \ldots, l$ is given by the following formula

$$P_{lm}(x) = \frac{(-1)^m}{2^l l!} (1 - x^2)^{m/2} \frac{d^{l+m}}{dx^{l+m}} (x^2 - 1)^l. \tag{B.9}$$

The Legendre polynomials, P_l are given by Rodrigues' formula, $P_l(x) = \frac{1}{2^l l!} \frac{d^l}{dx^l} (x^2 - 1)^l$. By expanding the radiance, phase function, and source terms of the transport equation (eq. (B.1)) in spherical harmonics and evaluating the integral over the solid angle using the orthogonality relations for spherical harmonics,

$$\int Y_{lm}(\theta, \phi) Y_{l',m'}(\theta, \phi) d\Omega = \delta(l - l') \delta(m - m') \tag{B.10}$$

the transport equation can be rewritten as [186]

$$\sum_{l,m} \left[\frac{1}{c} \frac{\partial \phi_{l,m}}{\partial t} + \mu_t^{(l)} \phi_{l,m} - q_{l,m} \right] Y_{l,m}(\hat{s}) + \nabla \cdot (\phi_{l,m} Y_{l,m}(\hat{s}) \hat{s}) = 0 \tag{B.11}$$

where $\mu_t^{(l)} = \mu_s(1-g_l) + \mu_a/g_l$ (note that $\mu_t^{(0)} = \mu_a$) is the coefficient for the lth moment of the normalized phase function. For the Henyey-Greenstein phase function, $g_l = g^l$,

where g is the average cosine of the scattering angle [181]. The P_N approximation is obtained by truncating the expansions in equations (B.5) - (B.7) at $l = N$, where N is the order of approximation. The resulting set of coupled differential equations can be solved to determine the corresponding moments of the radiance.

The P_1 approximation, also known as the diffusion approximation, has been widely used to model photon transport in tissue. With this approximation, only $l = 0, 1$ is considered, and the radiance can be written as [182, 183]

$$L(\vec{r}, \hat{s}, t) = \frac{1}{4\pi}\phi(\vec{r}, t) + \frac{3}{4\pi}J(\vec{r}, t) \cdot \hat{s}, \tag{B.12}$$

where the fluence rate is given by $\phi(\vec{r}) = \int_{4\pi} L(\vec{r}, \hat{s}, t)d\Omega$ and has units of mW/cm^2, and the photon flux (or current density) is given by $J(\vec{r}, t) = \int_{4\pi} L(\vec{r}, \hat{s}, t)\hat{s}d\Omega$ and has units of mW/cm^2.

The source term can be written as [182, 183]

$$S(\vec{r}, \hat{s}, t)\frac{1}{4\pi}S_0(\vec{r}, t) + \frac{3}{4\pi}S_1(\vec{r}, t) \cdot \hat{s}, \tag{B.13}$$

where $S_0(\vec{r}, t)$ and $S_1(\vec{r}, t)$ are the monopole (isotropic) and dipole moments of the source, respectively. By inserting equations (B.12) and (B.13) into equation (B.1) and integrating over $\hat{s}$, we can get [183]

$$\frac{1}{c}\frac{\partial}{\partial t}\phi(\vec{r}, t) + \mu_a\phi(\vec{r}, t) + \nabla \cdot J(\vec{r}, t) = S_0(\vec{r}, t). \tag{B.14}$$

By inserting equations (B.12) and (B.13) into equation (B.1) and multiplying by $\hat{s}$ and then integrating over $\hat{s}$, we can get [183]

$$\frac{1}{c}\frac{\partial}{\partial t}J(\vec{r}, t) + (\mu_s' + \mu_a)J(\vec{r}, t) + \frac{1}{3}\nabla \cdot \phi(\vec{r}, t) = S_1(\vec{r}, t). \tag{B.15}$$

By decoupling equations (B.14) and (B.15) for $\phi(\vec{r}, t)$, the P_1 equation can be obtained [183]

$$-D\nabla^2\phi(\vec{r}, t) + \mu_a\phi(\vec{r}, t) + \frac{1}{c} \cdot \frac{\partial\phi(\vec{r}, t)}{\partial t} + \frac{3D}{c}\left[\mu_a\frac{\partial\phi(\vec{r}, t)}{\partial t} + \frac{1}{c}\frac{\partial^2\phi(\vec{r}, t)}{\partial t^2}\right]$$
$$= S_0(\vec{r}, t) + \frac{3D}{c}\frac{\partial S_0}{\partial t} - 3D\nabla \cdot S_1(\vec{r}, t), \tag{B.16}$$

where the diffuse coefficient is $D = \frac{1}{3(\mu_a+\mu'_s)}$, and the reduced scattering coefficient is given by $\mu'_s = (1 - g)\mu_s$. The standard photon diffusion equation for the P_1 approximation is obtained when certain terms are dropped from equation (B.16). The dipole moment term of the source can be dropped when assuming an isotropic source. Collimated sources are treated as isotropic sources displaced one mean free path into the scattering medium from the collimated source, thus supporting this assumption. The last term on the left-hand side of the equation is dropped as well. In the frequency domain, the time dependence of the source is taken as $e^{-i\omega t}$. When the intensity of the source is sinusoidally modulated, the photon fluence becomes $\phi(\vec{r})e^{-i\omega t}$. The time derivative can be replaced by $-i\omega$ and the rest of the term can be ignored when $3D\omega/c^2 \ll 1$ [183]. This is equivalent to $c\mu'_s/\omega \gg 1$, which means that the scattering frequency $(c\mu'_s)$ must be much larger than the modulation frequency (ω). Given these assumptions, the photon diffusion equation can be rewritten as the following

$$-D\nabla^2\phi(\vec{r}, t) + \mu_a\phi(\vec{r}, t) + \frac{1}{c}\frac{\partial\phi(\vec{r}, t)}{\partial t} = S_0(\vec{r}, t). \tag{B.17}$$

The even-order approximations do not significantly change the degree of anisotropy in the radiance that is modeled, and inconsistencies arise at the boundaries with the solutions [181, 186, 187]. Therefore, the odd-order approximations are widely used. This approximation is good when the albedo, $a = \mu_s/(\mu_s + \mu_a)$, is close to 1, the

phase function is not too anisotropic, and the source-detector separation is large when compared to $1/(\mu_s(a - g_1))$ [186].

In the tissue-non-scattering medium interface, the boundary condition consistent with the P_1 approximation is obtained by integrating equation (B.4) over all angles Ω over 2π [186]

$$\phi(\vec{r}) - 2AD\hat{n} \cdot \nabla\phi = 0, \tag{B.18}$$

where $\hat{n}$ is the normal direction of the boundary, D is the diffusion coefficient, and A is a dimensionless internal reflection coefficient that accounts for the reflectance and transmission because of the mismatch of the indicies of refraction between the two media ($A = 1$ for a matching interface and $A = 2.95$ for an air-tissue interface) [181]. In the scattering-scattering medium boundary with mismatching indices of refraction, the boundary condition consistent with P_1 approximation can be expressed as discontinuous fluence rate, $\phi_1/\phi_2 = (n_1/n_2)^2$, and continuous flux, $D_1\hat{n} \cdot \nabla\phi_1 = D_2\hat{n} \cdot \nabla\phi_2$ [188].

For a point source in an infinite homogeneous medium, the source term becomes $S_0(\vec{r}) = S_0\delta(\vec{r})$, where $\vec{r}$ is the position at which fluence rate is measured and the position of the source is at 0, the origin. The steady-state solution of the fluence rate becomes [181, 189].

$$\phi(\vec{r}) = \frac{S_0}{4\pi Dr} \exp(\mu_{eff} r), \tag{B.19}$$

where r is the distance to the point source and $\mu_{eff} = \sqrt{3\mu_a \cdot (\mu_a + \mu_s')}$.

The P_3 approximation is often necessary in regions of high tissue absorption of proximity to the light source position. For the P_3 approximation, moments greater than $l = 3$ are ignored, so $\phi_{l,m} = 0$ for $l > 3$ in equation (B.11). Equations (B.5) - (B.7) simplify to for a point source in steady-state condition since only the $m = 0$

term needs to be considered because of spherical symmetry.

$$L(\vec{r}, \hat{s}) = \sum_{l=0}^{3} \frac{2l+1}{4\pi} \phi_l(r) P_l(\vec{r}, \hat{s}) \tag{B.20}$$

$$S(\vec{r}, \hat{s}) = \sum_{l=0}^{3} \frac{2l+1}{4\pi} q_l(r) P_l(\vec{r}, \hat{s}) \tag{B.21}$$

$$f(\hat{s}, \hat{s}') = \sum_{l=0}^{3} \frac{2l+1}{4\pi} g_l(r) P_l(\hat{s}, \hat{s}') \tag{B.22}$$

Inserting these into equation (B.1) and ignoring the time-dependent term resulted in (B.11) with $m = 0$ only. Multiplying the resulting equation by P_l and integrating over all solid angles yields the following equation set for ϕ_l in an infinite homogeneous medium [181, 190, 191].

$$\frac{1}{2l+1} \cdot \left\{ \left[(l+1)\frac{\partial \phi_{l+1}}{\partial r} + l\frac{\partial \phi_{l-1}}{\partial r} \right] + \frac{1}{r}[(l+1)(l+2)\phi_{l+1}(r) - l(l-1)\phi_{l-1}(r)] \right\}$$
$$+ \mu_t^{(l)}\phi_l(r) = q_l \tag{B.23}$$

Here, $l = 0, 1, 2, 3$, and the orthogonality properties of the Legendre polynomials were used: $\int P_l(x)P_{l'}(x)dx = \frac{2}{2l+1}\delta(l - l')$. This equation set yields 4 coupled differential equations ($\phi_{-1} = \phi_0 = 0$). The right hand side of equation (B.23) has the moments of the source distribution. We can assume that the source is an isotropic point source such that $q_l = 0$ for $l > 0$, if we are a few scattering lengths from the source. For an infinite medium, the solution of equation (B.23) for ϕ_0, the light fluence rate, has been solved by Hull and foster for an isotropic point source at the

origin $q_0 = \delta(r)$ as [181]

$$\phi_0(r) = \left[\frac{-C_-(\nu^-)^2}{2\pi}\right]\frac{\exp(-\nu^-r)}{(-\nu^-r)} + \left[\frac{-C_+(\nu^+)^2}{2\pi}\right]\frac{\exp(-\nu^+r)}{(-\nu^+r)}, \qquad \text{(B.23)}$$

where

$$C_- = \frac{\nu^{-3}(3\mu_a\mu_t^{(1)} - \nu^{+2})}{6\mu_a^2\mu_t^{(1)}(\nu^{-2} - \nu^{+2})}$$

$$C_+ = \frac{\nu^{-3}(3\mu_a\mu_t^{(1)} - \nu^{-2})}{6\mu_a^2\mu_t^{(1)}(\nu^{+2} - \nu^{-2})}$$

$$\nu^\pm = \left(\frac{\beta \pm \sqrt{\beta^2 - \gamma}}{18}\right)^{1/2}$$

$$\beta = 27\mu_a\mu_t^{(1)} + 28\mu_a\mu_t^{(3)} + 35\mu_t^{(2)}\mu_t^{(3)}$$

$$\gamma = 3780\mu_a\mu_t^{(1)}\mu_t^{(2)}\mu_t^{(3)}$$

Unlike the analytical solution for the P_1 approximation, the analytical solution for the P_3 approximation includes two exponential terms: one rapidly decaying term with an attenuation coefficient ν^- and another slower decaying term with an attenuation coefficient ν^+ that is corresponding to the solution for the P_1 approximation. Under the condition that $\beta \gg \gamma$ and $\mu_t^{(l)} \ll \mu_t^1$, $l = 2, 3$, one has $\mu^+ = \mu_{eff}$ and $C_+ = \mu_{eff}/2\mu_a$ so that the second term takes the same form as equation (B.1.1), as the first term disappears since $\nu^- = 0$ under this condition. For this reason, the second term in equation (B.1.1) is also called the asymptotic solution of P_3 approximation according to Hull and Foster [181].

Appendix C

List of Publications

C.1 Peer Reviewed Publications

1. P. P. Mohapatra, C. O. Chiemezie, A. Kligman, **M. M. Kim**, T. M. Busch, T. C. Zhu, A. Greer, "31P NMR Evidence for Peroxide Intermediates in Lipid Emulsion Photooxidations: Phosphine Substituent Effects in Trapping," *Photochem. Photobiol.* Accepted, in press (2017).
2. R. Penjweini, **M. M. Kim**, T. C. Zhu, "Three-dimensional finite-element based deformable image registration for evaluation of pleural cavity irradiation during photodynamic therapy," *Med. Phys.* 44(7): 3767-3775 (2017).
3. **M. M. Kim**, R. Penjweini, T. C. Zhu, "Evaluation of singlet oxygen explicit dosimetry for predicting treatment outcomes of benzoporphyrin derivative monoacid ring A-mediated photodynamic therapy," *J. Biomed. Opt.* 22(2): 028002 (2017).
4. **M. M. Kim**, A. Ghogare, A. Greer, T. C. Zhu, "On the in vivo photochemical rate parameters for PDT reactive oxygen species modeling," *Phys. Med. Biol.* 62(5): R1-R48 (2017).
5. H. Qiu, **M. M. Kim**, R. Penjweini, J. Finlay, T. M. Busch, T. Wang, W. Guo, K. A. Cengel, C. B. Simone, E. Glatstein, T. C. Zhu, "A Comparison of Dose Metrics to Predict Local Tumor Control for Photofrin-mediated Photodynamic Therapy," *Photochem. Photobiol.* 93(4): 1115-1122 (2017).
6. N. R. Gemmell, A. McCarthy, **M. M. Kim**, I. Veilleux, T. C. Zhu, G. S. Buller, B. C. Wilson, R. H. Hadfield, "A compact fiber-optic probe-based singlet oxygen luminescence detection system," *J. Biophotonics* 10(2): 320-326 (2017).
7. **M. M. Kim**, R. Penjweini, N. R. Gemmell, I. Veilleux, A. McCarthy, G. S. Buller, R. H. Hadfield, B. C. Wilson, T. C. Zhu, "A Comparison of Singlet Oxygen Explicit Dosimetry (SOED) and Singlet Oxygen Luminescence Dosimetry (SOLD) for Photofrin-Mediated Photodynamic Therapy," *Cancers (Basel)* 8(12):

109 (2016).

8. **M. M. Kim**, R. Penjweini, X. Liang, T. C. Zhu, "Explicit macroscopic singlet oxygen modeling for benzoporphyrin derivative monoacid ring A (BPD)-mediated photodynamic therapy," *J. Photochem. Photobiol.* B. 164: 314-322 (2016).

9. R. Penjweini*, **M. M. Kim***, B. Liu, T. C. Zhu, "Evaluation of the 2-(1-Hexyloxyethyl)-2-devinyl pyropheophorbide (HPPH) mediated photodynamic therapy by macroscopic singlet oxygen modeling," *J. Biophotonics* 9(11-12): 1344-1354 (2016). *Authors share equal contribution

10. H. Qiu, **M. M. Kim**, R. Penjweini, T. C. Zhu, "Macroscopic singlet oxygen modeling for dosimetry of Photofrin-mediated photodynamic therapy: an in-vivo study," *J. Biomed. Opt.* 21(8): 88002 (2016).

11. R. Penjweini, B. Liu, **M. M. Kim**, T. C. Zhu , "Explicit dosimetry for 2-(1-hexyloyethyl)-2-devinyl pyropheophorbide-a-mediated photodynamic therapy: macroscopic singlet oxygen modeling," *J. Biomed. Opt.* 20(12): 128003 (2015).

12. T. C. Zhu, X. Liang, **M. M. Kim**, J. C. Finlay, A. Dimofte, C. Rodriguez, C. B. Simone, J. S. Friedberg, K. A. Cengel, "An IR Navigation System for Pleural PDT," *Frontiers in Physics* 3(9): 1-12 (2015).

13. T. C. Zhu, **M. M. Kim**, X. Liang, J. C. Finlay, T. M. Busch, "In-vivo singlet oxygen threshold doses for PDT," *Photon Lasers Med.* 4(1): 59-71 (2015).

C.2   Invited Book Chapter

1. T. C. Zhu, B. Liu, **M. M. Kim**, "Dynamic Processes in Photodynamic Therapy" in *Computational Bioengineering*, Guigen Zhang Ed., CRC Press, May 2015.

C.3   Conference Proceedings

1. **M. M. Kim**, R. Penjweini, Y. H. Ong, J. C. Finlay, T. C. Zhu, "Oxygen measurements to improve singlet oxygen explicit dosimetry," *Proc. SPIE.* 10047: 100470A-1-7 (2017).

2. T. C. Zhu, **M. M. Kim**, Y. H. Ong, R. Penjweini, A. Dimofte, J. C. Finlay, C. E. Rodriguez, K. A. Cengel, "A summary of light dose distribution using an IR navigation system for Photofrin-mediated pleural PDT," *Proc. SPIE.* 10047: 1004709-1-7 (2017).

3. Y. H. Ong, **M. M. Kim**, C. E. Rodriguez, A. Dimofte, J. C Finlay, T. M. Busch, A. G. Yodh, K. A. Cengel. S. Singhal, T. C. Zhu, "Monitoring and assessment of tumor hemodynamic responses during pleural photodynamic therapy," *Proc. SPIE.* 10047: 100470C-1-7 (2017).

4. **M. M. Kim**, R. Penjweini, Y. H. Ong, T. C. Zhu, "Singlet oxygen explicit dosimetry to predict long-term local tumor control for BPD-mediated photodynamic therapy," *Proc. SPIE.* 10047: 100470X-1-8 (2017).

5. R. Penjweini, **M. M. Kim**, Y. H. Ong, T. C. Zhu, "Singlet oxygen explicit dosimetry to predict local tumor control for HPPH-mediated photodynamic therapy," *Proc. SPIE.* 10047: 1004710-1-8 (2017).

6. R. Penjweini, **M. M. Kim**, Y. H. Ong, T. C. Zhu, "Singlet oxygen explicit dosimetry to predict local tumor control for Photofrin-mediated photodynamic therapy," *Proc. SPIE.* 10047: 1004711-1-8 (2017).

7. Y. H. Ong, **M. M. Kim**, J. C. Finlay, A. Dimofte, K. A. Cengel, T. C. Zhu, "Four-Channel PDT Dose Dosimetry for Pleural Photodynamic Therapy," *Proc. SPIE.* 10047: 1004717-1-9 (2017).

8. **M. M. Kim**, R. Penjweini, N. R. Gemmell, I. Veilleux, A. McCarthy, G. Buller, R. H. Hadfield, B. C. Wilson, T. C. Zhu, "A feasibility study of singlet oxygen explicit dosimetry (SOED) of PDT by intercomparison with a singlet oxygen luminescence dosimetry (SOLD) system," *Proc. SPIE.* 9694: 969406-1-9 (2016).

9. **M. M. Kim**, A. Darafsheh, M. Ahmad, J. C. Finlay, T. C. Zhu, "PDT dose dosimeter for pleural photodynamic therapy," *Proc. SPIE.* 9694: 96940Y-1-6 (2016).

10. **M. M. Kim**, R. Penjweini, J. C. Finlay, T. C. Zhu, "Determination of the low concentration correction in the macroscopic singlet oxygen model for PDT," *Proc. SPIE.* 9694: 96940D-1-6 (2016).

11. R. Penjweini, **M. M. Kim**, J. C. Finlay, T. C. Zhu, "Investigating the impact of oxygen concentration and blood flow variation on photodynamic therapy," *Proc. SPIE.* 9694: 96940L-1-7 (2016).

12. R. Penjweini, **M. M. Kim**, A. Dimofte, J. C. Finlay, T. C. Zhu, "Deformable medical image registration of pleural cavity for photodynamic therapy by using finite-element based method," *Proc. SPIE.* 9701: 970106-1-7 (2016).

13. H. Qiu, **M. M. Kim**, R. Penjweini, T. C. Zhu, "Dosimetry study of PHOTOFRIN-mediated photodynamic therapy in a mouse tumor model," *Proc. SPIE.* 9694: 96940T-1-7 (2016).

14. R. Penjweini, **M. M. Kim**, T. C. Zhu, "Modeling of the Singlet Oxygen Distribution in Photofrin-Photodynamic Therapy of the Pleural Cavity," Proc. COMSOL, Bioscience and Bioengineering, USA: 1-5 (2015).

15. **M. M. Kim**, R. Penjweini, T. C. Zhu, "In vivo outcome study of BPD-mediated PDT using a macroscopic singlet oxygen model," *Proc. SPIE.* 9308: 93080A-1 8 (2015).

16. R. Penjweini, **M. M. Kim**, T. C. Zhu, "In-vivo outcome study of HPPH mediated PDT using singlet oxygen explicit dosimetry (SOED)," *Proc. SPIE.* 9308: 93080N-1-6 (2015).

17. **M. M. Kim**, J. C. Finlay, T. C. Zhu, "Macroscopic singlet oxygen model incorporating photobleaching as an input parameter," *Proc. SPIE.* 9308: 93080V-1-6 (2015).

18. T. C. Zhu, **M. M. Kim**, S. L. Jacques, R. Penjweini, A. Dimofte, J. C. Finlay, C. B. Simone II, K. A. Cengel, J. Friedberg, "Real-time treatment light dose guidance of Pleural PDT: an update," *Proc. SPIE.* 9308: 930809-1-6 (2015).

19. **M. M. Kim**, X. Liang, T. C. Zhu, "Anisotropic modeling for IR navigation-based PDT dosimetry," *Proc. SPIE.* 8931: 893118-1-6 (2014).

20. **M. M. Kim**, B. Liu, J. Miller, T. M. Busch, T. C. Zhu, "Parameter determination for BPD mediated vascular PDT," *Proc. SPIE.* 8931: 89311D-1-6 (2014).

21. T. C. Zhu, B. Liu, **M. M. Kim**, D. D. McMillan, J. C. Finlay, T. M. Busch, "Comparison of singlet oxygen threshold dose for PDT," *Proc. SPIE.* 8931: 89310I-1-10 (2014).

22. B. Liu, **M. M. Kim**, S. M. Gallagher-Colombo, T. M. Busch, T. C. Zhu, "Comparison of PDT parameters for RIF and H460 tumor models during HPPH-mediated PDT," *Proc. SPIE.* 8931: 89311C-1-6 (2014).

23. **M. M. Kim**, T. C. Zhu, "A novel near real-time laser scanning device for geometrical determination of pleural cavity surface," *Proc. SPIE.* 8568: 856812-1-7 (2013).

24. B. Liu, **M. M. Kim**, T. C. Zhu, "A theoretical comparison of macroscopic and microscopic modeling of singlet oxygen during Photofrin and HPPH mediated PDT," *Proc. SPIE.* 8568: 856805-1-12 (2013).

25. D. D. McMillan, D. Chen, **M. M. Kim**, X. Liang, T. C. Zhu, "Parameter determination for singlet oxygen modeling of BPD-mediated PDT," *Proc. SPIE.* 8568: 856810-1-8 (2013).

26. T. C. Zhu, **M. M. Kim**, X. Liang, B. Liu, J. L. Meo, J. C. Finlay, A. Dimofte, C. Rodriguez, C. B. Simone, K. A. Cengel, J. S. Friedberg, "Real-time treatment feedback guidance of pleural PDT," *Proc. SPIE.* 8568: 86580O-1-6 (2013).

References

[1] T. J. Dougherty, "Photodynamic Therapy," *Photochem. Photobiol.* 58(6), 896–900 (1993).

[2] M. R. Stringer, C. J. Kelty, and S. B. Brown, "Light dosimetry measurements during ALA-PDT of Barrett's oesophagus," *Photodiagn. Photodyn.* 3(1), 19–26 (2006).

[3] T. J. Dougherty, C. J. Gomer, et al., "Photodynamic therapy," *J. Natl. Cancer Inst.* 90(12), 889–905 (1998).

[4] J. Usuda, H. Kato, et al., "Photodynamic therapy (PDT) for lung cancers," *J. Thorac. Oncol.* 1(5), 489–493 (2006).

[5] N. C. Zeitouni, A. R. Oseroff, and S. Shieh, "Photodynamic therapy for non-melanoma skin cancers: Current review and update," *Mol. Immunol.* 39(17-18), 1133–1136 (2003).

[6] R. R. Allison, H. C. Mota, and C. H. Sibata, "Clinical PD/PDT in North America: an historical review," *Photodiagn. Photodyn.* 1(4), 263–277 (2004).

[7] U. Schmidt-Erfurth and T. Hasan, "Mechanisms of action of photodynamic therapy with verteporfin for the treatment of age-related macular degeneration," *Surv. Ophthalmol.* 45(3), 195–214 (2000).

[8] A. Johansson, J. Svensson, et al., "mTHPC pharmacokinetics following topical administration," *Proc. SPIE* 6094, 6094C–1–C–8 (2006).

[9] J. P. A. Marijnissen, W. M. Star, et al., "In situ light dosimetry during whole bladder wall photodynamic therapy: clinical results and experimental verification," *Phys. Med. Biol.* 38(5), 567–582 (1993).

[10] J. C. Finlay, T. C. Zhu, et al., "Interstitial Fluorescence Spectroscopy in the Human Prostate During Motexafin Lutetium-Mediated Photodynamic Therapy," *Photochem. Photobiol.* 82, 1270–1278 (2006).

[11] U. Sunar, D. Rohrbach, et al., "Monitoring photobleaching and hemodynamic responses to hpph-mediated photodynamic therapy of head and neck cancer: a case report," *Opt. Express* 18(14), 14969–14978 (2010).

[12] S. M. Hahn, R. P. Smith, and J. S. Friedberg, "Photodynamic Therapy for Mesothelioma," *Curr. Treat. Options Oncol.* 2, 375–383 (2001).

[13] J. S. Friedberg, M. J. Culligan, et al., "Radical pleurectomy and intraoperative photodynamic therapy for malignant pleural mesothelioma," *Ann. Thorac. Surg.* 93(5), 1658–1667 (2012).

[14] J. Moan, "Porphyrin photosensitization and phototherapy," *Photochem. Photobiol.* 43(6), 681–690 (1986).

[15] M. T. Jarvi, M. J. Niedre, et al., "Singlet Oxygen Luminescence Dosimetry (SOLD) for Photodynamic Therapy: Current Status, Challenges and Future Prospects," *Photochem. Photobiol.* 82, 1198–1210 (2006).

[16] B. C. Wilson, M. S. Patterson, and L. Lilge, "Implicit and explicit dosimetry in photodynamic therapy: a new paradigm," *Laser. Med. Sci.* 12(4), 182–199 (1997).

[17] D. R. Braichotte, G. A. Wagnieres, et al., "Clinical Pharmacokinetic Studies of Photofrin by Fluorescences Spectroscopy in the Oral Cavity, the Esophagus, and the Bronchi," *Cancer* 75(11), 2768–2778 (1995).

[18] J. L. Sandell and T. C. Zhu, "A review of in-vivo optical properties of human tissues and its impact on PDT," *J. Biophoton.* 4(11-12), 773–787 (2011).

[19] W.-F. Cheong, S. A. Prahl, and A. J. Welch, "A Review of the Optical Properties of Biological Tissues," *IEEE J. Quant.* 26(12), 2166–2185 (1990).

[20] H. B. Stone, M. Brown, et al., "Oxygen in Human Tumors: Correlations between Methods of Measurements and Response to Therapy," *Radiat. Res.* 136, 422–434 (1993).

[21] B. C. Wilson, M. S. Patterson, and D. M. Burns, "Effect of photosensitizer concentration in tissue on the penetration depth of photoactivating light," *Lasers Med. Sci.* 1(4), 235–244 (1986).

[22] T. H. Foster, R. S. Murant, et al., "Oxygen Consumption and Diffusion Effects in Photodynamic Therapy," *Radiat. Res.* 126, 296–303 (1991).

[23] T. H. Foster, D. F. Hartley, et al., "Fluence Rate Effects in Photodynamic Therapy of Multicell Tumor Spheroids," *Cancer Res.* 53, 1249–1254 (1993).

[24] T. M. Sitnik, J. A. Hampton, and B. W. Henderson, "Reduction of tumour oxygenation during and after photodynamic therapy in vivo: effects of fluence rate," *Br. J. Cancer* 77(9), 1386–1394 (1998).

[25] B. H. Henderson, T. M. Busch, and J. W. Snyder, "Fluence Rate as a Modulator of PDT Mechanisms," *Lasers Surg. Med.* 38, 489–493 (2006).

[26] J. S. Friedberg, "Photodynamic therapy as an innovative treatment for malignant pleural mesothelioma," *Semin. Thorac. Cardiovasc. Surg.* 21(2), 177–187 (2009).

[27] T. C. Zhu, M. M. Kim, et al., "In-vivo singlet oxygen threshold doses for PDT," *Photon Lasers Med.* 4(1), 59–71 (2015).

[28] X.-H. Hu, Y. Feng, et al., "Modeling of a Type II Photofrin-mediated Photodynamic Therapy Process in a Heterogeneous Tissue Phantom," *Photochem. Photobiol.* 81, 1460–1468 (2005).

[29] F. Wilkinson and J. G. Brummer, "Rate Constants for the Decay and Reactions of the Lowest Electronically Excited Singlet State of Molecular Oxygen in Solution," *J. Phys. Chem. Ref. Data* 10(4), 809–999 (1981).

[30] T. C. Zhu, J. C. Finlay, et al., "Macroscopic modeling of the singlet oxygen production during PDT," *Proc. SPIE* 6427, 1–12 (2007).

[31] H. J. C. M. Sterenborg and M. J. C. van Gemert, "Photodynamic therapy with pulsed light sources: a theoretical analysis," *Phys. Med. Biol.* 41, 835–849 (1996).

[32] F. Wilkinson, W. P. Helman, and A. B. Ross, "Quantum yields for the photosensitized formation of the lowest electronically excited singlet state of molecular oxygen in solution," *J. Phys. Chem. Ref. Data* 22(1), 113–262 (1993).

[33] K. Plaetzer, B. Krammer, et al., "Photophysics and photochemistry of photodynamic therapy: fundamental aspects," *Lasers Med. Sci* 24(2), 259–68 (2009).

[34] M. M. Kim, A. A. Ghogare, et al., "On the in vivo photochemical rate parameters for PDT reactive oxygen species modeling," *Phys. Med. Biol.* 62(5), R1–R48 (2017).

[35] M. Kasha, "Singlet Oxygen Electronic Structure and Energy Transfer," in A. A. Frimer, editor, "Singlet O2," volume 1, pp. 1–12, CRC Press, Boca Raton, FL (1985).

[36] A. Greer, A. T. Balaban, and J. F. Liebman, *The Chemistry of Peroxides*, volume 3, Wiley (2014).

[37] D. Weldon, T. D. Poulsen, et al., "Singlet Sigma: The "Other" Singlet Oxygen in Solution," *Photochem. Photobiol.* 70(4), 369–379 (1999).

[38] M. A. J. Rodgers and P. C. Lee, "Singlet Molecular Oxygen in Micellar Systems. 2. Quenching Behavior in AOT Reverse Micelles," *J. Phys. Chem.* 88(16), 3480–3484 (1984).

[39] J. Catalan, C. Diaz, and L. Barrio, "Analysis of mixed solvent effects on the properties of singlet oxygen (1?g)," *Chem. Phys.* 300(1-3), 33–39 (2003).

[40] L. Musbat, H. Weitman, and B. Ehrenberg, "Azide Quenching of Singlet Oxygen in Suspensions of Microenvironments of Neutral and Surface Charged Liposomes and Micelles," *Photochem. Photobiol.* 89, 253–258 (2013).

[41] C. Lambert and R. W. Redmond, "Triplet energy level of β-carotene," *Chem. Phys. Lett.* 228(4-5), 495–498 (1994).

[42] J. C. Finlay, D. L. Conover, et al., "Porphyrin Bleaching and PDT-induced Spectral Changes are Irradiance Dependent in ALA-sensitized Normal Rat Skin In Vivo," *Photochem. Photobiol.* 73(1), 54–63 (2001).

[43] K. K. Wang, S. Mitra, and T. H. Foster, "A comprehensive mathematical model of microscopic dose deposition in photodynamic therapy," *Med. Phys.* 34(1), 282–293 (2007).

[44] K. K. Wang, J. C. Finlay, et al., "Explicit dosimetry for photodynamic therapy: macroscopic singlet oxygen modeling," *J. Biophoton.* 3(5-6), 304–318 (2010).

[45] M. A. Weston and M. S. Patterson, "Calculation of Singlet Oxygen Dose Using Explicit and Implicit Dose Metrics During Benzoporphyrin Derivative Monoacid Ring A (BPD-MA)-PDT In Vitro and Correlation with MLL Cell Survival," *Photochem. Photobiol.* 87, 1129–1137 (2011).

[46] M. M. Kim, A. Darafsheh, et al., "PDT Dose Dosimeter for Pleural Photodynamic Therapy," *Proc. SPIE* 9694, 96940Y–1–6 (2016).

[47] T. C. Zhu, B. Liu, and M. M. Kim, "Computer models of the dynamic processes in photodynamic therapy," in G. Zhang, editor, "Computational Bioengineering," pp. 231–264, CRC Taylor & Francis (2015).

[48] T. C. Zhu, B. Liu, and R. Penjweini, "Study of tissue oxygen supply rate in a macroscopic photodynamic therapy singlet oxygen model," *J. Biomed. Opt.* 20(3), 038001 (2015).

[49] T. C. Zhu and B. Liu, "Singlet Oxygen Modeling of PDT incorporating Local Vascular Oxygen Diffusion," *Proc. COMSOL User Conference* pp. 1–4 (2013).

[50] J. C. Finlay, S. Mitra, et al., "Photobleaching kinetics of Photofrin in vivo and in multicell tumour spheroids indicate two simultaneous bleaching mechanisms," *Phys. Med. Biol.* 49, 4837–60 (2004).

[51] J. Moan and K. Berg, "The photodegradation of porphyrins in cells can be used to estimate the lifetime of singlet oxygen," *Photochem. Photobiol.* 53(4), 549–553 (1991).

[52] M. J. Niedre, M. S. Patterson, and B. C. Wilson, "Direct Near-infrared Luminescence Detection of Singlet Oxygen Generated by Photodynamic Therapy in Cells In Vitro and Tissues In Vivo," *Photochem. Photobiol.* 75(4), 382–391 (2002).

[53] J. S. Dysart and M. S. Patterson, "Characterization of Photofrin photobleaching for singlet oxygen dose estimation during photodynamic therapy of MLL cells in vitro," *Phys. Med. Biol.* 50, 2597–2616 (2005).

[54] J. S. Dysart, G. Singh, and M. S. Patterson, "Calculation of singlet oxygen dose from photosensitizer fluorescence and photobleaching during mTHPC photodynamic therapy of MLL cells," *Photochem. Photobiol.* 81, 196–205 (2005).

[55] J. N. Demas and G. A. Crosby, "The Measurement of Photoluminescence Quantum Yields. Review," *J. Phys. Chem.* 75(8), 991–1024 (1971).

[56] R. Bensasson, C. Chachaty, et al., "Nanosecond irradiation studies of biological molecules - I. coenzyme Q 6 (ubiquinone-30)," *Photochem. Photobiol.* 16, 27–37 (1972).

[57] S. J. Strickler and R. A. Berg, "Relationship between abosorption intensity and fluorescence lifetime of molecules," *J. Chem. Phys.* 37(4), 814–822 (1962).

[58] J. S. Dysart and M. S. Patterson, "Photobleaching kinetics, photoproduct formation, and dose estimation during ALA induced PpIX PDT of MLL cells under well oxygenated and hypoxic conditions," *Photochem. Photobiol. Sci.* 5(1), 73–81 (2006).

[59] A. Walsh, "The application of atomic absorption spectra to chemical analysis," *Spectrochim. A.* 7, 108–117 (1955).

[60] K. Fuwa and B. L. Valle, "The Physical Basis of Analytica Atomic Absorption Spectrometry. The Pertinence of the Beer-Lambert Law," *Anal. Chem.* 35(8), 942–946 (1963).

[61] B. M. Aveline, R. M. Sattler, and R. W. Redmond, "Environmental Effects on Cellular Photosensitization: Correlation of Phototoxicity Mechanism with Transient Absorption Spectroscopy Measurements," *Photochem. Photobiol.* 68(1), 51–62 (1998).

[62] M. Krieg, M. B. Srichai, and R. W. Redmond, "Photophysical properties of 3, 3?-dialkylthiacarbocyanine dyes in organized media: unilamellar liposomes and thin polymer films," *Biochim. Biophys. Acta* 1151(2), 168–174 (1993).

[63] M. Krieg and R. W. Redmond, "Photophysical properties of 3,3'-dialkylthiacarbocyanine dyes in homogeneous solution," *Photochem. Photobiol.* 57(3), 472–479 (1993).

[64] K. Konig, H. Schneckenburger, et al., "In vivo photoproduct formation during PDT with ALA induced endogenous porphyrins," *J. Photochem. Photobiol. B.* 18(2-3), 287–290 (1993).

[65] D. J. Robinson, H. S. de Bruijn, et al., "Fluorescence Photobleaching of ALA-induced Protoporphyrin IX during Photodynamic Therapy of Normal Hairless Mouse Skin: The Effect of Light Dose and Irradiance and the Resulting Biological Effect," *Photochem. Photobiol.* 67(1), 140–149 (1998).

[66] B. M. Aveline, T. Hasan, and R. W. Redmond, "Photophysical and photosensitizing properties of benzoporphyrin derivative monoacid ring A (BPD-MA)," *Photochem. Photobiol.* 59(3), 328–35 (1994).

[67] S. Kim, T. Y. Ohulchanskyy, et al., "Organically modified silica nanoparticles co-encapsulating photosensitizing drug and aggregation-enhanced two-photon absorbing fluorescent dye aggregates for two-photon photodynamic therapy," *J. Am. Chem. Soc.* 129(9), 2669–2675 (2007).

[68] J. Wezgowiec, M. B. Derylo, et al., "Electric field-assisted delivery of photofrin to human breast carcinoma cells," *J. Membrane Biol.* 246(10), 725–735 (2013).

[69] J. R. Lakowicz, H. Szmacinski, et al., "Fluorescence lifetime imaging," *Anal. Biochem.* 202(2), 316–330 (1992).

[70] M. Kress, T. Meier, et al., "Time-resolved microspectrofluorometry and fluorescence lifetime imaging of photosensitizers using picosecond pulsed diode lasers in laser scanning microscopes," *J. Biomed. Opt.* 8(1), 26–32 (2003).

[71] A. U. Khan and M. Kasha, "Red Chemiluminescence of Molecular Oxygen in Aqueous Solution," *J. Chem. Phys.* 39, 2105–2106 (1963).

[72] A. U. Khan and M. Kasha, "Rotational Structure in the Chemiluminescence Spectrum of Molecular Oxygen in Aqueous Systems," *Nature* 204, 241–243 (1964).

[73] A. U. Khan and M. Kasha, "Chemiluminescence arising from simultaneous transitions in pairs of singlet oxygen molecules," *J. Am. Chem. Soc.* 92(11), 3293–3300 (1970).

[74] S. J. Arnold, E. A. Ogryzlo, and H. Witzke, "Some New Emission Bands of Molecular Oxygen," *J. Chem. Phys.* 40, 1769–1770 (1964).

[75] J. S. Arnold, R. J. Browne, and E. A. Ogryzlo, "The red emission bands of molecular oxygen," *Photochem. Photobiol.* 4(6), 963–969 (1965).

[76] A. A. Krasnovskii, "Photosensitized Luminescence of Singlet Oxygen in Solution," *Biofizika* 21(4), 748–749 (1976).

[77] A. U. Khan and M. Kasha, "Direct spectroscopic observation of singlet oxygen emission at 1268 nm excited by sensitizing dyes of biological interest in liquid solution," *Proc. Nat. Acad. Sci.* 76(12), 6047–6049 (1979).

[78] J. R. Hurst, J. D. McDonald, and G. B. Schuster, "Lifetime of singlet oxygen in solution directly determined by laser spectroscopy," *J. Am. Chem. Soc.* 104(7), 2065–2067 (1982).

[79] J. R. Kanofsky, "Quenching of singlet oxygen by human plasma," *Photochem. Photobiol.* 51(3), 299–303 (1990).

[80] R. Higgins, C. S. Foote, and H. Cheng, "Chemistry of Singlet Oxygen," in R. F. Gould, editor, "Advances in Chemistry," volume 77, pp. 102–117, American Chemical Society, Washington D. C. (1968).

[81] E. L. Clennan, P. Dobrowolski, and A. Greer, "Reaction of Singlet Oxygen with Thietane. A Novel Example of a Self-Catalyzed Reaction Which Provides Evidence for a Thiadioxirane Intermediate," *J. Am. Chem. Soc.* 117(39), 9800–9803 (1995).

[82] J. A. Celaje, D. Zhang, et al., "Chemistry of trans-Resveratrol with Singlet Oxygen: [2 + 2] Addition, [4 + 2] Addition, and Formation of the Phytoalexin Moracin M," *Org. Lett.* 13(18), 4846–4849 (2011).

[83] J. M. Wessels and M. A. J. Rodgers, "Detection of the O2(l?g)-O2(3?g-1) transition in Aqueous Environments: A Fourier-transform near-infrared luminescence study," *J. Phys. Chem.* 99, 15725–15727 (1995).

[84] C. Marti, S. Nonell, et al., "Photophysical Properties of Neutral and Cationic Tetrapyridinoporphyrazines," *Phochem. Photobiol.* 71(1), 53–59 (2000).

[85] N. R. Gemmell, A. McCarthy, et al., "A compact fiber-optic probe-based singlet oxygen luminescence detection system," *J. Biophoton.* 10, 320–326 (2017).

[86] P. R. Ogilby and C. S. Foote, "Chemistry of singlet oxygen. 42. Effect of solvent, solvent isotopic substitution, and temperature on the lifetime of singlet molecular oxygen (1?g)," *J. Am. Chem. Soc.* 105, 3423–3430 (1983).

[87] R. L. Jensen, J. Arnbjerg, and P. R. Ogilby, "Temperature effects on the solvent-dependent deactivation of singlet oxygen," *J. Am. Chem. Soc.* 132(8098-8105) (2010).

[88] R. D. Shonat and A. C. Kight, "Oxygen tension imaging in the mouse retina," *Ann. Biomed. Eng.* 31, 1084–1096 (2003).

[89] D. C. Poole, B. J. Behnke, et al., "Measurement of muscle microvascular oxygen pressures: Compartmentalization of phosphorescent probe," *Microcirculation* 11, 317–326 (2004).

[90] T. Hirano, E. Kohno, and M. Nishiwaki, "Detection of near infrared emission from singlet oxygen in PDT with an experimental tumor bearing mouse," *J. Jpn. Soc. Laser Surg. Med.* 22, 99–108 (2002).

[91] K. R. Weishaupt, C. J. Gomer, and T. J. Dougherty, "Identification of singlet oxygen as the cytotoxic agent in photo-activation of a murine tumor," *Can. Res.* 36, 2326–2392 (1976).

[92] E. L. Clennan and C. S. Foote, "Endoperoxides," in W. Ando, editor, "Organic Peroxides," pp. 255–318, Wiley, Chichester, UK (1992).

[93] J.-M. Aubry, C. Pierlot, et al., "Reversible bindig of oxygen to aromatic compounds," *Acc. Chem. Res.* 36(9), 668–675 (2003).

[94] H. Kotani, K. Ohkubo, and S. Fukuzumi, "Photocatalytic oxygenation of anthracenes and olefins with dioxygen via selective radical coupling using 9-mesityl-10-methylacridinium ion as an effective electron-transfer photocatalyst." *J. Am. Chem. Soc.* 126(49), 15999–16006 (2004).

[95] K. Ohkubo, T. Nanjo, and S. Fukuzumi, "Efficient photocatalytic oxygenation of aromatic alkene to 1,2-dioxetane with oxygen via electron transfer," *Org. Lett.* 7(19), 4265–4268 (2005).

[96] G. D. Ouedraogo and R. W. Redmond, "Secondary Reactive Oxygen Species Extend the Range of Photosensitization Effects in Cells: DNA Damage Produced Via Initial Membrane Photosensitization," *Photochem. Photobiol.* 77(2), 192–203 (2003).

[97] A. Chakraborty, K. D. Held, et al., "Bystander Effects Induced by Diffusing Mediators after Photodynamic Stress," *Radiat. Res.* 172(1), 74–81 (2009).

[98] X. Ragas, A. Jimenez-Banzo, et al., "Singlet oxygen photosensitisation by the fluorescent probe Singlet Oxygen Sensor Green," *Chem. Commun.* 20, 2920–2922 (2009).

[99] S. Kim, T. Tachikawa, et al., "Far-Red Fluorescence Probe for Monitoring Singlet Oxygen during Photodynamic Therapy," *J. Am. Chem. Soc.* 136(33), 11707–11715 (2014).

[100] S. K. Pedersen, J. Jolmehave, et al., "Aarhus Sensor Green: A Fluorescent Probe for Singlet Oxygen," *J. Org. Chem* 79(7), 3079–3087 (2014).

[101] A. Baumstark, *Advances in Oxygenated Processes*, Advances in Oxygenated Processes, JAI Press, Greenwich, CT (1988).

[102] W. Adam and A. V. Trofimov, "Contemporary trends in dioxetane chemistry," in Z. Rappoport, editor, "Chemistry of Peroxides, 2 (Pt. 2)," pp. 1171–1209, John Wiley and Sons, Inc. (2006).

[103] N. J. Turro, V. Ramamurthy, and J. C. Scaiano, *Modern Molecular Photochemistry of Organic Molecules*, University Science Book, Sausalito, CA (2010).

[104] A. Gollmer, J. Arnbjerg, et al., "Singlet Oxygen Sensor Green: Photchemical Behavior in Solution and in a Mammalian Cell," *Photochem. Photobiol.* 87, 671–679 (2011).

[105] H. Lin, Y. Shen, et al., "Feasibility Study on Quantitative Measurements of Singlet Oxygen Generation Using Singlet Oxygen Sensor Green," *J. Fluoresc.* 23, 41–47 (2013).

[106] K. Setsukinai, Y. Urano, et al., "Development of Novel Fluorescence Probes That Can Reliably Detect Reactive Oxygen Species and Distinguish Specific Species," *J. Biol. Chem.* 278(5), 3170–3175 (2003).

[107] M. Price, J. J. Reiners, et al., "Monitoring Singlet Oxygen and Hydroxyl Radical Formation with Fluorescent Probes During Photodynamic Therapy," *Photochem. Photobiol.* 85, 1177–1181 (2009).

[108] M. Price, L. Heilbrun, and D. Kessel, "Effects of the Oxygenation level on Formation of Different Reactive Oxygen Species During Photodynamic Therapy," *Photochem. Photobiol.* 89(3), 683–686 (2013).

[109] L. Yuan, W. Lin, and J. Song, "Ratiometric fluorescent detection of intracellular hydroxyl radicals based on a hybrid coumarincyanine platform," *Chem. Commun.* 46, 7930–7932 (2010).

[110] N. B. Yapici, S. Jockusch, et al., "New Rhodamine Nitroxide Based Fluorescent Probes for Intracellular Hydroxyl Radical Identification in Living Cells," *Org. Lett.* 14(1), 50–53 (2012).

[111] L. Meng, Y. Wu, and T. Yi, "A ratiometric fluorescent probe for the detection of hydroxyl radicals in living cells," *Chem. Commun.* 50, 4843–4845 (2014).

[112] Z. Huang, "A review of progress in clnical photodynamic therapy," *Technol. Cancer Res. Treat.* 4, 283–93 (2005).

[113] P. Agostinis, K. Berg, et al., "Photodynamic therapy of cancer: an update," *CA Cancer J. Clin* 61, 250–81 (2011).

[114] E. W. B. Jeffes, "Levulan: the first approved topical photosensitizer for the treatment of actinic keratosis," *J. Dermatol. Treat.* 13, s19–s23 (2002).

[115] A. Lapini, A. Minervini, et al., "A comparison of hexaminolevulinate (Hexvix®) fluorescence cystoscopy and white-light cystoscopy for detection of bladder cancer: results of the HeRo observational study," *Surg. Endosc.* 26(12), 3634–3641 (2012).

[116] T. D. Mody, "Pharmaceutical development and medical applications of porphyrin-type macrocycles," *J. Porphyrins Phthalocyanines* 4(4), 362–367 (2000).

[117] R. Penjweini, B. Liu, et al., "Explicit dosimetry for 2-(1-Hexyloxyethyl)-2-devinyl pyropheophorbide-a (HPPH) mediated photodynamic therapy: macroscopic singlet oxygen modeling," *J. Biomed. Opt.* 20(12), 128003 (2015).

[118] T. C. Zhu, B. Liu, et al., "Comparison of singlet oxygen threshold doses for PDT," *Proc. SPIE* 8931, 89310I–1–10 (2014).

[119] D. D. McMillan, D. Chen, et al., "Parameter determination for singlet oxygen modeling of BPD-mediated PDT," *Proc. SPIE* 8568, 856810 (2013).

[120] M. M. Kim, R. Penjweini, et al., "Explicit macroscopic singlet oxygen modeling for benzoporphyrin derivative monoacid ring A (BPD)-mediated photodynamic therapy," *J. Photochem. Photobiol. B.* 164, 314–322 (2016).

[121] M. M. Kim, B. Liu, et al., "Parameter determination for BPD-mediated vascular PDT," *Proc. SPIE* 8931, 89311D–1–6 (2014).

[122] R. Bonnet, C. Lambert, et al., "The triplet and radical species of hematoporphyrin and some of its radical species," *Photochem. Photobiol.* 38, 1–8 (1983).

[123] J. A. Russell, K. R. Diamond, et al., "Characterization of Fluorescence Lifetime of Photofrin and Delta-Aminolevulinic Acid Induced Protoporphyrin IX in Living Cells Using Single- and Two-Photon Excitation," *IEEE J. Sel. Top. Quant. Electron.* 14(1), 158–166 (2008).

[124] S. Mitra and T. H. Foster, "Photophysical Parameters, Photosensitizer Retention and Tissue Optical Properties Completely Account for the Higher Photodynamic Efficacy of meso-Tetra-Hydroxyphenyl-Chlorin vs Photofrin," *Photochem. Photobiol.* 81, 849–859 (2005).

[125] I. Georgakoudi, M. G. Nichols, and T. H. Foster, "The Mechanism of Photofrin Photobleaching and Its Consequences for Photodynamic Dosimetry," *Photochem. Photobiol.* 65(1), 135–144 (1997).

[126] M. M. Kim, R. Penjweini, and T. C. Zhu, "Evaluation of singlet oxygen explicit dosimetry (SOED) for predicting treatment outcomes of benzoporphyrin derivative monoacid ring A (BPD-MA)-mediated photodynamic therapy," *J. Biomed. Opt.* 22(2), 028002 (2017).

[127] J. F. Lovell, T. W. Liu, et al., "Activatable Photosensitizers for imaging and therapy," *Chem Rev* 110, 2839–2857 (2010).

[128] J. M. Fernandez, M. D. Bilgin, and L. I. Grossweiner, "Singlet oxygen generation by photodynamic agents," *J. Photochem. Photobiol. B.* 37, 131–140 (1997).

[129] R. W. Redmond and J. N. Gamlin, "A Compilation of Singlet Oxygen Yields from Biologically Relevant Molecules," *Photochem. Photobiol.* 70(4), 391–475 (1999).

[130] M. M. Kim, R. Penjweini, et al., "A Comparison of Singlet Oxygen Explicit Dosimetry (SOED) and Singlet Oxygen Luminescence Dosimetry (SOLD) for Photofrin-Mediated Photodynamic Therapy," *Cancers* 8(12), 109 (2016).

[131] C. Tanielian, L. Golder, and C. Wolff, "Production and quenching of singlet oxygen by the sensitizer in dye-sensitized photo-oxygenations," *J. Photochem.* 25(2), 117–125 (1984).

[132] P. C. C. Lee and M. A. J. Rodgers, "Laser flash photokinetic studies of rose bengal sensitized photodynamic interactions of nucleotides and DNA," *Photochem. Photobiol.* 45(1), 79–86 (1987).

[133] G. R. Fleming, A. W. E. Knight, et al., "Picosecond fluorescence studies of xanthene dyes," *J. Am. Chem. Soc.* 99(13), 4306–4311 (1977).

[134] L. E. Cramer and K. G. Spears, "Hydrogen Bond Strengths from Solvent-Dependent Lifetimes of Rose Bengal Dye," *J. Am. Chem. Soc.* 100(1), 221–227 (1978).

[135] J. Paczkowski, J. J. M. Lamberts, et al., "Photophysical properties of rose bengal and its derivatives (XII)," *J. Free Radic. Biol. Med.* 1(5), 341–351 (1985).

[136] E. Gandin, Y. Lion, and A. Van de Vorst, "Quantum yield of singlet oxygen production by xanthene derivatives," *Photochem. Photobiol.* 37(3), 271–278 (1983).

[137] W. M. Star, "The relationship between integrating sphere and diffusion theory calculations of fluence rate at the wall of a spherical cavity," *Phys. Med. Biol.* 40(1), 1–8 (1995).

[138] A. Dimofte, T. C. Zhu, et al., "In-vivo Light Dosimetry for Pleural PDT," *Proc. SPIE* 7164, 71640A–1–7 (2009).

[139] A. Dimofte, T. C. Zhu, et al., "In vivo light dosimetry for motexafin lutetium-mediated PDT of recurrent breast cancer," *Lasers Surg. Med.* 31(5), 305–312 (2002).

[140] T. J. Farrell, M. S. Patterson, and B. Wilson, "A diffusion theory model of spatially resolved, steady?state diffuse reflectance for the noninvasive determination of tissue optical properties in vivo," *Med. Phys* 19(4), 879–888 (1992).

[141] A. Dimofte, J. C. Finlay, and T. C. Zhu, "A method for determination of the absorption and scattering properties interstitially in turbid media," *Phys. Med. Biol.* 50, 2291–2311 (2005).

[142] T. C. Zhu, J. C. Finlay, and S. M. Hahn, "Determination of the distribution of light, optical properties, drug concentration, and tissue oxygenation in-vivo in human prostate during motexafin lutetium-mediated photodynamic therapy," *J. Photochem. Photobiol. B* 79(3), 231–241 (2005).

[143] R. J. Crilly, W.-F. Cheong, et al., "Forward-adjoint fluorescence model: Monte Carlo integration and experimental validation," *Appl. Opt.* 36(25), 6513–6519 (1997).

[144] J. C. Finlay and T. H. Foster, "Recovery of hemoglobin oxygen saturation and intrinsic fluorescence with a forward-adjoint model," *Appl. Opt.* 44(10), 1917–1933 (2005).

[145] S. M. Gallagher-Colombo, H. Quon, et al., "Measuring the Physiologic Properties of Oral Lesions Receiving Fractionated Photodynamic Therapy," *Photochem. Photobiol.* 91(5), 1210–1218 (2015).

[146] Y. H. Ong, M. M. Kim, et al., "PDT Dose dosimetry for Photofrin-mediated pleural photodynamic therapy (pPDT)," *Phys. Med. Biol.* In Press (2017).

[147] R. K. Chowdhary, L. G. Ratkay, et al., "Uptake of Verteporfin® by articular tissues following systemic and intra-articular administration," *Biopharm. Drug Dispos.* 19(6), 395–400 (1998).

[148] L. Lilge, C. O'Carroll, and B. C. Wilson, "A solubilization technique for photosensitizer quantification in ex vivo tissue samples," *J. Photochem. Photobiol. B.* 39(3), 229–235 (1997).

[149] T. M. Busch, S. M. Hahn, et al., "Hypoxia and Photofrin uptake in the intraperitoneal carcinomatosis and sarcomatosis of photodynamic therapy patients," *Clin. Cancer Res* 10(14), 4630–4638 (2004).

[150] C. S. Foote, "Definition of type I and type II photosensitized oxidation," *Photochem. Photobiol.* 54(5), 659 (1991).

[151] C. S. Foote, "Photosensitized Oxidation and Singlet Oxygen: Consequences in Biological Systems," in W. A. Pryor, editor, "Free Radicals in Biology," pp. 85–133, Academic Press, New York (1976).

[152] P. P. Mohapatra, C. O. Chiemezie, et al., "31P NMR Evidence for Peroxide Intermediates in Lipid Emulsion Photooxidations: Phosphine Substituent Effects in Trapping," *Photochem. Photobiol.* In Press (2017).

[153] N. R. Gemmell, A. McCarthy, et al., "Singlet oxygen luminescence detection with a fiber-coupled superconducting nanowire single-photon detector," *Opt. Express* 21(4), 5005–5013 (2013).

[154] M. T. Jarvi, M. J. Niedre, et al., "The Influences of Oxygen Depletion and Photosensitizer Triplet-state Dynamic During Photodynamic Therapy on Accurate Singlet Oxygen Luminescence Monitoring and Analysis of Treatment Dose Response," *Photochem. Photobiol.* 87, 223–234 (2011).

[155] F. Wilkinson, W. P. Helman, and A. B. Ross, "Rate constants for the decay and reactions of the lowest electronically excited singlet state of molecular oxygen in solution. An expanded and revised compilation," *J. Phys. Chem. Ref. Data* 24(2), 663–677 (1995).

[156] T. C. Zhu, A. Dimofte, et al., "Light dosimetry at tissue surfaces for small circular fields," *Proc. SPIE* 4952, 56–67 (2003).

[157] Y. H. Ong and T. C. Zhu, "An analytic function for predicting light fluence rate of circular fields on a semi-infinite turbid medium," *Opt. Express* 24(23), 26261–26281 (2016).

[158] L. Wang, S. L. Jacques, and L. Zheng, "MCML-Monte Carlo modeling of light transport in multi-layered tissues," *Comp. Meth. Prog. Biomed.* 47, 131–146 (1995).

[159] S. L. Jacques and L. Wang, "Monte Carlo modeling of light transport in tissues," in A. J. Welch and v. Gemert, editors, "Optical-Thermal response of laser-irradiated tissue," Plenum, New York (1995).

[160] S. A. Prahl, M. Keijzer, et al., "A Monte Carlo model of light propagation in tissue," *Proc. SPIE* IS5, 102–111 (1989).

[161] B. C. Wilson and G. Adam, "A Monte Carlo model for the absorption and flux distributions of light in tissue," *Med. Phys.* 10(6), 824–830 (1983).

[162] S. M. Hahn, M. E. Putt, et al., "Photofrin Uptake in the Tumor and Normal Tissues of Patients Receiving Intraperitoneal Photodynamic Therapy," *Clin. Cancer Res.* 12(18), 5464–5470 (2006).

[163] K. K. Wang, S. Mitra, and T. H. Foster, "Photodynamic dose does not correlate with long-term tumor response to mTHPC-PDT performed at several drug-light intervals," *Med. Phys.* 35(8), 3518–3526 (2008).

[164] B. Chen, B. W. Pogue, et al., "Tumor Vascular Permeabilization by vascular-targeting photosensitization: Effects, Mechanism, and Therapeutic Implications," *Clin. Can. Res.* 12(3), 917–923 (2006).

[165] M. T. Jarvi, M. S. Patterson, and B. C. Wilson, "Insights into Photodynamic Therapy Dosimetry: Simultaneous Singlet Oxygen Luminescence and Photosensitizer Photobleaching Measurements," *Biophys. J.* 102, 661–671 (2012).

[166] C. C. Lee, B. W. Pogue, et al., "Spatial heterogeneity and temporal kinetics of photosensitizer (AlPcS2) concentration in murine tumors RIF-1 and MTG-B," *Photochem. Photobiol. Sci.* 2, 145–150 (2003).

[167] I. Georgakoudi and T. H. Foster, "Singlet Oxygen- Versus Nonsinglet Oxygen-Mediated Mechanisms of Sensitizer Photobleaching and Their Efects on Photodynamic Dosimetry," *Photochem. Photobiol.* 67(6), 612–625 (1998).

[168] T. M. Busch, X. Xing, et al., "Fluence rate-dependent intratumor heterogeneity in physiologic and cytotoxic responses to Photofrin photodynamic therapy." *Photochem. Photobiol. Sci.* 8(12), 1683–1693 (2009).

[169] T. C. Zhu, A. Lu, and Y.-H. Ong, "An improved analytic function for predicting light fluence rate in circular fields on a semi-infinite geometry," *Proc. SPIE* 9706, 97061D (2016).

[170] M. M. Kim, R. Penjweini, et al., "Singlet oxygen explicit dosimetry to predict long-term local tumor control for BPD-mediated photodynamic therapy," *Proc. SPIE* 10047, 100470X (2017).

[171] R. Penjweini, M. M. Kim, et al., "Evaluation of the 2-(1-Hexyloxyethyl)-2-devinyl pyropheophorbide (HPPH) mediated photodynamic therapy by macroscopic singlet oxygen modeling," *J. Biophotonics* 9(11-12), 1344–1354 (2016).

[172] T. C. Zhu, X. Liang, et al., "An IR Navigation System for Pleural PDT," *Front. Phys.* 3(9), 1–12 (2015).

[173] T. C. Zhu, M. M. Kim, et al., "Real-time treatment light dose guidance of Pleural PDT: an update," *Proc. SPIE* 9308, 930809–1–6 (2015).

[174] T. C. Zhu, M. M. Kim, et al., "A summary of light dose distribution using and IR navigation system for Photofrin-mediated Pleural PDT," *Proc. SPIE* 10047, 1004709–1–7 (2017).

[175] T. C. Zhu, X. Liang, et al., "A real-time treatment guidance system for pleural PDT," *Proc. SPIE* 8210, 82199A–1–8 (2012).

[176] G. Weagle, P. E. Paterson, et al., "The nature of the chromophore responsible for naturally occurring fluorescence in mouse skin," *J. Photochem. Photobiol. B* 2(3), 313–320 (1988).

[177] H. Holmes, J. C. Kennedy, et al., "A recipe for the preparation of a rodent food that eliminates chlorophyll-based tissue fluorescence," *J. Photochem. Photobiol. B* 29(2-3), 199 (1995).

[178] A. Ishimaru, *Wave Propagation and Scattering in Random Media*, Oxford Univ. Press, Oxford, UK (1997).

[179] W. M. Star, "Light Dosimetry in vivo," *Phys. Med. Biol.* 42, 763–787 (1997).

[180] L. G. Henyey and J. L. Greenstein, "Diffuse radiation in the galaxy," *Astrophys. J.* 93, 70–83 (1941).

[181] E. L. Hull and T. H. Foster, "Steady-state reflectance spectroscopy in the P3 approximation," *J. Opt. Soc. Am. A* 18(3), 584–599 (2001).

[182] D. A. Boas, *Diffuse Photon Probes of structure and dynamic properties of turbid media: Theory and biomedical application*, Thesis, University of Pennsylvania (1996).

[183] R. C. Haskell, L. O. Svaasand, et al., "Boundary conditions for the diffusion equation in radiative transfer," *J. Opt. Soc. Am. A* 11(10), 2727–41 (1994).

[184] J. D. Jackson, *Classical Electrodynamics*, John Wiley & Sons, Inc., New York, second edition (1975).

[185] D. A. Boas, H. Liu, et al., "Photon migration within the P3 approximation," *Proc. SPIE* 2389, 240–247 (1995).

[186] D. A. Boas, L. E. Campbell, and A. G. Yodh, "Scattering and imaging with diffusing temporal field correlations," *Phys. Rev. Lett.* 75(9), 1855–1858 (1995).

[187] B. Davison, *Neutron Tranport Theory*, Oxford Univ Press, Oxford (1957).

[188] H. Dehghani, B. Brooksby, et al., "The effects of internal refractive index variation in near-infrared optical tomography: a finite element modelling approach," *Phys. Med. Biol.* 48, 2713–2727 (2003).

[189] J. B. Fishkin, S. Fantini, et al., "Gigahertz photon density waves in a turbid medium: theory and experiments," *Phys. Rev. E* 53, 2307–2319 (1996).

[190] K. M. Case and P. F. Zweifel, *Linear Transport Theory*, Addison-Wesley Publishing Company, Reading, MA (1967).

[191] D. J. Dickey, R. B. Moore, et al., "Light dosimetry using the P3 approximation," *Phys. Med. Biol.* 45, 2359–2370 (2001).